Dissertation

submitted to the
Combined Faculties of the Natural Sciences and Mathematics
of the Ruperto-Carola-University of Heidelberg, Germany
for the degree of
Doctor of Natural Sciences

Put forward by
MSc. Physics Veit Walter Stooß
born in Reutlingen

Oral examination: July 11th, 2018

Strong-Field Spectroscopy: From Absorption to Time-Resolved Dynamics in Strong Fields

Referees: **Prof. Dr. Thomas Pfeifer**
Prof. Dr. Selim Jochim

Deutsche Zusammenfassung Das Thema dieser Arbeit ist die Elektronendynamik atomarer Systeme zu untersuchen, die mit starken und kurzen Laserfeldern wechselwirken. Hierzu wird die sogenannte Methode der Starkfeld-Spektroskopie verwendet, für die in dieser Arbeit eine neue Technik der simultanen Aufnahme von Absorptions- und Referenzsignal entwickelt wird. Diese gleichzeitig gemessene Referenz erhöht die Sensitivität signifikant und ermöglicht so die Beobachtungen kleinster zeitabhängiger Absorptionsänderungen. Zusätzlich wird eine Methode zur Rekonstruktion der komplexen zeitabhängigen Dipolantwort aus einem einzigen Absorptionsspektrum eingeführt. Diese erlaubt die explizit zeitabhängige Dynamik angeregter Zustände zu untersuchen, die nichtlinear von einem starken Laserpuls beeinflusst werden. Beide Techniken werden in der Starkfeld-Spektroskopie kombiniert, um die nichtlineare Dynamik in starken Laserfeldern von atomaren und molekularen Systemen zu beobachten. Als erste Anwendung wird die Dynamik in stark korrelierten doppelt angeregten Zuständen in Helium untersucht. Weiterhin wird eine Messmethode im Rahmen der Starkfeld-Spektroskopie präsentiert, welche die Wechselwirkung mit Laserpulsen hoher Intensität nutzt, um der kohärenten Antwort eines Quantensystems ein künstliches Zeitfenster aufzuerlegen. Diese Methode kann dazu genutzt werden den zeitabhängigen Aufbau von Resonanzphänomenen in physikalischen Systemen zu studieren und wird erfolgreich auf die Messung des zeitabhängigen Ausbildung einer Fano-Resonanz und einer Rydberg-Serie hoch angeregter Zustände angewendet.

English Abstract The goal of this work is to study and understand dynamics of atomic systems interacting with strong fields. To this end, a method referred to as strong-field spectroscopy is used, which measures the absorption spectrum of atoms interacting with such fields. In the scope of this work, a technique which allows the simultaneous measurement of absorption spectra of attosecond pulses and their reference signal is developed, which significantly increases the sensitivity to absorption changes. Additionally, a reconstruction method is introduced which retrieves the time-dependent evolution of the dipole response of an atomic system directly from a single absorption spectrum. Strong-field spectroscopy combines these techniques to examine the nonlinear strong-field dynamics in atomic and molecular systems and is applied to study the strongly correlated doubly excited states in helium. Furthermore, a measurement approach is introduced which uses the interaction with a high-intensity laser pulse to impose a time gate on the evolution of the coherent response of a system, which has previously been excited by an ultrashort laser pulse. With this approach the buildup of resonance phenomena in a wide range of physical systems can be studied. As a first application, the time-dependent buildup of a Fano resonance as well as the buildup of a whole Rydberg series are investigated.

List of Publications

Parts of this work have been published or prepared in the following references:

V. Stooß, S. Donsa, S.M. Cavaletto, A. Blaettermann, P. Birk, C.H. Keitel, I. Brezinova, J. Burgdörfer, C. Ott and T. Pfeifer *Real-time reconstruction of complex non-equilibrium quantum dynamics of matter*.
arXiv:1706.07218 (2017).

A. Kaldun, A. Blättermann, V. Stooß, S. Donsa, H. Wei, R. Pazourek, S. Nagele, C. Ott, C. D. Lin, J. Burgdörfer and T. Pfeifer
Observing the ultrafast buildup of a Fano resonance in the time domain.
Science **354**, 738–741 (2016).

Further publications with own contributions:

V. Stooß, A. Kaldun, A. Blättermann, T. Ding, C. Ott, and T. Pfeifer.
Inversion symmetry breaking of atomic bound states in strong and short laser fields.
arXiv:1506.01182 (2015).

A. Blättermann, C. Ott, A. Kaldun, T. Ding, V. Stooß, M. Laux, M. Rebholz, and T. Pfeifer.
In situ characterization of few-cycle laser pulses in transient absorption spectroscopy.
Opt. Lett. **40**, 3464–3467 (2015).

T. Ding, C. Ott, A. Kaldun, A. Blättermann, K. Meyer, V. Stooß, M. Rebholz, P. Birk, M. Hartmann, A. Brown, H. Van Der Hart and T. Pfeifer
Time-resolved four-wave-mixing spectroscopy for inner-valence transitions.
Opt. Lett. **41**, 709–712 (2016).

Contents

Abstract v

List of Publications vii

1. Introduction 1

2. Theoretical Background 5
2.1. Description and Generation of Strong and Ultrashort Laser Pulses 5
2.1.1. Mathematical Description 6
2.1.2. Generation of Optical Femtosecond Laser Pulses 10
2.2. Interaction with Strong Fields 13
2.2.1. Strong-field Ionization 15
2.2.2. Creation of Attosecond Pulses with High-Harmonic Generation . 17
2.3. Quantum Dynamics 19
2.3.1. Time-Dependent Perturbation Theory 20
2.3.2. Field Driven n-Level Systems 22
2.4. Multi-Electron Systems 25
2.4.1. Autoionization and Fano Theory 26
2.4.2. Interaction with Strong Fields 29
2.4.3. The Helium Atom 30
2.5. Absorption Spectroscopy in the Time Domain 33
2.5.1. Linear Response Theory 33
2.5.2. The Time-Dependent Dipole Response 35
2.5.3. Linear Absorption & Lambert–Beer's Law 38

3. Numerical Methods 41
3.1. Discrete Basis TDSE 41
3.1.1. Hamilton Operator and Interactions for Doubly Excited Helium . 42
3.1.2. Autoionization and Strong-Field Ionization 44
3.1.3. Numerical Solution 44
3.2. *Ab-initio* 1D TDSE for Two Electrons 45
3.2.1. Hamilton Operator and Interactions 45
3.2.2. Wave Function Interpretation 46
3.2.3. Numerical Solution 47
3.3. *Ab-initio* 3D TDSE for Helium 48

4. Experimental Setup 51
4.1. Laser System & Optical Pulse Characterization 53
4.1.1. Femtosecond Laser System 53
4.1.2. Characterization of Optical Pulses 56
4.2. Experimental Setup for Time Resolved Absorption Spectroscopy 58
4.2.1. High-Harmonic Generation 58
4.2.2. Pulse Control & Interferometric Setup 59
4.2.3. Experimental Target & High-Resolution XUV Spectrometer . . . 64
4.3. Data Acquisition & Evaluation 66
4.4. *In-Situ* Reference Spectrometer for High Sensitivity Transient Absorption Measurements 67

5. Strong-field Spectroscopy 73
5.1. Reconstruction of Strong-Field-Driven Temporal Responses 73
5.1.1. Mathematical Proof of Full Response Reconstruction 76
5.1.2. Fourier Reconstruction for Finite Pulse Duration 78
5.1.3. Numerical Proof of Viability for Complex Systems 80

5.2. Real-Time Response of Strongly Driven Doubly Excited Helium 82
5.2.1. Experimental Data 83
5.2.2. Application of the Reconstruction to Measured Spectra 85
5.2.3. Normalization and Correction for Spectrometer Resolution 87
5.2.4. Determining the Error of the Reconstructed Response 88
5.2.5. Real-Time-Resolved Response of the 2s2p Helium State in Strong Fields 88
5.2.6. Time-Delay-Dependence of the Response 93
5.3. Studying Electron Correlation in States with Different Symmetries 94
5.3.1. Experimental Results 96
5.3.2. Analysis of $sp_{2,n+}$ and $sp_{2,n-}$ Series 98
5.4. Intensity-Dependent Ionization Threshold for Different Excited-State Manifolds in Helium 101
5.4.1. Experimental Data 102
5.4.2. Numerical 1D-TDSE Simulations 104

6. Observation of Resonance Buildup 107
6.1. Observing Ultrafast Processes with Time-Gating based on Strong-Field Ionization 107
6.2. Time-Resolved Buildup of a Fano Resonance 107
6.2.1. Experimental Results 109
6.2.2. Comparison to Theoretical Models 110
6.3. Time-Resolved Buildup of a Rydberg Series 112
6.3.1. High Resolution Time-Delay Scan 112
6.3.2. Comparison to Dipole Control Model 113

7. Conclusion and Outlook 117

A. Atomic Units 121

B. Numerical Simulations of Helium: Equations of Motion 123
B.1. Few-Level Model 123
B.2. Few-Level Model for Complex Systems 125

C. NIR Pulse Characterization 127
C.1. Response Reconstruction and Fano Resonance Buildup Measurements . . 127
C.1.1. Temporal Characterization 127
C.1.2. Intensity Calibration 128
C.2. $sp_{2,n\pm}$ and Rydberg Buildup Measurements 128
C.2.1. Temporal Characterization 128
C.2.2. Intensity Calibration 128

Bibliography 129

Danksagung 155

1. Introduction

Time and the dynamical changes of matter depending on it are fundamental aspects of nature. While many dynamic (time-dependent) events, like the trajectory of a thrown ball, cooking food, the growth of plants or the passing of the celestial objects like the sun can be easily observed by humans, already the course of the fast motion of the legs of a galloping horse was unclear until the 1870s, when a recording method was invented which could take images in fast enough succession to sample the motion accurately and conclusively [1]. For all these processes, not only the beginning or the end is significant, but especially the dynamic evolution is of importance if they are to be understood or even controlled. However, the observation of any time-dependent process which takes place on time scales outside the human perception, which can be assumed between milliseconds up to a few years requires additional tools. This becomes clear when moving away from human scales toward macroscopic or cosmic scales where processes like galaxy and star formation or the evolution of life take place, or when going to the microscopic quantum world governed by processes like chemical and nuclear reactions which are elementary for matter on larger scales and life as we know it. This work is concerned with the study of dynamic processes in atoms and molecules on their associated natural time scale of few femtoseconds (10^{-15} s) down to attoseconds (10^{-18} s). On this scale, electronic motion in atoms, molecules and solids as well as nuclear motion in molecules and solids determine the fundamental dynamic processes. They include breaking and formation of chemical bonds, formation of complex molecules out of simpler building blocks as well as their final alignment (folding of DNA double helix), charge migration and lattice dynamics in crystals or in general solid compounds (e.g. organic semi conductors) and signal processing on ultrafast time scales.

As it was the case with the motion of the galloping horse, these unimaginably fast dynamics can only be studied if it is possible to sample the motion multiple times during its evolution. Thus events shorter than the observed dynamics are needed. For processes depending on electronic motion, the interaction with ultrashort pulses of electromagnetic radiation is a widespread method used to fulfill this requirement. Recent years have seen great development in sources capable of producing such pulses. Depending on their duration, energy and generation method, they can have very different properties. Progress in laser technology lead to the technique of Kerr-lens modelocking [2], which was pushed to provide laser pulses in the infrared and visible spectral range of durations down to a few femtoseconds [3–5]. These pulses are already short enough to study nuclear motion in molecules [6]. Furthermore, as they can reach intensities of $\sim 10^{16}$ W/cm^2, they are also frequently used to drive strongly non-linear dynamics in quantum systems. Even shorter time scales became accessible through the discovery of high-order harmonic generation (HHG) [7–10] a non-linear frequency-conversion process, typically driven by the above

mentioned femtosecond pulses. Using the interaction of the resulting attosecond pulses in the extreme ultraviolet spectral range with microscopic quantum systems, the measurement of the fast motion of valence electrons in atoms and molecules came within reach for the first time.

The dynamics of such microscopic systems and their interaction with electromagnetic fields (of moderate intensities as stated above) are described by non-relativistic quantum mechanics and governed by the time-dependent Schrödinger equation

$$i\hbar\frac{\partial}{\partial t}\left|\Psi(t)\right\rangle = \hat{H}\left|\Psi(t)\right\rangle, \tag{1.1}$$

which is the general equation of motion for a system represented by the quantum state $|\Psi(t)\rangle$, where the Hamilton operator $\hat{H}$ describes the energy of the system. Furthermore, following this equation, the time evolution can be described by the operator with the same name $\hat{U}(t) = \exp[-i\hat{H}t]$. The form of $\hat{U}(t)$ immediately shows that the dynamics of the general state $|\Psi(t)\rangle$ are encoded in complex phases and that these phases are directly related to the energy and the time dependence in the system. This means that by measuring the phase evolution of a system at different energies, access to its time evolution can be attained. Unfortunately, the direct measurement of (absolute) phases is not possible, because detectors with high enough resolution and sensitivity do not exist yet. The solution to this problem is the powerful concept of interferometry which can determine phase changes with very high sensitivity. Usually, changes of an observable, which is related to the phase evolution of the system, are detected with high precision. The most prominent example for this technique in recent time is the detection of gravitational waves [11]. Here, the changes in space itself caused by the gravitational waves are observed by very precisely measuring distances using laser interferometry. A very well accessible experimental observable for quantum systems, which is directly related to their phase evolution, is the energy of particles or photons interacting with or emitted by the system. While techniques based on time-of-flight measurements are used to determine the energies of particles like electrons and ions leaving the system, dispersive spectrometers measure the response to interactions with photons. Using photons as a probe of a system's time-evolution is especially useful for several reasons. First, the emission of photons is determined by the motion of the charge distribution in the atom, which in turn is characterized by the involved quantum states and their relative phases. Thus, measuring them gives direct access to bound state dynamics. Second, any interferometric technique requires a reference which has very well defined phase properties itself, or in other words possesses a high level of coherence. The ultrashort laser pulses acting as probes of the quantum mechanical system meet this requirement. Third, the Fourier-relation between time and energy [12] directly shows that in any process, temporal duration and frequency bandwidth are directly related. Thus, laser pulses capable of probing ultrafast dynamics display a very broad spectral bandwidth which can in turn be used for interferometric measurements on a wide range of energies simultaneously. Finally, the coherence properties of the laser pulses can also provide control over the phases of the quantum systems by coupling quantum states of different energies, shifting their energies or trigger ionization processes.

Making use of these advantages, many experimental techniques employing ultrashort laser pulses as probes of electronic and nuclear dynamics in atoms, molecules and solids have been developed. In general, two or more pulses interact with the system of interest in a pump–probe configuration, where one pulse initiates dynamics and the other pulses detect the dynamical changes in the system depending on the temporal separation between the pulses. One technique measuring the response of the system to these pulses based on photon detection is called transient absorption spectroscopy (TAS). While it was first used to study nuclear dynamics in molecules using femtosecond pulses, it was extended to the domain of electron dynamics with the advent of attosecond pulse production based on HHG. In attosecond transient absorption spectroscopy, femtosecond and attosecond pulses are used in a pump–probe measurement scheme, where the response of the system to the attosecond pulse in the extreme ultraviolet spectral range is measured. The spectrally extremely broad attosecond probe pulses propagate together with the radiation resulting from the electronic response of the quantum system to the spectrometer. The dispersive element then separates the spectral components according to their energy making each component infinitely long. The spectral contributions of the probing field and the system's response interfere on the detector, which creates absorption features following the phase information imprinted on each spectral component by the dynamic response of the system. This information can be modified by the additional (femtosecond) pulse(s). Usually, time-dependent information about the dynamic processes is gained by varying the time delay between the interaction events and examining the changes in the observable spectrum.

This work introduces new measurement concepts to the well established ATAS technique. These concepts utilize the nonlinear interaction with a strong femtosecond pulse in a method referred to as Strong-Field Spectroscopy (SFS). This approach tries to understand the dynamics induced in excited atoms and molecules by very strong and short electric fields. To this end, a method for reconstructing the full time-dependent dipole response of a system in a non-equilibrium state from a single absorption spectrum is presented first. It is based on linear response theory and a time-domain picture of absorption, which will be presented in the course of this work. The idea is, that a precisely determined spectral line shape of a resonance already carries the full information of the dynamic response of the underlying quantum state even if it is additionally modified by strong interactions. Furthermore, a new method of measuring a spectral reference signal for the ultrashort attosecond pulses is presented, which significantly increases the sensitivity to time-dependent changes in the absorption spectrum. Combined with the SFS method, this is used to study the strong field dynamics of different excited state configurations in helium, including access to the correlated motion and dynamics of its two electrons. Second, a timing gate technique using the strong femtosecond pulse within the SFS approach is introduced and applied to the measurement of the buildup of the spectral line of an autoionizing Fano resonance in helium. Building on this, the timing gate method is used to study the formation of the very closely spaced and highly excited states of a Rydberg series.

This thesis is structured in the following chapters: in chapter 2, the basic concepts of light-

matter interaction and its time-dependent mathematical treatment are introduced, together with response theory and a time-domain picture of absorption as a precursor to the presented reconstruction method. In chapter 3, the main numerical methods and models used to describe the dynamics of multi-electron dynamics in atoms are presented. This includes few-level and *ab-initio* simulations. In chapter 4, an overview of the experimental techniques and the setup that was used for the time-resolved SFS measurements is given. Furthermore, the data acquisition and evaluation as well as a newly developed technique for measuring an *in-situ* reference in the extreme ultraviolet spectral range is discussed. In chapter 5, the first main result, the reconstruction of the full time-dependent dipole response from absorption measurements using attosecond trigger pulses is presented. Afterwards, in chapter 6, the results of different applications of SFS in helium are discussed. Finally, chapter 7 gives a short summary and an outlook on possible applications and future developments of the presented concepts and results.

2. Theoretical Background

The general goal of this work is to investigate the nature of light-matter interaction on the natural time scale of electronic motion using absorption spectroscopy. As an interaction itself implies time dependence, it is necessary to introduce concepts that allow the description of light, matter and their dynamic interaction in a time-dependent manner. This chapter presents these fundamental theoretical concepts of the physics of ultrafast and strong light fields, as well as atomic systems and their time evolution. In the first section the basics of the generation of ultrashort pulses and their mathematical description are discussed. In the second part the treatment of the quantum n-level system together with the concepts of time-dependent perturbation theory are described. The main quantity relating matter and light is the time-dependent dipole response. It is introduced in the third section together with a time-domain picture of absorption. Finally the physics of different strong-field ionization mechanisms relevant to the investigation of multi-electron dynamics in strong laser fields are reviewed. Unless stated otherwise, the equations in this chapter are given in atomic units.

2.1. Description and Generation of Strong and Ultrashort Laser Pulses

For the resolution of dynamics on very short time scales the tools used for their observation need to possess controllable properties on the same or even shorter time scale. A prominent example being the shutter of a camera which has to be faster than the motion it records in order to sample different distinct points during the motion. In the realm of atoms and molecules the typical time scale of motion ranges from picoseconds for rotations down to attoseconds for electronic dynamics. The shutter needed to observe these dynamics is nowadays realized by ultrashort laser pulses. The uncertainty principle linking time and energy [13], reading

$$\Delta E \Delta t \geq \frac{\hbar}{2}, \tag{2.1}$$

shows that for such pulses to be realized, a very broad spectrum and knowledge of the behavior of the relative phase between the spectral components during generation and propagation is necessary. This relation can also be understood in the framework of Fourier analysis [12], which provides a link between time-domain and energy/frequency-domain descriptions of physical phenomena. In this section, a general formalism for the treatment of these pulses and the techniques used to generate them are presented. More detailed information can be found in review articles [14–16] and the following textbooks [17–19].

2.1.1. Mathematical Description

As a measurable quantity, the electric field of an ultrashort linearly polarized light pulse at a given point in space can be described by a one-dimensional real-valued function of time $E(t)$. This function can be decomposed into the slowly varying pulse envelope $\mathcal{E}(t)$ and a more rapidly oscillating term describing the carrier wave:

$$E(t) = \mathcal{E}(t)\cos[\phi(t)]. \tag{2.2}$$

For mathematical convenience $E(t)$ can be written in complex form, where the real part still represents the measurable physical quantity:

$$E(t) = \mathcal{E}(t)\exp[i\phi(t)]. \tag{2.3}$$

The shape of $\mathcal{E}(t)$ gives the overall temporal structure and duration of the pulse which is commonly defined as the full width at half maximum (FWHM) of the intensity profile $I(t)$ where $I(t) \propto \mathcal{E}(t)^2$. In general, $\mathcal{E}(t)$ is non-trivial but is often approximated by analytical functions (Gaussian, $\cos^2$, sech^2) in theory. For the Gaussian case, the envelope and duration are given by

$$\mathcal{E}_G(t) = \mathcal{E}_0 \exp\left[-\left(\frac{t}{t_G}\right)^2\right] \text{ and } t_G = \frac{t_{FWHM}}{\sqrt{2\ln 2}} \approx 0.849 \cdot t_{FWHM}, \tag{2.4}$$

respectively. Using a Taylor expansion the temporal phase $\phi(t)$ can be written as

$$\phi(t) = \sum_{k=0}^{\infty} \frac{\phi(t-t_0)^{(k)}}{k!}(t-t_0)^k|_{t_0=0} = \phi_{CEP} + \omega_c t + \phi_{(2)}t^2 + \phi_{(3)}t^3 + ... \tag{2.5}$$

In this expansion ϕ_{CEP} stands for the constant phase shift between the pulse envelope and the carrier wave which in the literature is called 'carrier-envelope phase' (CEP). This phase becomes important once the pulse duration is on the order of one cycle of the carrier wave. In this case ϕ_{CEP} significantly determines the wave form as well as the intensity distribution and maximum intensity (as shown in figure 2.1). The frequency ω_c gives the central frequency of the carrier wave and $\phi_{(k)}$ ($k \geq 2$) are constants of higher order phase variations which lead to a modulation of the frequency across the pulse. This can be further understood by calculating the instantaneous frequency (rate of phase change) defined as:

$$\omega_{inst} = \frac{\mathrm{d}\phi(t)}{\mathrm{d}t} = \omega_c + \frac{\mathrm{d}\Phi(t)}{\mathrm{d}t}, \text{with } \Phi(t) = \phi_{(2)}t^2 + \phi_{(3)}t^3 + ..., \tag{2.6}$$

where ω_c is the carrier frequency of the pulse. The instantaneous frequency ω_{inst} only changes if the non-linear phase $\Phi(t) \neq 0$ which is the case if any of the constants $\phi_{(k)}$ ($k \geq 2$) are non-zero. In this case, the pulse is considered chirped because its frequency

changes over its duration. The first non-constant term of the instantaneous frequency $\omega_{inst,2} = 2\phi_{(2)}t$, it shows that for $\phi_{(2)} > 0$ the frequency linearly increases ('up-chirped') and if $\phi_{(2)} < 0$ the frequency decreases linearly ('down-chirped'). Higher order terms in $\Phi(t)$ contribute non-linear chirps to the frequency behavior of the pulse. An equivalent mathematical description can be given in the frequency domain. It is connected to the time domain field $E(t)$ via its Fourier transform:

$$\tilde{E}(\omega) = \mathcal{F}[E(t)] = \frac{1}{\sqrt{2\pi}} \int_{+\infty}^{-\infty} E(t) \exp[-i\omega t]\, \mathrm{d}t, \tag{2.7}$$

$$E(t) = \mathcal{F}^{-1}[\tilde{E}(\omega)] = \frac{1}{\sqrt{2\pi}} \int_{+\infty}^{-\infty} \tilde{E}(\omega) \exp[i\omega t]\, \mathrm{d}t. \tag{2.8}$$

The spectrum $\tilde{E}(\omega)$ is complex valued and symmetric around $\omega = 0$, because $E(t)$ is a real valued function. As for the time-domain field, the frequency domain representation can be expressed with an envelope $\tilde{\mathcal{E}}(\omega)$ and a phase function $\tilde{\phi}(\omega)$:

$$\tilde{E}(\omega) = \tilde{\mathcal{E}}(\omega) \exp[-i\tilde{\phi}(\omega)]. \tag{2.9}$$

The spectral phase can also be analyzed using a Taylor expansion similar to equation 2.5:

$$\tilde{\phi}(\omega) = \sum_{k=0}^{\infty} \frac{\phi(\omega_c)^{(k)}}{k!} (\omega - \omega_c)^k \tag{2.10}$$

$$= \tilde{\phi}_0 + \tau_{GD}(\omega - \omega_c) + \chi_{GDD}(\omega - \omega_c)^2 + \chi_{TOD}(\omega - \omega_c)^3 + ... \tag{2.11}$$

Analogous to the instantaneous frequency a relation giving the derivative of the spectral phase can be introduced, which yields the temporal shift of the spectral components with respect to each other:

$$\tau(\omega) = \frac{\mathrm{d}\tilde{\phi}(\omega)}{\mathrm{d}\omega} = \tau_{GD} + \frac{\mathrm{d}\tilde{\Phi}(\omega)}{\mathrm{d}\omega}, \text{with } \tilde{\Phi}(\omega) = \chi_{GDD}(\omega - \omega_c)^2 + \chi_{TOD}(\omega - \omega_c)^3 + ... \tag{2.12}$$

Again the first two terms of equation 2.11 do not affect the shape or duration of the pulse, the second term, linear in ω describes a temporal shift of the pulse by the retardation time τ_{GD} which is the mean delay of all spectral components and also known as the group delay of the pulse. The third term again represents a chirp where the frequency components are linearly shifted and thus arrive at different times, while the fourth term introduces non-linear chirp. χ_{GDD} and χ_{TOD} are related to the group delay dispersion (GDD) and third order dispersion (TOD). A chirped pulse no longer minimizes the time-bandwidth product which means that it is no longer as short as the spectral bandwidth would allow (it no longer saturates 2.1) as can be seen in figure 2.1. The frequency dependent delay characterized by equation 2.12 shows that for chirped pulses different spectral components arrive at times different from the group delay τ_{GD}. For linear chirps this leads to an increase in pulse duration while for higher order chirps. For higher order chirps higher

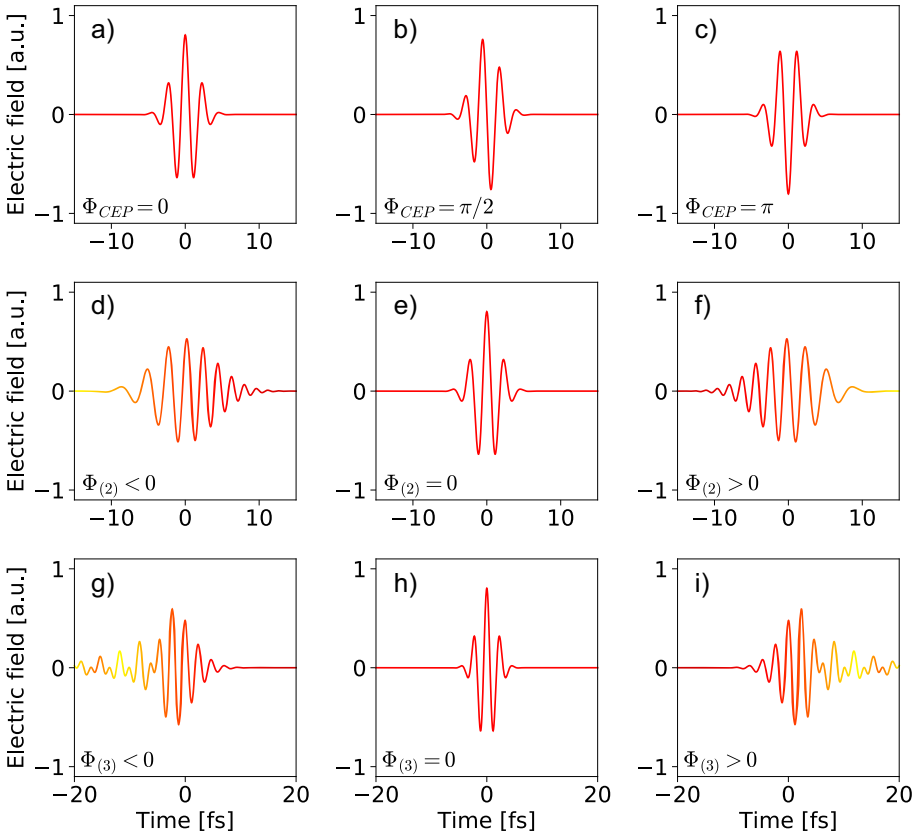

Figure 2.1.: **Pulse Characteristics for different parameters $\phi_{(k)}$.** Panels a)-c) show unchirped few-cycle pulses with varied carrier envelope phase (CEP). In this regime the CEP is already important for the maximum field strength of the pulse. Plots d)-f) illustrate the effect of second order phase terms $\phi_{(2)} \neq 0$ which chirp the pulse linearly, meaning the frequency changes linearly across the duration of the pulse. In panels g)-i) pulses with $\phi_{(3)} \neq 0$ are shown. Different frequency components interfere on the same side of the pulse, which creates pre/post pulses to the pulse shape. Only pulses without additional phase terms are transform limited and display the shortest possible pulse duration.

and lower frequency components can be shifted to a single side of the pulse leading to interference (beating) and the formation of pre- or post pulses.

Such dispersion effects occur when a pulse travels through and interacts with a (linear) dielectric medium during propagation. In the simplest case, the equation of motion for the propagation of electromagnetic fields through a dielectric medium in one dimension is given in the frequency domain by the Helmholtz equation

$$\left[\frac{\partial^2}{\partial z^2} + k^2\right] \tilde{E}(\omega, z) = 0. \tag{2.13}$$

Because of the superposition principle, any laser pulse can be decomposed into a coherent sum over a range of monochromatic waves. Considering plane waves, the solution of the

homogeneous equation 2.13 is given by

$$\tilde{E}(\omega,z) = \tilde{E}(\omega,0)\exp\left[+ik(\omega)z\right], \tag{2.14}$$

where $\tilde{E}(\omega,0)$ is the spectral amplitude according to equation 2.9 and $k(\omega)$ is the wave vector which is proportional to the frequency-dependent refractive index $n(\omega)$:

$$k(\omega) = \frac{\omega}{c}\cdot n(\omega) \tag{2.15}$$

The impact of $n(\omega)$ on the phase can be approximately obtained by expanding $k(\omega)$ in a Taylor series around the central frequency ω_c:

$$k(\omega) = \frac{\omega_c}{c}n(\omega_c) + \left[\frac{n(\omega_c)+n'(\omega_c)\omega_c}{c}\right](\omega_c-\omega) + \frac{1}{2}\left[\frac{2n'(\omega_c)+n''(\omega_c)\omega_c}{c}\right](\omega_c-\omega)^2 + ..., \tag{2.16}$$

where c is the speed of light. Here, the first-order coefficient $\mathrm{d}k(\omega_c)/\mathrm{d}\omega$ can be identified as the inverse group velocity (GV) v_g and the second-order coefficient gives the group velocity dispersion (GVD) in terms of $n(\omega)$. Comparing this to equation 2.11 expressions for group delay τ_{GD} and group delay dispersion χ_{GDD} depending on the material properties can be derived:

$$\tau_{GD} = \frac{n(\omega_c)+n'(\omega_c)\omega_c}{c}\,z\,,\ \chi_{GDD} = \frac{1}{2}\frac{2n'(\omega_c)+n''(\omega_c)\omega_c}{c}\,z. \tag{2.17}$$

The pulse will only propagate without distortion if the condition $n(\omega) = n_{const}$ holds, which for frequencies in the optical spectral range can only be achieved in vacuum. The frequency-dependent delay imprinted on a pulse propagating along the z-direction by a dielectric material is given by applying equation 2.12 to the phase of the wave in 2.14:

$$\tau_{prop}(\omega,z) = -t + \tau_{GD}\,z + \chi_{GDD}(\omega_c-\omega)z \tag{2.18}$$

up to second order. The influence of propagation in media with frequency dependent dispersion is illustrated in figure 2.2. The material properties $n(\omega)$, $\mathrm{d}n/\mathrm{d}\omega$ and $\mathrm{d}^2n/\mathrm{d}\omega^2$ are positive in the most common materials (e.g. air, glass) which will cause a propagating pulse to become both delayed and more positively chirped for increasing travel distance z by optical elements in its path.

For example 1 mm of fused silica introduces $+35\mathrm{fs}^2$ at a wavelength of 800 nm, meaning adjacent spectral components will be delayed by 35fs per Petahertz with respect to this wavelength. Thus, this is especially problematic for optics used with pulses which possess very broad bandwidth, because as stated above these dispersion effects will increase pulse duration and distort the pulse shape. These effects can be compensated by optical elements which exhibit negative GVD and in turn introduce negative chirp. Examples for such devices are setups with angular dispersive elements which separate the spectral components such that the low frequency components can travel longer optical paths than the high frequency parts. Another possibility are multilayer mirrors [20] which achieve the same effect by reflecting lower frequency components deeper inside the mirror than higher frequencies. By precisely designing the thickness of the layers as a function of depth an almost arbitrary phase change can be introduced to compensate propagation effects. The concepts described in this section are important for building experiments which utilize pulse shaping [21, 22] and realizing light sources which generate pulses in the femtosecond regime. The latter one will be discussed in the next sections.

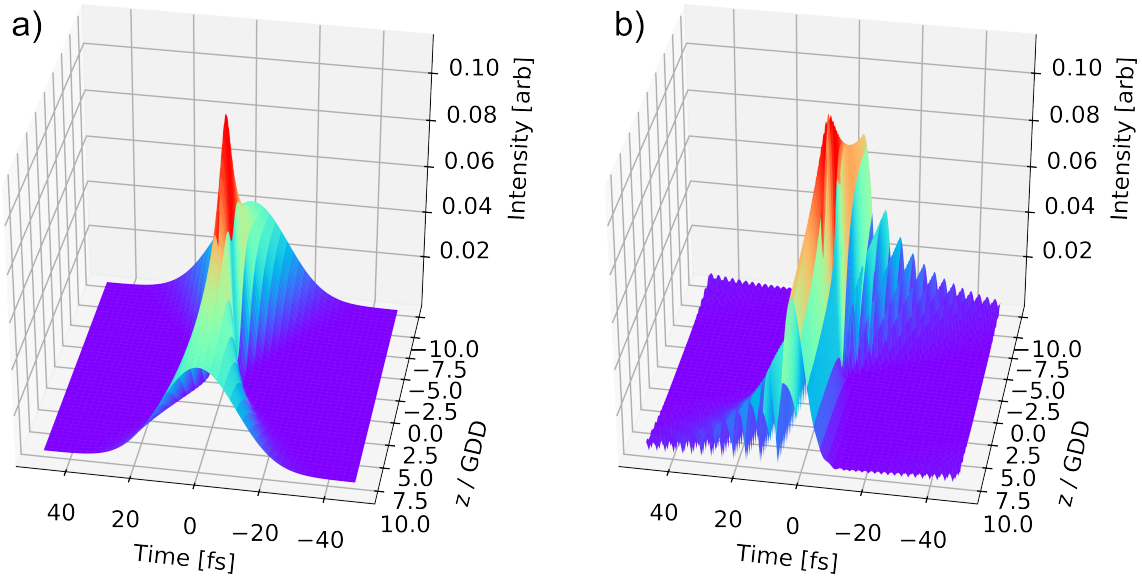

Figure 2.2.: **Second and third order dispersion effects on pulse propagation:** a) Effect of non-zero GDD on the pulse shape depending on propagated distance z in a medium. b) Propagation effect for a medium with non-zero TOD. This shows, that in both cases there is an optimum material thickness to achieve the shortest possible pulse. If this thickness is varied in an experiment it can be used to optimize the pulse duration.

2.1.2. Generation of Optical Femtosecond Laser Pulses

Most modern state-of-the-art experiments using strong fields and ultrafast laser pulses rely on titanium sapphire laser technology for the production of strong femtosecond pulses. In this section the working principles of these laser systems will be introduced while the actual laser system used in this work will be discussed later on. Generally, the first stage of common laser systems for ultrafast pulse production is the broadband femtosecond oscillator which provides pulses used to seed a subsequent amplification stage [23,24]. The main principle for pulsed operation of the oscillator cavity is known as modelocking [25]. It refers to a method of forcing a large number of longitudinal resonator modes which have to fulfill $\nu_k = k \cdot c_0/2L$ (c_0 speed of light, L resonator length, k integer) to oscillate in phase while staying in a single transverse mode of the resonator [26] (preferably TEM_{00}). The superposition of these modes, defined by the cavity, also called frequency comb [27] results in a train of pulses separated by the repetition rate which is related to the mode spacing:

$$\nu_{rep} = \frac{1}{\tau_{RT}} = \frac{c_0}{2L} = \frac{(k+1)c_0}{2L} - \frac{kc_0}{2L} = \nu_{k+1} - \nu_k = \delta\nu, \tag{2.19}$$

with τ_{RT} being the cavity round trip time. Typical repetition rates range from ~ 10 MHz up to few GHz. The stable operation of a modelocked cavity requires a mechanism which favors pulsed over continuous operation. Self-amplitude modulation (SAM) in the form of the nonlinear Kerr-lens effect [28] meets this requirement. The nonlinear Kerr effect is a modification of the refractive index of a dielectric medium depending on the intensity

of the field propagating through it according to

$$n(r,t) = n_0 + \Delta n \cdot I(r,t), \tag{2.20}$$

where Δn describes the change in refractive index caused by the non-linear susceptibility which couples to the intensity $I(r,t)$. According to Kerr-lens modelocking (KLM) [2], the self-focusing due to the Kerr-lens effect shown in figure 2.3 increases the gain per round trip for the high-peak powers during pulsed operation compared to the low-power beam in continuous operation. This is due to better overlap of the self-focused beam with the pump-laser focal volume. SAM additionally keeps the propagating pulses short by suppressing weak leading or trailing edges of the pulse profile, since these weak power parts experience less self-focusing and thus less gain than the high-power central part of the pulse.
The pulse duration is fundamentally limited by spectral bandwidth supported by the gain medium. Because of their broad laser transition titanium sapphire (Ti:Sa) crystals are very suitable for the generation of short pulses. The fluorescence spectrum of Ti:Sa ranges from 650 nm to 1050 nm with a maximum at 780 nm (1.59 eV) [29]. In spite of this broad gain bandwidth, pulse durations in the femtosecond regime can only be achieved with additional spectral broadening. Again the Kerr effect inside the gain medium is utilized. In addition to self focusing the beam experiences a process called self-phase modulation (SPM) [30]. This introduces an additional phase term $\phi_{Kerr}(t) = \omega_c n(t) L/c$, with L being the propagation distance in the medium, that is added to the temporal phase $\phi(t)$ (see section 2.1.1). As a consequence the instantaneous frequency $\omega_{inst}(t)$ is modulated according to

$$\Delta\omega(t) = \frac{\partial \phi_{Kerr}}{\partial t} = \frac{\omega_c}{c} \Delta n \frac{\partial I(t)}{\partial t} L \,. \tag{2.21}$$

Thus, the leading pulse edge generates higher and the trailing edge generates lower frequencies. Since the process accumulates positive GDD, the cavity must contain optical elements which compensate for this with negative GDD. This is usually achieved with specially designed chirped mirrors. If set up correctly, the combination of SPM, SAM and negative GDD leads to the stable production of sub-5-fs pulses [31, 32].
If the pulses generated in this way are to be used to drive highly nonlinear processes the pulse energy of a few nJ typically delivered by standard oscillators is not sufficient. With some exceptions [33, 34], the oscillator pulses generally have to be amplified in a separate stage in order to reach the typically necessary intensities of $\sim 10^{14}\mathrm{W/cm^2}$. Since direct amplification of the femtosecond pulses would damage the gain medium and optics in the amplifier, a method called chirped pulse amplification (CPA) [35] is used. In this scheme the oscillator pulses are stretched to pico- or nanosecond durations prior to the amplification step and re-compressed afterward. The pulses are stretched by passing blocks of glass, where they accumulate GDD as well as higher-order dispersion. While the recompression is typically realized with prism or grating compressors, the TOD acquired in the stretcher is compensated by special mirrors which leave the GDD unaffected. During the amplification itself the stretched pulses pass again a Ti:Sa crystal pumped by a pulsed pumplaser (Q-switched, nanosecond durations, kHz repetition rates with several 10 W power). In practice there are two common designs of the amplification stage. The first one, called multi-pass amplifier, uses a predetermined beam path that passes the gain

medium a fixed number of times to achieve the desired output power. The second one, called the regenerative amplifier employs a cavity similar to the oscillator from which the pulses are released after a given number of round trips. The factor limiting the output power is the thermal load on the gain medium which in practice limits the achievable power to $\sim 10-20$ W. If pulse energies of few mJ have to be reached, the repetition rate has to be dropped from MHz down to the kHz regime. This is done by selecting single pulses from the oscillator pulse train synchronized to the output of the amplifier pumplaser using the Pockels effect and a polarizer while the rest is dumped. A Pockels cell switches the polarization of a single pulse, which then propagates through the amplifier and depletes the gain in the pumped medium.

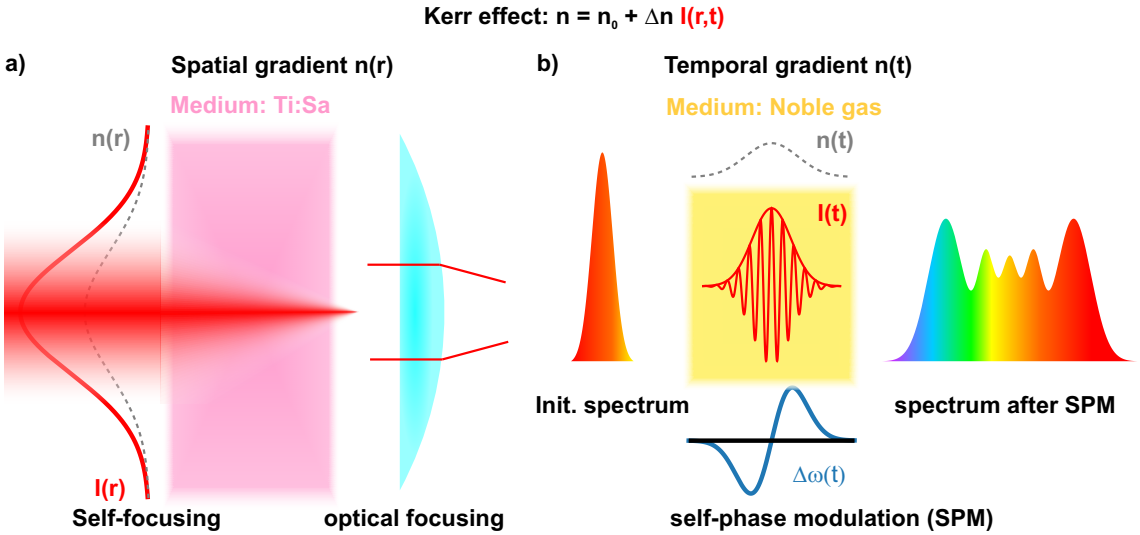

Figure 2.3.: **Illustration of the spatial and temporal Kerr effect:** The non-linear Kerr effect introduces an intensity dependence to the refractive index. This leads to self-focusing due to a Kerr-lens being formed because of the spatial intensity distribution $I(r)$ of a beam propagating through a medium shown in a). The spatial dependence of the refractive index $n(r)$ has a similar effect to the focusing caused by an ordinary lens. b) Illustration of self phase modulation caused by the temporal intensity profile of a pulse. The temporal change in phase $\Delta\phi(t)$ creates additional spectral components which increases the bandwidth of the pulse. As these components are added on the leading and trailing edge, the broadened pulse exhibits an almost linear chirp around the center frequency.

As the amplification is influenced by a process called gain-narrowing, uniform amplification of the whole spectral bandwidth is not possible and the duration of the amplified pulses is generally longer compared to the output of the oscillator. Typical output parameters of modern amplifiers are several mJ pulse energy with a duration of ~ 20 fs. However, the desired duration for most experimental applications is in the few-cycle regime and therefore the spectrum after the amplifier has to be broadened. For this purpose SPM in a noble gas can be used in two ways. The beam can be guided through a gas-filled hollow-core fiber, where only confined high-power modes propagate and make SPM ef-

ficient [36, 37]. Another option is using a plasma filament, where Kerr-lens self focusing and plasma defocusing act together to create an extended, unguided high-intensity zone in the gaseous medium enabling SPM [38, 39]. The achieved broadening depends on many parameters such as gas species (neon, argon, helium, ...), gas pressure, length of the medium and available intensity (laser power, beam mode, fiber diameter). The acquired GDD during SPM is afterward compensated with chirped mirrors and a pair of glass wedges to fine tune the dispersion [20]. TOD contributions can be compensated by special birefringent crystals (e.g. ADP) which introduce negative TOD along one optical axis [40]. Typical pulse durations achieved with such setups range from $4-10$ fs [4, 5] and are in principle limited by the supported bandwidth of the chirped-mirror compressor. It is however possible to reach even shorter durations by using a method called light-wave synthesis, which separates the components of a very broad spectrum, compresses each part separately and recombines them in order to achieve pulse durations of ~ 1 fs [4, 5]. For very high pulse energies ionization and defocusing effects become more significant which makes filamentation unstable and can have detrimental effects on fiber incoupling and beam stability after passing the medium. To counteract these effects, differentially pumped fiber setups are used which generate a pressure gradient suppressing ionization effects at the beginning of the medium [41, 42]. An alternative to SPM, which suffers relatively high losses and problems for high pulse energies, is optical parametric amplification (OPA). Here, nonlinear properties of crystals are used for close to loss-less frequency conversion processes [43, 44]. Also with this technology different parts of the spectrum can be separately amplified and compressed to achieve sub-cycle pulse durations [45]. Regardless of the production method, the few-cycle pulses can be further applied either directly in experiments to study interactions with strong laser fields or to drive the generation of even shorter pulses making use of a process called high-harmonic generation (HHG), which will be described in the next sections.

2.2. Interaction with Strong Fields

With the techniques described in the previous section, laser pulses of a few mJ and durations in the femtosecond regime and peak intensities on the order of $10^{14}-10^{15}$ W/cm^2 can be achieved with corresponding electric field strengths of 10^8-10^9 V/cm. This is on the order of the atomic unit field strength $\mathcal{E}_{a.u.} = 5.14\cdot 10^9$ V/cm which equals the electric field experienced by an electron in the ground state of the hydrogen atom. The interaction with such pulses cannot be treated perturbatively anymore and is the origin of nonlinear strong-field effects like non-sequential double ionization [46], tunnel-ionization, above-threshold ionization (ATI) or high-harmonic generation (HHG). While these effects are described in much detail in literature [14, 15], the focus of this section will be mainly on HHG as a means of attosecond pulse production and strong-field ionization as a prerequisite for HHG as well as a theoretical foundation for many effects observed in the course of this work.

For the interaction of atoms with strong fields, perturbative treatment is no longer viable. For strong enough fields, where effects of the atomic potential become less important,

the classical equations of motion of an electron in a linearly polarized electric field can be used to obtain an understanding of the electron's motion. However this is only accurate for non-relativistic field strengths, where the electron moves significantly slower than the speed of light and effects of the magnetic field component can be neglected. Following Newton's law, the equation of motion is given by $a(t) = -eE(t)/m_e$, where e is the electron charge and m_e is the electron mass. The velocity $v(t)$ and position $x(t)$ can be obtained simply by integrating and inserting initial conditions (v_0, x_0) for the integration constants. The mean kinetic energy of an electron initially at rest, moving in a monochromatic electric field $E(t) = \mathcal{E}_0 \cos(\omega t)$ is then given by

$$U_p = \frac{1}{2} m_e \langle v(t)^2 \rangle_{cyc} = \frac{e^2 \mathcal{E}_0^2}{4 m_e \omega^2} \,. \tag{2.22}$$

Here, U_p is called the ponderomotive energy which gives the energy of the electron's quiver motion in the field. The amplitude of this motion is known as the ponderomotive radius given by

$$x_p = \frac{e\mathcal{E}_0}{m_e \omega^2}. \tag{2.23}$$

In general the interaction of an atom with a strong electric field is described with a semi-classical approach, where the atomic system is treated quantum mechanically while the field is treated classically. It is often the case that only one electron in an atom significantly contributes to the dynamics, in which case the so-called single active electron approximation (SAE) can be employed. This simplifies the problem by describing only one electron moving in a mean-field potential of the nucleus shielded by the remaining electrons. If the electric field and its coupling is expressed in the length gauge, the equation of motion is given by the Schrödinger equation in the form

$$i\frac{\partial}{\partial t}|\Psi(\vec{x},t)\rangle = \left(\frac{\hat{\vec{p}}}{2} + V(\hat{\vec{x}}) + \hat{d} \cdot \vec{E}(t) \right) |\Psi(\vec{x},t)\rangle. \tag{2.24}$$

Another commonly used gauge is the velocity gauge which expresses the interaction with the electric field via the vector potential $\vec{A}(t)$ according to $\vec{A}(t) = \int \vec{E}(t) \mathrm{d}t$ and the coupling via a kinetic momentum $\vec{\pi} = \vec{p} + \vec{A}(t)$ (see also [14]). If the atom is included in the description the ionization potential I_p represents an important parameter of the system interacting with the field. This quantity gives the energy needed to remove one electron from its bound state in the system. Values of I_p for the noble gas atoms are given in table 2.1.

Table 2.1.: Values of I_p for all of the noble gases

	He	Ne	Ar	Kr	Xe	Ra
I_p (eV)	24.59	21.56	15.76	14.00	12.13	10.70
I_p (a.u.)	0.9036	0.7925	0.5792	0.5145	0.4458	03932

Once the electric field can provide this energy an electron can be removed from the atom. The next section will describe prominent mechanisms describing the ionization of quantum systems in strong fields.

2.2.1. Strong-field Ionization

The study of strong-field ionization effects goes back to the 1960s. It is in most cases very different from the photoeffect [47] as the absorption of a single photon of a system in the ground state is very often not enough to overcome the ionization potential. In general, there are two pictures to treat ionization due to the interaction with a strong electric field: Multiphoton ionization (MPI) and tunneling ionization. Multiphoton ionization is the nonlinear absorption of several photons to overcome the ionization potential. In the case of tunneling ionization, the Coulomb potential is bent by the electric field such that the bound electron can tunnel through the formed barrier. A special case of this process is over barrier ionization (OBI) which occurs at very high field strengths, where the potential is distorted to the point where the ground state of the system is no longer bound. The critical field strength $\mathcal{E}_{crit}$ needed for OBI gives another reference parameter for the electric field [48] and is defined by:

$$\mathcal{E}_{crit} = \frac{I_p^2}{4Z}, \tag{2.25}$$

with Z being the charge of the nucleus of the atomic system. The work of Keldysh [49] shows that both processes, MPI and tunneling ionization, can be described within a unified theory. He introduced the parameter γ, thereafter named after Keldysh, which provides a measure for the dominant mechanism of ionization [50, 51]. It is the ratio between the laser frequency ω and the tunneling frequency ω_T defined as the inverse of the time the barrier remains formed in the field and the electron can tunnel out. The Keldysh parameter describes the adiabaticity of the atomic response to the field and is given by

$$\gamma = \frac{\omega}{\omega_T} = \omega\sqrt{\frac{2I_p}{I}} = \sqrt{\frac{I_p}{2U_p}}, \tag{2.26}$$

where U_p is the ponderomotive potential according to equation 2.22 and I is the field intensity. For $\gamma \gg 1$ the electric field changes much faster than the response of the electrons. In this limit the multiphoton description can be applied where multiple photons are absorbed to overcome the ionization potential. If $\gamma \ll 1$ holds, the field oscillates slowly compared to the electronic response. In this case, the field can be considered as static which allows the description of the ionization with the tunneling process. An overview of the Keldysh theory of strong field ionization can be found in more current reviews [52]. In the multiphoton regime ($\gamma \gg 1$) simultaneous absorption of n photons, meeting the condition $n\hbar\omega \geq I_p$, leads to the ionization of the system. The corresponding ionization rate is given by [51, 53]:

$$\Gamma_n = \sigma_n I^n, \tag{2.27}$$

where σ_n denotes the generalized cross section including non-linear terms usually calculated by high-order perturbation theory. If n is bigger than the minium number of photons

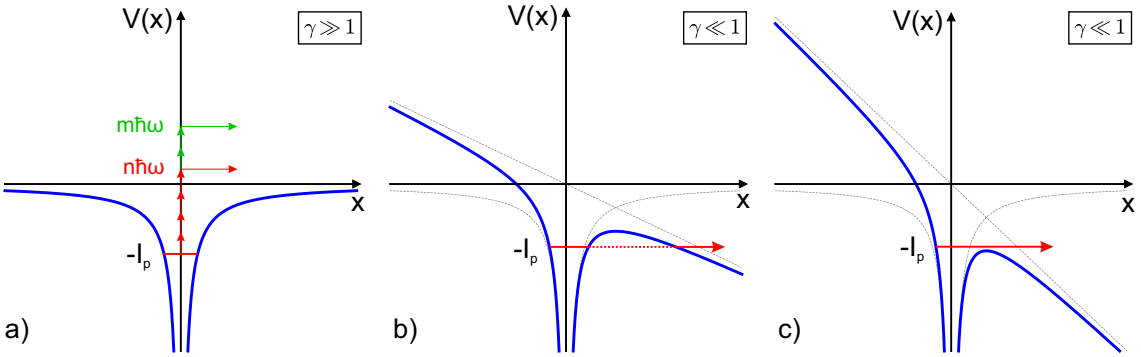

Figure 2.4.: **Strong-field-ionization mechanisms:** a) Multiphoton ionization for $\gamma \gg 1$. n photons are simultaneously absorbed to overcome the ionization potential I_p. Absorption of additional photons leads to above-threshold ionization. b) Tunnel ionization for $\gamma \ll 1$. The Coulomb potential (blue) is modified by the electric field and forms a barrier. The electron can tunnel through this barrier into the continuum. c) Over barrier ionization. The electric field is so strong that the barrier is completely suppressed and the electron can leave the atom.

required for ionization a special case of MPI occurs, called above-threshold ionization (ATI) [53, 54]. Here the electrons carry excess energy at intervals of the photon energy.

In the limit of tunneling ionization ($\gamma \ll 1$) the deformation of the potential due to the electric field can be treated with a quasi-stationary approximation. By expanding Keldysh's theory the so-called ADK formula [50, 52, 55–57] (named after the authors) was developed. It gives the ionization rate from a bound quantum state, characterized by the principal, the angular momentum and the magnetic quantum numbers (n, l, m), in a system interacting with a linearly polarized electric field. According to [55] it is given by:

$$\Gamma_{ADK}(t) = \sqrt{\left(\frac{2e}{n^*}\right)\frac{1}{2\pi n^*}}\frac{(2l+1)(l+|m|)!}{2^{|m|}(|m|)!(l-|m|)!}\left(\frac{3\mathcal{E}(t)}{\pi(2I_p)^{3/2}}\right)^{1/2} I_p \times \left(\frac{2(2I_p)^{3/2}}{\mathcal{E}(t)}\right)^{2n^*-|m|-1} \exp\left[-\frac{2(2I_p)^{3/2}}{3\mathcal{E}(t)}\right] \quad (2.28)$$

Here, n^* is the effective principle quantum number in the single active electron approximation, where the active electron can be thought of as moving in a modified Bohr orbit characterized by $n^* = Z/\sqrt{2I_p}$, e is Euler's number and $\mathcal{E}(t)$ is the electric field envelope. For linearly polarized light, ionization from the $m = 0$ orbitals is preferred. The time-dependent field yields a time dependent ionization rate, averaged over one cycle of the electric field. If the instantaneous ionization rate is to be considered, the factor $3\mathcal{E}(t)/\pi(2I_p)^{3/2})^{1/2}$ resulting from the cycle average has to be omitted and the field envelope has to be replaced by the electric field itself [48]. While equation 2.28 is derived for $\gamma \ll 1$ it also gives good results for $\gamma \simeq 1$. More recent work even resulted in an expression of the ionization rate for arbitrary values of γ [58]. Thus, tunneling ionization, can be

used to describe the first step of many strong-field processes mentioned in the beginning. Aside from the ongoing discussion on 'tunneling-time' [59], it represents a well-defined starting point for dynamics after the electron leaves the atom and explains the sub-cycle nature of non-linear strong-field processes like high-harmonic generation.

2.2.2. Creation of Attosecond Pulses with High-Harmonic Generation

As stated in the previous section, the observation of dynamics on the attosecond time scale, the natural time scale of electronic motion, is only possible if these dynamics can be excited, and if the laser pulses used for this purpose are themselves short enough to resolve the dynamics. The typical photon energies required for this purpose are on the order of 10 eV or higher, meaning in the XUV and soft X-ray spectral range. With these energies not only single excitation of bound states is possible, but also multiple electrons as well as strongly bound inner-valence or core electrons can be excited. The process of high-harmonic generation (HHG) is able to meet these conditions [15, 16]. Since its discovery it was possible to achieve photon energies of higher than 1 keV [60] as well as pulse durations of well below 100 as (current record: 43 as) [5,61,62]. While this section will give a short overview over the main aspects of HHG many detailed descriptions of this process exist in literature [3,4,15,16,63,64].

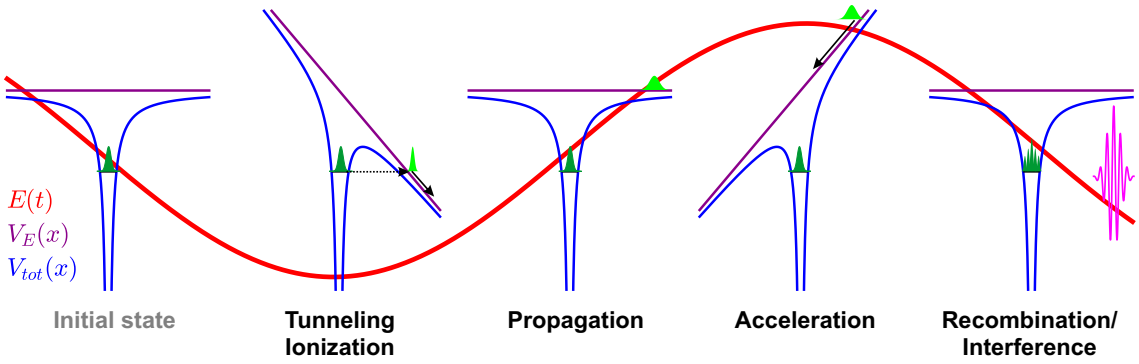

Figure 2.5.: **Illustration of the three-step model:** The main steps of ionization, acceleration and recombination are shown in sequence. After the initial tunneling ionization through the potential barrier (blue curves) the electron wave packet (green) propagates (black arrows) in the field (red), gets accelerated and returns with a certain probability to the parent ion. During the recombination a high-energy photon is emitted.

Involving both quantum-mechanical tunneling and highly non-linear light-matter interaction the process of HHG can still be quite accurately described by a quasi-classical model. The 3-step-model [9, 65], introduced in 1993 and illustrated in figure 2.5 separates the interaction with the field in three parts. The ionization step is described in the tunneling-ionization framework introduced in section 2.2.1 and equation 2.28. Here, typically a target consisting of noble-gas atoms interacts with a strong light pulse of intensities of more than 10^{14} W/cm^2 leading to an electron being ionized from the atom. Once in

the continuum, the electron trajectories can be described by classical equations of motion in the second step. The electron is driven away from its parent ion after ionization and can re-encounter it with additional kinetic energy $E_{kin}^{(r)}$ gained in the field. If the electron interacts again with its parent ion it may recombine into the initial bound state during the third step. In this case, the difference in energy in addition to the excess kinetic energy is converted into a single high energy photon:

$$\hbar\omega_{HHG} = E_{kin}^{(r)} + I_p. \tag{2.29}$$

Each kinetic energy at the moment of recombination $E_{kin}^{(r)}$ corresponds to two classical trajectories within one laser cycle, the so-called short and long trajectories. This 3-step process can occur within each half-cycle of the pulse and interfere with events from different cycles. This half-cycle periodicity and interference gives rise to harmonic photon energies which are spaced by $2\hbar\omega_c$, where ω_c is the central frequency of the driving laser field.
While the 3-step model gives already good agreement with experimental observations, the HHG process can also be understood in a full quantum-mechanical treatment of the electron motion, where the strong field is described classically [66]. This theory employs the strong field approximation which neglects the influence of the ion core once ionization has taken place [51, 67]. In this picture part of the ground state wave function gets ionized, propagates in the continuum and finally interferes with the remaining part of the wave function around the parent ion. This interference constitutes a rapidly oscillating dipole moment which in turn is the source for the emission of the high-energy harmonic radiation.

More detailed analysis of the trajectories shows that the energy gained by the electron critically depends on the time of ionization within the driver pulse. The maximum energy $E_{kin,max}^{(r)}$ is gained close to a maximum of the electric field. Calculating the classical trajectories depending on the point of ionization within the pulse, the maximum recombination energy is found to be

$$E_{kin,max}^{(r)} = 3.17U_p, \tag{2.30}$$

where U_p is the ponderomotive potential defined in equation 2.22. Hence, long wavelengths λ and high intensities are needed for higher XUV photon energies. However, due to the longer propagation times in the continuum and the associated wave function spread, re-collision becomes increasingly unlikely. This in turn leads to lower conversion efficiency (which scales with $\sim \lambda^{-7}$ [68]). The spectrum of high harmonic generation displays a universal behavior. The intensity of the low order harmonics drops quickly, then extends at constant values over a broad spectral range called the plateau region and finally shows a rather sharp cut-off at the maximum achievable photon energy given by

$$\hbar\omega_{HHG} = I_p + 3.17U_p. \tag{2.31}$$

If the driving pulse consists of multiple half cycles a train of attosecond pulses [69] is generated which leads to a rather discrete comb structure in the spectrum. Because of the periodicity of the process this structure represents odd harmonic orders of the fundamental

frequency ω_c spaced by $2\omega_c$. Only if single attosecond pulses are produced using gating mechanisms based on intensity [70] or polarization gating of the driver pulse [71–74], the spectrum becomes continuous over a broad spectral range corresponding to the duration of the attosecond pulse [75]. One of the major downsides of high-harmonic generation in a gaseous conversion medium as a light source is the relatively low overall conversion efficiency of 10^{-4} to 10^{-6}. It is thus currently not easily possible to apply the generated pulses to study nonlinear processes. Current research explores HHG in targets with higher density like liquid droplets [76] or even solids [77] in order to improve the XUV photon flux. However, the attosecond pulses represent excellent tools to probe or coherently excited systems at very well defined times, which is utilized in this work. A description of the technical aspects of the HHG source realized in the experiment is given in the next chapter.

2.3. Quantum Dynamics

Apart from strong nonlinear effects like ionization, the interaction of a quantum system with external sources (electric fields, etc.) causes dynamic transitions between different states of the system. In general, the state and the dynamics of a quantum-mechanical system are fully characterized by the wave function ψ and its time evolution. In quantum mechanics the time evolution of a system is described by the unitary time translation operator $\hat{U}(t,t_0)$ characterized by the generating function $\hat{H}$. The function $\hat{H}$ is generally known as the Hamilton operator, describing the energy of the system. In the non-relativistic case the equation of motion is given by the time-dependent Schrödinger equation

$$i\frac{\partial}{\partial t}|\psi(t)\rangle_S = \hat{H}|\psi(t)\rangle_S. \tag{2.32}$$

Its derivation from first principles as well as the following derivations can be found in many textbooks [78–80]. In this instance the state vector given by the wave function $|\psi(t)\rangle_S$ carries the time dependence, which is commonly named the Schrödinger-picture representation. Another possible representation is the so-called Heisenberg picture, where the operators are time dependent and the state vector is independent of time. The Hamilton operator can be generally divided into two parts

$$\hat{H} = \hat{H}_0 + \hat{H}_{int} \tag{2.33}$$

where $\hat{H}_0$ is the Hamiltonian of the unperturbed system and $\hat{H}_{int}$ describes a perturbation, which can include all interactions with external sources (electric, magnetic fields, etc.). If $\hat{H}$ is constant in time, the time-evolution operator takes the form $\hat{U}(t,t_0) = \exp[-i\hat{H}\cdot(t-t_0)]$. If $\hat{H} = \hat{H}(t)$ is time dependent, one can find an expression for the time-evolution operator by plugging $|\psi(t)\rangle_S = \hat{U}(t,t_0)|\psi(t_0)\rangle_S$ into 2.32 and rewriting the equation as an integral equation. This yields a self-consistent equation for $\hat{U}(t,t_0)$ which can be used to

derive the expression as a Dyson-Series, time-ordered in $H(t)$, at times t_n, reading

$$\hat{U}(t,t_0) = \mathbb{I} + \sum_{n=1}^{\infty} (-i)^n \int_{t_0}^{t} \mathrm{d}t_1 \int_{t_0}^{t_1} \mathrm{d}t_2 ... \int_{t_0}^{t_{n-1}} \mathrm{d}t_n \, \hat{H}(t_n)...\hat{H}(t_1). \tag{2.34}$$

Because $H(t)$ appears as a time-ordered sequence with $t_0 \leq t_1 \leq ... \leq t_n \leq t$, the above equation can also be formally written as

$$\hat{U}(t,t_0) = \hat{T} e^{-i\int_{t_0}^{t} \mathrm{d}t' H(t')}, \tag{2.35}$$

with $\hat{T}$ being the time-ordering operator. For arbitrary (time-dependent) interactions and interaction strengths it can be impossible to find analytical expressions for the time-evolution of the system. A very common method to treat this problem is the application of perturbation theory, which is described in the following.

2.3.1. Time-Dependent Perturbation Theory

Given a well known system described by $\hat{H}_0$ with exact eigenstates $|n\rangle$ and eigenvalues E_n, the goal of perturbation theory is to get approximate eigenstates and eigenvalues fulfilling equation 2.32 for the case of $\hat{H}_{int} \neq 0$. If the perturbation is weak (small compared to the energies and energy separations in the system) the Hamiltonian can be expressed as

$$\hat{H} = \hat{H}_0 + \lambda \hat{V}(t), \tag{2.36}$$

with λ being a small scaling parameter of the perturbation. For the stationary case $\mathrm{d}\hat{H}/\mathrm{d}t = 0$ an expansion of E_n and $|n\rangle$ in powers of λ will yield correction terms to the eigenstates and energies caused by the perturbation (for details see [79]).
In the case of $\mathrm{d}\hat{H}/\mathrm{d}t \neq 0$ however, a time-dependent version of perturbation theory has to be used. It is convenient to turn to a different representation which only considers the dynamic changes to the wave function due to the time-dependent perturbation $H_{int} = \hat{V}(t)$. This is known as the interaction picture, a 'mixture' of both Schrödinger and Heisenberg pictures, where the evolution due to H_0 is shunted to the operators. The transformation into this picture is given by

$$|\psi(t)\rangle_I = e^{i\hat{H}_0 t} |\psi(t)\rangle_S \, , \; |\psi(0)\rangle_I = |\psi(0)\rangle_S. \tag{2.37}$$

In this picture the wave function $|\psi(t)\rangle_I$ and the perturbation $V(t)$ obey the equations

$$i\frac{\partial}{\partial t}|\psi(t)\rangle_I = \hat{V}_I(t)|\psi(t)\rangle_I \, , \; \text{with} \hat{V}_I(t) = e^{i\hat{H}_0 t} V(t) e^{-i\hat{H}_0 t}. \tag{2.38}$$

The wave function can always be written as an expansion in a complete set of basis states, the eigenstates of the unperturbed system $|\psi(t)\rangle_I = \sum_n c_n(t)|n\rangle$. Inserting this into equation 2.38 and contracting over a general basis state $|m\rangle$ yields the relation for the coupled time dependent state coefficients $c_n(t)$

$$i\frac{\partial}{\partial t}c_m(t) = \sum_n \langle m|V(t)|n\rangle e^{i(E_m-E_n)t}c_n(t). \tag{2.39}$$

To obtain a relation for these time dependent coefficients of a general state $|\psi(t)\rangle_I = \sum_n c_n(t)|n\rangle$, they are written as a perturbative expansion in powers of the interaction

$$c_n(t) = c_n^{(0)} + c_n^{(1)}(t) + c_n^{(2)}(t) + \dots , \tag{2.40}$$

where $c_n^{(i)} \propto \mathcal{O}(\lambda^i)$ and $c_n^{(0)}$ represents the initial state without the perturbation $V(t)$. As it is the case for the Schrödinger picture, the time evolution within the interaction picture starting at time t_0 can be described by a time-evolution operator

$$|\psi(t)\rangle_I = \hat{U}_I(t,t_0)|\psi(t_0)\rangle_I. \tag{2.41}$$

Similar to the procedure to acquire equation 2.34 an expression for $\hat{U}_I(t,t_0)$ can be derived

$$\hat{U}_I(t,t_0) = \mathbb{I} + \sum_{n=1}^{\infty}(-i)^n \int_{t_0}^{t} \mathrm{d}t_1 \int_{t_0}^{t_1} \mathrm{d}t_2 \dots \int_{t_0}^{t_{n-1}} \mathrm{d}t_n \, \hat{V}_I(t_n)\dots\hat{V}_I(t_1). \tag{2.42}$$

Considering now a system in a general initial state $|i\rangle$ and inserting the identity $\mathbb{I} = \sum_n |n\rangle\langle n|$ into equation 2.41 a relation for the coefficients can be identified

$$\hat{U}_I(t,t_0)|i\rangle = \sum_n |n\rangle\langle n|\hat{U}_I(t,t_0)|i\rangle \ , \ c_n(t) = \langle n|\hat{U}_I(t,t_0)|i\rangle. \tag{2.43}$$

Combining equations 2.43 and 2.42 and comparing it to 2.40 expressions for the correction terms to the state coefficients can be derived as

$$c_n^{(1)}(t) = -i\int_{t_0}^{t} \mathrm{d}t' \langle n|V(t')|i\rangle e^{i(E_m-E_n)t'} \tag{2.44}$$

$$c_n^{(2)}(t) = -\sum_m \int_{t_0}^{t} \mathrm{d}t' \int_{t_0}^{t'} \mathrm{d}t'' \langle n|V(t')|m\rangle\langle m|V(t'')|i\rangle e^{i(E_n-E_m)t'+i(E_m-E_i)t''}. \tag{2.45}$$

It has to be noted that since the orders emerge iteratively from the previous one, it is possible to compute k-th order $c_n^{(k)}$ directly from the $(k-1)$-th order numerically with a single integration.

2.3.2. Field Driven n-Level Systems

The description of complex systems requires a moderate to big number of states n, which can only be treated numerically. However this changes for simple systems of very few states. The simplest system exhibiting nontrivial dynamics while interacting with an electromagnetic field is the two-level system consisting of two discrete states $|i\rangle$ and $|j\rangle$ with respective energies E_i and E_j that are coupled by an oscillating electric field. This model can be applied to describe the physics of many interesting applications, like for example Q-bits [81], atomic clocks [82] and spinor dynamics [83]. For weak field strengths the interaction can be analytically treated with perturbation theory using the formalism in section 2.3.1. However, if the intensity is increased the dynamics enter the regime of strong coupling. Here, perturbation theory no longer applies since considerable population is transferred between the coupled states and changes in the energy of states take place. It can even happen that the populations are transferred back and forth between the states during the interaction. This is commonly known as Rabi oscillations [83]. For the two-level system it is possible to derive approximate analytical solutions describing these effects.

The Hamiltonian of a two-level system interacting with a linearly polarized electric field $E(t)$ in dipole approximation is given by

$$\hat{H} = \hat{H}_0 + \hat{H}_{int} = \hat{H}_0 + \hat{d} \cdot E(t) \ . \tag{2.46}$$

with $\hat{H}_0$ the Hamiltonian of the non-interacting states and $\hat{d} = -e \cdot \hat{x}$ the dipole operator. The general state of this system can be expanded into the two basis states

$$|\psi\rangle = c_i |i\rangle + c_j |j\rangle \ . \tag{2.47}$$

With this expansion, equation 2.32 becomes a set of two coupled linear differential equations, which is given in matrix representation as:

$$i\frac{\mathrm{d}}{\mathrm{d}t}\begin{pmatrix} c_i \\ c_j \end{pmatrix} = \begin{pmatrix} E_i & d_{ij} \cdot E(t) \\ d_{ji} \cdot E(t) & E_j \end{pmatrix} \cdot \begin{pmatrix} c_i \\ c_j \end{pmatrix} \ . \tag{2.48}$$

Here, the Hamiltonian appears also in matrix representation in the basis of $|i\rangle$ and $|j\rangle$ with $d_{ij} = \langle i|\hat{d}|j\rangle$. To find a solution, equation 2.48 is transformed into the rotating frame of the coupling laser field by a phase rotation

$$\begin{pmatrix} \tilde{c}_i \\ \tilde{c}_j \end{pmatrix}(t) = \hat{T} \cdot \begin{pmatrix} c_i \\ c_j \end{pmatrix}(t) \ \text{ with } \ \hat{T} = e^{i\frac{\omega_j+\omega_i}{2}t}\begin{pmatrix} e^{-i\frac{\omega_L}{2}t} & 0 \\ 0 & e^{+i\frac{\omega_L}{2}t} \end{pmatrix} \tag{2.49}$$

with a laser frequency $\omega_L = \omega_{ij} - \Delta$ close to resonance with the atomic transition frequency $\omega_{ij} = \omega_j - \omega_i$ between the two states, where Δ is the detuning of the laser. Inserting the electric field $E(t) = E_0 \cos(\omega_L t) = \frac{E_0}{2}(e^{i\omega_L t} + e^{-i\omega_L t})$, this transformation applied to equation 2.48 yields

$$i\hbar\frac{\partial}{\partial t}\begin{pmatrix}\tilde{c}_i\\ \tilde{c}_j\end{pmatrix} = \frac{1}{2}\begin{pmatrix}\Delta & d_{ij}\cdot E_0\cdot(e^{-i\Delta t}+e^{i(\omega_L+\omega_{ij})t})\\ d_{ij}\cdot E_0\cdot(e^{-i\Delta t}+e^{i(\omega_L+\omega_{ij})t}) & -\Delta\end{pmatrix}\cdot\begin{pmatrix}\tilde{c}_i\\ \tilde{c}_j\end{pmatrix}. \tag{2.50}$$

As it was assumed that the laser couples the states near or exactly on resonance, the rotating-wave approximation (RWA) can be used. Its effect shows if equation 2.50 is integrated. On the one hand, the contribution of the rapidly oscillating factors $e^{i(\omega_L+\omega_{ij})t}$ vanishes considering the mean value after the integration over time. On the other hand the factors $e^{i(\omega_L-\omega_{ij})t} = e^{-i\Delta t} \approx 1$, so that in the end only the component of the monochromatic wave that rotates opposite to the phase evolution of the system is relevant for the coupling. Applying this approximation, the differential equations can be separated and one gets for the Hamiltonian of the interaction in the rotating frame

$$\hat{H}_I = \frac{1}{2}\begin{pmatrix}\Delta & \Omega_R\\ \Omega_R & -\Delta\end{pmatrix}. \tag{2.51}$$

Here, $\Omega_R = E_0 \cdot d$ is the Rabi frequency. The eigenvalues of this Hamiltonian are

$$\lambda_{1,2} = \pm\frac{1}{2}\sqrt{\Delta^2+\Omega_R^2} = \pm\frac{1}{2}\tilde{\Omega}_R\,, \tag{2.52}$$

with $\tilde{\Omega}_R = \sqrt{\Delta^2+\Omega_R^2}$ being the generalized Rabi frequency. In the rotating frame these are the time-independent energies of the so-called laser-dressed states of the system and they appear centered around the energy levels defined in the rotating-frame transformation 2.49. After transformation back to the Schrödinger picture the state energies of the interacting system can be written in terms of the unperturbed state energies $E_{i,j}$, the Rabi frequency Ω_R and the laser detuning Δ as

$$E_j^{\pm} = E_j - \frac{\Delta}{2} \pm \frac{1}{2}\tilde{\Omega}_R\,, \tag{2.53}$$

$$E_i^{\pm} = E_i + \frac{\Delta}{2} \pm \frac{1}{2}\tilde{\Omega}_R\,. \tag{2.54}$$

These equations show the repulsion of energy levels that arises from coupling with an oscillating electric field also known as the linear AC Stark effect [84] which is the analogue to the magnetic Zeeman effect. In figure 2.6 the shifted energy levels depending on the field strength of the coupling electric field are shown. In the weak coupling limit ($\Omega_R \ll \Delta$) both field-free states appear in each dressed system. For the case of strong coupling ($\Omega_R \gg \Delta$), high field strength or resonant coupling Δ can be neglected and the states appear separated by the Rabi frequency Ω_R and centered around the mean value of

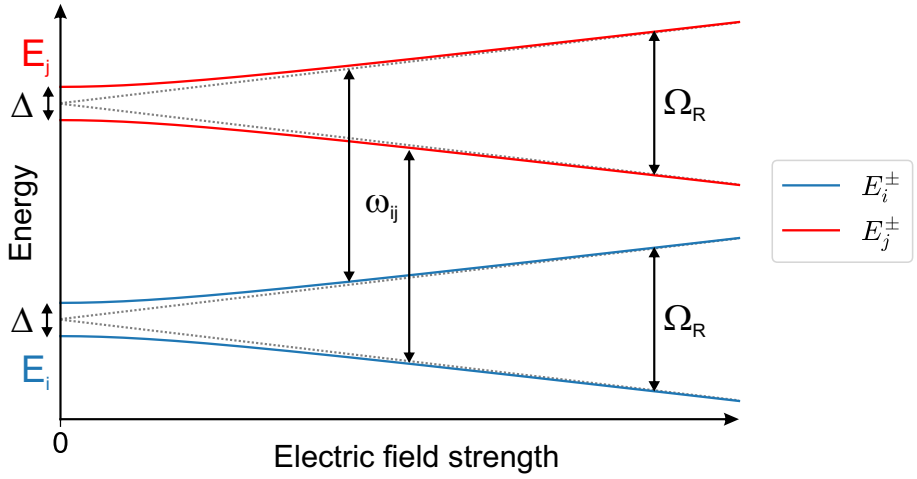

Figure 2.6.: **Stark-effect for a two-level system with level energies E_i, E_j and detuning Δ:** In the laser field, new states are formed which mutually repel each other with increasing field strength. For sufficiently large field strengths, Δ can be neglected and the level splitting is given by the Rabi frequency Ω_R.

the energy of each dressed-state pair in the low field limit. If these states are probed by a weak laser field from a third level, the corresponding pairs of observed spectral lines are known as Autler–Townes doublets [84].

After diagonalizing the Hamiltonian in equation 2.51 the new eigenstates in the dressed-state picture corresponding to the energies in equation 2.53 and equation 2.54 can be expressed in terms of the unperturbed state $|i\rangle$ and $|j\rangle$ as

$$|+\rangle = \sin(\theta)\,|i\rangle + \cos(\theta)\,|j\rangle \ , \tag{2.55}$$
$$|-\rangle = \cos(\theta)\,|i\rangle - \sin(\theta)\,|j\rangle \ . \tag{2.56}$$

Here, the state $|+\rangle$ has the higher energy and the so-called mixing angle θ is defined as

$$\tan(2\theta) = -\frac{\Omega}{\Delta} \qquad \left(0 \leq \theta < \frac{\pi}{2}\right) \ , \tag{2.57}$$

where Ω and Δ are the Rabi frequency and detuning as given above. This picture is convenient to examine the mixing of states with different symmetries in an electromagnetic field which alters the excitation and dynamic behavior of the system under investigation. These dressed states are the new eigenstates of the interacting system with constant populations in time. To understand the effects of Rabi oscillations, the solutions for the time-dependent coefficients of the bare states $|i\rangle$ and $|j\rangle$ have to be considered. For the initial conditions of a system in the lower energy (ground state) at time zero with $\tilde{c}_i(0) = 1$ and $\tilde{c}_j(0) = 0$ the solutions for the coefficients can be found from the coupled equations 2.50 in the rotating frame. They can be decoupled by differentiation in time and substituting the original equations. With the ansatz for the general solution $c(t) = A \cdot \cos(\omega t) + B \cdot \sin(\omega t)$,

this leads to the solutions for the coefficients given by

$$\tilde{c}_j(t) = -i\frac{\Omega_R}{\tilde{\Omega}_R}\sin\left(\frac{\tilde{\Omega}_R}{2}t\right) \tag{2.58}$$

$$\tilde{c}_i(t) = \cos\left(\frac{\tilde{\Omega}_R}{2}t\right) + i\frac{\Delta}{\tilde{\Omega}_R}\sin\left(\frac{\tilde{\Omega}_R}{2}t\right). \tag{2.59}$$

These equations show that the state populations $|c(t)_{i,j}|^2$ are transferred back and forth between the two levels of the system by the interaction with the coupling field. The detuning Δ together with the field strength E_0 determine the oscillation frequency as well as the maximum amount of population that is transferred in one Rabi cycle.
While the derivation is based on a continuous wave, it is in principle possible to define a time-dependent Rabi frequency $\Omega_R(t) = d_{ij} \cdot E_0(t)$ for a varying envelope function of a laser pulse for example. However if the duration of the pulse becomes comparable to the duration of one Rabi cycle $T_{cyc} = 2\pi/\tilde{\Omega}_R$, the RWA starts to break down and the interpretation of $\Omega_R(t)$ in this framework becomes difficult.

2.4. Multi-Electron Systems

As it is the case in classical physics, the two-body problem is analytically solvable in quantum mechanics. However, for few- to many-body systems like multi-electron atoms and molecules this is no longer possible. Because electrons are indistinguishable particles correlations due to exchange symmetries as well as Coulomb interactions have to be taken into account [85, 86]. As electrons are fermions the overall symmetry of the electronic wave function for the exchange of two particles has to be antisymmetric. The Hamiltonian of an atom with n electrons in the rest frame of the nucleus and nuclear charge $Z = n \cdot e$ is given by

$$\hat{H} = \sum_{i=1}^{n}\frac{\hat{p}_i^2}{2m_e} - \sum_{i=1}^{n}\frac{1}{4\pi\varepsilon_0}\frac{ne^2}{\hat{r}_i} + \sum_{i\neq j}\frac{1}{4\pi\varepsilon_0}\frac{e^2}{|\hat{r}_i - \hat{r}_j|}. \tag{2.60}$$

Because of the interaction between the electrons mediated by the Coulomb force $F_C = 1/4\pi\varepsilon_0 \cdot e^2/|r_i - r_j|$ the spatial wave function of such a system can not be decomposed into products of single-electron wave functions

$$\Psi^{(n)}(r_1, ..., r_n) \neq \prod_{i=1}^{n}\Psi^{(1)}(r_i)\ . \tag{2.61}$$

This is due to a correlation induced by the Coulomb repulsion between the electrons. It is not only important for the theoretical description of multi-electron states in atoms where various approximations have been developed to describe these correlations [85] but also in covalent bonds between different atoms of molecules. The dynamics of a

single excited valence electron in such a system can be treated similarly to the two-body problem, using mean field corrections of the remaining electrons to the overall potential experienced by the 'active' electron (see SAE in section 2.2). Apart from this, multi-electron systems allow for configurations with two or even more simultaneously excited electrons from the valence shell or for bigger atoms from inner valence or core states [87]. These configurations can be excited using high energy photons and exhibit highly nontrivial and correlated dynamics, leading to many interesting processes like single-photon double excitation, autoionization or (cascading) Auger ionization [88]. States involving multiple excited electrons carry energy above the single-ionization threshold and are thus degenerate with the continuous states of a free electron after ionization. The theory behind these particular states was worked out by Fano [89, 90] and is discussed in the following.

2.4.1. Autoionization and Fano Theory

The process of autoionization, leading to a change in line shape can occur in systems with two or more electrons. In such systems simultaneous excitation of two electrons at once may form quasi-stationary quantum states also known as doubly excited states (DES) with lifetimes much shorter compared to single-electron excitations. These states can decay by the ejection and the following rearrangement of the remaining electrons in the created ion which is commonly referred to as autoionization. The cause of the ionization process in DES is strong correlation between the excited electrons, which is caused by their Coulomb interaction. The resulting asymmetric resonance line shape was first observed by Hans Beutler [91] and theoretically described by Ugo Fano [90], who delivered a general expression for the resonance line shape based on interference between quantum transition amplitudes. This theory is in principle applicable to any case where interference can occur between different possible quantum pathways especially if there are contributions from discrete as well as continuous states.
The discussion of Fano's theory is kept close to the original notation. In the original work the problem is treated time-independently in the energy domain. First, a bound state $|\alpha\rangle$ and a set of continuum states $|\beta_E\rangle$ are considered. The bound-state energy E_α is degenerate with the energy spectrum E of the continuum. The eigenvalues of the Hamiltonian of this system are as follows:

$$\langle\alpha|\hat{H}|\alpha\rangle = E_i \,, \tag{2.62}$$

$$\langle\beta_E|\hat{H}|\alpha\rangle = V_E \,, \tag{2.63}$$

$$\langle\beta_E|\hat{H}\left|\beta'_E\right\rangle = E\delta(E'-E) \,. \tag{2.64}$$

E_i and E, E' are the energies of the states and the off-diagonal elements V_E describe the interaction. The ground state is neglected because it can be assumed far away from the relevant energies. In order to get the system's eigenstates this Hamiltonian has to be

diagonalized. These new states can be expanded as a superposition of the original basis and are, according to [90], given by

$$|\Psi_E\rangle = a_E\,|\alpha\rangle + \int \mathrm{d}E' b_{EE'}\,|\beta_E\rangle\ . \tag{2.65}$$

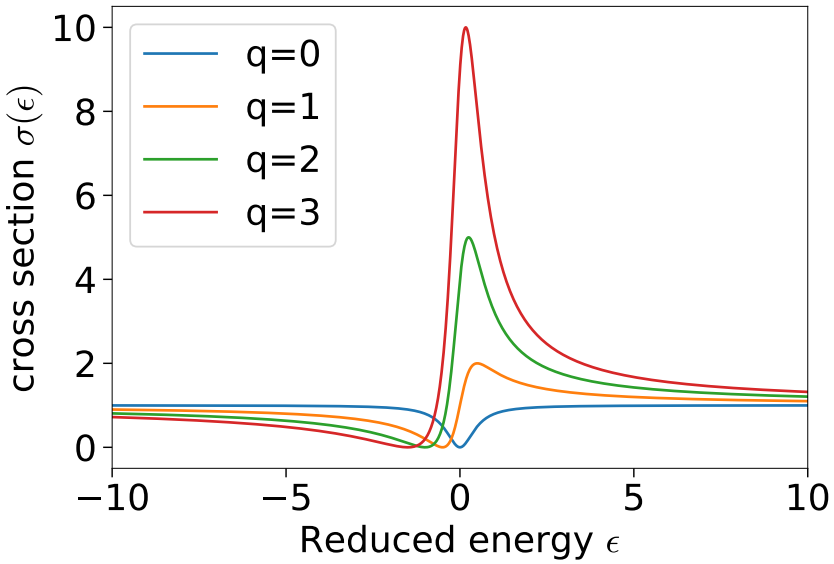

Figure 2.7.: **Asymmetric Fano resonance lines for different values of the parameter q:** The cross section of a resonance embedded in a continuum is plotted in arbitrary units depending on the normalized energy ε. For higher values of q the absorption minimum lies at smaller energy values. The cross section changes to a Lorentz line shape for $q \to \pm\infty$.

This reduces the problem to the determination of the coefficients a_E and $b_{EE'}$. These expansion coefficients are energy dependent and can be found by evaluation $\langle\Psi_E|\,\hat{H}\,|\Psi_E\rangle$ using equations 2.62 to 2.64. The full calculation can be found in [90]. In the end the recovered new eigenstates are found to be

$$|\Psi_E\rangle = \frac{\sin\Delta_E}{\pi V_E}\,|\phi_E\rangle - \cos\Delta_E\,|\beta_E\rangle\,, \tag{2.66}$$

with a modified bound state

$$|\phi_E\rangle = |\alpha\rangle + \mathcal{P}\int \mathrm{d}E' \frac{V_{E'}}{E-E'}\,|\beta_{E'}\rangle\,, \tag{2.67}$$

where the configuration interaction V_E mixes continuum states with the original discrete bound state. The parameter Δ_E is given by

$$\Delta_E = -\arctan\frac{\pi|V_E|^2}{E-E_\alpha-F(E)} \quad \text{with} \quad F(E)=\mathcal{P}\int \mathrm{d}E'\frac{|V_{E'}|^2}{E-E'} \tag{2.68}$$

Here, $F(E)$ gives an energy dependent energy shift caused by the variation of V_E across the spectrum of the continuum and $\mathcal{P}$ denotes the principal value integrals around the poles at $E = E'$. In principle, the transition $\hat{T}$ from a ground state $|g\rangle$ to $|\Psi_E\rangle$ has two contributions, namely transition into $|\phi_E\rangle$ and directly into the continuum $|\beta_E\rangle$. These contributions interfere with opposite phase on each side of the resonance which generates the asymmetric resonance profile. The asymmetry can be parametrized by comparing this transition probability to the transition into the unperturbed continuum:

$$\frac{|\langle\Psi_E|\hat{T}|g\rangle|^2}{|\langle\beta_E|\hat{T}|g\rangle|^2} = \frac{|q+\varepsilon|^2}{1+\varepsilon^2}\,, \tag{2.69}$$

with the parameters

$$\varepsilon = \frac{E-(E_\alpha+F(E))}{\Gamma/2} = \frac{E-E_\phi}{\Gamma/2}\,, \text{ and } \Gamma = 2\pi V_E^2\,, \tag{2.70}$$

$$q = \frac{\langle\phi_E|T|g\rangle}{\pi V_E\langle\beta_E|T|g\rangle}\,. \tag{2.71}$$

Here, ε is the reduced energy with the resonance position E_ϕ and the width Γ. The parameter q gives the ratio between the transitions from the ground to the modified bound state $|\phi\rangle_E$ and the transitions from the ground state directly to a continuum state $|\beta_E\rangle$. Equation 2.69 describes the Fano profile observable in a measurement and is plotted in figure 2.7 for different values of the parameter q.
The Fano theory is a general description of atomic excitation dynamics. For excited states without continuum channels $\langle\beta_E|\hat{T}|g\rangle \to 0$, $V_E \to 0$ or $q \to \pm\infty$ the Fano line shape changes into the standard Lorentzian line shape. In special cases the q-parameter can also approach 0, which causes an inversion of the spectral line because the direct transition into $|\phi\rangle_E$ is suppressed. This case is usually referred to as window resonance. As stated above, any given resonance can be uniquely described by three parameters in the energy domain: the position E, the linewidth Γ and the line-shape parameter q. Because the line shape arises from the interference of quantum pathways it is very sensitive to the exact phase of the different state contributions. Just like their optical counterparts (Michelson interferometer) these microscopic quantum interferometers can be used to study dynamics with high sensitivity if one or both of the pathways can be influenced and controlled. This is for example possible if the system in such a configuration interacts with strong and short electric fields.

2.4.2. Interaction with Strong Fields

While Fano's theory is time independent and assumes only weak excitations, more recent work has generalized it to the time dependent case of interaction with (additional) strong electric fields. In this regime non-perturbative effects like Rabi oscillations are expected to be modified compared to usual bound states by the additional interactions with the degenerate continuum states. A first analytical treatment of autoionizing states interacting with strong laser fields was developed by Lambropoulos and Zoller [92] and Eberly [93, 94]. Their approach makes use of the eigenstates $|\Psi_E\rangle$ of a system consisting of interacting discrete and continuous states given in equation 2.66 and describes their coupling to a discrete state $|g\rangle$ or other autoionizing states $\left|\Psi_E^i\right\rangle$ in a non-perturbative fashion. For the first case the time-dependent system is described by the state $|\Psi(t)\rangle$ and the Hamiltonian $\hat{H}$ in dipole approximation:

$$|\Psi(t)\rangle = c_g(t)\,|g\rangle + \int \mathrm{d}E' c_{E'}(t)\left|\Psi'_E\right\rangle \quad , \quad \hat{H} = \hat{H}_0 + \hat{d}\cdot E(t). \tag{2.72}$$

In the Hamiltonian $\hat{d}$ denotes the dipole operator and $E(t)$ gives the time-dependent electric field. The solution for the time-dependent coefficients $c_g(t)$ and $c_{E'}(t)$ can be determined as outlined in section 2.3.2 with the additional complication of the continuous properties of the autoionizing state which requires an energy integration in the $c_{E'}(t)$ coefficient.

According to [92] this yields an effective Rabi frequency which includes the interference effects due to the mixing with the continuum $|\beta\rangle_E$ encoded in $|\phi\rangle_E$

$$\Omega_R^E = \langle\phi_E|\,\hat{d}\,|g\rangle\cdot\mathcal{E}_0/\hbar \tag{2.73}$$

Additionally, a modification of the Rabi frequency by a factor of $(1-i/q)$ is present in the given solution. Furthermore, a radiation-induced shift in energy S_g and width γ_g of the bound state $|g\rangle$ caused by the strong coupling to the continuum $|\beta\rangle_E$ is also described. The full results can be found in [92] and subsequent publications [95–99]. It is emphasized that the described effects are only present because of the strong interaction and interference effects with the continuum.

Finally, the case of multiple autoionizing states coupled by a strong field is briefly described. In this case, the expansion for the general state includes more autoionizing state contributions

$$|\Psi(t)\rangle = c_g(t)\,|g\rangle + \sum\int \mathrm{d}E' c_{E'}^{(i)}(t)\left|\Psi_E'^{(i)}\right\rangle. \tag{2.74}$$

Also, the dynamics are described by modified Rabi frequencies and radiation induced shifts of the state energies and widths. Additionally, the coupling of different autoionization continua $\left|\beta_E^{(i)}\right\rangle$, $\left|\beta_E^{(j)}\right\rangle$ or autoionizing states $\left|\phi_E^{(i)}\right\rangle$ with other continua $\left|\beta_E^{(j)}\right\rangle$ is

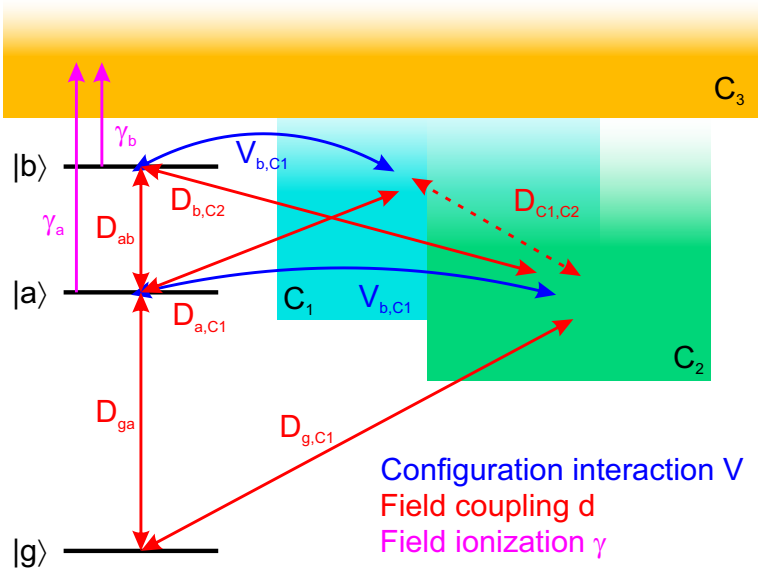

Figure 2.8.: **Level scheme of autoionizing state dynamics in strong fields:** The states embedded in the continua C_1 and C_2 experience configuration interaction (blue arrows) but can also be coupled to other states and to continua with different symmetries (red arrows). The coupling between continua (red dashed arrow) is expected to play a role only for very high intensities $I > 10^{14}$ W/cm^2. The autoionizing states can also undergo direct field ionization (purple arrow) into C_3 (see section 2.2.1).

possible. For intensities below 10^{14} W/cm^2 however the coupling between continua can be neglected [92]. An illustration of the possible couplings in such systems is given in figure 2.8. As the intensities discussed in the experiments of this work range between 10^{12} W/cm^2 and 10^{13} W/cm^2 these effects have to be taken under consideration.

2.4.3. The Helium Atom

The investigation of the dynamics of correlated electrons in atoms and molecules is the goal of this work. To this end, the most simple system with correlated electrons, the helium atom is chosen as the main spectroscopy target. As it has two electrons, the wave function of the helium atom can be written as

$$\Psi = \psi^{(2)}(\vec{r}_1, \vec{r}_1) \cdot \chi(s_1, s_2), \tag{2.75}$$

where ψ describes the spatial degrees of freedom and χ accounts for the spin of the electrons. The spin degrees of freedom live on a separate Hilbert space and are for the purposes of this work decoupled from the investigated dynamics. The multi-electron states discussed below follow the notation $^{2S+1}L^{\lambda}$, where S is quantum number of the total spin, L is the quantum number of the total angular momentum and λ indicates the parity of the state (even or odd). All states that are spectroscopically accessed in this work are singlet

states ($S = 0$), implying an antisymmetric spin wave function χ. Consequently the spatial wave function has to be symmetric to satisfy fermionic exchange symmetry. Considering interactions in dipole approximation, only transitions between states of different parity are allowed. This means that from the ground state $1s^2$ of ${}^1S^e$ symmetry only states of ${}^1P^o$ symmetry are accessible via 1-photon transitions.

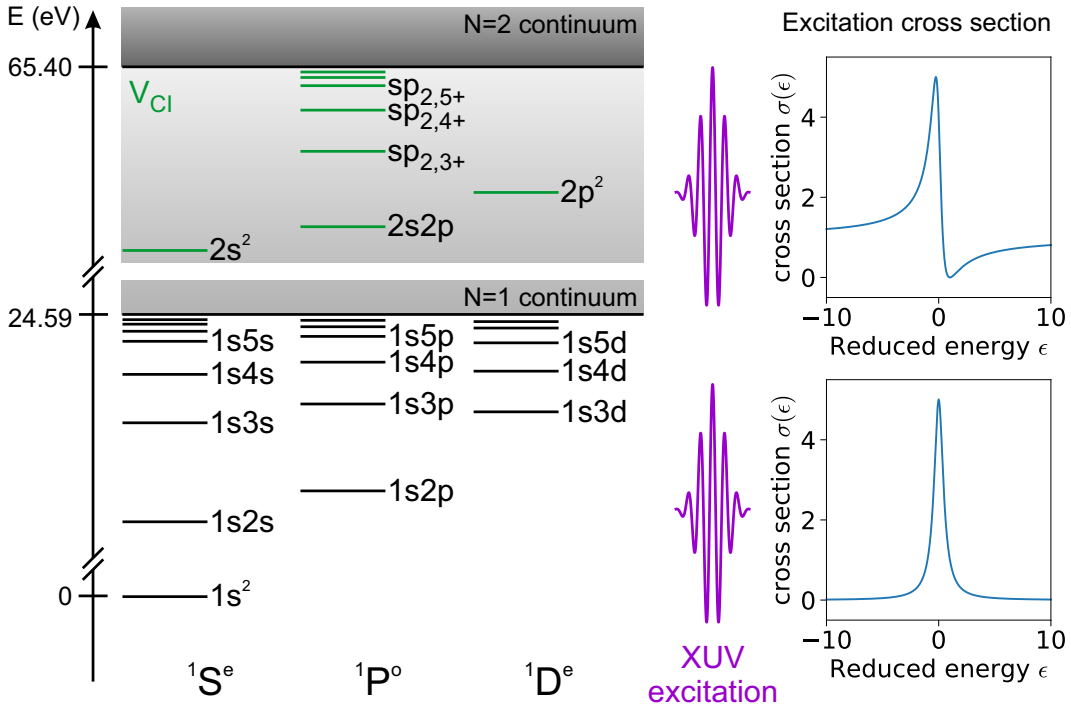

Figure 2.9.: **Level scheme of the helium atom:** The corresponding line shapes for singly and doubly excited states are shown in the insets. The energy positions are taken from [100].

Due to the wide range of photon energies accessible through high-harmonic generation, multiple configurations of excited electronic states in helium can be accessed. The manifold of singly excited states (SES) with only one electron excited from the ground state, denoted by $N = 1$ as the remaining electron is in the ground state with $n = 1$ ranges from 21.22 eV, the position of the first excited state up to the threshold of single ionization at 24.59 eV. The absorption lines visible in the experiment without any additional perturbations are the dipole-allowed transitions into the angular momentum states with P-symmetry. This series is denoted as 1snp with $n = 2,3,4,\ldots$ for the corresponding sub shells and converges towards the $N = 1$ ionization threshold as shown in figure 2.8. The 1sns and 1snd series of ${}^1S^e$ and ${}^1D^e$ symmetry are not accessible from the ground state.

For energies above this threshold the system can either ionize directly or both electrons are excited simultaneously. For these doubly excited states (DES) with $N = 2$ there are three possible configuration series, the 2snp, 2pns and the 2pnd series [101] which converge to the threshold of the N=2 ionization at 65.40 eV. As the states of the first two series are not distinguishable, they appear in linear combinations of the orbital configurations

configuration	Energy (eV)	Γ (meV)	q
1s2p	21.2180	0.0074	$-\infty$
1s3p	23.0870	0.0023	$-\infty$
1s4p	23.7421	0.0010	$-\infty$
1s5p	24.0458	0.0005	$-\infty$
1s6p	24.2110	0.0003	$-\infty$
1s7p	24.3107	0.0002	$-\infty$
1s8p	24.3755	0.0001	$-\infty$

Table 2.2.: Tabulated spectroscopic values for the first levels of the 1snp singly excited series of helium. The data is taken from [100]

$$\frac{1}{\sqrt{2}}(2s\mathit{n}\mathrm{p} \pm 2p\mathit{n}\mathrm{s}) \text{ , denoted } \mathrm{sp}_{2,n\pm}, \tag{2.76}$$

for historic reasons [102, 103]. The '+'-series appears the strongest, while the '-'-series is less pronounced in absorption spectra and the third series appears much weaker still. It was only detected by using high-resolution measurements at a synchrotron [104, 105]. As these states are degenerate with the continuum of single ionization, they may undergo autoionization and thus possess much shorter life times of $\sim$ 17fs for the 2s2p state and $\sim$ 100fs for higher excited states, compared to the SES with (radiative) life times on the order of few nanoseconds. Additionally, the interaction of the degenerate configurations of the DES and the continuum states causes a change in the spectral line shape described in the previous section by the asymmetry parameter q. The unperturbed energies, linewidths and Fano-q parameters taken from [100, 104–106] are given in table 2.3 for both the SES and the DES manifolds.

configuration	Energy (eV)	Γ (meV)	q
$2s^2$	57.7900	123.6	–
2s2p	60.1503	37.6	−2.74
$2p^2$	62.0600	6	–
$sp_{2,3-}$	62.7580	0.5	−3.5
$sp_{2,3+}$	63.6575	8.3	−2.53
$sp_{2,4-}$	64.1350	0.3	−3.2
$sp_{2,4+}$	64.4655	3.4	−2.58
$sp_{2,5-}$	64.6570	<0.1	−3.2
$sp_{2,5+}$	64.8200	1.8	−2.54
$sp_{2,6+}$	65.0000	1.0	–
$sp_{2,7+}$	65.1100	0.7	–

Table 2.3.: Tabulated spectroscopic values for the first levels of the 2snp doubly excited series of helium, classified in the '±'-series. The data is taken from [100, 104–106].

With increasing values for the quantum number N, classifying the highly excited DES on the basis of single-electron orbitals becomes more and more challenging because the

number of overlapping Rydberg series increases as well as the number of continua which contribute to the autoionization channel. However, group-theoretical approaches along hyperspherical coordinates are able to give a rigorous classification of DES even for large values of N [107–110]. This classification is based on a new set of correlation quantum numbers, which order correlations between the electrons in the radial and angular coordinates. An overview of the current development of the theory of two-electron atoms can be found in [111]. As this work is mostly concerned with states fulfilling $N \leq 2$ this is not discussed in more detail and the older notations are utilized to distinguish states with different correlation properties.

2.5. Absorption Spectroscopy in the Time Domain

Shining light through matter and determining the change in the spectral intensity distribution is a key technique in many branches of physics. Observing the changes introduced by the interaction with a sample, details about its internal structure and dynamics can be determined. This chapter will introduce basic principles of the description of signals interacting with a medium, how this leads to absorption and how this can be understood in a time domain and frequency domain picture.

2.5.1. Linear Response Theory

The general relation between input or driving force $f(t)$ and output $y(t)$ of a system (e.g., a force and the systems response to it) can in general be described by a so called Volterra expansion [112] in orders of the input signal $f(t)$

$$y(t) = f_0 + \sum_n \int_{-\infty}^{t} \dots \int_{-\infty}^{t} \chi^{(n)}(t'_1,\dots,t'_n) \prod_{i=1}^{n} f(t-t'_i)\mathrm{d}t'_i. \tag{2.77}$$

Here, f_0 is a constant offset that can usually be set to zero if only dynamical changes are considered and $\chi^{(n)}(t'_1,\dots,t'_n)$ is an n-th order tensor describing the systems response properties to the input. The integrals describe convolutions of the input signal with the response function $\chi^{(n)}(t'_1,\dots,t'_n)$ which means that the response of the system at a certain time t depends on all its history, meaning its states at all times $t' < t$. In practice however, even though it is in reality not exactly the case, the approximation of instantaneous response is made which replaces the time dependence in $\chi^{(n)}(t'_1,\dots,t'_n)$ with a product of delta functions $\delta(t-t'_i)$. With this, the integrations can be performed and the $\chi^{(n)}$ becomes constant with components depending on the material. An example for this is the description of the polarization $\vec{P}(t)$ (output) of a dielectric material within a strong electric field (input) which can have non-linear components depending on the susceptibility χ (response function). With the above approximation the expansion reads

$$\vec{P}(t) = \varepsilon_0(\chi^{(1)}\vec{E}(t) + \chi^{(2)}\vec{E}(t)^2 + \dots). \tag{2.78}$$

The exact form of χ is highly dependent on the material properties (polarizability, crystal symmetries etc.).
In the case of only linear responses for example during the interaction with weak electromagnetic fields, the expansion in equation 2.77 can be truncated after the first term. This yields an expression for the linear response of a system for a general external input $f(t)$ (or driving force) without the use of the approximation for instantaneous responses given by

$$y(t) = \int_{-\infty}^{t} \chi(t-t')f(t'). \tag{2.79}$$

As this depends linearly on the input $f(t)$, it becomes just a product if a Fourier transform to the frequency domain is applied according to the convolution theorem

$$\tilde{y}(\omega) = \tilde{\chi}(\omega)\tilde{f}(\omega) \rightarrow \tilde{\chi}(\omega) = \frac{\tilde{y}(\omega)}{\tilde{f}(\omega)} \tag{2.80}$$

If the signal is known and the response is measured it is possible to get access to the response function χ. Especially, if the input signal describes an impulsive interaction (exactly at one point in time) $f(t) \propto \delta(t-t_0)$. In this case, $\tilde{f}(\omega)$ becomes constant and $\tilde{\chi}(\omega)$ in equation 2.80 becomes directly proportional to the measured response signal $\tilde{y}(\omega)$. Furthermore, for the more general case of a causal response $y(t)$, meaning $y(t) = 0$ for all $t < t_0$, there exist analytical relations between the real and imaginary parts of the complex response function $\tilde{\chi}(\omega) = \tilde{\chi}_{Re}(\omega) + i\tilde{\chi}_{Im}(\omega)$, called the Kramers–Kronig relations

$$\tilde{\chi}_{Re}(\omega) = \frac{1}{\pi}\mathcal{P}\int_{-\infty}^{+\infty} \frac{\tilde{\chi}_{Im}(\omega')}{\omega'-\omega}\mathrm{d}\omega' \quad \text{and} \quad \tilde{\chi}_{Im}(\omega) = -\frac{1}{\pi}\mathcal{P}\int_{-\infty}^{+\infty} \frac{\tilde{\chi}_{Re}(\omega')}{\omega'-\omega}\mathrm{d}\omega', \tag{2.81}$$

where $\mathcal{P}$ denotes the principal value integral. A derivation of these relations can be found in many textbooks and the original publications [113, 114].
A full formalism of a system's linear response to a (weak) external force can be found in [115]. The derivation is done for the more general case of a statistical ensemble in quantum and classical mechanics and arrives at equation 2.80 with expressions for the response function ('after-effect function') $\chi(t)$ given as

$$\chi_{cl}(t) = -\int \mathrm{d}\Gamma\{A,\rho\}Q(t) \;\; (\text{classical}), \tag{2.82}$$

$$\chi_{qu}(t) = \frac{1}{i\hbar}\mathrm{Tr}[\hat{A},\hat{\rho}]\hat{Q}(t) \;\; (\text{quantum}-\text{mechanical}). \tag{2.83}$$

Here, $Q(t)$ is a physical quantity influenced by the interaction with $f(t)$, ρ is the phase space distribution of the ensemble and A is the degree of freedom $f(t)$ couples to. $\{,\}$

denote the Poisson brackets, $[,]$ is the commutator and $\int \mathrm{d}\Gamma$ is the integral over phase space [115]. Thus the presented formalism can also be applied to systems governed by quantum mechanics if the appropriate treatment of the response function is used. A concrete example for the application of this formalism is given by the interaction of a gaseous spectroscopy target to a weak and short laser field. In this case, the ensemble is given by a cloud of atoms, the measurable dynamical quantity is the electric field radiated from the atoms, $f(t)$ represents the driving electric field and A is given by the electric dipole moment of a single atom which couples to the electric field. This special case is discussed in more detail in the next section.

2.5.2. The Time-Dependent Dipole Response

The origin of a resonance line appearing in spectroscopy of radiation from microscopic systems is the target's temporal dipole response meaning the time-dependent dipole moment $d(t)$ of the excited system which is determined by its internal structure. These resonances can be probed using the interaction with electric fields which can be treated in the time domain using response theory. Starting from a single atom, the interaction with an electromagnetic field causing absorption of a photon will transfer population from the ground state into one or more (depending on the available photon energy range) excited states. The overall wave function $\Psi(t)$ of this coherent superposition of states, called wave packet, evolves in time and represents a time-dependent electron distribution where the expectation values $\langle \hat{x} \rangle_\Psi$ for the electron position differs on average from the position of the nucleus. This constitutes a dipole moment $d(t)$ that changes in time where

$$d(t) = \langle \Psi(t) | \hat{x} | \Psi(t) \rangle \,. \tag{2.84}$$

After some time the excited system will spontaneously emit exactly one photon. It is not possible to predict the exact time of emission. As it is a statistical process, it is however possible to measure the probability distribution of the time dependent process of emission if a large number of events are observed. Knowing this distribution a life time τ can be assigned to the excitation in the system which also gives the spectral width Γ of the emitted photons as $\Gamma = 1/\tau$.
For this to be visible in the spectrum, either a single atom has to be measured for a long time interacting with many photons, or an ensemble of a large number of atoms has to be used as a target. In both cases one can use the correspondence principle to describe the large number of photons in terms of classical fields and atomic systems in terms of driven responses (also in the single-atom case) using classical electrodynamics. In terms of response theory, the input signal $f(t)$ corresponds to the incoming electric field, χ is the complex electric susceptibility, given by the properties (internal structure) of the system and $y(t)$ corresponds to the electric field generated by the dipole response.
In terms of classical electrodynamics, the most simple case of a transition between a ground state $|g\rangle$ and one excited state $|e\rangle$ with energies E_g and E_e, as described above, results in a time-dependent dipole moment. This dipole oscillation decays exponentially due to the emission of radiation. The amplitude evolution starting after the excitation

at time $t_0 = 0$, if the excitation is treated in the framework of perturbation theory (see section 2.3.1), is given by the state $|\Psi(t)\rangle = |g\rangle - i\exp(-i\omega_e t)\exp(-\Gamma/2)c_e(t_0)\,|e\rangle$ with $c_g(t_0) \sim 1$ and $E_g = 0$

$$d(t) = \langle\Psi(t)|\,\hat{x}\,|\Psi(t)\rangle \propto |\,\langle e|\,\hat{x}\,|g\rangle\,|\exp(-\Gamma/2)\sin(\omega_e t)\theta(t). \tag{2.85}$$

Here, ω_e is the transition energy, $\Gamma = 1/\tau$ is the natural decay rate of the excited state and $c_e(t_0)$ is its initial population at t_0, which is given by $c_e(t_0) = c_g(t_0)\cdot\mu_{g,e}\mathcal{E}$, where $\mu_{g,e}$ is the dipole matrix element and $\mathcal{E}$ is the excitation field strength. The Heaviside theta function $\theta(t)$ results from the assumption of an instantaneous excitation in the system. The spectrum of the radiation emitted by this dipole is given by the Fourier transform of $d(t)$. It is easy to show that d(t) fits the imaginary part of the complex function $r(t) = A\exp(-\Gamma/2 - i\omega_r t)$ with some amplitude A. This function can be easily Fourier transformed into:

$$\tilde{r}(\omega) \propto \frac{iA}{\frac{\Gamma}{2} - i(\omega-\omega_e)} \propto A\left[-\frac{\omega-\omega_e}{\frac{\Gamma^2}{4}+(\omega-\omega_e)^2} + i\frac{\Gamma/2}{\frac{\Gamma^2}{4}+(\omega-\omega_e)^2}\right]. \tag{2.86}$$

The imaginary part of the expression represents the frequency domain response of the decaying dipole oscillation of the transition at energy E_e and width Γ. It describes the well known Breit-Wigner line shape of resonances measured in absorption. The real part gives the dispersion across the resonance experienced by the external field interacting with the system. Both contributions to the response are illustrated in figure 2.9.

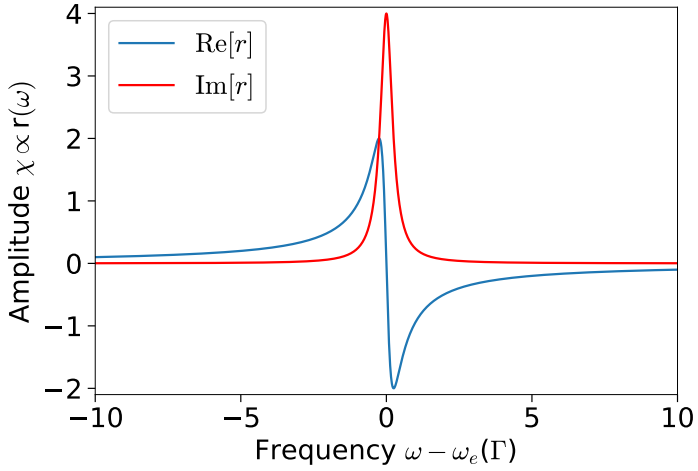

Figure 2.10.: **Complex response profile:** Real and imaginary part of the response function for a decaying dipole response given by equation 2.86.

This description was derived for discrete bound states and becomes more complex to describe the response if transitions to configurations with multiple excited electrons are

involved. In this case the states and dynamics have to be treated according to section 2.4.1. While this theory was mainly given in the frequency domain, it was recently shown, that not only the position E and the linewidth Γ but also the q-parameter can be mapped from the energy domain to the time-domain and vice versa (via a Fourier transformation) [116]. The main result presented in [116] is that the time-domain representation of q is a phase offset of the time-dependent dipole response of the observed system. The most general form of a dipole response involving states $|i\rangle$ with configuration interaction to continua is:

$$d(t) \propto c_q \delta(t) + c_i e^{-\frac{\Gamma}{2}t + i[-\omega_i t + \phi(q)]} \,. \tag{2.87}$$

The Dirac delta function corresponds to a continuum of excited states oscillating at all possible frequencies of the system scaled with a parameter c_q describing ionization properties while the decaying function describes dipole emission which results in a symmetric Lorentzian line shape. The phase offset term $\phi(q)$ describes how much the response is out of phase compared to the moment of excitation. The analytically obtained mapping between this phase shift and the q-parameter yields the relations:

$$\phi(q) = 2\arg(q-i) \qquad\qquad q(\phi) = -\cot\left(\frac{\phi}{2}\right) \,. \tag{2.88}$$

The consequence of this is that if the phase offset can be manipulated, the line shape of a resonance can be tuned at will as shown in [116]
A manipulation of the phase offset has been achieved experimentally on highly excited states in atomic systems where loosely bound electrons receive additional energy in a short laser pulse due to their quivering motion in the laser field, which is known as the ponderomotive energy (see equation 2.22). During the interaction with the laser pulse of duration T the excited electron acquires an additional phase according to

$$\Delta\phi = \int_0^T U_p \mathrm{dt} \,. \tag{2.89}$$

This gives the field strength or the intensity, respectively, as an obvious control parameter for the manipulation of the line shape of observed resonances as reported in [116]. Here, the excitation and manipulation of the dipole radiation was achieved in a transient-absorption spectroscopy experiment where an ultra-short XUV pulse excites the system and a strong infrared pulse can be used to manipulate the target system's dipole response. It is noteworthy that in this scheme destructive interference of emitted radiation from the sample and transmitted radiation can be turned into constructive interference by means of the phase manipulation of the dipole response or in other words, absorption can be changed into emission.

2.5.3. Linear Absorption & Lambert–Beer's Law

Absorption experiments are rarely carried out on single atoms but on gaseous or even liquid and solid targets. Therefore, a connection from the microscopic time domain description of absorption to macroscopic ensembles of atoms each contributing to the overall absorption process has to be drawn. For a dilute gas the description of the response in the time domain has to be extended to describe the combined emitted field of a plane A full of N oscillating dipoles at a point P far from this plane (e.g. the spectrometer) which is carried out in [117] and illustrated in figure 2.11. The radiated electric field of a single dipole oscillating with frequency ω_d at position Q is proportional to the acceleration of its charge and retarded in time. At P in a large distance r from Q it is given by

$$E_{d,single}(r,t) \propto \frac{\omega_d^2 d_0(t) e^{i\omega_d(t-r/c)}}{r} \tag{2.90}$$

Here, $d_0(t)$ gives the time evolution of the amplitude of the dipole oscillation. The total field is then calculated by integrating over contributions from each point on the plane A and thus all N dipoles, which yields

$$E_{d,total} \propto -iN\omega_d d_0(t) e^{i\omega_d(t-z/c)} \propto -N\omega_d d_0(t) e^{i\omega_d(t-z/c)+i\pi/2} \propto -i\eta E_{d,single}(t). \tag{2.91}$$

Here, $\eta \ll 1$ depends on the given number of emitters/atoms in the system, the central frequency ω_d and the constant distance to the sources r. This total response far away from the plane A shows a phase shift of $\pi/2$ also described in [118, 119] and is proportional to the single dipole response. Additionally if the excitation field is driving the dipole resonantly, its phase is shifted by $\pi/2$ against the phase of the driving field if the system is measured in the far-field of the dipole [120]. Overall the total phase shift with respect to the driving field is π, which means that if both (driving and dipole) fields are observed in a spectrometer, destructive interference will occur. The observed spectrum $S(\omega)$ will show the spectral intensity of the driving field with an absorption line at the position of the central dipole emission frequency ω_d. If photons are measured, one of the main experimental quantities describing the interaction which are accessible in the lab are the transmission $T(\omega)$ or absorption $A(\omega) = 1 - T(\omega)$ given by

$$T(\omega) = \frac{I_{out}(\omega)}{I_{in}(\omega)}\,. \tag{2.92}$$

Inserting the complex fields derived above, the transmission $T(\omega)$ and consequently the absorption $A(\omega)$ reads

$$T(\omega) = \frac{|\mathcal{F}\{E_{in}(t)\} + \mathcal{F}\{E_{d,total}(t)\}|^2}{|\mathcal{F}\{E_{in}(t)\}|^2} = \frac{|\mathcal{F}\{E_{in}(t)\} - i\eta\mathcal{F}\{E_{d,single}(t)\}|^2}{|\mathcal{F}\{E_{in}(t)\}|^2} \tag{2.93}$$

$$T(\omega) \approx 1 - 2\eta \mathrm{Im}\left[\frac{\mathcal{F}\{E_{d,single}(t)\}}{\mathcal{F}\{E_{in}(t)\}}\right] \quad , \quad A(\omega) \approx 2\eta \mathrm{Im}\left[\frac{\mathcal{F}\{E_{d,single}(t)\}}{\mathcal{F}\{E_{in}(t)\}}\right] . \tag{2.94}$$

Here, equation 2.91 with $\eta \ll 1$ for a dilute gas target (relatively small number of emitters N) was used to arrive at the final form. The Fourier transform which represents the action of the spectrometer is denoted by $\mathcal{F}$. The crucial result being that the absorption measured in the experiment is directly related to the dipole response that is generated in the medium during the interaction with the external field. This connection is most important for one of the main results of this work and will be used later on.

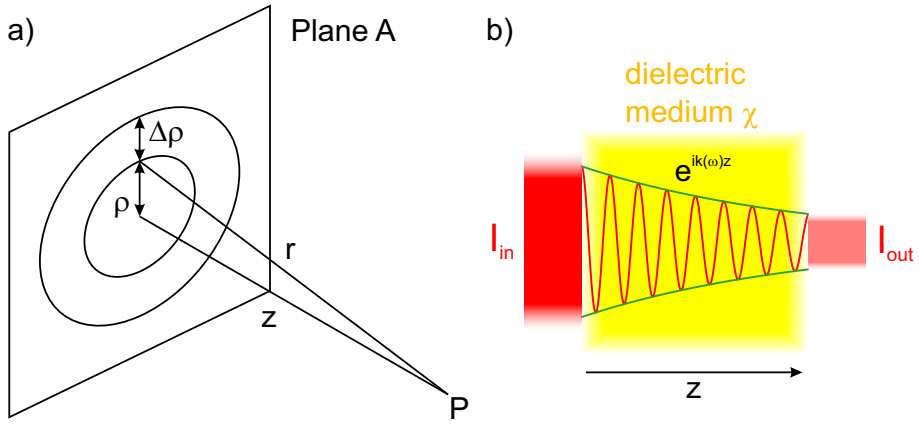

Figure 2.11.: **a)** Illustration of the calculation for the response of a plane of oscillating dipoles as expressed in equation 2.91. **b)** Attenuation of a propagating wave due to the complex refractive index $n(\omega) = \sqrt{1+\chi(\omega)}$.

A different approach on describing the absorption process for an electromagnetic wave propagating through a medium is to look at the macroscopic polarization. Following Maxwell's theory on electrodynamics, the polarization $\vec{P}$ given in the frequency domain basically describes the collective response of a medium to an external electric field of frequency ω. It is expressed in the frequency domain in terms of the electric field $E(\omega)$ and the dielectric susceptibility $\chi(\omega)$ as

$$P(\omega) = \varepsilon_0 \chi(\omega) E(\omega) , \tag{2.95}$$

where ε_0 is the dielectric permittivity in vacuum. In general, the polarization can be expanded in a power series (see equation 2.78) and as stated above $\chi(\omega)$ is the system's response function. Because only dilute targets are considered no propagation effects due to multiple absorption and reemission have to be considered and for weak field the interaction can be treated in linear order. An extension of the description including higher orders can be found in [121, 122]. In order to conveniently account for the phases of the electric field and the atomic responses in the field with respect to each other, the quantities $P(\omega)$ and $E(\omega)$ and consequently $\chi(\omega)$ are usually described with complex values:

$$\chi(\omega) = \chi'(\omega) + i\chi''(\omega) . \tag{2.96}$$

An electromagnetic field propagating along the z-direction through a medium, depicted in figure 2.11, experiences phase changes according to the values of the complex wave number $k(\omega) = \omega n(\omega)/c$

$$E(\omega, z) = E(\omega, 0) \cdot e^{ik(\omega)\cdot z} \tag{2.97}$$

The refractive index is related to $\chi(\omega)$ by $n(\omega) = \sqrt{1+\chi(\omega)}$. For dilute media, a Taylor expansion to first order can be applied and the complex wave number $k(\omega)$ becomes:

$$k(\omega) = \frac{\omega}{c} \cdot n(\omega) \simeq \frac{\omega}{c} \cdot \left(1 + \frac{\chi'}{2} + i\frac{\chi''}{2}\right) . \tag{2.98}$$

Inserting this into the general expression of the electromagnetic field, it becomes clear that the real part of $k(\omega)$ represents dispersion whereas the imaginary part represents the absorption of waves propagating in a given medium:

$$E(\omega, z) = E(\omega, 0) \cdot \exp\left(i\frac{\omega}{c} \cdot \left(1 + \frac{\chi'}{2}\right) \cdot z\right) \exp\left(-\frac{\omega}{c} \cdot \chi''(\omega) \cdot z\right) . \tag{2.99}$$

The approximations above are only valid for small values of χ which is the case for a dilute gas targets. The general expression for Lambert–Beer's law is

$$I_{sig}(\omega, z) = I_{in}(\omega, 0) e^{-\rho_N \sigma(\omega) z}, \tag{2.100}$$

where ρ_N gives the atomic number density and $\sigma_{abs}(\omega)$ is the absorption cross section. Comparing this to equation 2.99 and noting that the overall polarization is composed of single dipole responses according to $P(\omega) = \rho_N \cdot d_{single}(\omega)$ yields a relation between the cross section and the imaginary part of the dipole polarization response χ of a single atom

$$\sigma_{abs}(\omega) = \frac{2\omega}{c\rho_N} \mathrm{Im}\left[\frac{P(\omega)}{E_{in}(\omega)}\right] = \frac{2\omega}{c} \mathrm{Im}\left[\frac{d_{single}(\omega)}{E_{in}(\omega)}\right] . \tag{2.101}$$

Again the overall absorption for dilute targets can be written as $A(\omega) = N \cdot \sigma_{abs}(\omega)$. This is in agreement with the results for the time-domain picture of absorption derived in equation 2.94. The intensities $I_{in}(\omega, 0)$ and $I_{sig}(\omega, z)$ appearing in equation 2.100 represent the signals commonly observed in absorption experiments. Typically, the data is evaluated and interpreted as the so-called optical density (OD) in a sample of thickness l:

$$\mathrm{OD}(\omega) = \log_{10}\left(\frac{I_{sig}(\omega)}{I_{in}(\omega)}\right) = \frac{\sigma(\omega)}{\ln 10} \cdot \rho_N \cdot l . \tag{2.102}$$

3. Numerical Methods

The wave function carries all the information about the system, including interaction with external fields and correlation effects in multi-particle systems. While for the system of hydrogen, one electron bound to a proton, analytical solutions for the wave function can be found (shown in many textbooks [85, 123, 124]), up until now this is not possible for more complex systems. In this case it is necessary to numerically approximate solutions of the (time-dependent) Schrödinger equation (TDSE). One common method is the Hartree-Fock (HF) approach [85], which involves the antisymmetric linear combination of all involved single-electron orbitals including their spin, the so-called Slater determinant. Electron exchange correlation enters due to the mixing of different single-electron orbital product wave functions. The weight of these orbitals making up the real wave function are then determined from initial values via an iterative optimization algorithm that minimizes the energy of the overall state in the given potential. There exist many extensions to this technique, like solutions for the time-dependent case (TDHF) and introducing further mixing of multi-configuration states (MCTDH, MCTDHF) to include electron-electron interactions approximately. An overview of these methods can be found in [125]. Another approach is given by density functional theories (DFT) and their time-dependent variant (TDDFT). Here, the wave function is described as a functional of the electron density. DFT is used to calculate collective many-electron effects and is discussed in more detail in [126]. If the participating states and their couplings are known it is however possible to use the discrete basis approach for solving the TDSE.

3.1. Discrete Basis TDSE

If an *ab-initio* approach, which treats the whole wave function on a discrete grid in position and momentum space is used, numerical calculations quickly become very expensive because the n-particle Schrödinger equation including all interaction potentials has to be solved. An alternative method is the expansion of the wave function into a set of discrete (or continuous) basis states depending on the features of the system that have to be captured. For a set of n discrete and m continuum states $|i\rangle$ and $|\alpha\rangle$ the expansion reads:

$$\psi = \sum_{i=1}^{n} c_i |i\rangle + \sum_{k=1}^{m} \int \mathrm{d}E \; c_k(E) |\alpha_k(E)\rangle, \tag{3.1}$$

where $c_i = \langle i|\psi\rangle$. In the basis of n discrete states (continua are omitted for simplicity) the description of the system can be cast into n-dimensional vector and a Hermitian $n \times n$ matrix representation:

$$\hat{H}_{ij} = \langle i|\hat{H}|j\rangle \ , \ \psi_i = \langle i|\psi\rangle = c_i \tag{3.2}$$

While the elements H_{ii} represent the energies E_i of the basis states, the entries H_{ij} with $i \neq j$ are coupling terms between different states. In the case of interaction with an electromagnetic field $E(t)$ these elements introduce a time dependence and can be written within the dipole approximation and in length gauge [85] as:

$$H_{ij}(t) = e\langle i|\hat{x}|j\rangle E(t) = d_{ij}E(t). \tag{3.3}$$

Here, e is the electron charge, $\hat{x}$ is the position operator and d_{ij} are the dipole transition matrix elements. Within this framework a multitude of effects during the interaction with external fields can be described if energies and transition matrix elements gained from spectroscopy or *ab-initio* calculations are available. In the matrix representation the time-dependent Schrödinger equation turns into a set of coupled differential equations of the state coefficients $c_i(t)$ which can be solved numerically with significantly less computational effort than a full *ab-initio* treatment would require.

3.1.1. Hamilton Operator and Interactions for Doubly Excited Helium

As the principal method of investigation of this work is time-resolved absorption spectroscopy using XUV and NIR light pulses, the main target helium is modeled as a few-level system interacting with these fields. For this a previously used model [127] is further generalized in order to properly account for multi-photon ionization and strong coupling to other additional states in the presence of intense NIR pulses (see also [92, 99, 128, 129] and sections 2.2.1, 2.4.2). The states used to describe the system include the ground state $|g\rangle \equiv 1s^2\,{}^1S^{\mathrm{e}}$, of energy $E_g = 0$, and the four doubly excited autoionizing states $|a\rangle \equiv 2s^2\,{}^1S^{\mathrm{e}}$, $|b\rangle \equiv 2s2p\,{}^1P^{\mathrm{o}}$, $|c\rangle \equiv 2p^2\,{}^1S^{\mathrm{e}}$ and $|d\rangle \equiv sp_{2,3+}\,{}^1P^{\mathrm{o}}$, with their respective energies E_a, E_b, E_c and E_d given in table 2.3. The coupling of the doubly excited states with the degenerate $N = 1$ continuum states $|\varepsilon p\rangle \equiv 1s\varepsilon p\,{}^1P^{\mathrm{o}}$ and $|\varepsilon s\rangle \equiv 1s\varepsilon s\,{}^1S^{\mathrm{e}}$ is described by the configuration interaction V_{CI}. The continuum states are approximated by a set of non-interacting momentum states, which is described in more detail below. The parameter values of this interaction are adjusted to reproduce the line shape known from experiment and theory given by the values in table 2.3. Using the states listed above, and considering that autoionization is the main process resulting in the experimentally observed line shape and resonance width, the state-vector of the system is expanded into

$$|\psi(t)\rangle = c_g(t)|g\rangle + c_a(t)|a\rangle + c_b(t)|b\rangle + c_c(t)|c\rangle + c_d(t)|d\rangle + c_{\varepsilon p}(t)|\varepsilon p\rangle + c_{\varepsilon s}(t)|\varepsilon s\rangle, \tag{3.4}$$

with the complex expansion coefficients $c_n(t)$. Its time evolution is given by the solution of the Schrödinger equation in matrix representation:

$$i\partial_t \vec{c}(t) = \hat{H}\vec{c}(t) \tag{3.5}$$

with $\vec{c} = (c_g, c_a, c_b, c_c, c_d, c_{\varepsilon p}, c_{\varepsilon s})^T$ and $\hat{H}$ being the Hamilton operator with entries following equation 3.2. Since the system is in principle time-reversal symmetric (the continuum is approximated by a finite set of states), the basis states can be chosen to be real. Thus all dipole-moment and configuration-interaction matrix elements are real. The full coupled differential equations of motion for all coefficients can be found in appendix B.
The dynamics introduced by the interaction with the electric fields are described by electric-dipole-($E1$-)allowed transitions given in equation 3.3. They are characterized by the non-vanishing dipole-moment matrix elements μ_{gb}, μ_{gd}, μ_{ab}, μ_{bc}, μ_{cd} and $\mu_{g,\varepsilon p}$. The symmetry-allowed states $|b\rangle$ and $|d\rangle$ are excited perturbatively from the ground state by the XUV pulse $\mathcal{E}_{XUV}(t)$. The direct transition into the continuum states $|\varepsilon p\rangle$ is described by an energy-independent dipole-moment matrix element $\mu_{g,\varepsilon p}$. For the low XUV intensities achievable in the experiment, the action of the XUV pulse can be treated in first-order perturbation theory, according to section 2.3.1 and assuming that $\partial_t c_g = 0$ ($E_g = 0$), i.e., $c_g = 1$. The rotating-wave approximation (RWA) is applied for the XUV field. This allows the coupling to be written in terms of the complex positive- and negative-frequency components of the electric field, $\mathcal{E}^+_{XUV}(t)$ and $\mathcal{E}^-_{XUV}(t) = [\mathcal{E}^+_{XUV}(t)]^*$, respectively, with $\mathcal{E}_{XUV}(t) = \mathcal{E}^+_{XUV}(t) + \mathcal{E}^-_{XUV}(t)$. This way, only the counter-rotating term $\mathcal{E}^+_{XUV}(t)$ is taken into account in the perturbative excitation.
The interaction with the NIR pulse $\mathcal{E}_{NIR}(t)$ couples the four autoionizing states via symmetry-allowed transitions $\langle a|\hat{T}|b\rangle$, $\langle b|\hat{T}|c\rangle$ and $\langle c|\hat{T}|d\rangle$. Here, the real time-dependent representation of $\mathcal{E}_{NIR}(t)$ is used in order to account for effects beyond the RWA and $\hat{T}$ denotes the dipole operator. The $2s^2$ state is included in order to better model the strong-field driven population transfer dynamics in the $2s2p$ state. However, the coupling between this state and $|d\rangle = sp_{2,3+}\,{}^1P^o$ is not included, as the NIR pulse frequency is significantly detuned from the corresponding transition energy. The $2s^2\,{}^1S^{\mathrm{e}}$ characterized by the energy $E_a = 57.79\,\mathrm{eV}$ and autoionization decay width $\Gamma_a = 123.6\,\mathrm{meV}$. The $2s2p\,{}^1P^{\mathrm{o}}$ state features energy $E_b = 60.15\,\mathrm{eV}$, autoionization decay width $\Gamma_b = 37.6\,\mathrm{meV}$, and Fano q parameter $q_b = -2.74$. The $2p^2\,{}^1S^{\mathrm{e}}$ state is given by $E_c = 62.06\,\mathrm{eV}$ and $\Gamma_c = 6\,\mathrm{meV}$. Analogous parametrization is used for the $sp_{2,3+}\,{}^1P^{\mathrm{o}}$ state, with $E_d = 63.65\,\mathrm{eV}$, $\Gamma_d = 8.3\,\mathrm{meV}$, and $q_d = -2.58$. Dipole-moment matrix elements between autoionizing states were obtained through full *ab-initio* calculations and are given by $\mu_{ab} = -1.56\,\mathrm{a.u.}$, $\mu_{bc} = 2.17\,\mathrm{a.u.}$ and $\mu_{cd} = -0.81\,\mathrm{a.u.}$.
The NIR-induced ionization of doubly excited states to the $N = 1$ continuum was neglected for the utilized intensities $I_{NIR} < 10^{13}\mathrm{W/cm^2}$ [99,128]. Furthermore, the coupling between states in continua with different symmetry induced by the NIR field is negligible for the intensities available in the experiment [92]. Other contributions of excited states in the $N = 2$ Rydberg series are not accounted for because they are either far off-resonant or possess significantly lower coupling strengths to the states included in this model, at least for moderate field strengths.

3.1.2. Autoionization and Strong-Field Ionization

The numerical model treats the interaction of a bound state degenerate with a continuum using a quasi-discrete approximation for the actual physical continuum above the first ionization threshold. The $N = 1$ continuum states called $|\varepsilon p\rangle$ and $|\varepsilon s\rangle$ for their respective symmetries, are given as a set of non-interacting states, with canonical momentum p, energy $p^2/2$, and momentum separation Δp. Here, we have neglected the contribution coming from the vector potential $A_{NIR}(t) = -\int_{-\infty}^{\infty} \mathcal{E}_{NIR}(t')\,\mathrm{d}t'$ to the energy of the continuum states [51, 130]. Constant, energy-independent decay rates $\Gamma_{\varepsilon p}$ and $\Gamma_{\varepsilon s}$ are employed in order to broaden these quasi-discrete states and reach mutual overlap in order to approximate the continuum.
The bound states interact with each of the n states of the quasi-discrete continuum sequentially. In this way, only the interaction described by a 2×2 Hamiltonian has to be solved n times, instead of the computationally more expensive solution of an $(n+1) \times (n+1)$ system for each time step.
The energies of the quasi-discrete states used to model $N = 1$ continuum states $|\varepsilon p\rangle$ and $|\varepsilon s\rangle$ range from $p_{min} = \pm 1.35$ a.u., i.e., $E_{min} = 24.8\,\mathrm{eV}$, to $p_{max} = \pm 2.80$ a.u., i.e., $E_{max} = 106.7\,\mathrm{eV}$, with 100 steps $\Delta p = \pm 0.0145$a.u. and decay rates $\Gamma_{\varepsilon p} = \Gamma_{\varepsilon s} = 0.1$ a.u.. The parameters $V_{a,\varepsilon s}, V_{b,\varepsilon p}, V_{c,\varepsilon s}, V_{d,\varepsilon p}, \mu_{gb}, \mu_{gd}$, and $\mu_{g,\varepsilon p}$ are assumed to be independent of the energy of the continuum states, in accordance with [90, 92, 99] and were adjusted in order to reproduce known experimental and theoretical line shapes [127].

We explicitly include NIR-induced multi-photon ionization of the doubly excited states $|b\rangle$, $|c\rangle$ and $|d\rangle$. This is modeled in terms of ionization rates $\Gamma_4 = \alpha_4 I_{NIR}^4(t)$, $\Gamma_3 = \alpha_3 I_{NIR}^3(t)$ for the four and three-photon ionization of the $|c\rangle = 2s2p$ and $|c\rangle = 2p^2$ states, and $\Gamma_2 = \alpha_2 I_{NIR}^2(t)$ for the two-photon ionization of the $|d\rangle = sp_{2,3+}$ state, with $I_{NIR}(t)$ being the time-dependent NIR pulse intensity, and α_2, α_3 and α_4 are free parameters determined through comparison with experimental data for a variety of NIR intensities. The α-parameters are calibrated for the highest intensity and then kept constant for the other calculations (they do not constitute fit-parameters in each individual simulation).

3.1.3. Numerical Solution

With the assumption that $c_g = 1$, the time-dependent XUV dipole response of the system is given by $d(t) = \mu_{gb} c_b(t) + \mu_{gd} c_d(t) + \mu_{g,\varepsilon p} c_{\varepsilon p}(t) + \text{c.c.}$. The corresponding transient-absorption spectrum $A(\omega)$ is proportional to the cross section $\sigma(\omega)$ and can be modeled according to section 2.5.3 as $\sigma(\omega) \propto \omega\,\mathbf{Im}\left\{\frac{\mathcal{F}[d(t)]}{\mathcal{F}[\mathcal{E}_{XUV}(t)]}\right\}$. The following definitions for the Fourier transform of a function $f(t)$ are used throughout the calculations:

$$\tilde{f}(\omega) = \mathcal{F}[f(t)] = \int_{-\infty}^{\infty} f(t) \mathrm{e}^{i\omega t}\,\mathrm{d}t, \tag{3.6}$$

$$f(t) = \mathcal{F}^{-1}[\tilde{f}(\omega)] = \frac{1}{2\pi}\int_{-\infty}^{\infty} \tilde{f}(\omega) \mathrm{e}^{-i\omega t}\,\mathrm{d}\omega. \tag{3.7}$$

In order to obtain $d(t)$ the time dependent coefficients $c_i(t)$ have to be calculated. This is achieved from an initial state via a so-called split step time evolution algorithm [131]. This algorithm works on a grid of discrete time steps t_i separated by Δt and solves the equation of motion iteratively for each time step. First, the changes to the state vector coefficients $c_i(t)$ due to perturbative interaction with the XUV is calculated. The result is then propagated in time with the split step method to second order accuracy in the time step Δt [132], which changes between the two diagonal bases of H_0 and H_{int}. The time steps were set to $\Delta t = 0.5$ a.u., in order to sample one cycle of the XUV field (duration 69 as at 60 eV). The operations performed during one step $t_i \rightarrow t_{i+1} = t_i + \Delta t$ of the time evolution are:

1. Stationary evolution of the bound states for half a time step with the unperturbed energy-eigenvalues using the unitary operator $\hat{U}_0 = e^{-\frac{1}{2}i\hat{H}_0\Delta t}$
2. Transformation to the basis in which the matrix of the interaction Hamiltonian is diagonal with the unitary operator $\hat{U}_{trans}$ gained from diagonalizing $\hat{H}_{int}$
3. Time evolution of the bound states in the new diagonal basis with the operator $\hat{U}_{int} = e^{-i\hat{H}_{int}(t_i)\Delta t}$
4. Transformation to the basis in which the matrix of the unperturbed atomic system is diagonal using $\hat{U}^{-1}_{trans}$
5. Stationary evolution of the bound states for half a time step with the unperturbed energy-eigenvalues using the operator $\hat{U}_0 = e^{-\frac{1}{2}i\hat{H}_0\Delta t}$

3.2. *Ab-initio* 1D TDSE for Two Electrons

In the special case of linear polarized and non-relativistic electric fields the description of the helium atom can be carried out in one dimension for each electron making the wave function effectively two dimensional (instead of six dimensions for the full problem). This is still manageable by modern computers if the grid used for the wave function representation is not chosen too large. A detailed overview of the ansatz discussed in the following can be found in [133–136]. The first assumption in this approach to describe the helium atom is that the system is made up of a point-like nucleus carrying a double positive charge and two point-like negatively charged electrons which are not distinguishable. The dynamics are considered in the rest-frame of the nucleus, which means that the nuclear motion is not taken into account at all. Furthermore, as stated above, the motion of each electron is restricted to only one dimension x represented by a discrete grid.

3.2.1. Hamilton Operator and Interactions

With these approximations the potentials acting in the model atom between both electrons and the nucleus are approximated by a Coulomb potential, which is modified by a 'soft-core'-parameter a. This form of the potential avoids the singularity (numerical divergence) at $x = 0$ and is known as the Rochester one dimensional potential [137, 138]. The Hamiltonian of the non-interacting (free) system is given by

$$H_0(x_1,x_2,p_1,p_2) = \frac{1}{2}\sum_{i=1}^{2} p_i^2 - \sum_{i=1}^{2} \frac{2}{\sqrt{x_i^2+a^2}} + \frac{1}{\sqrt{(x_1-x_2)^2+b^2}} \tag{3.8}$$

where the middle term represents the potentials for the interaction of the electrons with the nucleus and the last term describes the mutual Coulomb repulsion of the electrons. The parameters a and b adjust the soft-core potential and may be used to change the energies of the bound states in order to be close to the real 3D system. An example for the full potential in two dimensions is shown in figure 3.1.
External fields act simultaneously on both electrons in the plane of polarization. As the motion of the particles is limited to one dimension no effects of the magnetic field are taken into account (valid for non-relativistic field strength and motion). The electric field $E(x,t)$ changes the systems potential which is expressed in length gauge

$$V_{int} = (x_1+x_2)E(t)|_{x=0} \text{ with } E(t) = \mathcal{E}(t)\cos(\omega t+\phi). \tag{3.9}$$

In the dipole approximation the field $E(x=0,t) = E(t)$ can be assumed constant across the extension of the atomic system. The electric field is given by a pulse of frequency ω, CEP ϕ and a Gaussian envelope function $\mathcal{E}(t) = \mathcal{E}_0 \exp[(t-t_0)^2/\tau_G^2]$. With this the complete Hamiltonian for helium interacting with an external electric field reads

$$H(x_1,x_2,p_1,p_2) = \frac{1}{2}\sum_{i=1}^{2} p_i^2 - \sum_{i=1}^{2} \frac{2}{\sqrt{x_i^2+a^2}} + \frac{1}{\sqrt{(x_1-x_2)^2+b^2}} + (x_1+x_2)E(t), \tag{3.10}$$

and the time dependent Schrödinger equation of the system takes the form

$$i\partial_t |\Psi(x_1,x_2;t)\rangle = H(x_1,x_2,p_1,p_2)\,|\Psi(x_1,x_2;t)\rangle\,. \tag{3.11}$$

3.2.2. Wave Function Interpretation

The overall wave function in equation 3.11 is represented on a two-dimensional discrete grid of $n \times n$ points, where the maximum number of grid points is usually $n = 4096$ to ensure low enough duration of the calculations. Each of the discrete grid points represents a position space eigenstate $|x_1,x_2\rangle$ and the wave function is represented in position space by projecting the full wave function on these states $(x_1,x_2) = \langle x_1,x_2|\,|\Psi(x_1,x_2;t)\rangle$. The calculations use periodic boundary conditions. To avoid the propagation of the wave function over the edge, causing interference on the other side and in order to simulate ionization effects, a cylindrically symmetric imaginary potential $B(r)$ is introduced on the grid, which acts as an absorbing boundary for the wave function. This boundary is defined as

$$B(r,R_{min},R_{max}) = \begin{cases} \cos^2\left(\frac{\pi}{2}\frac{r}{R_{max}-R_{min}}\right) & \text{for } R_{min} < r < R_{max} \\ 0 & \text{for } r < R_{min} \\ 1 & \text{for } r > R_{max} \end{cases} \tag{3.12}$$

Figure 3.1 b) shows the grid and the absorbing boundary as a shadowed area. In order to interpret the physics described by the wave function, the grid is partitioned into several different sections as it is discussed in several studies of ionization in small atoms and molecules using a simulation similar to the one described here [139–142]. Changes in the amplitude of the wave function in each segment can be interpreted as a different dynamical effect. Section V in the center of the grid defines the size of the atom with less than 1% of the wave function of the unperturbed ground state wave functions, shown in 3.1 c) and d) for the singly and doubly excited states, is not inside this segment. Starting from this, an increase of the amplitude in sections II, IV, VI and VIII indicates the process of single ionization (SI) where one electron is near its coordinate origin and the other one is far away from the nucleus. If the amplitude in sections I, III, VII and IX increases, the second electron is also far away from the core indicating double ionization (DI). The green areas indicate the case of electrons leaving the atom back to back in DI, whereas the purple ares show the process of electrons leaving side by side. DI can occur as a sequential and a non-sequential process. In the first case, the second electron is ionized after the first electron left the atom, indicated by a flow of the wave function perpendicular to the closest SI region. In the other case, the electrons leave simultaneously which manifests itself in diagonal structures in the flow of the wave function.

3.2.3. Numerical Solution

With the total wave function in the discrete spatial representation, the solution of equation 3.11 uses a slightly different approach than described in section 3.1. For this model of the wave function, the split step algorithm separates the Hamiltonian into spatial and momentum dependent parts $H(x_1,x_2,p_1,p_2;t) = H_x(t) + H_p(t)$. With this, the time evolution operator to second order in Δt [132] is given by

$$U(t,t+\Delta t) = \exp[-i(H_x(t)+H_p(t))\Delta t] \tag{3.13}$$

$$= \exp\left(-\frac{i}{2}H_x(t)\Delta t\right)\exp\left(-iH_p(t)\Delta t\right)\exp\left(-\frac{i}{2}H_x(t)\Delta t\right) + \mathcal{O}(\Delta t^3), \tag{3.14}$$

similar to the previous section. In order to make use of the fact, that the operators $\hat{x}$, $\hat{p}$ and consequently $H_x(t)$, $H_p(t)$ are diagonal in position and momentum space respectively, the Fourier transform $\mathcal{F}$ is used to change between the position and momentum space representation of the wave function $|\Psi(p_1,p_2;t)\rangle = \mathcal{F}\{|\Psi(x_1,x_2;t)\rangle\}$. With this one step in the time evolution is given by applying the following operations to the state vector $|\Psi(x_1,x_2;t)\rangle$ from right to left

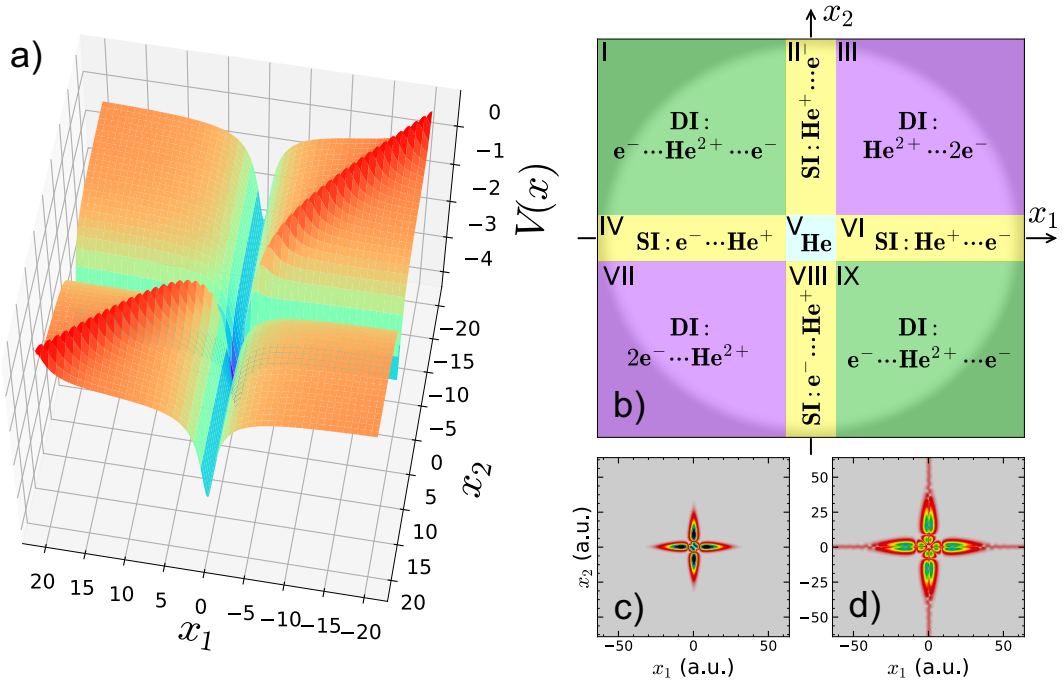

Figure 3.1.: **a)** Illustration of the full two dimensional potential $V(x_1,x_2)$ given by equation 3.8. **b)** Partition scheme for the interpretation of the dynamic processes described by the wave function **c)** SES Wave function **d)** DES Wave function

$$|\Psi(t+\Delta t)\rangle = e^{\frac{i}{2}H_x(t)\Delta t}\mathcal{F}^{-1}e^{-iH_p(t)\Delta t}\mathcal{F}e^{-\frac{i}{2}H_x(t)\Delta t}|\Psi(t)\rangle \tag{3.15}$$

3.3. *Ab-initio* 3D TDSE for Helium

It is nowadays possible to solve the complete three dimensional Schrödinger equation for helium. This was done in collaboration with the group of Joachim Burgdörfer at the Technical University of Vienna. In the approach utilized in this work (see [143] for a detailed description), the two-electron time-dependent Schrödinger equation is solved using the time-dependent close coupling method [144–146]. In this way, the full time evolution of the wavefunction can be obtained. The radial discretization of the wavefunction is implemented with a finite-element discrete variable representation [147–149], where 11 basis functions are used for each radial element of 4 a.u. in size. The close-coupling scheme uses an angular momentum expansion with $L_{\max} = 10$, $l_1 = 10$ and $l_2 = 7$. The temporal propagation utilizes the short iterative Lanczos method [150, 151] with automatic time-stepping and error control. As it is the case for the discrete few-level approach and the two dimensional TDSE calculation, the linearly polarized laser fields are treated in dipole approximation. Furthermore, it was verified that length and velocity gauge give equivalent results.

The XUV pulses are given by a central energy of 60.15 eV, a Gaussian envelope for the intensity profile with a pulse duration of 250 as FWHM, and a peak intensity of 10^{12} W/cm^2. For the NIR pulse, the wavelength of 740 nm with a Gaussian envelope for the intensity

profile (7 fs FWHM) and varying peak intensity was used. The time-dependent dipole moment $d(t)$ is calculated according to equation 2.84 by taking the wave function within a relatively small radial box of 128 a.u. around the nucleus, where an absorbing boundary starts at 102 a.u..

4. Experimental Setup

Time-dependent processes in physics are in general described by an initial state, dynamically changing intermediate states and a specific final state, a paramount example being chemical reactions between atoms and molecules. It is imperative to precisely characterize the quantum states of these systems in order to gain insight into the processes at work. To this end, various techniques detecting photo-electrons, scattered electrons, ions or photons have been devised. While an overview of these methods can be found in many physics textbooks [86, 121, 124, 152], the following discussion is only concerned with techniques measuring photons, as they are particularly well suited for the experimental study of the internal structure of atoms and molecules. They do not interact with each other or stray electromagnetic fields and are not affected by space charge effects. Furthermore, the measurement of photons is possible within a broad spectral range and with high sensitivity using modern solid state detectors [153, 154]. Combined with high resolution spectrometers photon absorption has been used very successfully to study bound quantum states and transitions from the very first observation of electronic levels in atoms in 1814 [155] to state of the art techniques like doppler-free absorption spectroscopy [86] used to measure quantum-electrodynamic effects like the Lamb shift [156]. In general, the setup for absorption spectroscopy consists of the following parts illustrated in figure 4.1: a photon source, e.g. (pulsed) laser, synchrotron source or free electron laser; a spectroscopy target e.g. gases of atoms and molecules, liquids or solid material; a spectrometer consisting of a dispersive element (prism, grating) and a detector (fluorescent materials, charge coupled devices).

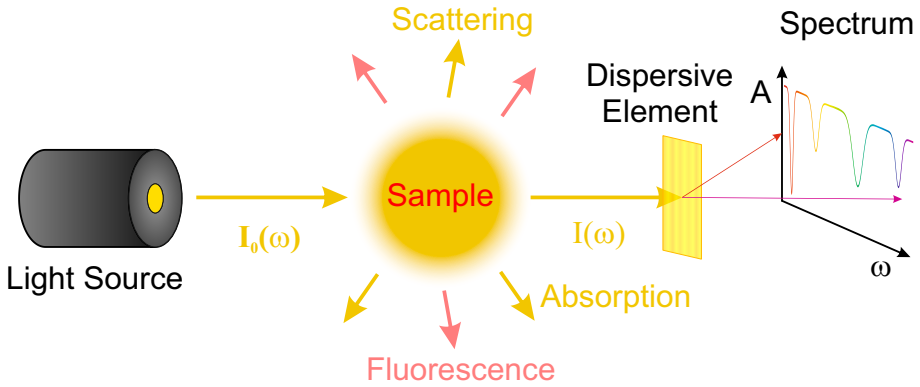

Figure 4.1.: **Absorption spectroscopy:** The radiation from the light source interacts with a sample, where it is scattered, absorbed or converted into fluoresence. The outgoing photons can be spectrally resolved and detected to study the interaction.

For the investigation of *time-dependent* quantum processes the introduction of a relative timing is necessary in order to reference separate points in time. A very successful scheme of time-resolved spectroscopy is based on using two or more laser pulses with durations shorter than the characteristic time-scale of the dynamic processes under investigation. In general, the first pulse initiates dynamics and the subsequent pulse(s) are used to probe the response of the system after a certain time delay by projecting the system onto a final state that is detected. Typically, a strong and short laser pulse in the near infrared to visible spectral range starts dynamic processes by ionization or excitation. A subsequent weaker pulse then probes the system by an additional ionization step out of the excited state. The delay between both events is varied and either the electrons, ions and molecular fragments or the photon signals of the pulses are measured depending on this delay. This approach is used in various techniques to extract information about atomic and molecular dynamics. Reaction microscopes (REMI) or cold target recoil ion momentum spectroscopy (COLTRIMS) [157–162] detect electrons and ions with time-of-flight measurements and coincident detection for full reconstruction of the initial momenta in the ionization and dissociation dynamics. However, as stated above, for bound state dynamics the measurement of photons provides complementary access and is thus interesting from an experimental point of view. The method of transient-absorption spectroscopy (TAS) [163–165] measures the absorption of the pulses in the medium depending on the time-delay parameter and other control parameters such as the pump pulse intensity, as illustrated in figure 4.2.

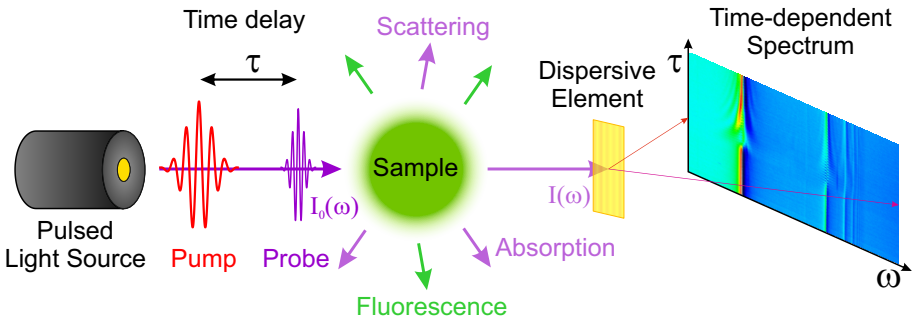

Figure 4.2.: **Pump-probe absorption spectroscopy:** Two laser pulses interact with the sample, where one typically starts some dynamic process (ionization) and the other is used as a probe of the system after the variable time delay τ. The first pulse can also be used to excite a coherent response in the system which is afterwards modified by the second pulse (as shown in the illustration). The response can be probed by measuring the absorption signal of the first pulse.

This general concept of time-resolved spectroscopy has been realized in many spectral regimes and on a wide range of time scales in order to access different properties of matter. For example, depending on the energy scale rotational (μeV), vibrational (meV) or electronic (eV) degrees of freedom can be probed. Especially the study of electron dynamics is challenging because it requires high photon energy in the extreme ultra-violet (XUV) and soft x-ray regime [128, 166] together with very short time durations due to the characteristic time scales on the order of attoseconds. The advent of attosecond science with the construction of soft X-ray free electron lasers (FEL) [167] and the discovery of

high-harmonic generation (HHG) [7,8,69,75,168] provided for the first time laser pulses which meet these requirements. While pulses from FELs possess statistic pulse shapes but very high pulse energy making them candidates for non-linear XUV interactions, HHG represents a table-top source of attosecond pulses, albeit only at low pulse energies. These pulses where utilized in many pump-probe spectroscopy schemes to study electron dynamics. Aside from REMI and related techniques, time-of-flight measurements for photo-electron spectroscopy are applied in high harmonic spectroscopy [169–171] and the attosecond streak camera [172–176]. Photon detection, can be used as a complement to these methods. Attosecond pulses provided by HHG were applied in TAS to observe bound state electron dynamics [177–180], like electronic wave packets in krypton ions [181]. Here, the attosecond pulse was used as a probe to detect the ionic states after ionization. However, the attosecond transient-absorption spectroscopy (ATAS) technique can also be interpreted in another picture. In this alternative scheme, the XUV pulse is considered as the pump and initially excites the system. This coherent excitation starts the dipole response described in section 2.5.2 which is then perturbed by the time-delayed interaction with the near-infrared (NIR) pulse of variable intensity. The dynamics caused by the NIR pulse leave a characteristic imprint on the response which can be measured in absorption. Thus, the dynamics induced by the NIR can be studied by measuring the so-called perturbed polarization decay initiated by the XUV pulse. As the NIR field can have very high intensity, this approach can also be used to study strong-field processes in atoms and molecules as it is presented in this work.

This chapter describes the technical details of the experimental setup and techniques used to realize time-resolved strong-field spectroscopy down to the attosecond time scale, based on the principles discussed in the previous chapter. It will also present the major changes introduced to the previously existing experimental setup described in [182–184]. First, the methods for ultrashort pulse generation and characterization are presented. Second, the experimental setup and all its elements are discussed. The final part of this chapter includes a description of the data acquisition and evaluation methods.

4.1. Laser System & Optical Pulse Characterization

4.1.1. Femtosecond Laser System

The laser setup used in this work is the commercial Ti:Sapphire multi-pass amplifier laser system FEMTOPOWER^{TM} HE/HR CEP4, including a hollow-core fiber with a subsequent chirped-mirror compression stage, which was installed in the scope of this work as an upgrade for the previous laser system (Femtolasers Compact Pro). After compression, this system generates CEP stabilized, NIR laser pulses of 4-5 fs duration, central wavelength of 760 nm, $\sim$1 mJ pulse energy and 3 kHz repetition rate compared to the old system with 6-7 fs duration, 750 nm central wavelength, $\sim$300 μJ pulse energy and 4 kHz repetition rate. In the following only the current system is described, while information about the components of the previous system and its performance can be found in [182–184].

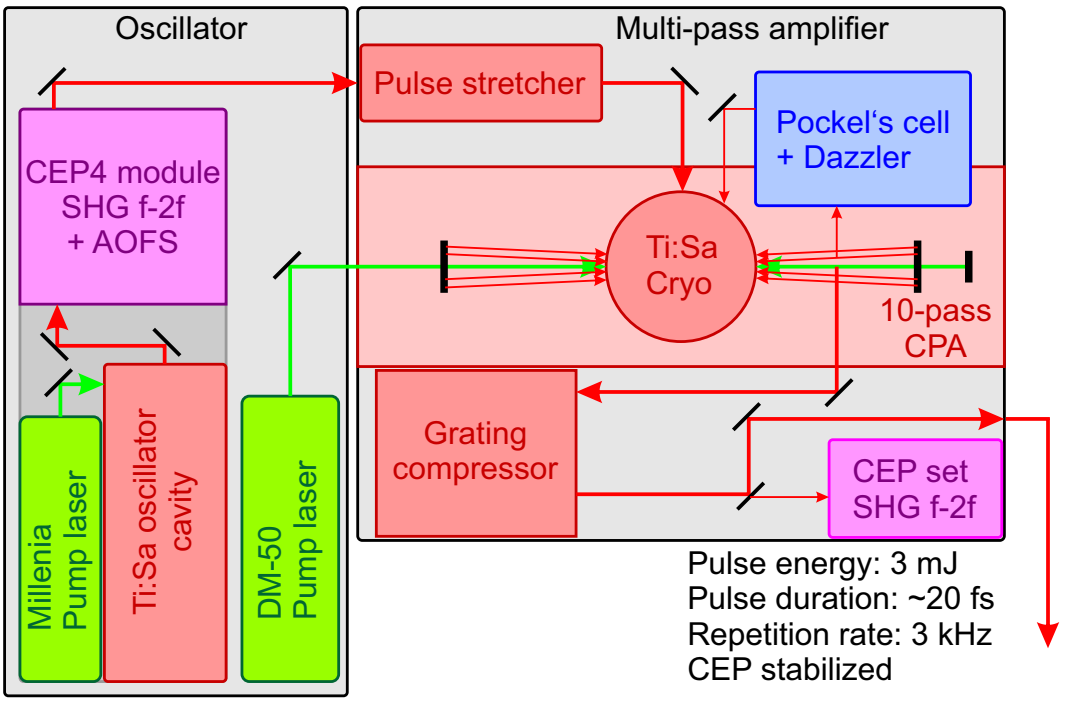

Figure 4.3.: **Schematic diagram of the femtosecond laser system:** The seed pulses are produced in a Ti:Sa oscillator and subsequently CEP stabilized using and f-2f-interferometer together with diffraction from an AOFS. The pulses are amplified in a multi-pass CPA scheme using a cryogenically cooled Ti:Sa crystal. After amplification the pulses pass a grating compressor and a second f-2f-interferometer for additional CEP stabilization against slow drifts. Output: Pulse energy 3 mJ, pulse duration ∼20 fs, repetition rate 3 kHz

A schematic view of the components of the new laser system is shown in figure 4.3. The first stage consists of the oscillator system and a CEP-stabilization module. The oscillator itself uses a titanium-doped sapphire (Ti:Al_2O_3, short Ti:Sa) crystal as gain medium and achieves mode-locking using Kerr-lens self-focusing (see section 2.1.2). The medium is pumped by a Spectra Physics Millenia pump laser at ∼3.5 W. The cavity delivers pulses of ∼6 nJ pulse energy at a repetition rate of 75 MHz. These pulses are then CEP stabilized in the CEP4 module. This stage uses an f-2f-interferometer to determine the carrier envelope offset frequency f_{CEO} and stabilizes the CEP by diffracting the pulses off an acoustic wave in an acousto-optic frequency shifter (AOFS). This so-called feed forward scheme [185] can shift the frequency of the light pulses by tens of MHz and thus set the usually fluctuating and previously measured f_{CEO} to a stabilized set value. A detail description of this technique can be found in [186]. The subsequent amplification scheme uses chirped pulse amplification (CPA) in order to achieve high pulse energies without damaging the gain medium. The seed pulses are first stretched to several tens of picoseconds by propagating through fused-silica which introduces positive group delay dispersion (GDD). Afterwards, the pulses propagate ten times through another cryogenically cooled Ti:Sa crystal acting as gain medium, pumped by a high power Q-switched pump laser (DM-50, Photonics Industries at 40 W). The cryogenic cooling compensates for heat losses during

pumping and has to take place under high vacuum conditions (10^{-7} mbar). After 4 passes through the crystal, one pulse of the pulse train is selected by a Pockel's cell, triggered by the pump pulse timing and effectively changing the repetition rate of the output pulses to 3 kHz. This only changes the polarization of the selected pulse which completes the remaining six passes while the other pulses of the seed pulse train are dumped. After the Pockel's cell the pulses pass the Dazzler module, a second acousto-optic modulator (AOM) crystal which works similar to the AOFS but is used to imprint phase corrections to the pulse shape of the amplified pulses by changing the wave form of the acoustic wave interacting with the light pulse during the diffraction in the crystal. Once the selected pulses have completed the ten passes, they are re-compressed using a grating compressor which introduces negative GDD. The final output pulses have a center wavelength of 780-790 nm and are slightly longer than the seed pulses with a duration of ∼20 fs due to gain narrowing in the amplification process. The pulses are delivered at 3 mJ pulse energy with a repetition rate of 3 kHz. A second f-2f-interferometer after the compressor together with fast control over the propagation length in the stretcher stabilizes the CEP after the amplification step against slow drifts of f_{CEO} caused by pressure and temperature fluctuations on the order of tens of seconds. With this a single shot CEP stability of 300 mrad after the amplifier can be achieved.

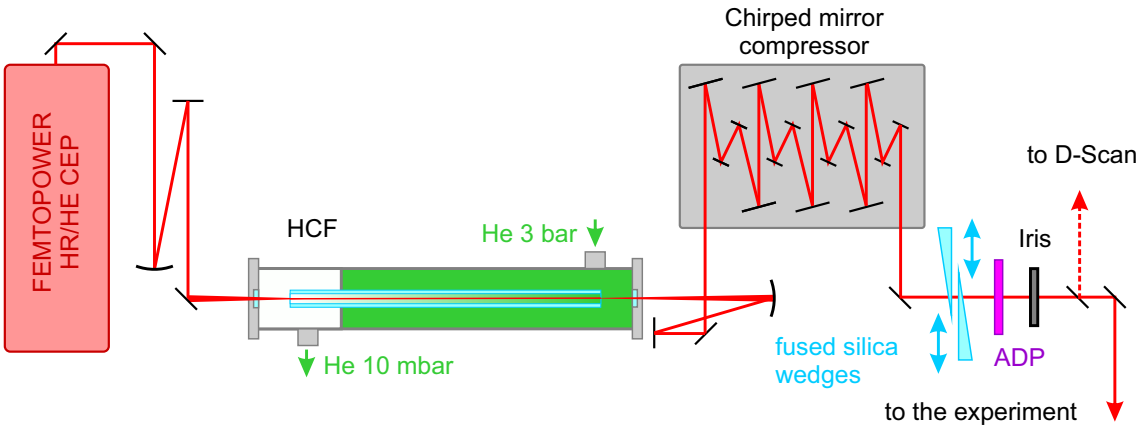

Figure 4.4.: **Schematic of the HCF compressor system for few-cycle pulse generation:** The NIR pulses from the laser system are focused into a differentially pumped hollow-core fiber filled with helium. During propagation self-phase modulation (section 2.1.2) broadens the spectrum. A set of chirped mirrors overcompensates the GDD accumulated in the fiber. The subsequent pair of glass wedges is used to tune the dispersion for optimal pulse duration in the HHG focus. After the compressor the pulses can be characterized using the D-Scan method.

In order to support and generate few-cycle pulses needed to drive high harmonic generation (HHG) with single attosecond pulses, the spectrum of the output pulses has to be broadened further and subsequently re-compressed. This is done in the KALEIDOSCOPE hollow fiber system including a modified chirped mirror compressor shown in figure 4.4. The beam is focused into a 1 m long hollow-core fiber with a core diameter of ∼310 μm mounted in a vacuum tube with two compartments. This setup is then filled

with helium and differentially pumped at the entrance side down to ∼10 mbar, while the exit remains at 2.5-3.0 bar. The pressure gradient inside the fiber reduces ionization and thus plasma effects in the high-intensity focus at the entrance of the fiber. It is furthermore important to use pure helium gas as non-linear medium in order to avoid ion sputtering damage to the inside of the hollow core fiber, especially in the high-pressure region at the exit. In the non-linear medium self-phase modulation (see section 2.1.2) generates additional frequency components and introduces positive GDD. During the propagation in the fiber higher-order spatial modes are exponentially suppressed and ideally a TEM_{00} mode remains at the exit. To avoid distortions of this mode which would be detrimental to the HHG process, the input power is reduced to 66% of the amplifier maximum output in order to reduce plasma focusing effects in the high pressure reservoir. After the fiber the broadened and long pulses are guided through a chirped mirror compressor consisting of seven double angle chirped mirror pairs (PC70, Ultrafast innovations) [187]. The introduced negative GDD overcompensates the dispersion accumulated in the fiber and during the propagation in air (GDD +35 fs^2 per 1m propagation). The compressor is followed by a pair of movable glass wedges, made of fused silica with anti-reflective coating (450-950 nm) and 4° apex angle (by Lens optics). These wedges are used to adjust for optimal GDD compensation at the point of HHG in the experimental apparatus. In addition, a 1 mm thick ADP birefringent crystal is used to compensate the third order dispersion accumulated during the non-linear interaction in the fiber [40]. This suppresses any satellite pulses and decreases pulse durations close to the Fourier limit. The pulse durations achievable with this setup range between 4-5 fs at a repetition rate of 3 kHz and a pulse energy of 1 mJ after the fiber. The method used to characterize these pulses is described in the next section.

4.1.2. Characterization of Optical Pulses

In order to be able to control the HHG process properly and to understand the physics of the interaction with the few-cycle pulses, their pulse shape has to be characterized. For such short pulses with durations of only a few femtoseconds this poses quite a challenge. However, a lot of techniques have been developed to solve this problem. Measuring a short event in time always requires a shorter event to refer to. As the pulses themselves are usually the shortest events available a lot of techniques use copies of the pulse and non-linear effects involving both copies to measure the pulse properties. The most simple method using this principle is the autocorrelation setup, where one of the pulses is delayed and scanned over the other pulse by varying the time delay. Both pulses are focused into a birefringent crystal for second harmonic generation (SHG) and the intensity of the resulting light is measured which contains information about the pulse duration. However, the electric field or the temporal intensity cannot be recovered like this. Methods capable of this are for example frequency resolved optical gating (FROG) [188] and spectral-phase interferometry for direct electric field reconstruction (SPIDER) [189] and their extensions. FROG is based on autocorrelation with the addition that instead of the intensity the spectral response of a nonlinear process (e.g. SHG) is measured which creates a two-dimensional FROG trace (frequency over time-delay) from which the shape of the electric field can be extracted. SPIDER, on the other hand, measures spectral amplitude

and phase separately. The phase is determined by stretching one pulse and creating two copies of the short pulse. In the time domain the two copies will interact in the SHG crystal with different frequency components of the stretched pulse. The SHG spectrum then allows for the extraction of the phase difference between the two frequency components probed by the short pulse replicas. A scan over the whole frequency range then gives the overall spectral phase of the original pulse. Another method of pulse characterization is the so called streak camera, which gives access to the temporal shape of the electric field. An attosecond pulse is scanned in time delay over the measured pulse and ionizes a typically gaseous sample. The vector potential of the measured pulse at the moment of ionization is imprinted on the ionized electrons momentum which is then measured in a time of flight spectrometer. The time of flight varies depending on the vector potential and thus by scanning over the pulse its temporal electric field is measured. A detailed discussion of this method and its many applications can be found in [190, 191].

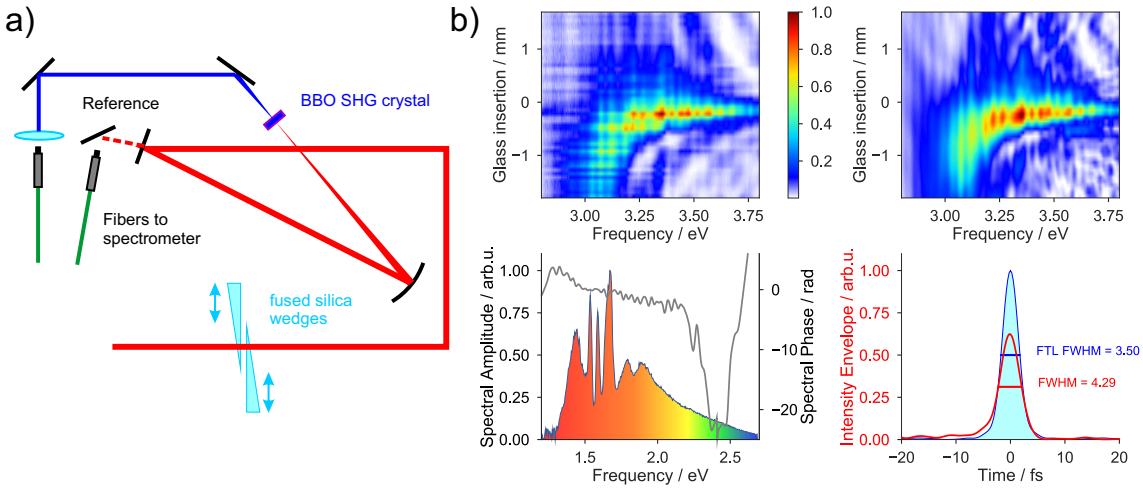

Figure 4.5.: **Schematic of the D-Scan setup:** a) After passing the chirped mirror compressor and the wedge pair the laser pulse can be coupled into the D-Scan setup. This setup records the fundamental spectrum and the SHG spectrum generated in a BBO crystal in non-collinear geometry depending on the wedge position (amount of glass inserted in the beam path). b) Both experimental D-Scan trace and the trace retrieved by the evaluation algorithm are shown on the top. In the lower panels, the spectral amplitude together with the spectral phase are plotted. The time domain pulse shape shows a FWHM of 4.3 fs.

In this work, the method called dispersion-scan (D-Scan) [192,193] is used to characterize the pulses generated from the laser system including the fiber compressor. It is based on measuring the spectrum of SHG light as well, but does not employ time-delayed copies of the pulse. Instead the glass wedges for optimizing the pulse dispersion are used to scan the dispersion added to the pulse by glass of thickness z. This results in the measured D-Scan trace $S(\omega, z)$ which can be expressed analytically as:

$$S(\omega,z) \propto \left| \int_{-\infty}^{+\infty} \left(\int_{-\infty}^{+\infty} E(\omega') e^{ik(\omega')z} e^{i\omega' t} \mathrm{d}\omega' \right)^2 e^{-i\omega t} \right|^2 \tag{4.1}$$

The procedure records the fundamental spectrum as input for the spectral amplitude and then fits and optimizes the spectral phase of the pulse in order to match the recorded D-Scan trace according to equation 4.1 using an iterative algorithm described in [187]. Figure 4.5 shows the schematic of the D-Scan setup as part of [187], together with a typical measurement of a sub-5 femtosecond pulse achievable with the laser system described above.

4.2. Experimental Setup for Time Resolved Absorption Spectroscopy

The complete experimental setup for high-harmonic generation and time-resolved absorption spectroscopy is shown in figure 4.6. As the experiment aims to perform photon spectroscopy in the vacuum- to extreme ultraviolet (XUV) spectral range the complete setup has to be placed under vacuum conditions. The typical photon energies achieved with HHG (20 eV up to 150 eV) are way beyond the ionization potentials of all molecules and rare gases in air (from $\sim$13 eV for Xenon to $\sim$24 eV for Helium) [194]. Thus the photons can ionize valence electrons from any atom in air and be absorbed in the process. The consequence is that the absorption length of XUV radiation at atmospheric pressure is just 1 mm [195]. However, for a pressure of 10^{-1} mbar it already extends above 1 meter. For a beamline of roughly 3 m length it is thus sufficient to operate at pressures of 10^{-3} mbar or below. In these rather loose pressure conditions the absorption of XUV photons can be neglected. In the following the features of the existing setup [182–184] and the modifications and improvements added to it are described in detail according to the schematic drawing of the beam path, optics and key elements of the beamline presented in figure 4.7.

4.2.1. High-Harmonic Generation

In the first step of the experimental procedure, the 1 mJ, sub 5 fs NIR pulses are focused into a rare gas acting as conversion medium. Rare gases are used for their high ionization potential which suppresses depletion in the leading edge of the NIR pulse and allows for HHG in the high-field strength parts of the pulse. The focusing geometry uses a silver-coated spherical mirror with $f = 500$ mm, which is hit under close-to-normal incidence to avoid astigmatism in the focus. This setup can achieve a focal size of about 50 μm, yielding peak intensities in the range of 10^{14}-10^{16} W/cm^2.
The rare gas conversion medium is contained in a cell of 2 mm inner and 3 mm outer diameter made of MACOR [196]. This glass ceramic part represents an upgrade to the previously used stainless steel tube and is able to withstand ablation by the high intensity

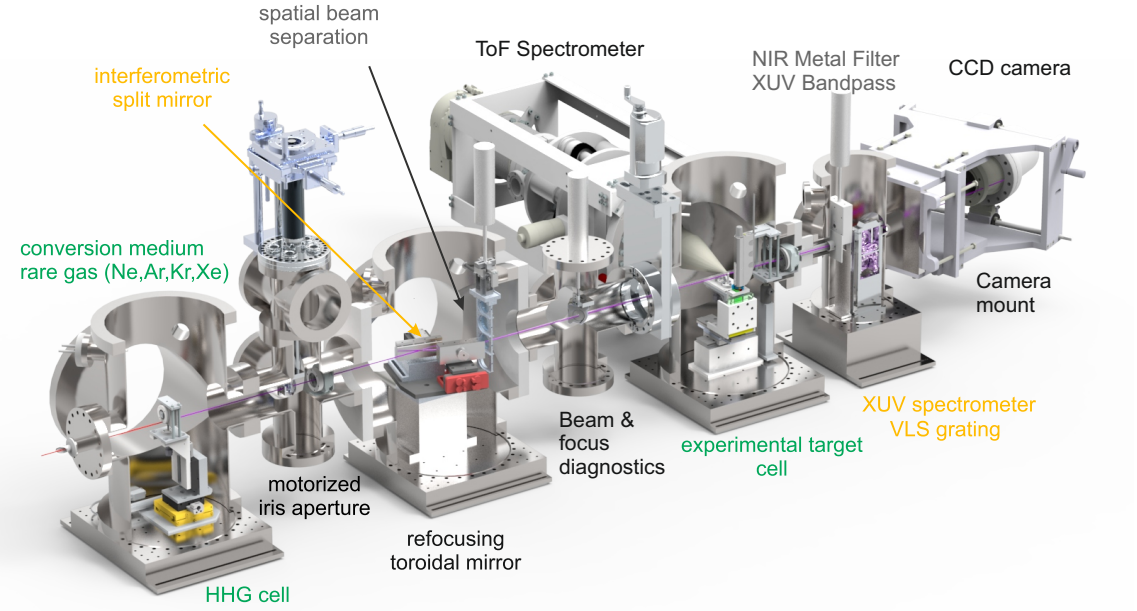

Figure 4.6.: **Construction drawing of the complete experimental setup.** The whole setup is placed under vacuum conditions to avoid re-absorption of the XUV radiation. All key parts, the HHG and target cell as well as the iris and time-delay mirror can precisely be controlled and aligned from the outside under vacuum operation. The filters in the mirror chamber as well as the HHG cell, the target cell and beam diagonstics have been upgraded compared to the previous setup [182–184].

NIR focus. This is important, as sublimated steel from the cell was found deposited on the highly sensitive optics down the beam path, which can now be avoided. The gas can effuse from this cell through two micro holes of 200 μm diameter on each end which allow the beam to pass the medium, while still limiting the background pressures in the generation chamber to acceptable values below 10^{-3} mbar. A schematic of the focus geometry inside the HHG cell can be found in figure 4.8. For efficient HHG the backing pressures of the rare gases range from $\sim$30 mbar up to $\sim$100 mbar depending on gas species. In order to achieve optimal phase-matching conditions for the HHG process the generation cell can be positioned using the self-built high precision XYZ-stage under vacuum and the backing pressure is adjusted by a control unit outside the vacuum.

4.2.2. Pulse Control & Interferometric Setup

In the time-resolved spectroscopy setup following the HHG target, the main experimental parameters are the intensity of the NIR pulses, which are further used after HHG and the time delay between femtosecond NIR and attosecond XUV pulses. The control over these parameters with high stability and reproducibility is achieved with the central part of the beamline, the interferometric mirror setup contained in the middle chamber and shown in figure 4.9. The control segment consists of a motorized iris aperture, two grazing-incidence mirror assemblies, one for temporal pulse separation, one for refocusing the

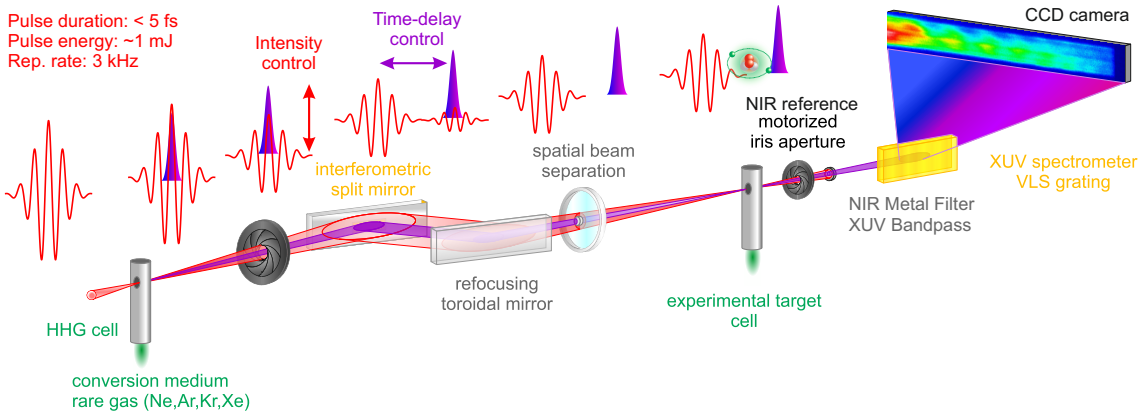

Figure 4.7.: **Schematic of the complete experimental setup:** After HHG the co-propagating beams are temporally and spatially separated by the split mirror and filter assemblies. Furthermore the iris aperture allows for variable NIR intensity.The pulses then interact with the spectroscopic sample in the target cell and pass another set of filters to remove the NIR radiation. Afterward the spectrum is measured using the flat-field spectrometer consisting of a VLS-grating and a CCD camera.

beam into the spectroscopy target, and a newly added variable filter array for spatial pulse separation. A detailed overview of the construction and alignment of the mirror setup can be found in [182].

The main experimental advantage of the monolithic beam path combined with grazing-incidence optics is achieving high reflectivity on a broad spectral bandwidth (compared to the limited bandwidth of multilayer mirrors in normal incidence [197]) together with a very high degree of interferometric stability between the XUV and NIR beams which propagate along the same path. Due to their difference in wavelength the spectral components of the beam after HHG do not have the same divergence. The XUV beam with $\sim$1 mrad is much less divergent along the beam path compared to the NIR beam which has a divergence of $\sim$15 mrad in the given focusing geometry. This property is first utilized in the intensity control using the closed-loop zero aperture iris in front of the interferometric mirror setup. Because of the difference in divergence the NIR beam has a larger diameter at the position of the iris. Thus, the iris can concentrically cut off part of the NIR beam to adjust the intensity reaching the rest of the setup without influencing the XUV beam. The intensity, depending on the iris aperture opening, can be calibrated *in situ* from measured data, which will be discussed in the next chapter.

The subsequent grazing-incidence optics are hit under an incident angle of $\theta = 15°$, where the angle is chosen as a trade off between possible reflectivity and tolerances for alignment errors. First, the beam passes the split mirror assembly which also makes use of the difference in beam divergence of the two spectral components. It consists of a fixed silver coated outer mirror which reflects the NIR beam and a moveable high quality gold coated inner mirror. The coating is optimized for high reflectivity of the respective beam components with the reflectivity of the XUV radiation between 20 and 130 eV being above 40% [195]. The inner mirror is used to introduce the time-delay between the pulses by varying the optical path length of the beam hitting the inner mirror compared to the path

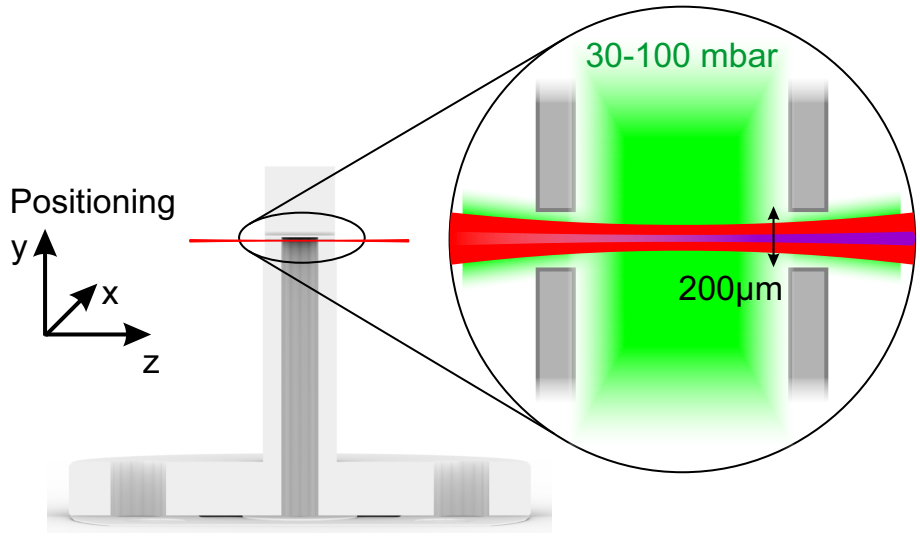

Figure 4.8.: **Construction drawing and schematic view of the focal region in the HHG cell:** The magnified view shows the coherent buildup of the XUV radiation (purple) in the focus of the NIR beam (red). The target cell is a slightly modified version of this model and shown in figure 4.12.

length over the outer mirror. If the inner mirror is moved a distance Δd from the overlap an additional path length of

$$\Delta s = 2\Delta d \sin(\theta) \tag{4.2}$$

is introduced. With the given incidence angle the relation between mirror displacement and introduced time delay is 1 μm $\cong$ 1.705 fs. The interferometric stability is measured by analyzing the intensity modulation of a HeNe laser reflected from the setup. The stability value was determined to be 17 as for a stability of the piezo-driven translation stage of $\sim$10 nm. After passing the time-delay mirror assembly the beam is reflected off a toroidal mirror to refocus it into the spectroscopic target. The gold coated toroidal mirror with focal length of $f = 350$ mm is used in a 1:1 imaging geometry in order to avoid unnecessary (coma) aberrations in the focus as studied in detail in [198–200].

While this combined interferometric and toroidal mirror geometry exhibits high stability, a good focus and support of a broad spectral range, it also has a minor disadvantage. Because the time delay is introduced by displacing one of the mirrors, there is a resulting parallel displacement of the XUV beam and thus, considering the image created by the toroidal mirror, a displacement of the focal point of the XUV with respect to the NIR like it is illustrated in the figure 4.9 inset. The relation between parallel displacement Δb of the beam and the movement of the mirror Δd is

$$\Delta b = \Delta d \frac{\sin(2\theta)}{\sin(\theta)}. \tag{4.3}$$

For a change in time-delay by $\Delta\tau = 1$ fs, this gives a parallel beam displacement of $\Delta b = 1.13$ μm and an accompanying wave-front tilt of the XUV beam compared to the

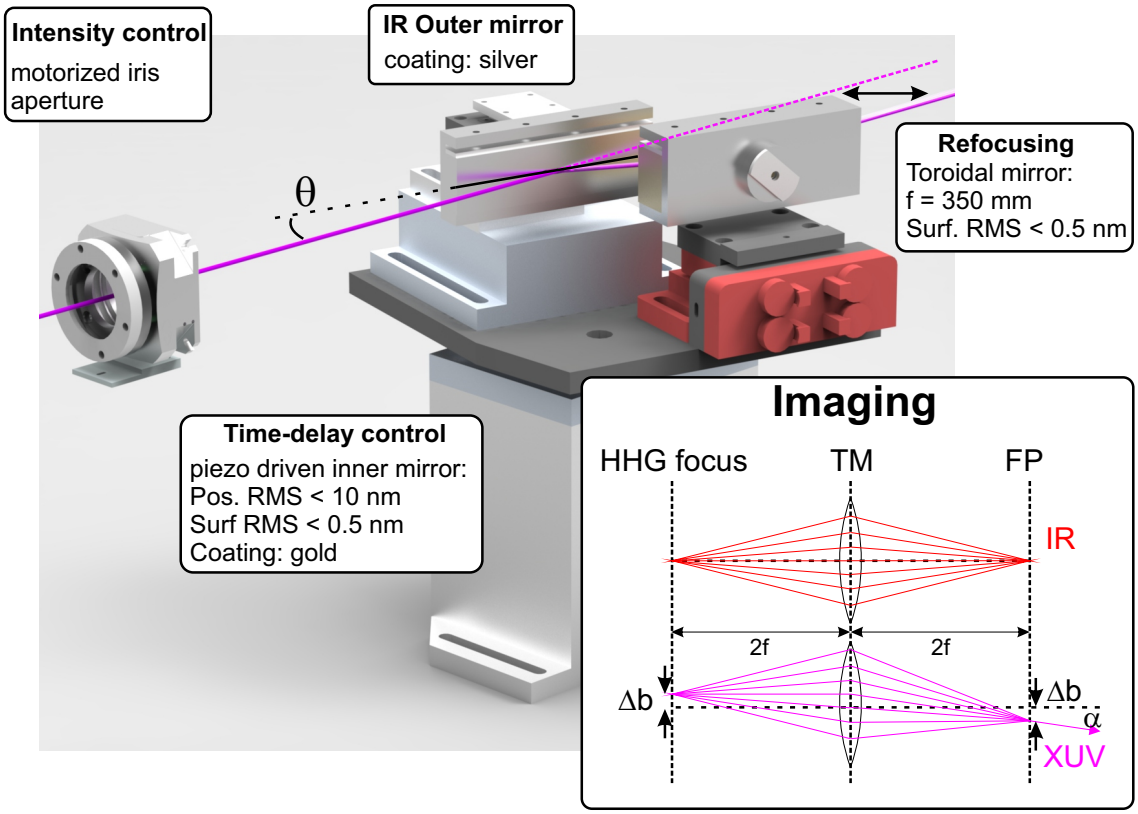

Figure 4.9.: **Illustration of the grazing-incidence interferometric-mirror pulse control setup:** The utilized grazing angle is $\theta = 15°$. The setup, as well as the movement of the inner mirror of the time-delay mirror assembly introduce a parallel beam displacement. This leads to a walk-off of the focus of the XUV beam compared to the NIR beam in the interaction region of the target, which is illustrated in the imaging inset.

NIR beam of $\phi = 3.22\ \mu$rad. The temporal averaging over a time interval of $2.15 \cdot 10^{-4}$ as for the achievable XUV focal spot size of 20 μm which is a consequence of the tilt is negligible. However, the geometrical overlap of the foci of both NIR and XUV beams is lost with increasing Δd and thus the accessible time-delay range where the same atoms are affected by both pulses is limited to about 50 fs. Furthermore, this walk-off can cause geometrical effects in the absorption spectra, if the displacement causes the beam to hit the inner walls of the target cell. This issue is addressed in the next section.

In order to get full spatial and temporal separation of the XUV and NIR beams a two-component band-pass filter in annular geometry is used. Compared to the older version the new filter setup introduced in this work supports multiple spectral regions with different metallic filters and a higher throughput by improving the basic and relative mounting of the filter components. A detailed drawing of the newly installed components is shown in figure 4.10. The concentric filter geometry itself consists of a thin membrane on the outer part which allows visible and infrared light to pass while blocking all XUV radiation on the outer mirror and a central metal filter which removes all NIR radiation reflected from the inner time-delay mirror. This overall assembly is realized in two ways. The first

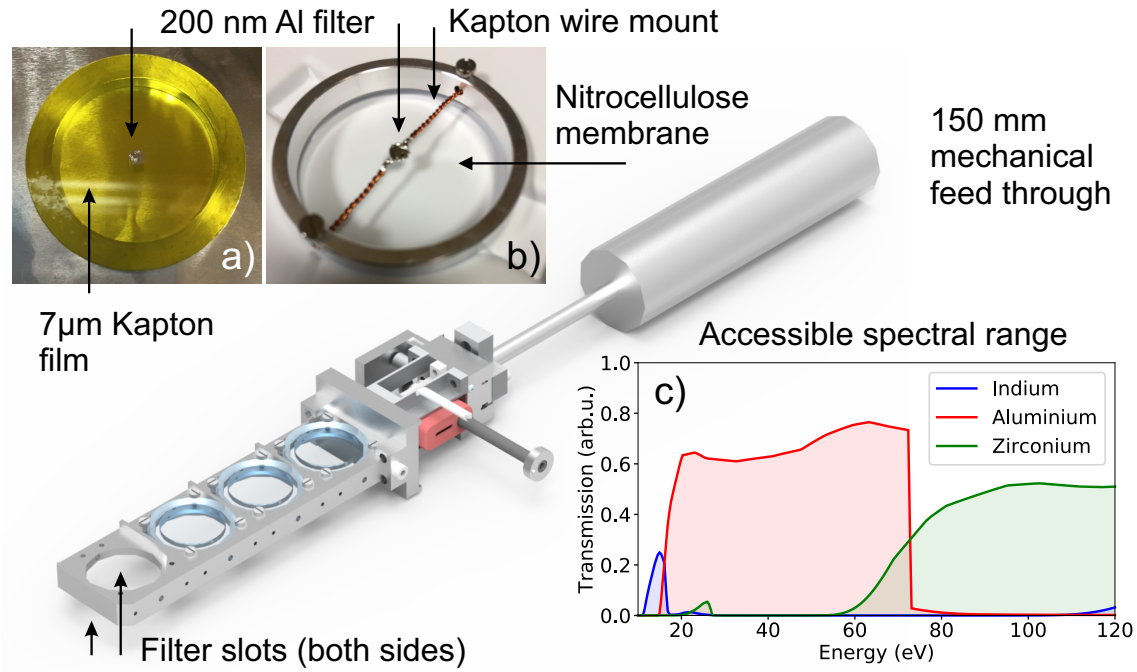

Figure 4.10.: **Illustration and pictures of the multi-band spatial filter setup:** The filter array can carry filters in the 4 slots on the front and back side. The filters are mounted on metal rings and either bought from LEBOW (inset a)) or held by home-built wire mounts (inset b)). They can be positioned via a 150 mm mechanical feedthrough (vertically) and a picomotor driven stage (horizontally). Each filter slot has to carry a metal filter (blocks NIR) for the central part and a Kapton or nitrocellulose (blocks XUV) membrane for the outer part of the beam. Using this array to carry a set of indium, aluminum and zirconium filters, a broad spectral range is accessible for XUV spectroscopy. The transmission curves of the used filters are plotted in inset c).

version, shown in figure 4.10 inset *a*), is directly bought from the company LEBOW [201] and fabricated with an 0.2 μm aluminum filter in the center which is applied to a 7 μm Kapton film with a hole in the center. The second version, shown in figure 4.10 inset *b*), consists of a 2 μm nitrocellulose membrane (by National Photo Color) with a hole at the position of the metal filter and a 0.2 μm aluminum filter (produced by LEBOW) which is held on a home-built wire mount. While the second setup is difficult to fabricate, it is considerably cheaper, introduces less dispersion due to the lower membrane thickness and is more flexible because different metal filters can be applied to the mount. The metal filters used for the experiment need to display significant transmission in the spectral range of interest while completely blocking NIR and visible light. Figure 4.10 c) shows the transmission curves of 200 nm thick aluminum (Al), indium (In) and zirconium (Zr) filters [202]. For the low energy region between 10 eV and 20 eV indium besides tin is the only viable filter option even though it has still just above 20% transmission. This makes measurements on molecules with electronic excitation energies in this energy region very challenging. Between 20 eV and 70 eV, with transmission above

60%, aluminum is well suited to study bound states in many rare gases especially helium with resonances around 20 eV (singly excited states) and 60 eV (doubly excited states). For the highest energies starting from 70 eV up to 130 eV, which are mainly interesting for streaking experiments, zirconium represents a suitable choice. It has to be noted that during filter manufacturing few little micro holes in the foils remain [201], which leave a weak remaining NIR pulse co-propagating with the XUV pulses. The present setup can simultaneously support all these filter types and makes it possible to exchange them during vacuum operation with the 150 mm mechanical feed through. The horizontal positioning is controlled with a picomotor-driven translation stage. Compared to the previous setup which used a short steel tube to mount the metal filters [183], the new geometry increased the overall throughput of the XUV flux by a factor of two with much less restrictions on the precise rotational alignment of the filter setup. Once the pulses have passed this part of the setup they reach the interaction region with the sample described in the next section.

4.2.3. Experimental Target & High-Resolution XUV Spectrometer

In the experimental chamber both beams are focused into the target medium contained in a second gas cell similar in design to the HHG cell. However, it was upgraded with a new design in the course of a master thesis supervised during this work [203] and is an adaptation of the design used in similar experiments of the research group [200, 204, 205]. The new setup is shown in figure 4.11 on the right and is able to position the target cell with high precision and speed. This allows for efficient scans of the focus along the propagation direction, or an operation mode which moves the cell in and out of the beam in quick succession in order to record sequential reference spectra to determine the absorption cross section of the medium according to equation 2.102. Furthermore, the motion-control measures and reads out the cell position which guarantees reproducibility and allows for the tracking of the XUV focus displacement resulting from the movement of the time-delay mirror. This effectively enhances the time-delay range which was previously limited by the geometry of the cell opening. However, the range is still limited by the size of the NIR focus because for large enough time-delay values the overlap between the two foci will decrease. In this case, it can happen that there is no target region which interacts with both pulses which in turn destroys the correct pump-probe spectroscopy signal.

A further modification of the setup, carried out during a Bachelor thesis [206], is an additional motorized iris aperture like the one used for intensity control, after the target cell. This aperture is used to block the biggest part of the NIR beam, which protects the thin metal filters used to hinder the NIR light from entering the XUV spectrometer. Furthermore, the scattered NIR light is collected with an optical fiber and measured with an Ocean Optics spectrometer. The recorded spectra can be used to monitor the spectrum of the NIR beam after the interaction with the HHG and target medium and to determine the plasma blue shift of the NIR light during the HHG process.

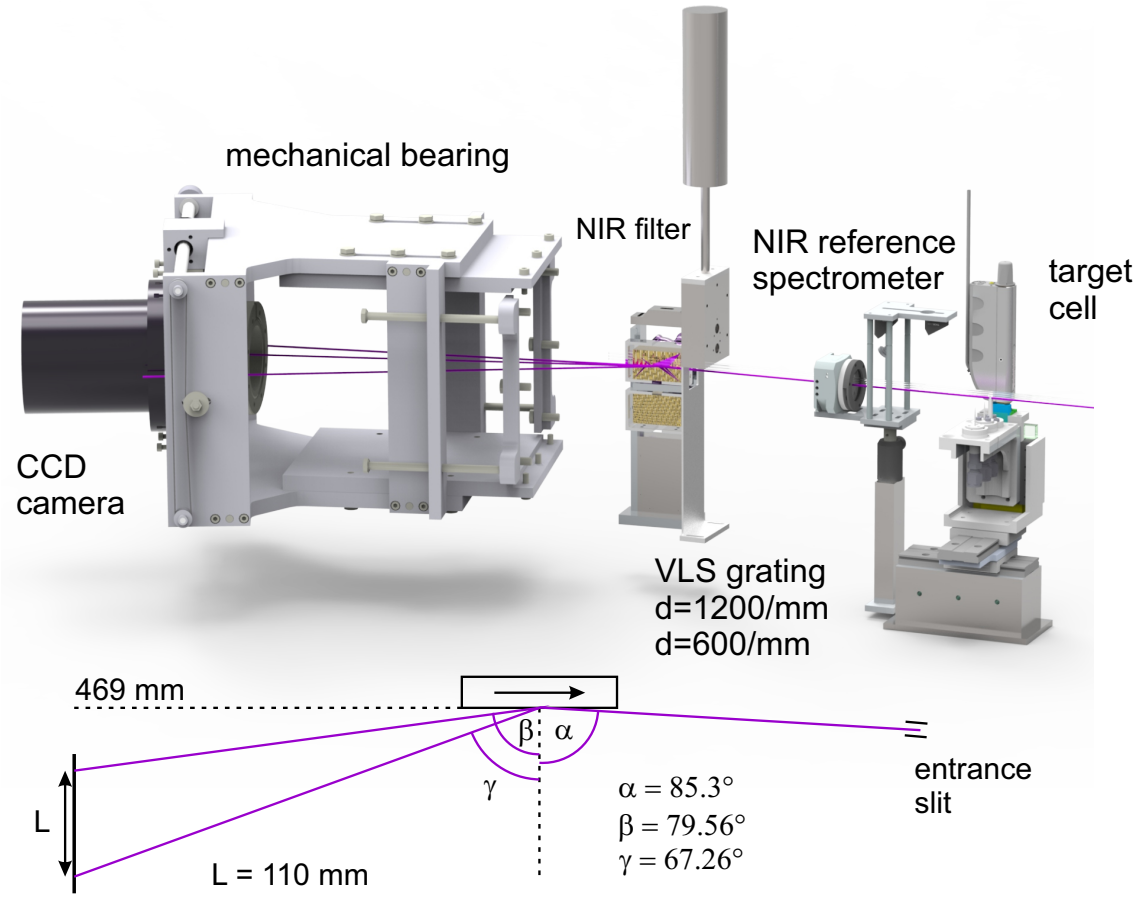

Figure 4.11.: **Drawing of the target and spectrometer setup:** The target can be moved fast and with high reproducibility for subsequent absorption and reference measurements. After the target a motorized iris aperture scatters the NIR-radiation which can be picked up by an optical fiber and measured for spectral monitoring of the NIR beam. The remaining NIR light is filtered out by additional metal filters before the spectrometer grating is reached. The grating itself can be exchanged to switch between better resolution for high or low energy radiation. The spectra are finally recorded with a CCD camera held in position in the flat field focusing plane of the concave VLS spectrometer grating. The beam geometry of this grating is shown below the setup. With the home-built mechanical bearing the camera can be moved along the spectrum and optimized for the optimal distance in the focal plane of the grating.

The target cell itself can contain gaseous media like rare gases and simple molecules like hydrogen, nitrogen, oxygen or carbon dioxide. The transmitted XUV radiation which contains information about the dipole response of the quantum systems in the sample is recorded by a high-resolution XUV spectrometer [207]. The first part of the spectrometer shown in figure 4.11 is an aberration-corrected concave grating which is designed with a variable spacing between grooves (variable line-spacing VLS) [208] and used in grazing incidence for the operation with XUV-radiation. The variable spacing between grooves is designed such that the separated spectral components are imaged onto a plane surface,

where it is easy to detect a signal with high spectral resolution over a broad spectral range with a CCD chip without imaging errors or the need to scan the grating rotation or detector position. This geometry resulting in a focus plane differs from common concave imaging gratings with equidistant grooves. Normally, the focus points of a concave grating are located on the so called Rowland-circle [209, 210]. Following the curved focus plane of such a geometry is mechanically very complex which is why the setup with a VLS-grating was chosen for this beam line.
The grating equation approximately describing the dispersion for this setup is given by

$$m\lambda = d(\sin(\alpha) + \sin(\beta)), \tag{4.4}$$

where m is the diffraction order, λ is the wavelength of the incoming beam and d is the effective grating constant. The other parameters are shown in the schematic of the grating geometry in figure 4.11. The grating holder was upgraded in order to accommodate two commercially available gratings by Hitachi with a groove density of 1200 mm^{-1} and 600 mm^{-1}. In order to switch the gratings under vacuum conditions the mount can be moved vertically by a Newport stepper motor. The gratings in use disperse the incoming spectrum between 11 nm and 62 nm ($\sim$20 eV to $\sim$120 eV) and 22 nm and 124 nm ($\sim$10 eV to $\sim$56 eV) onto an image plane of approximately 110 mm width where the second one was added to access lower energies to observe the dynamics in valence excitations of atoms and molecules and increase resolution in this part of the spectrum. From equation 4.4 it is clear that at one point of the imaging plane apart from the first order diffraction signal of wavelength λ also second and higher orders of diffraction n of wavelengths λ/n appear. While this can complicate the measured absorption spectra, it can also be utilized to observe signatures that are greatly separated in energy simultaneously. The entrance slit of the spectrometer is defined by the focal spot size of the XUV beam in the experimental chamber and is on the order of few tens of micrometers in diameter.
The overall accessible energy range of the dispersion of the used VLS grating is between $\sim$20 eV and 110 eV and is detected by a commercially available back-illuminated CCD-camera (Princeton Instruments, PIXIS series) [211] which is cooled thermo-electrically and is placed in the focusing plane of the grating. The CCD-chip built into the camera consists of 1340 x 400 pixels with a size of 20 x 20 μm^2 each. The size of the chip is not able to cover the whole dispersed spectrum delivered by the grating, therefore a home-built mechanical camera mount including a linear stage for the camera is used in order to move the chip along the focus plane. The energy scale as well as the resolution are calibrated *in situ* using information from the recorded absorption spectra.

4.3. Data Acquisition & Evaluation

In the configuration described above, the experiment can be carried out in multiple data recording modes. The simplest mode is for the target cell to remain fixed. Here, the time delay τ and intensity I_{NIR} are scanned and spectra are recorded over a fixed integration time (usually few hundreds of milliseconds) for each combination (τ, I_{NIR}). The camera records pictures as a two-dimensional data set which shows periodical peaks of the

XUV-radiation spectrum on a horizontal line. The absorption lines of the target gas are imprinted on the XUV spectrum. By integrating over a certain region of the chip which is selected form the LabVIEW software and then directly evaluated with hardware binning, the information along the integration axis is lost in favor of higher signal to noise ratio and faster read-out times during the measurement. This reduces drift and fluctuation effects of the laser during a prolonged period of data acquisition. The single recorded spectra $I_{sig}(\omega)$ at different time delays between XUV- and IR-pulse are then put together to form the two-dimensional data set of a time delay scan. As each spectrum $I_{sig}(\omega)$ displays a slow modulation across the whole recorded bandwidth, characteristic to the HHG process, a reference spectrum is needed in addition to the absorption signal in order to study the absorption effects. Using a Fourier low-pass filter to reconstruct a reference spectrum directly form the absortion signal $I_{sig}(\omega)$, like it is done in [116], an approximation of the optical density resulting from the resonant interaction with the sample can be attained. While it produces clean spectra and scan data, this method eliminates the contribution of non-resonant and very broad absorption features, which is a major drawback, especially if non-resonant continuum absorption or continuum edges need to be studied. As equation 2.94, 2.101, and 2.102 need the spectral intensity of the ingoing signal $I_{in}(\omega)$, the actual cross section can never be obtained with this method.
A more advanced mode of operation is the recording of subsequent absorption and reference spectra for each pair (τ, I_{NIR}). In this mode the fast positioning of the target cell moves it in and out of the beam in quick succession. The absorption $I_{sig}(\omega)$ and reference $I_{in}(\omega)$ pairs measured like this yield the optical density or cross section of the target material. As HHG is a highly non-linear process and also very sensitive to CEP of the driving pulse which can not be stabilized perfectly, the spectral intensity of the generated pulses greatly fluctuates. For subsequent recordings of signal and reference this is a problem, because the input for both measurements will always show deviations. This can be mediated by either setting very long integration times (several seconds) or by recording multiple spectra for each combination (τ, I_{NIR}). Both options significantly increase overall measurement times, which can pose a problem for lab condition and laser stability. Depending on experimental conditions, the resulting optical densities may still show rather big fluctuations both in the spectrum itself and within the 2D data set which makes it difficult to discern actual physical changes in absorption. Furthermore, moving the target cell in and out of the XUV focus can lead to geometrical absorption effects, meaning that the XUV beam is clipped by the edges of the opening of the target cell.
Optimally, the reference and the absorption spectrum are recorded simultaneously in order to guarantee the correct result from equations 2.101 and 2.102. The next section describes in detail the newly developed setup which made this *in-situ* measurement of the reference spectrum possible for the first time.

4.4. *In-Situ* Reference Spectrometer for High Sensitivity Transient Absorption Measurements

As stated above, the non-linearity of HHG and slight instability of the laser parameters (the fiber compressor is also driven by non-linear processes) cause the spectrum of the

input XUV pulses to be different for each recorded absorption spectrum. This represents a significant difficulty for the measurement of the optical density, as it can only be determined if both the absorption and reference spectrum are known. Considering the fluctuations of the XUV spectrum over time, they have to be recorded ideally at the same time. However, up to this point, the reference spectrum could only be recorded separate to the absorption signal. In previous measurements the reference was recorded by moving the target in and out of the beam, or by removing the target gas from the target cell. Thus spectra and references were always recorded sequentially which caused differences between input and reference spectrum.

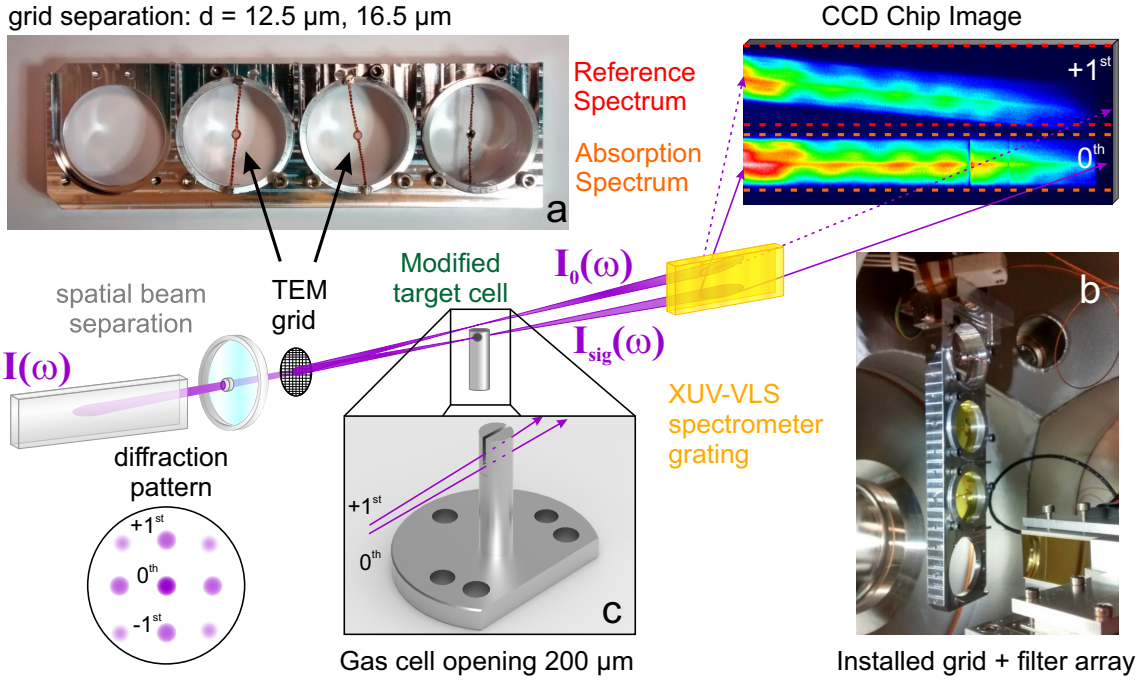

Figure 4.12.: **Illustration of the *in-situ* reference measurement method:** After passing the concentric filter assembly for spatial beam separation the XUV beam hits a TEM transmission grating which acts as a beam splitter. These gratings are mounted on Kapton wire shown in inset a) and placed behind the metal filters on the filter holder. The installed overall assembly is shown in inset b). The diffraction pattern of such a TEM grid is shown on the lower left. The 0^{th} diffraction order is used for the absorption measurement while the $+1^{st}$ order does not pass the sample and gives the reference spectrum. For this a target cell with a very small separation between the gas reservoir holes and a slit that allows the diffracted part to pass above without going through the sample is necessary. The design is shown in inset c). On the right, a typical full chip image of the CCD camera is shown which contains all information about the absorption (area between orange dashed lines) and reference spectrum (area between red dashed lines).

One of the main technical achievements of this work is the implementation of the simultaneous measurement of signal and reference. To achieve this, it is first of all necessary to

create a copy of the input signal $I_0(\omega)$. In the visible spectral range this is easily possible using a beamsplitter (most simply a thin fused silica plate). However, in the XUV region this is not possible. The developed setup illustrated in figure 4.12 uses a standard copper micro grid for transmission electron microscopy (TEM) as a dispersive element for the XUV-radiation. This element is a square grid of 5 μm wires on a 3 mm ring with a wire separation of several μm depending on the spectral range of the measurement. The idea is to use the 0^{th} order transmission as the input for the absorption measurement $I_{sig}(\omega)$ and the $+1^{st}$ order diffraction as the reference signal $I_{in}(\omega)$. The filters are mounted on the other side of the filter holder described in section 4.2.2 using the self-built Kapton wire mount in figure 4.12 a). To keep the spatial pulse separation they are installed together with the concentric Kapton-metal filters by LEBOW shown in figure 4.12 b). With the setup at hand, the two beams can only be separated by a maximum of $\sim$5 mm after the full travel distance $a = 1219$ mm from the TEM grid to the CCD chip. Otherwise, the two beams cannot pass all filters unhindered, fit on the spectrometer grating and be measured simultaneously. Furthermore, a minimum separation of $\sim$1.5 mm of the beams is given by the requirement that they have to be distinguishable along the chip height (see data presented in figure 4.12). Using the grating equation

$$m\lambda = d \cdot (\sin(\arctan(dx/a))), \tag{4.5}$$

with m the diffraction order, d the grating groove distance, dx the position of the first maximum with respect to the zeroth order and a the distance to the grating, the TEM grids with $d = 16.5\mu$m for the spectral bandwidth between 25 nm (50 eV) to 60 nm (20 eV, lower Al edge) and $d = 12.5\mu$m for the spectral bandwidth between 17 nm (70 eV, upper Al edge) to 35 nm (35 eV) were selected. Like this, a reference can be recorded over the whole range accessible with Al-filters.
A further restriction of the setup is the beam separation at the target focus and how only one of the foci can be exposed to the gaseous spectroscopy sample. In the current geometry the separation at the target position will roughly be a third of the final separation on the CCD chip. Therefore a new design for the target cell illustrated in figure 4.12 inset c) was worked out and very precisely manufactured in the mechanical workshop at MPIK. With this new setup reference spectra can be recorded simultaneously with the absorption spectra like it is shown on the full chip image in figure 4.12. The lower region shows the 0^{th} order with the absorption signal imprinted. The upper region gives $+1^{st}$ order of the diffraction pattern as the reference spectrum. It is tilted upwards toward lower energies, because they represent higher wavelengths which are diffracted more. This diffraction is overlaid with the spectrometer diffraction along the horizontal axis and gives the tilted image of the reference spectrum. In order to get the correct reference, the rotation of the TEM grid has to be adjusted before installing it. The reason for this is that both beams have to enter the spectrometer exactly in the same horizontal position. In other words, they have to hit the spectrometer grating in the same position vertically. Otherwise the different path lengths in the spectrometer lead to different dependencies on the wavelength in the lower and upper sections of the CCD image. This would further complicate the correct analysis and make separate calibration of the regions of interest necessary. Careful pre-alignment of the TEM-gratings is thus done outside the vacuum with a HeNe

laser. The aim is to adjust the rotation of the diffraction pattern parallel to the optical table as precisely as possible at a great distance from the TEM grid.

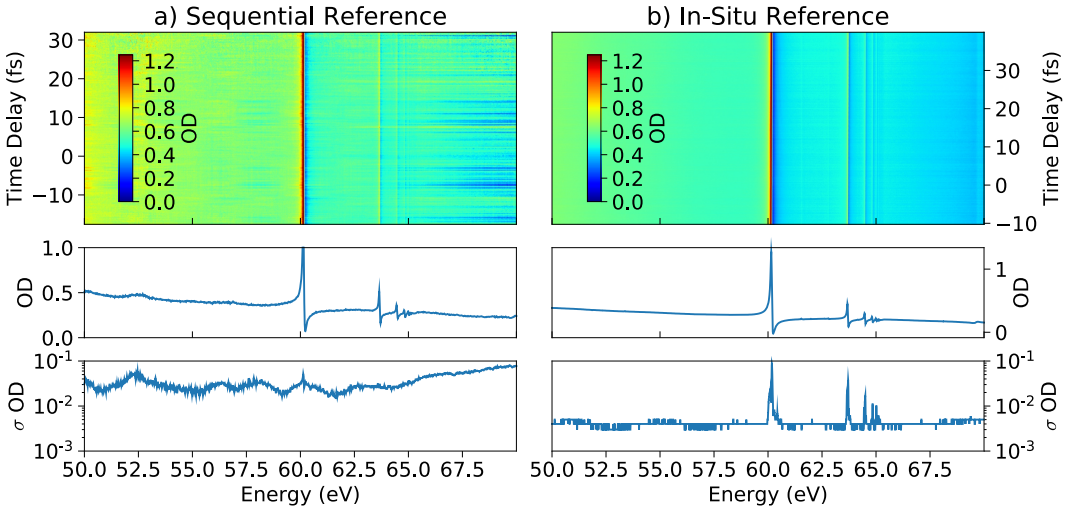

Figure 4.13.: **Comparison of the sequential and *in-situ* reference method:** a) 300 optical density (OD) spectra recorded at different time delays for zero NIR intensities. The references have been recorded after the absorption spectra and afterward matched to achieve the best fit to the shape of the harmonics. The lower panels show the mean value and the standard deviation using all spectra in the time delay scan. b) Analogous measurement showing ODs measured with the *in-situ* reference method. The lower panels again show the mean value and standard deviation of these spectra. Comparing the standard deviations of the different methods taking a difference of 3σ for detectable changes in the signal it can be seen, that the *in-situ* reference increases the sensitivity for changes in the OD down to $\sim$ 10 mOD. This represents an improvement of one order of magnitude.

The capabilities of this reference measurement technique are illustrated in figure 4.13, which compares the *in-situ* reference with the method of recording the reference sequentially (target in/out, gas on/off). Figure 4.13 a) shows the optical densities (OD) of a measurement of a time-delay scan over 300 values for zero NIR intensity. The ODs have been evaluated using a reference scan measured after the absorption spectra were recorded without the medium in the target cell. The references were matched to the absorption spectra by comparing the structure of the harmonics and choosing the best fit. The lower panels show the statistics from these 300 spectra. The mean value still exhibits slight modulations in the OD resulting from slight mismatches between sequentially recorded absorption signals and references. The standard deviation showing the magnitude of fluctuations in the measurements which ultimately limits the sensitivity to changes in the OD caused by physical effects. Here, the fluctuations are rather high across the whole spectrum. Compared to this method, figure 4.13 b) shows the same measurement performed with the *in-situ* reference method. Already the scan data is much more smooth without easily visible fluctuations between single OD spectra. Looking at the statistics of this data set, the mean value of the OD spectrum shows no slow modulations anymore. Furthermore, the overall standard deviation is much lower, with high values only at the positions

of the resonances which naturally fluctuate more. If a difference in OD of 3σ is considered as necessary for a detectable change in OD the *in-situ* method is sensitive to changes down to $\sim$ 10 mOD, while the sequentially recorded reference only manages to detect changes of $\sim$ 100 mOD on average. This is an improvement of one order of magnitude in sensitivity, which enables detailed studies of time-delay dependent absorption changes even in the continuum and precise determination of spectral line shapes as well as their modifications due to interactions.

5. Strong-field Spectroscopy

The experimental method of strong-field spectroscopy (SFS) is a versatile tool to study dynamic processes in quantum systems using absorption measurements. It relies on an ultrashort attosecond pulse which coherently excites atomic or molecular targets over a broad spectral range combined with a few-cycle strong near-infrared laser pulse which can drive the system in a nonlinear way. With this method, strong coupling, ionization and polarization effects for very high field strengths can be studied on the natural time scale of electronic motion. In this chapter possible applications of SFS are discussed.

5.1. Reconstruction of Strong-Field-Driven Temporal Responses

In the following, a novel application and extension of this technique, which was developed during this work and is published in [212], is presented. It amounts to the result, that a single absorption spectrum of an ultrashort probe signal transmitted through a medium contains time-resolved information about the full response (amplitude and non-trivial phase evolution). This holds even for coherently excited systems undergoing complex time-dependent processes, like the interaction with a strong and short laser field. The discussion of the results closely follows the publication in ref. [212].
As discussed in chapter 2, measuring very fast time-dependent processes in nature requires the observation of the (nonlinear) response of a system to precisely timed interactions which act as external probes and sample the dynamics at different times [121, 213]. Typically, two (or more) such events are needed (pump–probe spectroscopy), where the method of choice for the detection of electron dynamics are ultrashort pulses of light. The measured quantity in SFS is the absorption spectrum of one of the pulses. The principle of causality implies that an absorption spectrum of such an ultrashort signal can be used to retrieve the full complex response function [113–115] of the linear interaction with the ultrashort trigger pulse. This is supported by recent experiments and theoretical work [116, 214–217], which also suggest a strong relation between the precise spectral line shape and the amplitude and phase changes of the response function of a system underlying it. It is even possible to observe this link in the presence of strong, nonlinear interactions [83, 90, 92], which make the response explicitly time dependent. Up to this point, however, only the case of sudden (impulsive) modifications of the response was understood analytically, while the general case of the full response including complex time dependence caused by arbitrary interactions which evolves during the interaction with a strong and ultrashort laser pulse still has to be explored [218]. The presented re-

sults show that it is possible to reconstruct the full temporal response of a strongly driven time-dependent system from a single measured absorption spectrum, only requiring a sufficiently short pulse as input signal to initiate the coherent excitation of the system. The developed approach unlocks single-shot real-time-resolved signal reconstruction across time scales down to attoseconds for non-equilibrium states of matter. In the following, a system is considered to be in equilibrium if it does not exhibit explicit time dependence. This means at each point in time, it will respond the same way to a given probing event (e.g., the interaction with a photon). In other words, a system considered in equilibrium, interacting with a weak probe field of finite duration will always have the same response (in amplitude and phase) no matter when the interaction takes place. An explicit time dependence can be introduced by further external interactions which move the system out of the unperturbed time-translation-invariant state (out of equilibrium). In atomic physics such out-of-equilibrium processes include, e.g., the strong coupling between excited quantum states [83], the coupling of different multi-electron configuration channels [90], the polarization of the system in a strong field, or strong-field-modification of autoionization [92, 177]. Studying the nonlinear response of such processes is key to understanding, controlling and steering quantum dynamics on their natural attosecond time scale [21, 219–221].

Starting from systems initially in a stationary state (in equilibrium), the absorption spectrum $A(\omega)$ and thus the cross section $\sigma(\omega)$ is, according to equations 2.94 and 2.101, proportional to the imaginary part of the Fourier transform of the time-dependent dipole response $d(t)$ in the sample which is caused by a probing field $\mathcal{E}_{in}(t)$ (see also [222]):

$$\sigma(\omega) \propto A(\omega) \propto \mathrm{Im}\left[\frac{\mathcal{F}\{d(t)\}}{\mathcal{F}\{E_{in}(t)\}}\right], \tag{5.1}$$

where $\mathcal{F}\{d(t)\}$ is linearly proportional to $\mathcal{F}\{E_{in}(t)\}$. For systems in equilibrium without any explicit time-dependence, equation 5.1 serves as the starting point of probing physical systems by their linear response. In the limit of weak and short probing events (interactions that can be described via first-order perturbation theory) the causality properties of the generally complex response [113–115] draw a link between the imaginary part (absorption) and the real part (dispersion) of the response (see equation 2.86). The Fourier transform of the complete linear absorption spectrum then corresponds to the response of the system to a (virtual) broad-band excitation event. Consequently, the spectrum carries information about the internal structure of the probed system (e.g., through resonant excitations) including the natural exponential relaxation dynamics like spontaneous decay, autoionization or Auger decay, on the characteristic time scales T_d. For example, if the frequency of a cw-laser is tuned across the spectral line, its width can be measured. From the obtained spectrum, the natural decay times can be extracted even though probing fields $\mathcal{E}_{in}(t)$ with durations T_{in} much larger than the time scale of the dynamics in the system ($T_{in} \gg T_d$) are used. It is even possible to use an incoherent probe field $\mathcal{E}_{in}(t)$. In this case the system interacts with photons of various frequencies at random points in time and the obtained spectrum again yields the decay times. This is possible because in a time-translation-invariant system, the relative phases between frequency components

and consequently the arrival time of the probing photons are irrelevant. However for the case of a non-equilibrium state of matter, the time evolution cannot be accessed by long or incoherent fields as the system can exhibit an explicit time dependence, which makes the time of interaction with each frequency component crucial. The key question following this consideration is: How can an explicitly time-dependent response be temporally resolved?

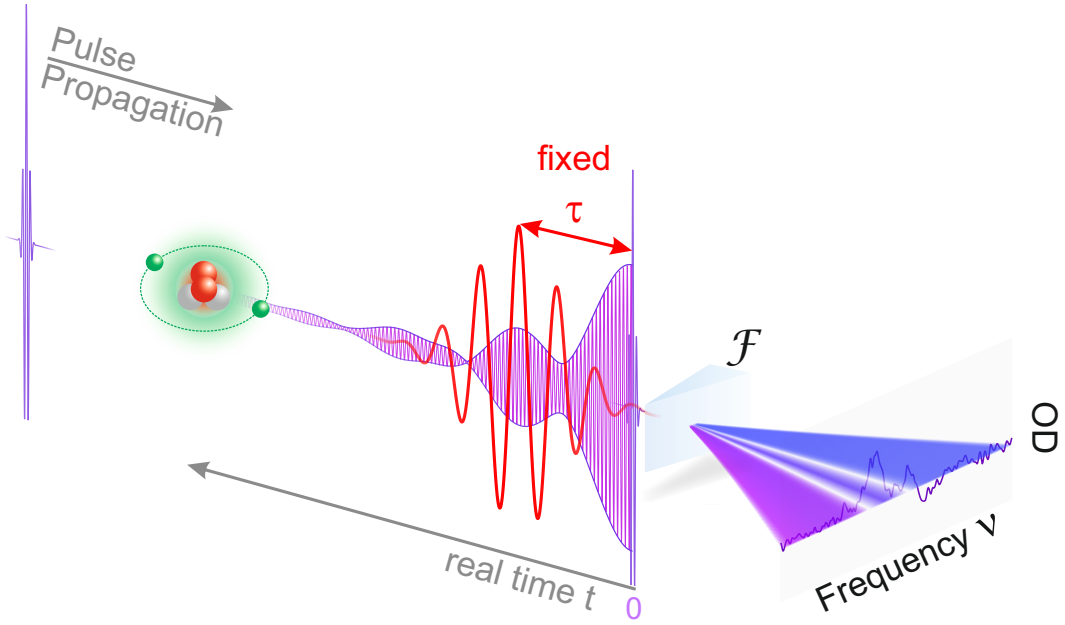

Figure 5.1.: **Illustration of the principles behind the Fourier reconstruction of the time-dependent response:** The non-equilibrium state of matter induced by a time-dependent perturbation $V(t)$ is probed using ultra-short laser pulses (blue) to trigger a response (purple), which is then modified for example by a strong external time-dependent electric field (red). From the measured absorption spectrum given by equation 5.1 the strongly driven response can be fully reconstructed if the initial excitation pulse is much shorter than the system's dynamics (equation 5.2), i.e., both the natural dynamics and those driven by the external perturber. In this case the initial excitation at $t = 0$ produces a causal response, and the response can be reconstructed using the Fourier transform of the measured spectrum.

The answer is provided by ultrashort laser pulses in the extreme ultraviolet (XUV) spectral range, which can nowadays be produced in the laboratory by means of HHG. In contrast to scanning the frequency or using incoherent sources, they represent a real broadband (effectively Dirac delta-like) event where all frequencies are effectively probed simultaneously. This makes the reconstruction of the non-equilibrium response from a single absorption spectrum possible. In the general case of a system subject to a time-dependent interaction $V(t)$, the response function becomes interaction- and time-dependent $d(V(t),t)$ which is illustrated by the temporal beating pattern imprinted on the purple dipole response function in figure 5.1. Following the arguments presented above, the response including an explicit time dependence can no longer be measured with incoherent light, i.e.,

photons arriving at random times. This problem is circumvented by considering the response to a coherent ultrashort probing pulse $\mathcal{E}_{in} = \mathcal{E}_{\mathrm{XUV}}(t)$, which precedes a generalized external perturbation $V(t)$. If the duration T_{XUV} of the pulse $\mathcal{E}_{\mathrm{XUV}}$ is much shorter than the time scale T_V of $V(t)$ and the natural decay time T_d of the system ($T_{\mathrm{XUV}} \ll T_V, T_d$) the interaction with the XUV pulse can be approximately treated in the impulsive limit. This limit is formally given by $\mathcal{E}_{\mathrm{XUV}}(t) = \mathcal{E}_{\mathrm{XUV}} \cdot \delta(t)$, with $\delta(t)$ being the Dirac delta function. Using this approximation, the absorption spectrum from equation 5.1 transforms into

$$\sigma(\omega) \propto A(\omega) \propto \mathrm{Im}\left[\mathcal{F}\{d(V(t),t)\}\right]. \tag{5.2}$$

Furthermore, it is immediately clear that $d(V(t),t)$ fulfills a sharp causality condition with $d(V(t),t) = 0$ for all $t < 0$, meaning there can be no response generated temporally before the excitation at $t = 0$. This implies that the real part $\mathrm{Re}[\mathcal{F}\{d(V(t),t)\}]$, and consequently the entire information of the coherent dipole $d(V(t),t)$ excited by the short pulse $\mathcal{E}_{\mathrm{XUV}}(t)$ is encoded in the absorption spectrum [113–115], and can be reconstructed from 5.2. The reconstruction simply applies the inverse Fourier transform to the spectrum and discards the results at negative times $t < 0$ due to causality. As no assumptions have been made about the nature of the interaction, this relation holds for arbitrary interactions $V(t)$, allowing the reconstruction even for strongly non-linearly driven dynamics. Because the full information is contained in the spectrum, no additional (probe) pulses are necessary to sample dynamical information. Furthermore, there is no need for scanning a time-delay in order to access the time-dependent information. Following this basic idea, the next section provides a mathematical description of the reconstruction method.

5.1.1. Mathematical Proof of Full Response Reconstruction

Following the time-domain picture of absorption introduced in section 2.5, a mathematical proof of the response reconstruction based on the Fourier transform is provided in this section. As discussed above, the goal of the reconstruction method is to access the real-time dipole response $d(t)$ of a quantum system initiated at $t_0 = 0$ by the XUV pulse $\mathcal{E}_{\mathrm{XUV}}(t)$, while the system experiences the subsequent interaction $V(t)$. This additional interaction introduces an explicit non-trivial time dependence to the response denoted as $d(V(t),t)$.

The mathematical derivation starts with the trivial case of $V(t) = 0$. This case is covered by linear-response theory, like it was introduced in chapter 2.5.1, where time-translation invariance is assumed. This means the dipole response of the system is not affected by the arrival time of the probing field. If $V(t) = 0$, the following holds for the transformation $t \to t + \Delta t$:

$$\mathcal{E}_{\mathrm{XUV}}(t) \to \mathcal{E}_{\mathrm{XUV}}(t + \Delta t) \;\text{ and }\; d(t) = d(t + \Delta t) \tag{5.3}$$

.

If there is an additional interaction $V(t) \neq 0$ at a time τ after the initial interaction, this time-translation invariance is broken. Consequently a shift of $\mathcal{E}_{\mathrm{XUV}}(t)$ by any value Δt will result in a different response of the system.

However, even in the case of a system which is not time-translation invariant, the response has to fulfill $d(t) = 0$ for times $t < 0$ due to causality. There can be no response before the interaction with the initial field $\mathcal{E}_{\mathrm{XUV}}(t)$. For such a 'causal' response, knowledge of only the imaginary part of the spectral response $\tilde{d}(\omega)$, which is closely related to the measured absorption signal, is enough to fully reconstruct the temporal response $d(V(t),t)$ using the Fourier transform and the causality condition. This can be shown, starting from the imaginary part of the spectral response $i\,\mathrm{Im}[\tilde{d}(\omega)]$, where the factor i needs to be taken into account to get the correct phase of the temporal response, following

$$\begin{aligned}
\mathcal{F}^{-1}\{i\,\mathrm{Im}[\tilde{d}(\omega)]\}(t) &= \frac{1}{\sqrt{2\pi}} \int i\,\mathrm{Im}[\tilde{d}(\omega)]\, \mathrm{e}^{i\omega t}\, \mathrm{d}\omega \\
&= \frac{1}{\sqrt{2\pi}} \int \frac{1}{2}[\tilde{d}(\omega) - \tilde{d}^*(\omega)]\, \mathrm{e}^{i\omega t}\, \mathrm{d}\omega \\
&= \frac{1}{2}\left[\frac{1}{\sqrt{2\pi}} \int \tilde{d}(\omega)\, \mathrm{e}^{i\omega t}\, \mathrm{d}\omega\right] - \frac{1}{2}\left[\frac{1}{\sqrt{2\pi}} \int \tilde{d}(\omega)\, \mathrm{e}^{i\omega(-t)}\, \mathrm{d}\omega\right]^* \\
&= \frac{1}{2}[d(t) - d^*(-t)] = \begin{cases} \dfrac{d(t)}{2} & \text{if } t > 0 \\ -\dfrac{d^*(-t)}{2} & \text{if } t < 0 \end{cases}
\end{aligned} \tag{5.4}$$

where the result is proportional to $d(t)$ for times $t > 0$.

If the excitation process is short compared to all other time scales in the response, the field $\mathcal{E}_{XUV}(t)$ can be approximated in the impulsive limit according to

$$\mathcal{E}_{XUV}(t) \approx \tilde{\mathcal{E}}_{XUV} \cdot \delta(t), \tag{5.5}$$

with an approximately constant spectral amplitude $\tilde{\mathcal{E}}_{XUV}(\omega)$. This spectral amplitude is then given by

$$\tilde{\mathcal{E}}_{XUV}(\omega) \approx \mathcal{E}_{XUV} \doteq \int \mathcal{E}_{XUV}(t)\, \mathrm{d}t\ . \tag{5.6}$$

According to [222], the absorption spectrum of such a signal can be written in terms of the excitation field and the spectral response as

$$A(\omega) \propto \omega \mathrm{Im}\left[\frac{\tilde{d}(\omega)}{\tilde{\mathcal{E}}_{XUV}(\omega)}\right]\ . \tag{5.7}$$

The absorption spectrum $A(\omega)$ can thus be used to reconstruct the real-time dynamics of the system encoded in the dipole response $d(t)$. In a quantum system there are generally many possible excited states which can contribute to a given response. It is possible to study the dynamics of these states separately by only considering one excited state $|\psi\rangle$ and its associated dipole response $d_{|\psi\rangle}(t)$. This is achieved by selecting a spectral range centered on the central energy $E_{|\psi\rangle}$ as long as the bandwidth is sufficiently broad to capture the full spectral line shape and thus resolve the fine temporal details induced by the interaction $V(t)$. As the proposed method uses ultrashort (attosecond) XUV pulses, the absorption spectrum and the accessible spectral range is limited by the bandwidth of the XUV pulse. This in turn implies that the temporal resolution is limited by the duration of the XUV pulse. However, if this excitation pulse is shorter than any time scale of the interaction $V(t)$ or any time scale of natural evolution of the excited states, this does not limit the reconstruction of the dynamics induced by $V(t)$.

Therefore, if the approximation of impulsive interaction is used, both ω and $\tilde{\mathcal{E}}_{XUV}(\omega)$ in equation 5.7 become constants in such a selected spectral range. It immediatly follows that the absorption spectrum $A(\omega)$ is now directly proportional to the imaginary part of the system's spectral response

$$A(\omega) \propto \omega \mathrm{Im}\left[\frac{\tilde{d}(\omega)}{\tilde{\mathcal{E}}_{XUV}(\omega)}\right] \approx \omega_{XUV}\frac{\mathrm{Im}[\tilde{d}(\omega)]}{\mathcal{E}_{XUV}}. \tag{5.8}$$

Inserting equation 5.8 into equation 5.4 then yields one of the main results of this work: the relation for the unique reconstruction of the time domain response $d(t)$ of the system for times $t > 0$ from the absorption spectrum, following the excitation by an ultrashort signal $\mathcal{E}_{XUV}(t)$:

$$\boxed{d(t) \propto \mathcal{F}^{-1}[iA(\omega)](t) = \frac{1}{\sqrt{2\pi}}\int iA(\omega)\,\mathrm{e}^{i\omega t}\,\mathrm{d}\omega \quad \text{for } t > 0.} \tag{5.9}$$

The real physical quantitiy of the time-dependent dipole moment which is defined as the expectation value of the position of the electron distribution can be retrieved by taken the real part of this expression.

5.1.2. Fourier Reconstruction for Finite Pulse Duration

The derivation of equation 5.9 which provides an analytic expression for the reconstruction of the general response from the absorption spectrum of a system uses the impulsive limit for the interaction with the XUV pulse as a key approximation. However, the real physical XUV pulse will always have a finite duration different from a Dirac delta distribution, it is necessary and instructive to examine this case in more detail. As stated in the discussion above, even if the approximation $\mathcal{E}_{\mathrm{XUV}}(t) \approx \mathcal{E}_{\mathrm{XUV}} \cdot \delta(t)$ is discarded, the XUV pulse still has to fulfill $(T_{\mathrm{XUV}} \ll T_V, T_d)$, where T_V, T_d are the time scales and durations of the interaction and the unperturbed response of the system under investigation. Only then is the picture of the XUV pulse initiating the dynamics and providing a well defined

starting point in time for the following explicit time evolution correct.

In order to study the effects of a finite pulse duration on the reconstruction scheme, an XUV pulse of finite duration, given by

$$\mathcal{E}_{XUV}(t) \approx \frac{\mathcal{E}_{XUV}}{T_{XUV}} \operatorname{sinc}\left(\frac{\pi t}{T_{XUV}}\right) \mathrm{e}^{-i\omega_{XUV}t}, \tag{5.10}$$

is considered, which still has no significant overlap with the action of $V(t)$.

The spectral amplitude is constant within a bandwidth $\Delta\omega = 2\pi/T_{XUV}$, which can be expressed as,

$$\tilde{\mathcal{E}}_{XUV}(\omega) \approx \mathcal{E}_{XUV}\, \Pi\left(\frac{\omega - \omega_{XUV}}{\Delta\omega}\right), \tag{5.11}$$

where the spectral amplitude shape is defined as $\Pi(x) = \theta(x+1/2) - \theta(x-1/2)$ in terms of the Heaviside step function $\theta(x)$. In the limit of $T_{XUV} \to 0$, $\Delta\omega \to \infty$ the approximation assuming impulsive interaction described by a Dirac δ-function is recovered. This pulse with a finite duration of T_{XUV} is now inserted into equation 5.8. Within the now limited pulse bandwidth $[\omega_{XUV} - \Delta\omega/2, \omega_{XUV} + \Delta\omega/2]$ equation 5.8 can still be applied to describe the absorption. However the limited bandwidth has to be taken into account explicitly and it becomes

$$A(\omega) \approx \omega_{XUV} \frac{\mathrm{Im}[\tilde{d}(\omega)]}{\mathcal{E}_{XUV}}\, \Pi\left(\frac{\omega - \omega_{XUV}}{\Delta\omega}\right). \tag{5.12}$$

Outside of the defined bandwidth, no photon is measured by the detector. If this expression is inserted into equation 5.9, one obtains the following expression for the reconstruction method

$$\begin{aligned} \mathcal{F}^{-1}[iA(\omega)](t) &\propto \frac{\omega_{XUV}}{2\pi\mathcal{E}_{XUV}} \int i\,\mathrm{Im}[\tilde{d}(\omega)]\, \Pi\left(\frac{\omega - \omega_{XUV}}{\Delta\omega}\right) \mathrm{e}^{i\omega t}\, \mathrm{d}\omega \\ &= \frac{\omega_{XUV}}{2\mathcal{E}_{XUV}} [d(t) - d^*(-t)] * \left[\frac{\mathrm{e}^{-i\omega_{XUV}t}}{T_{XUV}} \operatorname{sinc}\left(\frac{\pi t}{T_{XUV}}\right)\right] \end{aligned} \tag{5.13}$$

where the $*$-sign denotes the convolution of two functions according to the definition

$$x(t) * y(t) = \int x(t')\, y(t - t')\, \mathrm{d}t'. \tag{5.14}$$

The convolution theorem states that the Fourier transform of this expression is given by the product of the respective Fourier transforms:

$$\mathcal{F}[x(t) * y(t)] = \mathcal{F}[x(t)]\, \mathcal{F}[y(t)]. \tag{5.15}$$

Equation 5.13 immediately shows, that the duration T_{XUV} of the probe pulse used to trigger the dynamics of the system determines the time resolution with which the dipole response $d(t)$ can be reconstructed because the convolution with a function of finite width will effectively smooth over fine temporal details of the response. In turn, if T_{XUV} is much shorter than the time scale T_V of the interaction $V(t)$ and T_d of the system ($T_{XUV} \ll T_V, T_d$) like it is demanded for the reconstruction method, the effect of the convolution in equation 5.13 can be neglected. In the limit of $T_{XUV} \to 0$ the probe pulse can be approximated using the δ function and the convolution can be carried out analytically resulting again in equation 5.9. This shows, that the reconstruction method using the Fourier transform of the absorption spectrum is also viable for real pulses with finite duration, as long as they are short compared to all time scales of the dynamics that are to be investigated. In the following sections, the derived approach is tested both numerically and experimentally.

5.1.3. Numerical Proof of Viability for Complex Systems

For a proof-of-principle demonstration of the reconstruction method, the response of a prototype field-driven model system is numerically calculated. First, the Hamiltonian of a simple three-level system consisting of a ground state $|g\rangle$ and two excited states $|e_1\rangle$ and $|e_2\rangle$. $|e_1\rangle$ is initially coherently excited by a weak and broadband pulse, and subsequently strongly coupled to $|e_2\rangle$ by an intense short laser field representing $V(t)$ after a fixed time delay. The initial ultrashort broadband pulse and the subsequent strong driving pulses do not overlap temporally.

The resulting dipole response, driven and modified by a strong laser pulse at time delay 7 fs after the excitation, is calculated following the methods outlined in section 3.1 and is shown in figure 5.2 a). The resulting absorption spectrum $A(\omega)$ according to equation 5.1 is depicted in figure 5.2 b). The green lines indicate the width of a Gaussian filter window (FWHM) used to select a spectral region, like it is applied for the experimental data. The real-time coherent response $d_{rec}(V(t),t)$ of the whole system is retrieved by applying the Fourier reconstruction discussed in the previous section using equation 5.9 on the selected spectral region. The nearly perfect agreement between the reconstructed (figure 5.2 c)) and original (figure 5.2 a)) coherent dipole response, including the entire time-resolved holographic (amplitude and phase) information, confirms the validity of the approach for simple systems. It further illustrates the effects of a limited bandwidth on the results of the reconstruction. If only a limited spectral region and not the full spectrum (spectral response) is used for the reconstruction (Gaussian filter window, indicated by green lines), details like the fast oscillations on short time-scales (1 fs) in the overall response in figure 5.2 a) are not included in the reconstructed response. If however the spectral signatures outside the filter window around 56 eV and 64 eV are also included as input for the reconstruction, as it is indicated by the orange lines in figure 5.2 b), a broader spectral range is available which directly results in a higher temporal resolution of the reconstruction. Thus, also the fast oscillation on the response can be reconstructed which is shown in figure 5.2 d).

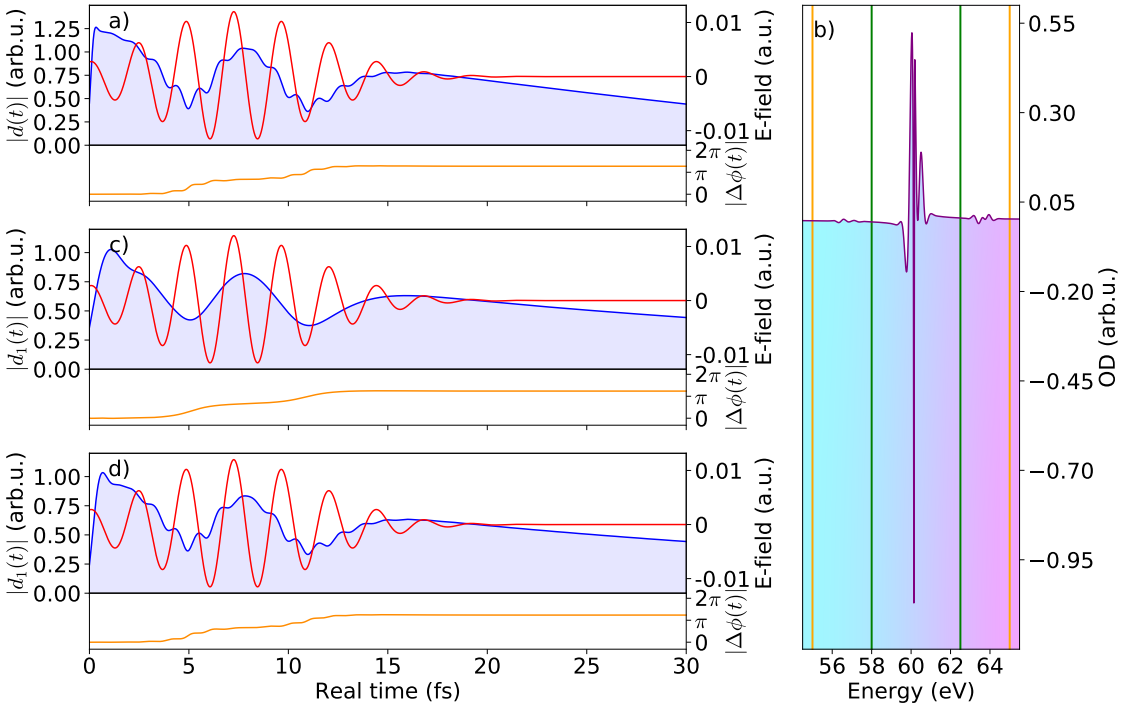

Figure 5.2.: **Numerical proof of the reconstruction method:** a) Amplitude (blue curve) and phase shift induced by the NIR field (modulo 2π, orange curve) of the numerically simulated time-dependent response function using a two-level model including a ground state and two coupled excited states. b) Calculated optical density from a) according to equation 5.1. c) Test of the reconstruction method of amplitude and phase of the response function by selecting (Gaussian filter window with its FWHM indicated by green lines) the plotted spectral range and taking the inverse Fourier transform of the observable spectrum b) restricted to the causal domain ($t \geq 0$). Due to the limited spectral bandwidth only the slow modulation features are reconstructed. d) Reconstruction with larger bandwidth (indicated by orange lines). This yields also the fast oscillations on the time dependent response.

As an extension to these calculations, a system mimicking complex dynamics was examined. To this end, the chosen Hamiltonian consists of the ground state $|g\rangle$ and now fifty excited states $|e_n\rangle$ with random energies and random dipole-coupling matrix elements to the ground state and to each other. As neither angular momentum nor parity are assumed to be good quantum numbers, dipole selection rules are not taken into account in the Hamiltonian. The simulation and calculation again follow the same line as discussed in section 3.1 and above. The results are shown in figure 5.3, where the spectral region for the reconstruction was chosen such that it includes all excited-state signatures using a Gaussian window filter (FWHM indicated by green lines). The reconstructed response plotted in figure 5.3 c) again shows very good agreement of the amplitude and phase evolution with the directly calculated response. Compared to the simple model discussed above, the full spectrum was selected as input for the reconstruction, which results in almost perfect agreement with the original, directly calculated response. This proofs the principle applicability of the reconstruction method to arbitrary complex systems as en-

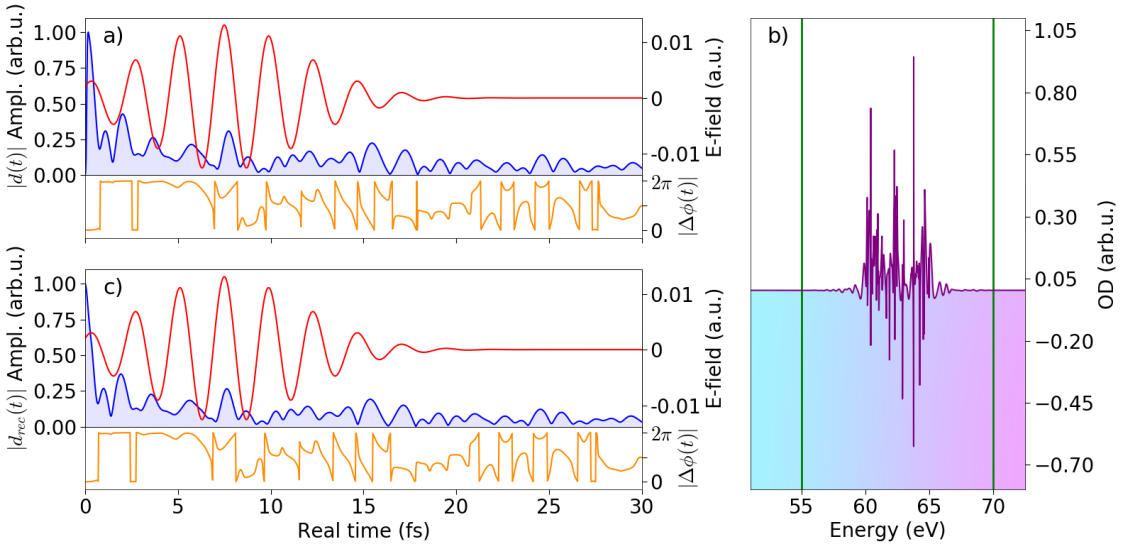

Figure 5.3.: **Extension of the numerical test to complex systems** The simulated system now includes fifty excited states with random energies, line widths and couplings. The red curve shows the electric field of the non-linearly interacting laser pulse. a) Calculated time-dependent response function. b) Calculated optical density from a) according to equation 5.1. c) Test of the reconstruction method of amplitude and phase of the response function. Even for very complex systems the response can be fully reconstructed if the whole bandwidth of the spectral signature is probed simultaneously.

countered in nature (e.g. biologically relevant molecules and condensed-matter systems).

5.2. Real-Time Response of Strongly Driven Doubly Excited Helium

For a first practical application and experimental proof of principle of the findings presented above, the reconstruction is directly applied to an important prototypical problem in strong-field atomic physics and attosecond science: the strong coupling between autoionizing states [95, 217] in an intense laser field. As we focus on the case where the initializing excitation and strong driving pulses arrive sequentially after each other, and by directly reconstructing the dipole response, we also avoid previously studied difficulties in extracting population dynamics in the temporal-overlap regime [214]. The target is the simplest atomic system with more than one active electron, namely the helium atom. The required pulse configuration for the observation of non-equilibrium dynamics in helium is provided by the transient-absorption setup described in chapter 4.

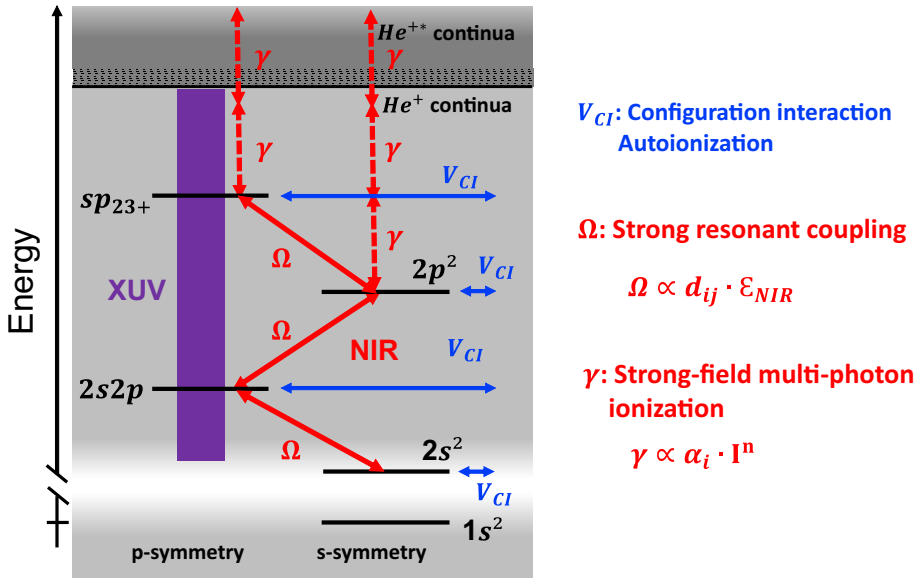

Figure 5.4.: **Scheme of the relevant states and couplings in strong-field-driven doubly excited helium:** The NIR pulse induces resonant couplings $\Omega_1, \Omega_2, \Omega_3$ between the autoionizing doubly excited states and also leads to resonantly enhanced strong-field multi-photon ionization γ into the N=2 continuum at the highest intensities of up to 20 TW/cm^2.

5.2.1. Experimental Data

In the experiment, the doubly excited states of helium (see figure 2.9 and 5.4) are coherently excited by extreme-ultraviolet (XUV) attosecond-pulsed light defining the time $t_0 = 0$ for the measurement. The spectrometer is tuned to optimum resolution (<50 meV) in the spectral range between 58 eV and 62 eV in order to resolve the signature of the dynamics between the $2s^2$, 2s2p, $2p^2$ and sp_{23+}-state if they are coupled by a strong 7-fs (full width at half maximum) NIR laser pulse. The pulse duration was extracted from data using the in-situ characterization technique described in [223] (see appendix C). The CEP of the NIR pulse was not stabilized for this measurement. Figure 5.4 illustrates the states, couplings and ionization channels mainly involved in the driven dynamics of doubly excited helium. The coupling dynamics manifest in the recorded spectrum as the Autler–Townes (AT) splitting in the vicinity of the 2s2p-state [177] as well as periodic changes of the line shapes depending on the time-delay.

For the measurement, a fixed time-delay value of the NIR pulse at $\tau = 7.4 \pm 0.1$ fs is chosen such that the AT splitting in the line shape is most pronounced and the overlap between the NIR and the XUV pulse is minimized. It is important to note, that the NIR pulse strongly drives the excited-state dynamics on a time scale (7 fs) comparable to the 2s2p natural life time (17 fs). The overall error of the time delay, $\delta\tau = 0.1$ fs, originates in the experimental systematic uncertainty of the sub-cycle determination of $\tau = 0$ fs in exact pulse overlap. As mentioned above, periodic sub-cycle line-shape changes, mainly due to resonant coupling with the sp_{23+} state, are observed [216], which depend on the exact time delay between the XUV and the NIR pulses and the CEP of the NIR pulse. It

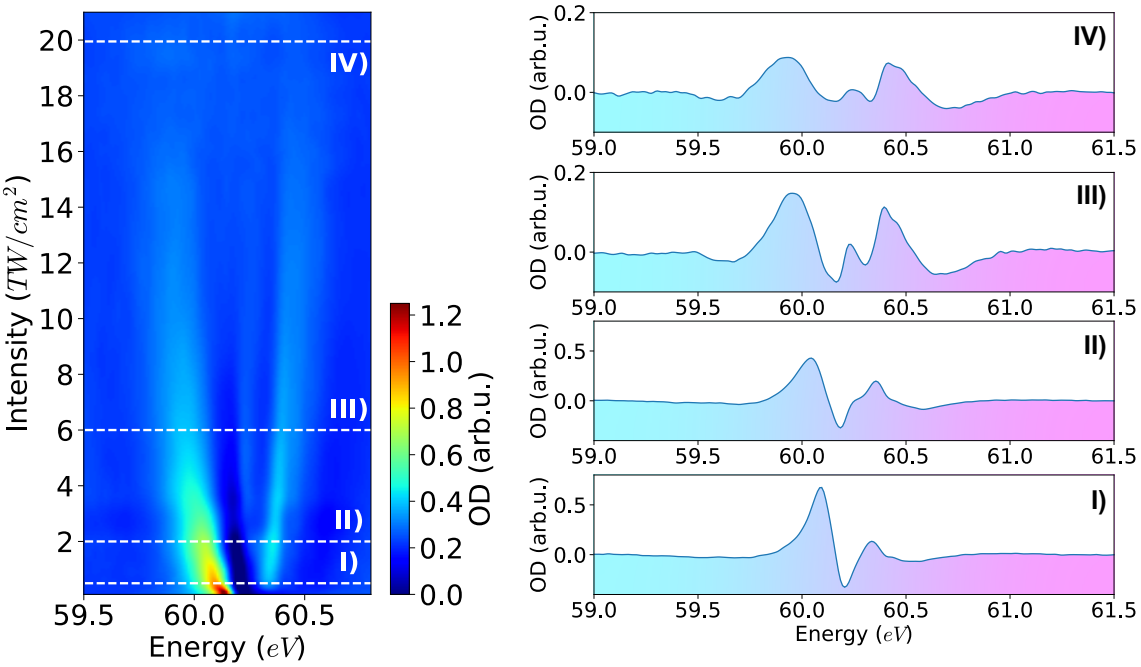

Figure 5.5.: **Experimental Data:** NIR intensity scan of Autler–Townes (AT) splitting [177] in doubly excited helium around the 2s2p state at 60.15 eV at fixed time delay $\tau = 7.4 \pm 0.1$ fs. The high spectrometer resolution allows for the observation of the line shape in great detail. White dashed lines (I)-(IV) indicate the intensities of the spectral lineouts shown on the right, which are used in the reconstruction discussed in figure 5.10.

has to be noted, that slight changes in CEP have the same effect as minimal changes in the time delay. Furthermore, the phase of the periodicity of these sub-cycle line shape modifications changes with the NIR intensity. Since the reconstruction method is sensitive to these changes, the sp_{23+} state is included in the simulation. As CEP and time-delay effects for very small changes cannot be distinguished, the CEP is kept fixed in the calculations and the time delay is adjusted within the given interval of $\tau = 7.4 \pm 0.1$ fs, to correctly reproduce the reconstructed time-dependent dipole response. The NIR intensity was calibrated by comparing the evaluated data to *ab-initio* numerical time-dependent Schrödinger-equation (TDSE) calculations described in section 3.3.
Figure 5.5 shows the recorded intensity scan of the 2s2p resonance which exhibits the well-known AT splitting [177] due to resonant coupling to the $2p^2$ state. The intensity ranges up to the maximum achievable value for the pulses in the experiment of 20 TW/cm^2. The lineouts (I)-(IV) show the different spectral line shapes at $I_{NIR} =$ 0.5, 2.0, 6.0, 20.0 TW/cm^2 NIR intensity in detail. They exhibit the asymmetry of Fano resonances as well as multiple maxima and amplitude changes for increasing intensity. These line shapes encode the full time-dependent evolution of the dipole response of the excited states during the interaction with the NIR pulse, which can be accessed using the reconstruction method introduced above.

5.2.2. Application of the Reconstruction to Measured Spectra

As the measured spectra contain non-resonant absorption of the continuum as well as the spectral information of the transmitted XUV light produced by high harmonic generation, the response of the doubly excited states has to be extracted using reference spectra and filtering. This section describes the reconstruction from experimentally recorded spectra in detail. The evaluation uses a directly measured reference of the XUV radiation shown in figure 5.6.

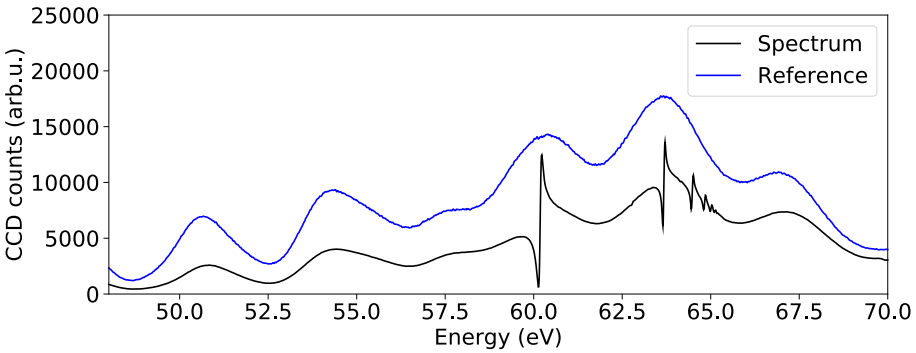

Figure 5.6.: **Raw Absorption Spectrum and XUV Reference Spectrum:** The plotted spectra are subsequently recorded measurements of the XUV spectrum with and without the target gas in the target cell.

Dividing the measured absorption spectra by this reference and taking the negative logarithm yields the optical density of the medium, which includes the resonant response of the discrete states and the non-resonant response of the continuum shown in figure 5.7. The remaining ~ 3 eV-oscillation of the optical density across the spectrum originates from the fact that the reference is recorded after the absorption measurement and not simultaneously. Because of the highly nonlinear process of high-harmonic generation the reference spectrum deviates slightly which introduces uncertainties in the measurements. The in-situ reference technique was not used for this data set, as it was not yet available at the time of the measurement. However, it is most likely that it will significantly improve the quality of the reconstruction method, as the exact line shapes can be measured now more accurately. This continuum response is fitted with a quadratic function and subtracted in order to isolate the resonant response from the non-resonant continuum response like it is illustrated in figure 5.8.

This way, only the resonant response of the observed system remains without the broadband response of the continuum which, would manifest as a pronounced peak for small times $t \sim 0$ fs in the Fourier reconstruction. The reconstruction method employing equation 5.9 uses these spectra of only the resonant part as input $A(\omega)$. Furthermore, the responses of single resonances can be studied by applying a Gaussian window function to the spectra illustrated in figure 5.9. The lowest panel of this figure shows the reconstructed response for such a selected resonance.

In contrast to the experimental data, the *ab-initio* simulations use a Fourier-low-pass filter with a Gaussian window function to separate the XUV response from the dipole response

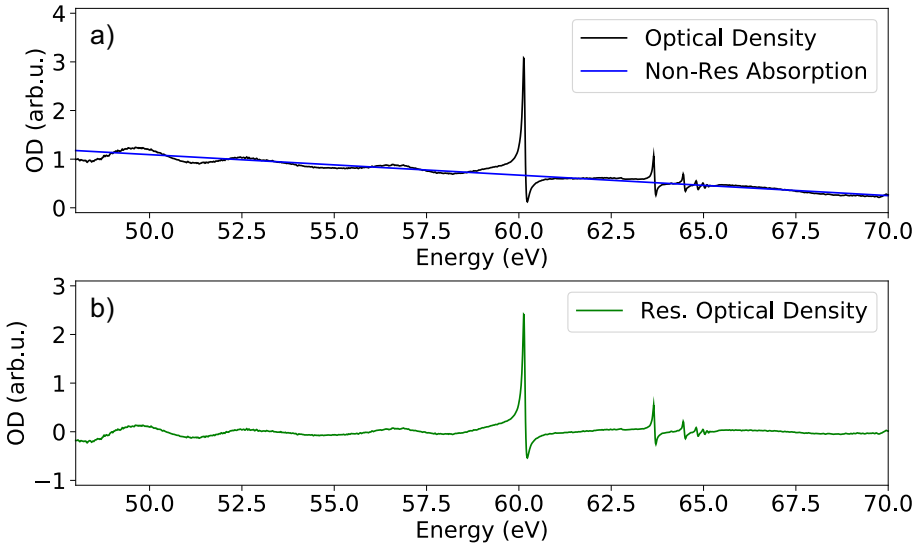

Figure 5.7.: **Evaluated optical density:** The Fano-resonances of doubly excited helium as well as the non-resonant continuum absorption are visible. The remaining modulation on the spectrum is due to the fact that the measured reference was not recorded simultaneously with the absorption spectrum and the XUV spectra fluctuate over time.

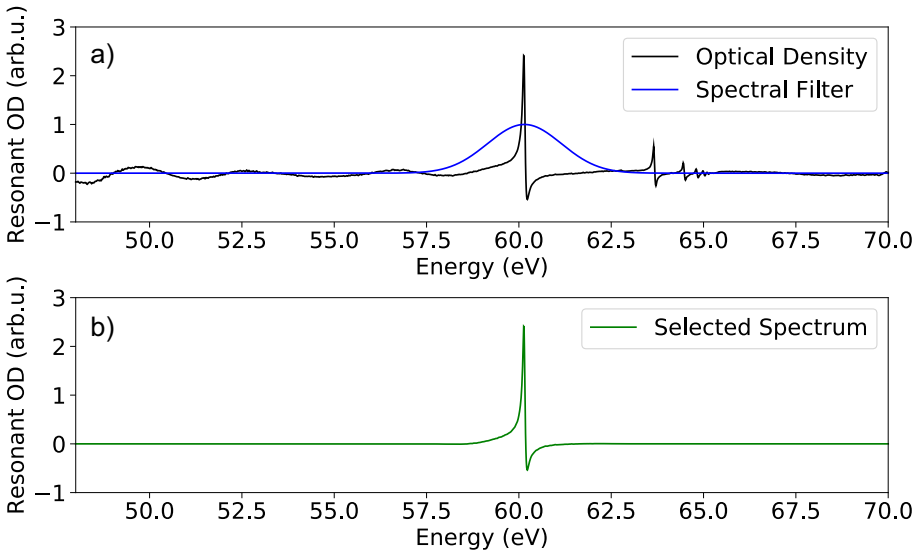

Figure 5.8.: **Resonant optical density:** Optical density before and after subtraction of the non-resonant continuum absorption.

of the states. This filter is applied in the time domain and cuts away the XUV response for short times. Only the resonant part remains in the calculation. By Fourier transforming the time-domain results, selecting a spectral range and applying equation 5.9 again the response from a single resonance can be obtained from the simulation.

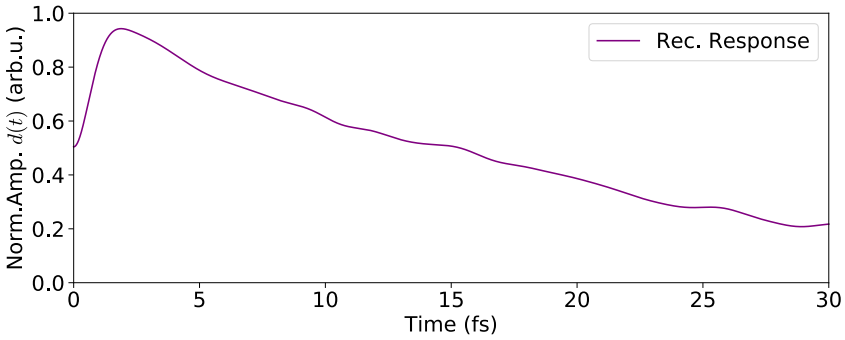

Figure 5.9.: **Selecting individual states:** In the resonant optical, density signatures of specific resonances can be selected with a Gaussian window function in order to study the response of separate states in time. The lower panel shows the reconstruction following equation 5.9 applied to the selected spectrum. As expected for an unperturbed state, the reconstructed time evolution shows a monotonous decay of the amplitude, which deviates from the theoretical exponential decay according to the state's life time because of the finite spectrometer resolution, which will be discussed in more detail in the next section. The kink for small times is the result of the removal of the continuum response (the broadband absorption would result in a strong response for short times).

5.2.3. Normalization and Correction for Spectrometer Resolution

In order to better compare experimental results and calculations, the data sets are each separately normalized by comparing the spectra to the case of zero NIR intensity. The function $f(t) = a \cdot \exp(-b \cdot t)$ is fitted to the reconstructed response at zero NIR intensity which should follow an exponential decay according to the natural life time of the examined states. The recovered parameter a is subsequently used to normalize all response curves of the corresponding intensity scan data set (a is determined separately for experiment, *ab-initio* or few-level calculation).
Furthermore, if the reconstructed dipole response is to be compared with a calculated response, the resolution of the spectrometer used in the experiment has to be taken into account explicitly. This limits the observable duration of the oscillating dipole response given by the reconstruction. It can easily be seen by considering again the convolution theorem

$$\frac{1}{2\pi}\mathcal{F}^{-1}[\mathcal{S}(\omega) * \mathrm{R}(\omega)] = \mathcal{F}^{-1}[\mathcal{S}(\omega)] \cdot \mathcal{F}^{-1}[\mathrm{R}(\omega)], \tag{5.16}$$

with $\mathcal{S}(\omega)$ being the spectral response of the system and $\mathrm{R}(\omega)$ being the spectrometer resolution function (typically Gaussian). It shows that any resolution function convolved with the physical spectrum results in a time window after the Fourier transform, which imposes a limit on the observable duration of the dipole oscillation that is reconstructed. The spectrometer resolution of $\Delta E \sim 40$ meV present in this setup limits the observable

TDDM oscillation to a duration of $T_{\mathrm{FWHM}} \sim 17$ fs (width of a Gaussian window in time). It was calibrated by fitting the Gaussian window multiplied with the *ab-initio* data for zero NIR intensity to the experimental data at zero NIR intensity, with the only fit-parameter being the width of the Gaussian window function.

5.2.4. Determining the Error of the Reconstructed Response

In order to estimate the statistical error of the reconstructed time-dependent response functions, the standard deviation of the values at each point in real time is calculated. The analysis is based on the data sets measured at time-delay τ and $\tau \pm T/2$ (where T is the duration of one optical cycle 2.02 fs of the NIR field). This provides a conservative, upper, estimate of the statistical error. The resulting error bars are plotted in figure 5.10 (shaded blue areas), and as error bars in figure 5.10. The systematic errors arising due to the uncertainty of the experimental pulse shape arriving in the interacting region, are not taken into account in this analysis. Furthermore, as the insitu reference measurement was not used for this experiment additional systematic errors are introduced. The deviations caused by slight discrepancies between the spectral intensity of the signal and the subsequently measured reference spectra of the XUV pulses, which are used to determine the optical density, do not enter in the evaluation of the statistical error.

5.2.5. Real-Time-Resolved Response of the 2s2p Helium State in Strong Fields

To retrieve the full time-resolved dipole dynamics of the 2s2p autoionizing state, the reconstruction method is applied to the intensity-dependent measured line profiles of the $1s^2$-2s2p transition. The results are presented in figure 5.10 for a wide range of NIR intensities. In this case, the response is the time-dependent dipole moment (TDDM) of the chosen resonance $d_{2s2p}(t)$. Both the amplitude and the phase (blue lines) are reconstructed using the presented method.
The reconstructed dipole response is compared to full *ab-initio* simulations (green lines) solving the time-dependent Schrödinger equation for helium in the presence of the XUV and NIR fields (see section 3.3). The validity of the impulsive-excitation approximation underlying the reconstruction algorithm (see equation 5.5) was verified by varying the pulse duration. This shows that the results are independent of the XUV pulse duration as long as the pulse is on the attosecond scale and short compared to time scales governing the dynamics of the coupled autoionizing states. In addition to the calculations described in section 3.3. It was verified that reconstructing $d(t)$ from the dipole acceleration yields the same results, assuring that the calculation is not influenced by the finite size of the grid used for the wavefunction representation. Propagation effects of the XUV radiation are not considered since the probability for reabsorption of photons is negligible in the investigated energy region and for the sufficiently low target densities in the experiment.
In order to more clearly identify the contribution of individual states and to obtain more insight on the underlying physics during the strong-field NIR interaction, we also devel-

oped a few-level model including the states shown in figure 5.4, as well as autoionization and multi-photon ionization (see section 3.1). The dipole responses from this calculation are represented by the orange lines in figure 5.10. All results shown in figure 5.10 are normalized to the curves at zero NIR intensity (see section 5.2.3).
The four NIR intensities in figure 5.10 represent different regimes of NIR strong-field interaction from the weak perturbative regime up to the regimes of strong coupling and strong-field ionization of autoionizing states. For NIR intensities of $I_{\mathrm{NIR}} = 0.5$ TW/cm^2 and $I_{\mathrm{NIR}} = 2.0$ TW/cm^2, the TDDM amplitude in figure 5.10 a), b) displays increasingly pronounced minima. For higher NIR intensities of $I_{\mathrm{NIR}} = 6.0$ TW/cm^2 and up to $I_{\mathrm{NIR}} = 20.0$ TW/cm^2 shown in figure 5.10 c), d) several oscillations of the amplitude are observed over time with rapid phase changes near each minimum of the amplitude. The *ab-initio* simulation allows for a direct and unambiguous determination of the full time-dependent dipole moment and confirms the reconstructed dipole response for this strongly driven helium system. Deviations at early (0-1 fs) and late times may result from the non-Gaussian experimental pulse shape and the experimental limitation of the measurement of temporally very broad and low-signal line shapes. An improvement would require longer measurement times and a more precise determination of the reference spectrum which was not yet possible at the time of the measurement.
The comparison with the few-level-model calculations allows for more detailed insights into the strong-field-driven coupling dynamics. For weak XUV excitations and subsequent interactions, which leave the ground state unaffected, the dipole is directly related to the amplitude (and thus population) of the excited state. The minima in the amplitude combined with the associated phase changes therefore indicate a significant resonant population transfer due to Rabi oscillations [83] mostly between the 2s2p and the 2p^2 states. The increasing number of minima with increasing NIR intensity directly follows from the field dependence of the generalized Rabi frequency $\Omega_{R,ij} = \sqrt{\Delta_{ij}^2 + \Omega_{ij}^2(t)}$, with $\Omega_{ij}(t) = \mathcal{E}_{NIR}(t) \cdot d_{ij}/\hbar$, $\mathcal{E}_{NIR}(t)$ being the NIR electric field, $d_{ij} = \langle i | d | j \rangle$ the transition dipole matrix element connecting two doubly excited states, and Δ_{ij} the respective detuning of the laser from the transition frequency between state $|i\rangle$ and $|j\rangle$.

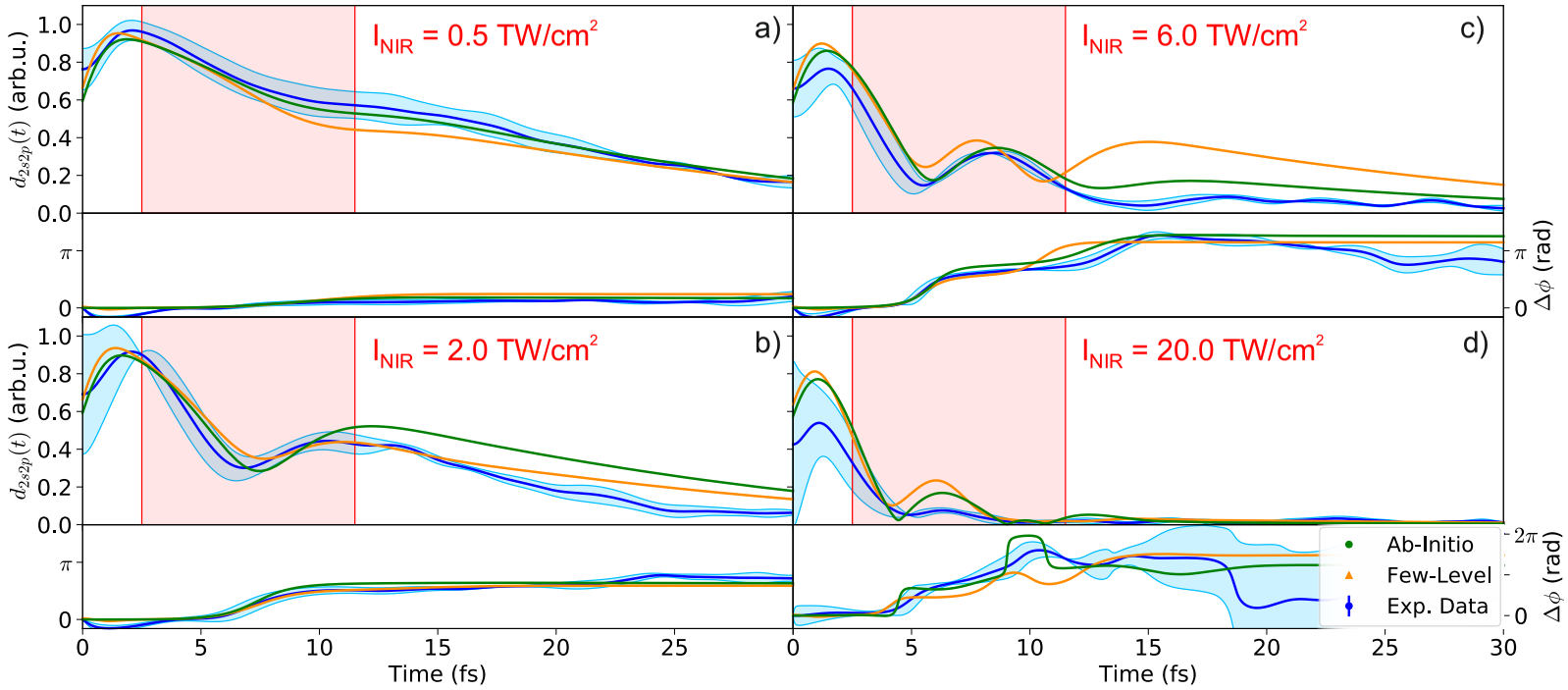

Figure 5.10.: **Reconstructed time-dependent dipole moment response (TDDM) $d_{2s2p}(t)$ of the 2s2p state of helium** (a)-(b) Reconstructed TDDM amplitude and phase change induced by the NIR interaction (modulo 2π, blue), showing the emerging departure from the simple exponential decay during the interaction with the central part of the NIR pulse (red shaded area) for the intensities $I_{\mathrm{NIR}} = 0.5,\ 2.0$ TW/cm^2. (c)-(d) The TDDM develops several minima and phase steps indicative of Rabi oscillations due to resonant coupling between the 2s2p and 2p^2-state. The onset of strong-field ionization and the resulting depletion of the states during the NIR pulse for higher intensities at $I_{\mathrm{NIR}} = 6.0,\ 20.0$ TW/cm^2 is visible. The error bars show the standard deviations of the reconstructed time-dependent responses. The orange curves show the calculated amplitude/phase evolution of the TDDMs using a few-level model including configuration interaction V_{CI} pathways and multi-photon ionization, where the latter becomes increasingly important at the highest laser intensities. The green lines represent *ab-initio* calculations which show very good agreement with the response retrieved from the experiment and thus prove the viability of the reconstruction method.

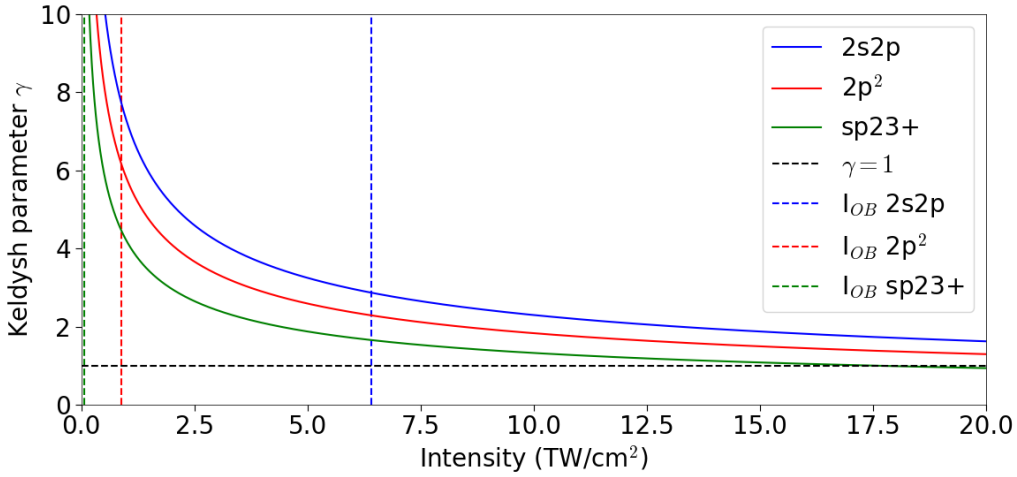

Figure 5.11.: **Keldysh parameter γ for doubly excited states in helium** The Keldysh parameter [49] for the 2s2p, 2p^2 and sp$_{2,3+}$ states is shown depending on the intensity of the NIR light (center wavelength $\lambda = 730$ nm). In addition, the critical intensity for over-the-barrier ionization is shown for the ionization potentials of each state. As the Keldysh parameter is $\gamma > 1$ up to the highest intensities and the critical intensity is reached for all involved states (no tunneling barrier), it is reasonable to describe the strong-field ionization channels using a multi-photon ionization model, meaning an ionization cross section which scales in intensity with the power of the number of involved photons.

At higher intensities, the decrease in the TDDM amplitude as a function of time shows that the contributions of NIR-driven ionization can no longer be neglected. In the absence of an analytical model for nonlinear laser ionization of doubly excited states, ionization rates $\Gamma_n = \alpha_n \cdot I_{NIR}(t)^n$ are employed in the few-level simulation, with $I_{NIR}(t)$ being the time-dependent NIR intensity envelope, n the order of the process (number of absorbed photons) and α_n are constants adjusted for each involved state but independent of intensity. This multi-photon ionization model is used following an analysis of the Keldysh parameter and the critical intensity needed for over-the-barrier ionization, shown in figure 5.11. The amplitude evolution of the TDDM predicted by this model still shows qualitative agreement with its experimentally reconstructed counterpart and the *ab-initio* results at higher NIR intensities. The phase evolution at high intensities even reveals the Rabi cycling to the 2s^2 excited state [129]. Although it is not resonantly coupled, it can be unambiguously detected by the phase jump of about $-\pi$ near 10 fs, which is absent if the 2s2 state is excluded from the model. Thus, this state significantly participates in the strongly driven bound-state dynamics and has to be accounted for explicitly in the few-level model in order to achieve agreement with the experimental results.

In addition, the TDDM-reconstruction approach allows for the examination of the transition from few-level to complex multi-level coupling dynamics in increasingly strong fields. For both theory and experiment, figures 5.12 a) and b) show the amplitude of

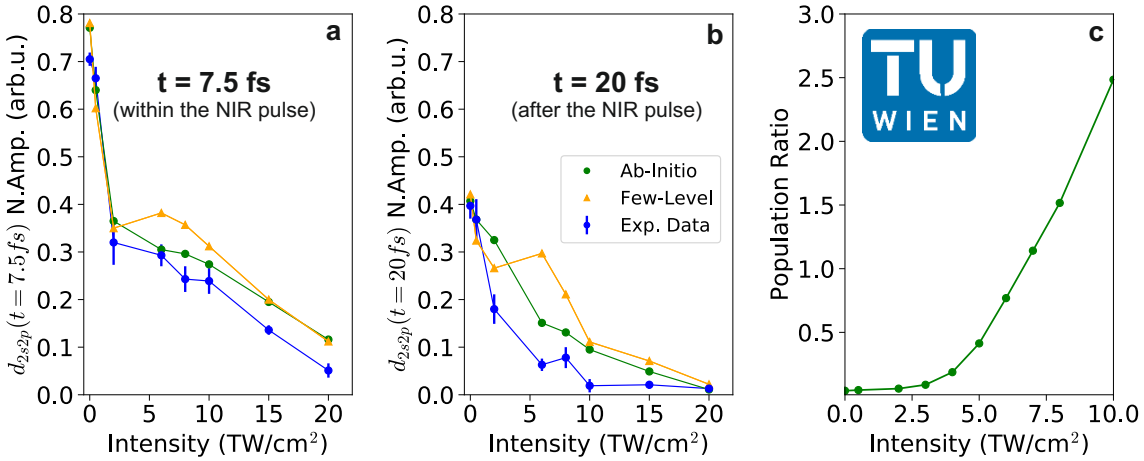

Figure 5.12.: **The onset of complex strong-field dynamics in a small quantum system:** (a) Amplitude of the reconstructed response at time $t = 7.5$ fs during the interaction with the NIR pulse (at time delay $\tau = 7.4$ fs). (b) Amplitude of the reconstructed response at real time $t = 20$ fs, i.e., after the interaction with the NIR pulse has concluded. The few-level model starts to significantly deviate from experiment and *ab-initio* simulation between 2.0 and 6.0 TW/cm^2 (c) Ratio between the population in 24 excited states, excluding the four states used in the few-level simulation, and the population in these four states after the strong-field interaction at $t = 20$ fs, extracted from the *ab-initio* simulation. The form of this curve explains the breakdown of the few-level model: the state space involved in the dynamics abruptly increases at a threshold value for the intensity. This value is reached at intensities between 2.0 and 6.0 TW/cm^2. For even higher intensities the interpretation in the framework of a few-state model is no longer reliable.

the reconstructed response at real time $t = 7.5$ fs and 20 fs, respectively. In both cases, the *ab-initio* simulation agrees well with the experiment. However, above an intensity threshold of about 2.0 TW/cm^2, the few-level model starts to disagree significantly not only quantitatively but also qualitatively. The explanation can be found when studying the results of the *ab-initio* simulation. Taking known wavefunctions (eigenfunctions) $|\phi_i\rangle$ for stationary states of the system, the population of these states after the interaction with the NIR laser pulse can be determined at different intensities of the pulse. This is done by calculating the projection of the wavefunction $|\psi(t)\rangle$ onto the eigenfunctions $|\phi_i\rangle$ of the corresponding states, using the non-conjugate dot-product

$$(\phi_i, \psi(t)) = \int \mathrm{d}\vec{r}_1 \mathrm{d}\vec{r}_2 \phi_i \cdot \psi(t). \tag{5.17}$$

The necessary eigenfunctions are obtained using exterior complex scaling [224]. Applying this analysis to a set of eigenfunctions which includes a lot more states than the few-level model provides an explanation for the observed deviations: a rapid increase of dynamical complexity in a small quantum system. The results presented in figure 5.12 show that above intensities of about 2.0 TW/cm^2, the number of states with significant population increases abruptly. Consequently the number of states contributing to the dynamics in the system grows significantly, which explains the breakdown of the few-level

model. Additionally, analysis of the photoelectron spectra of the fully propagated wavefunction in *ab-initio* simulation indicates that the approximation of neglecting ionization to the adjacent continua of different parity made in the few-level model is no longer viable.

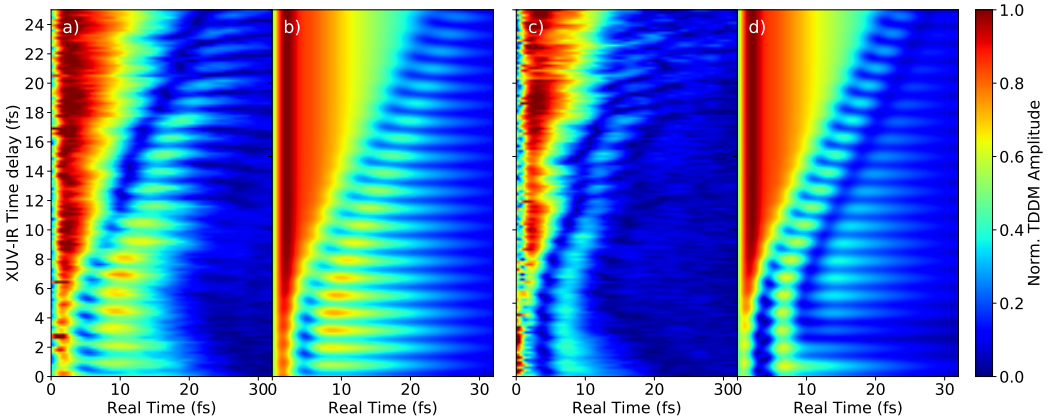

Figure 5.13.: **NIR time-delay scan of time-dependent dipole moment amplitude: a),c):** Time-delay scan of reconstructed TDDMs from experimental data for an intensity of 2.0, 6.0 TW/cm^2. The time of interaction imprinted on the response as well as sub-cycle changes with time delay are in very good agreement with the simulation. **b),d):** Scan of the time delay for the resolution corrected simulated TDDMs using the same intensity. The few-level model was used for the calculations. The biggest differences in the interaction region which is moving to later times for larger time delays originate in the experimental pulse shape deviating from the idealized Gaussian envelope used in the simulation.

5.2.6. Time-Delay-Dependence of the Response

Another very important aspect of the reconstruction method is, that it directly reveals the point in time at which the interaction with the NIR pulse takes place. In order to show this, the TDDM was reconstructed in dependence of the NIR time delay for a fixed NIR intensity of 2.0 and 6.0 TW/cm^2. The results are illustrated in figure 5.13 a), c), which shows a time-delay scan of the reconstructed TDDMs from measured data. This is compared to the resolution-corrected, simulated TDDMs in figure 5.13 b), d). The position of the nodes in the time evolution of the TDDM amplitude remain at a constant time delay until the NIR pulse moves out of overlap with the XUV pulse at $\tau \sim 7$ fs. The position then moves linearly with time delay to later times in both the measurement and the simulation. These plots confirm that the resulting Rabi oscillations and the correct and accurate time of interaction with the NIR field in the TDDM can be accessed using the reconstruction approach. The results further demonstrate the sub-cycle sensitivity of this method. The scan over the reconstruction applied to the experimental data shows periodic

changes in the obtained responses along the time-delay axis, on a time scale shorter than the duration of one cycle of the NIR field. As these changes match the simulated dipole responses very well and the simulation uses time-delay steps of 5 a.u. which samples several points within one cycle of the NIR field, the reconstruction is indeed sensitive to different responses caused by a change in the moment of interaction on a sub-NIR-cycle time scale. Differences between experiment and calculation appear mainly for later time delays, where the reconstructed responses show additional fluctuations and weaker minima. They originate in an experimental pulse shape which is not perfectly Gaussian but exhibits a weak post pulse.
These results show, that in contrast to conventional pump-probe schemes, there is no need for scanning time delays in order to access real-time information. Still varying the time delay grants access to additional information in the reconstruction of the dipole response. In principle this means that the reconstruction can be applied in single-shot measurements of absorption spectra with light pulses of high brilliance. This is the case for free electron lasers, where the single-shot capability of the method is especially useful due to the very high statistical fluctuations in the pulse spectra and pulse energies.

5.3. Studying Electron Correlation in States with Different Symmetries

The experimental approach of SFS in combination with the in-situ reference measurement technique developed as part of this work can furthermore be used to study electron correlation effects in different state manifolds of two-electron atoms. The high resolution of the XUV spectrometer together with the improved contrast and high sensitivity introduced by the new reference measurement allows for the simultaneous measurement of $sp_{2,n+}$ and $sp_{2,n-}$ states in doubly excited helium below the $N = 2$ ionization threshold. As outlined in section 2.4.3 these different manifolds emerged historically as a classification of doubly excited states $\left|sp_{2,n\pm}\right\rangle$, where the two orbitals of the excited states can couple in different ways

$$\left|sp_{2,n\pm}\right\rangle \approx \frac{1}{\sqrt{2}}(|2sn\mathrm{p}\rangle \pm |2pn\mathrm{s}\rangle). \tag{5.18}$$

In a classical picture, the joint motion of the electrons in such doubly excited states can be understood as the motion of two coupled springs with the electrons sitting at the end of each spring. Such a system can perform radial and angular oscillatory motion with both ends moving in or out of phase designated by the '$\pm$'-labels. The different phases in this motion can then be related to the vastly different lifetimes and excitation cross sections due to the different dipole matrix elements of these states. Of course this does not fully describe a real highly correlated quantum state. A much better approach is given by the treatment of this three-body problem in hyperspherical coordinates [109, 110]. Here, the doubly excited states are classified using a set of quantum numbers (n, N, $(K,T)^A$). In this notation, n is the main quantum number of the outer electron, N is the dissociation

limit and $(K,T)^A$ denotes a set of correlation quantum numbers, which orders the states by radial and angular correlation properties. Following the work presented in [109, 110] and [105], $sp_{2,n+}$, and $sp_{2,n+}$ series are given in this notation by (n, 2, $(0,1)^{+1}$) and (n, 2, $(1,0)^{-1}$). It directly follows that these states possess different correlation characteristics.

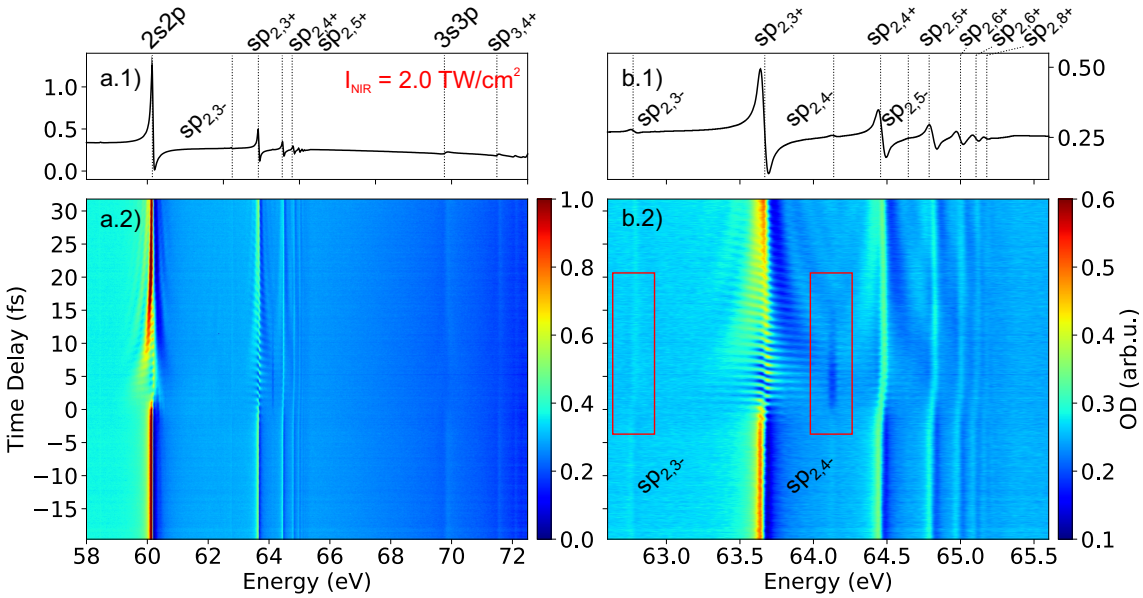

Figure 5.14.: **Transient absorption measurements of the $sp_{2,n+}$ and $sp_{2,n-}$ series in helium a.1),a.2):** Full Time-delay scan of the measured high resolution absorption spectra for an intensity of 2.0 TW/cm^2. In addition to the Autler–Townes splitting on the 2s2p state, the higher-lying doubly excited states of different symmetry are visible together with the $sp_{3,n+}$ series at the highest accessible energies. **b.1),b.2):** Zoom in along the energy axis on the higher excited $sp_{2,n+}$ and $sp_{2,n-}$ states. The red boxes indicate the dynamic changes on the $sp_{2,3-}$ and $sp_{2,4-}$ state which significantly differ from the behavior of the $sp_{2,n+}$ series.

The behavior of these states under the influence of DC and pulsed electric fields was already subject of experimental [225] and theoretical studies [226, 227], where different changes in ionization cross sections for the $sp_{2,n+}$, and $sp_{2,n-}$ based on their correlation properties were observed and calculated. Strong-field spectroscopy is now used to further study differences in the driven dynamics of these states both time-resolved and depending on the intensity of the applied laser pulses. Figure 5.14 shows an overview of the spectral lines accessible with the resolution of the setup. In figure 5.14 a.1) states of the series below $N = 2$ and even $N = 3$ are visible. These higher-lying states appear very weak because of their short lifetimes and small dipole couplings to the ground state. The fact that they are still visible, and even show time-delay-dependent changes again highlights the capabilities of the in-situ reference technique. Figure 5.14 a.2) gives the spectra of the time-delay scan at the intensity $I_{NIR} = 2.0$ TW/cm^2. In the energy zoom-in, which is given in figures 5.14 b.1), b.2) it is already clearly visible that the $sp_{2,n-}$ states exhibit delay-dependent changes which are strikingly different from the $sp_{2,n+}$ series both in amplitude

and line shape. These changes are studied in detail in the following sections.

5.3.1. Experimental Results

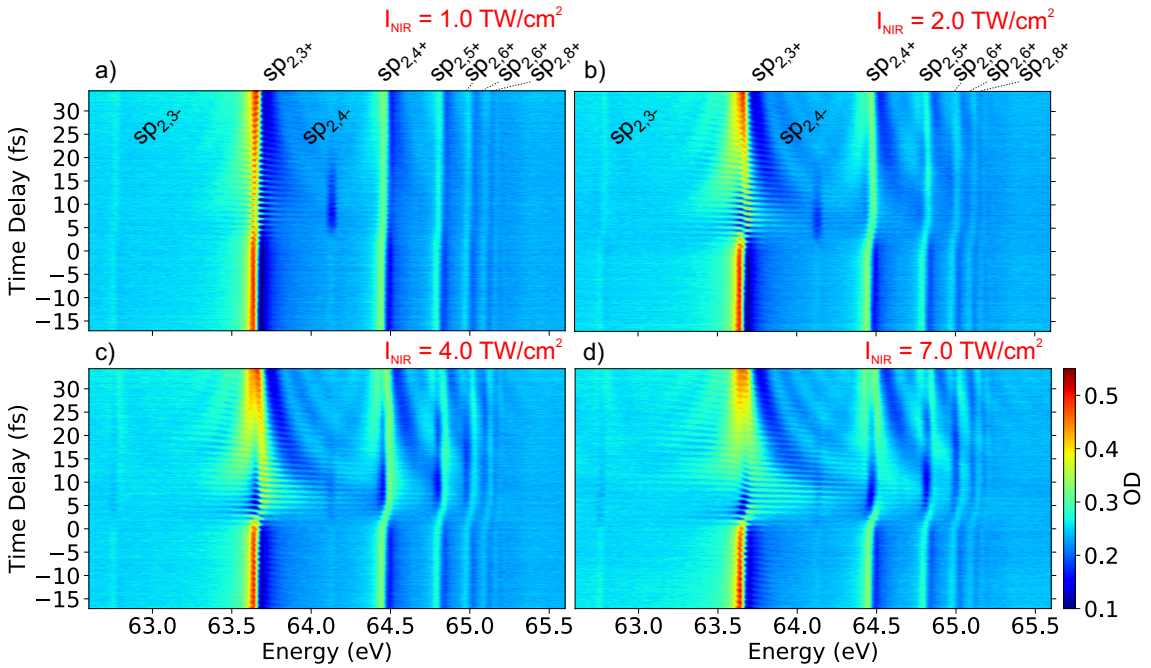

Figure 5.15.: **Measurements of the $sp_{2,n+}$ and $sp_{2,n-}$ series in helium a)-d):** High resolution time delay scans (steps of 85 as) for the moderate intensities of 1.0, 2.0, 4.0, 7.0 TW/cm^2.

In the presented measurement, the delay between XUV and NIR pulse was scanned and a spectrum was recorded for each position using the in-situ reference method. The time-delay range extends from -19 fs to +32 fs in steps of 85 as (50 nm mirror movement). The conversion medium used for HHG was neon, at a backing pressure of 110 mbar. The pressure of the helium gas target was kept at 75 mbar. The NIR pulse duration was characterized using a fit of the dipole control model [223], described in appendix C, which yields a pulse duration of $T_{NIR} = 5.7 \pm 0.1$ fs. This method was also used to calibrate the pulse overlap at $\tau = 0$ at the turning point of the fit which describes the phase change due to the NIR laser pulse. The intensity is calibrated by analyzing the Autler–Townes splitting of the 2s2p state also visible in figure 5.14. The results are shown as well in appendix C and give an intensity range of 0.1 up to $\sim$ 30.0 TW/cm^2. However, the interesting intensity range for the study of the dynamics in the $sp_{2,n+}$ and $sp_{2,n-}$ series lies between 1.0 and 10.0 TW/cm^2. Below this range, no significant changes can be observed, also due to the low absorption signature, and above this range the states are almost immediately washed out after the pulse overlap when the full NIR pulse interacts with the excited system. In between however, the two differently correlated manifolds show interesting changes, which are presented in figure 5.15.
Already at relatively low intensity, the $sp_{2,4-}$ shows significant changes. While the $sp_{2,n+}$ series only shows the ripples associated with resonant coupling to the 2s2p state [127,216]

and very slight modifications of the line shape, the $sp_{2,4-}$ resonance completely moves from a Fano resonance shape to an inverted Lorentz line. Most interestingly, this drastic change happens already at low NIR intensity, where the $sp_{2,n+}$ states are not yet significantly modified. This behavior continues for the higher intensities, where also the $sp_{2,3-}$ shows line-shape modifications which seem to match the evolution of the $sp_{2,n+}$ series. In order to further quantify and develop an understanding of these differences, the exact shape of the resonances is analyzed in detail in the next section.

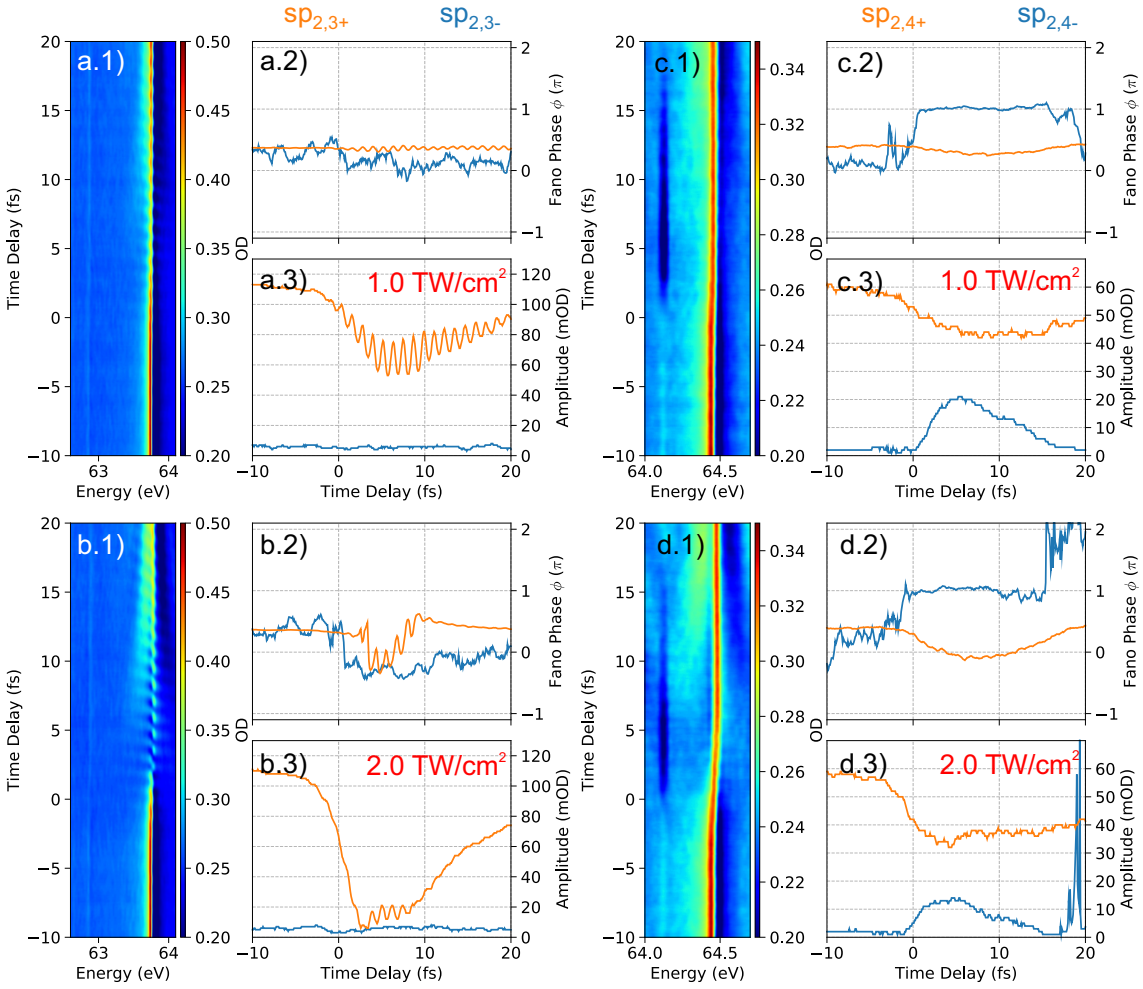

Figure 5.16.: **Analysis of the $sp_{2,3\pm}$ and $sp_{2,4\pm}$ states in helium** a.1-3) and b.1-3) show the time dependent spectral line of the $sp_{2,3\pm}$ states (orange, blue) as well as the fit results of equation 5.20 for the parameters A and ϕ_{mod} at NIR intensity of 1.0, 2.0 TW/cm^2. c.1-3) and d.1-3) show the same for $sp_{2,4\pm}$ states (orange, blue). The phases which should be limited to the range between $\pm\pi$ are unwrapped in order to avoid fast jumps which occur in fitted phases because of the low signal-to-noise ratio for the $sp_{2,n-}$ states.

5.3.2. Analysis of $sp_{2,n+}$ and $sp_{2,n-}$ Series

From the data presented in the previous section it is already evident that the state manifolds react very differently to dressing with a strong and short laser pulse. In the following section a first preliminary analysis of this work in progress is presented. In order to quantify the evolution of the resonance modifications, a general normalized Fano cross section is fitted to the data. The fit function is given by

$$F(E,E_R,\Gamma,\phi_{mod},A,B,C) = A\cdot\left(\frac{1+q(\phi_{org})^2}{1+q(\phi_{mod})^2}\right)\cdot\left(\frac{(\varepsilon+q(\phi_{mod}))^2}{\varepsilon^2+1}-1\right)+B+E\cdot C, \tag{5.19}$$

$$\text{with}\ \ \varepsilon = \frac{E-E_R}{\Gamma/2}, \tag{5.20}$$

where the energy E, the resonance energy position E_R, the linewidth Γ, the phase ϕ_{mod}, and the amplitude A are fit parameters describing the resonance, while B and C are parameters describing a linear absorption background. The phases ϕ_{mod}, ϕ_{org} determine the Fano-q parameter according to the relation $q = -\cot(\phi/2)$ given in [116]. Furthermore, ϕ_{org} is a fix constant which is determined by fitting the profile of the unperturbed resonance at zero NIR intensity. The results are shown in figure 5.16 and figure 5.17 for four different intensities of I_{NIR} =1.0, 2.0, 4.0, 7.0 TW/cm^2. The time-delay-dependent spectra are shown together with the calculated fit parameters A and ϕ_{mod} which characterize the evolution of the line shape. A sliding average over ten spectra along the time-delay axis has been applied to improve the very low signal-to-noise ratio especially for the $sp_{2,n-}$ resonances, while still retaining the quickly oscillating features in the spectra originating from resonant coupling. In the phase graphs, the phases ϕ_{mod} which are limited to the range $[-\pi,\pi]$ are shown unwrapped to avoid fast phase jumps around $\pm\pi$. The rapid phase changes result from a low signal-to-noise ratio and very low resonance amplitude for the weak spectral lines belonging to the unperturbed $sp_{2,n-}$ resonances, where the fit routine may not converge properly to the sensible set of parameters.

First, for the $sp_{2,3\pm}$ pair shown in figure 5.16, 5.17 a.1-3) and b.1-3), the spectral lines and fit results show several interesting features. The amplitude and phase of the $sp_{2,3+}$ exhibit a decrease and continuous shift as well as fast oscillations in the region after pulse overlap between 0 fs and +15 fs time delay. These features become more pronounced for increasing intensity. The oscillations originate in resonant two photon coupling to the 2s2p state which has been discussed in detail in [127, 216]. The changes in amplitude are caused by resonant population transfer during this coupling process and by the onset of strong-field ionization especially at the highest intensity of 7.0 TW/cm^2. For the lowest intensity the $sp_{2,3-}$ shows almost no changes. For increasing intensity however, the phase of the spectral line exhibits a rapid step by $\sim\pi$ at time delay $\tau = 0$ fs compared to the more steady changes in the phase of the $sp_{2,3+}$ resonance, while its amplitude remains mostly unaffected.
This peculiar phase and amplitude behavior is even more apparent in the $sp_{2,4\pm}$ pair. The fit results of these resonances are shown in figure 5.16, 5.17 c.1-3) and d.1-3). Here, even

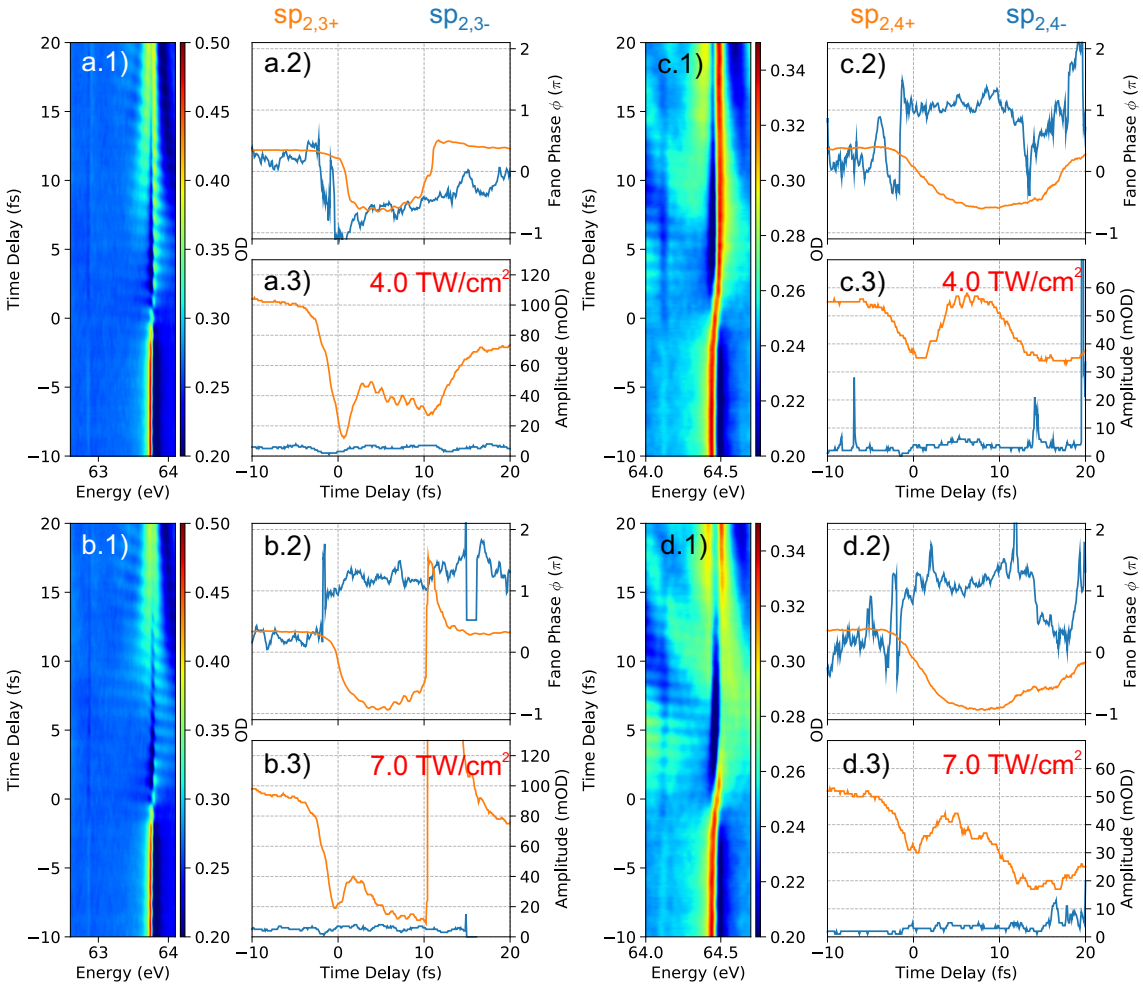

Figure 5.17.: **Analysis of the $sp_{2,3\pm}$ and $sp_{2,4\pm}$ states in helium** a.1-3) and b.1-3) show the time dependent spectral line of the $sp_{2,3\pm}$ states as well as the fit results of equation 5.20 for the parameters A and ϕ_{mod} at NIR intensity of 4.0, 7.0 TW/cm^2. c.1-3) and d.1-3) show the same for $sp_{2,4\pm}$ states. The phases which should be limited to the range between $\pm\pi$ are unwrapped in order to avoid fast jumps which occur in fitted phases because of the low signal to noise ration for the $sp_{2,n-}$ states.

for the smallest intensity there is a clear phase jump by $+\pi$ in the $sp_{2,4-}$ resonance at time delay $\tau = 0$ fs which persists until $\tau = 15$ fs to $\tau = 20$ fs. This fast change persist for all recorded intensities, while the phase change of the $sp_{2,4+}$ resonance again exhibits a smooth change towards negative values which becomes larger for increasing intensity. Also the amplitude of the $sp_{2,4-}$ increases by a factor of ten compared to the decrease of the $sp_{2,4+}$ resonance which is again due to coupling to other states and ionization for higher intensities. The large amplitude of the $sp_{2,4-}$ resonance decreases again for higher intensities which is due to overlap with the broadened features of neighboring resonances. Comparing the two pairs of resonances shows that the phase behavior of the $sp_{2,n+}$ and $sp_{2,n-}$ series are qualitatively consistent. However, the phase step of the $sp_{2,4-}$ line occurs more clearly even for the lowest intensity, whereas the $sp_{2,3-}$ only develops it for higher intensities values, where it assumes both $+\pi$ and $-\pi$ values. Furthermore, the changes in

amplitude between $sp_{2,3-}$ and $sp_{2,4-}$ appear completely different. As shown in table 2.3 the $sp_{2,3-}$ has a slightly larger linewidth, which means that this effect is not related to spectrometer resolution but caused by changes introduced during the interaction with the NIR pulse.
The more erratic features in the fits around time delay $\tau = 0$ and at later times are due to the fact that the fit algorithm has problems with following the evolution of the spectral lines for very small amplitudes. Also a line splitting due to resonant coupling is visible at later times between +5 fs and +20 fs which is not correctly included in the function used to fit the line shape. This explains the jump in the plots for the $sp_{2,3+}$ state in figure 5.17 b.2, b.3).
Concerning the different amplitude evolution of the $sp_{2,n-}$ states, it will be very interesting for future experiments to further improve the resolution and also look at the higher $sp_{2,n-}$ states to study if these amplitude modifications progress further for these states and if they are even more sensitive to the influence of the NIR pulse. Additional experiments with longer measurements times and increased statistics will also be necessary to further examine and possibly confirm the different asymtotic values of the phase shifts ($\pm\pi$) in the $sp_{2,3-}$ and $sp_{2,4-}$ states.

A first interpretation of these findings can be given by using a very simple picture. The evolution of the spectra observed in the experiment is determined by the time-dependent dipole moment of the excited states to the ground state which is for the '-'-states given by $d(t) = \langle 1s^2 | \hat{x} | sp_{2,n-} \rangle$. If this is expanded in the two possible configurations it becomes

$$d(t) = \langle 1s^2 | \hat{x} | 2snp \rangle - \langle 1s^2 | \hat{x} | 2pns \rangle . \tag{5.21}$$

Without the NIR field, the two contributions to the overall dipole moment are almost equal and can be thought of as approximately canceling each other, which can be illustrated as the electrons moving out of phase. This also gives an explanation for the much smaller amplitude of the spectral line compared with the '+'-states. In the presence of the NIR field, both during excitation (in pulse overlap) and afterwards, the contributions of these configurations are changed such that they no longer cancel and the overall dipole moment increases. The reason for this behavior could be different polarizabilities for orbitals of *n*s- and *n*p-character which contribute to the fully correlated states.
In order to fully understand the reason for this very interesting switching behavior of the phase at time delay $\tau = 0$ fs and the significant changes in amplitude, based on the correlation properties of the states, it is necessary to carry out more detailed theoretical studies, which take into account the different orbital contributions to the correlated states and can pinpoint which parts are responsible for the vastly different time-dependent behavior. Furthermore, experimental studies with higher spectral resolution and more statistics may provide further insights by observing the evolution for even higher-lying states, which are not currently accessible.

5.4. Intensity-Dependent Ionization Threshold for Different Excited-State Manifolds in Helium

A different application of strong-field spectroscopy is the study of the strong-field ionization of multi-electron systems from the perspective of the changes observed in bound-state resonances due to the ionization process. The ionization dynamics of multi-electron atoms and molecules include complex processes like autoionization, Auger decay, inter-atomic coulombic decay, shake-up and non-sequential double or multiple ionization. Especially for the case of strong-field ionization, the transition from a single-active-electron picture to (correlated) two-electron ionization effects for increasing field intensities is still a topic of interest.

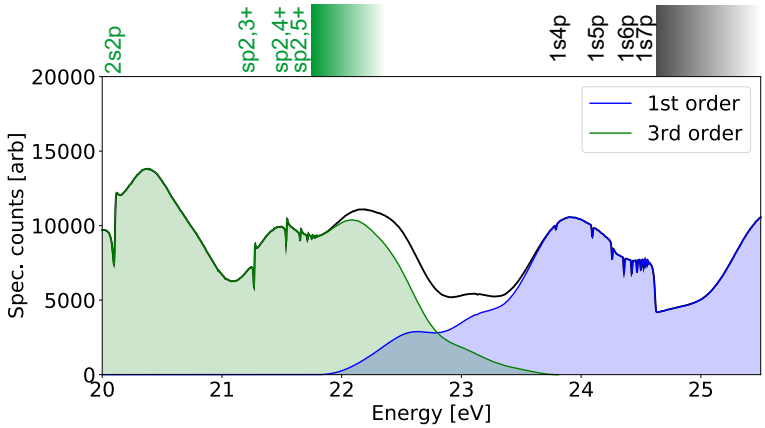

Figure 5.18.: **Multiple diffraction orders recorded simultaneously.** The spectrum is recorded at zero NIR intensity. Colors indicate spectrometer diffraction order. The first order XUV-spectrum shows the singly excited 1snp series, whereas the third order light contains the doubly excited states of the $sp_{2,n+}$ series.

Compared with the commonly utilized techniques of measuring photoelectrons and ions with time-of-flight spectrometers, the SFS method can be used to provide a complementary approach to the study of strong-field-ionization dynamics. Because of the broad accessible spectral range with simultaneous high spectral resolution, the role of two-electron effects in strong-field ionization can be studied by directly comparing the response of singly and doubly excited states in gas-phase helium.
Using the broadband XUV pulses, both state manifolds are excited simultaneously in the same measurement. The excited states then interact with a few-cycle near-infrared laser pulse of variable intensity at different time-delay values. In this configuration the onset of ionization and broadening of the spectral lines are measured depending on the intensity of the NIR pulse. As the effects of strong fields on the ionization dynamics of different bound-state configurations are studied, it is very important to know and control the intensity of the involved fields and to record the dynamics of the states simultaneously. In pump–probe experiments it is usually very challenging to exactly measure the NIR pulse intensity in the target during the experiment. Furthermore, it is very challenging to record absorption spectra with high resolution over a large spectral range. Therefore, the differ-

ent diffraction orders of our spectrometer grating are used to simultaneously observe the absorption lines of the singly excited and doubly excited states of helium. Figure 5.18 shows an example of a spectrum with zero NIR intensity obtained this way. The 1snp series up to the ionization threshold at 24.6 eV is visible, as well as the $sp_{2,n+}$ series of the doubly exited states starting at 60.15 eV in third order diffraction, which translates to a third order energy of 20.05 eV. This way, it is possible to record the spectral lines of both types of electron configurations at the same time making sure that both manifolds of resonances are affected by a NIR pulse of the same intensity. It is therefore possible to make reliable observations of different behavior for increasing NIR intensities.

5.4.1. Experimental Data

In the measurement, the experimental parameters were chosen such that the XUV spectrum extends up to 65 eV in order to excite the entire $sp_{2,n+}$ series but not below 22 eV, avoiding population in the 1s2p state which would coincide with the spectral signatures of the doubly excited states and obstruct the 1snp resonances with $n > 2$ due to resonant coupling effects described in [216, 228].

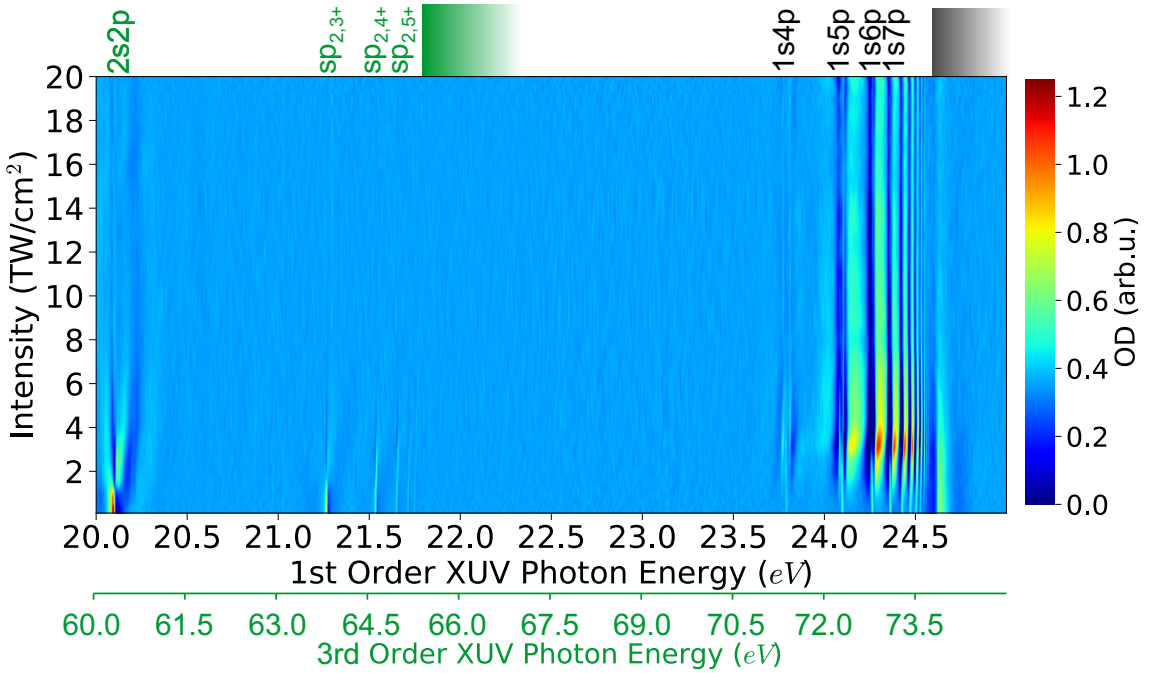

Figure 5.19.: **Cycle averaged intensity scan for singly and doubly excited helium resonances.** The resonances and continuum edges are indicated at the top. The data was evaluated using a reconstructed reference, described in section 4.3 and [116]. The Fourier filter creates artifacts at the continuum edges of the spectrum which are no physical effects. The doubly excited states are modified and vanish for the highest intensities while the singly excited states change their line shape and are still present.

With these settings, scans of the time delay τ between XUV and NIR pulse were recorded for a NIR intensity range between 0.1 and 20.0 TW/cm^2. Figure 5.19 shows the aver-

age over spectra for time delays across one laser cycle centered at a time-delay $\tau = 5$ fs depending on the NIR intensity. The data used in this plot was evaluated with the reconstructed reference method using a Fourier low pass filter, discussed in section 4.3. This method was chosen, because only resonant features are of importance and directly measuring a reference is further complicated by the multiple diffraction orders of the XUV visible in the spectrum. In figure 5.20 a)-d) lineouts of this scan at the intensities $I_{\mathrm{NIR}} = 0.5,\ 2.0,\ 5.0,\ 20.0$ TW/cm^2 are shown, respectively. For lower intensities the Autler–Townes splitting of the 2s2p state [177] is visible and modifications of the line shape arise for the singly and doubly excited states which have been explained as a modification of the Fano-q-parameter due to the strong NIR pulse [116]. However, for the highest intensities, the doubly excited resonances differ from the bound states with only one excited electron and become fully ionized. This is reflected by the vanishing of the spectral lines above $I_{\mathrm{NIR}} = 10.0$ TW/cm^2 while the resonance lines of the singly excited states are still clearly visible (figure 5.20 d)).

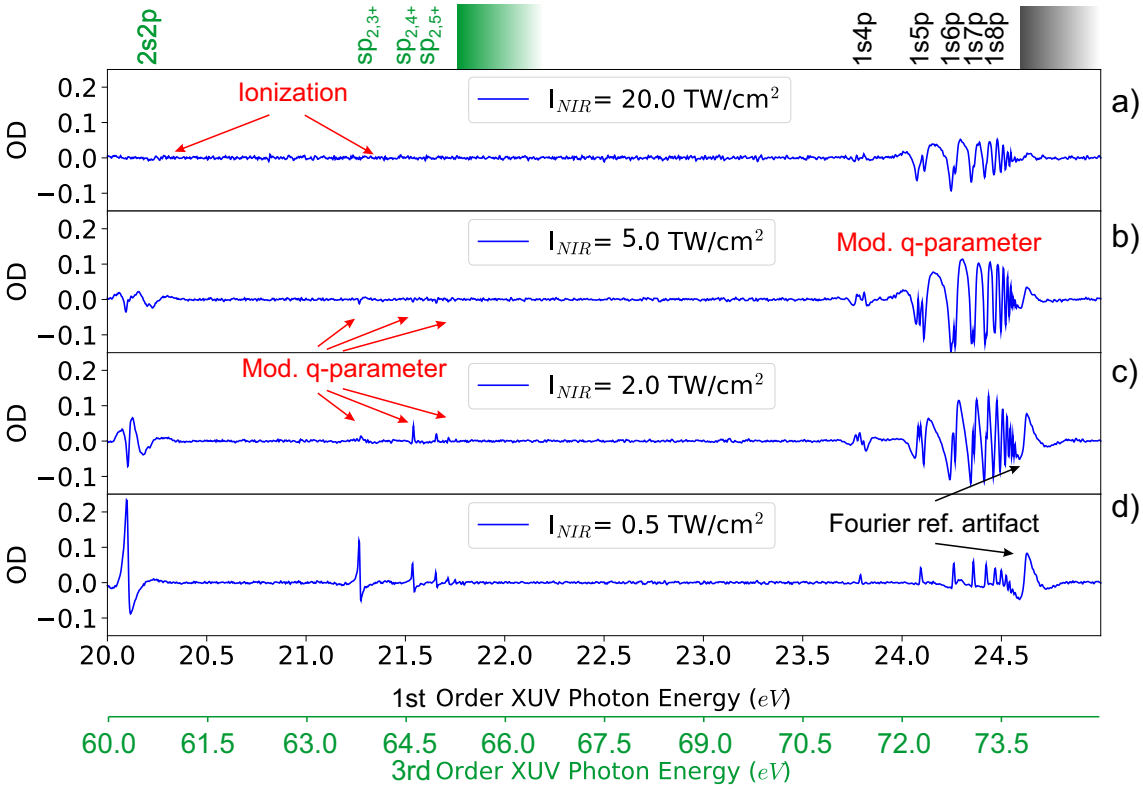

Figure 5.20.: **Lineouts taken from figure 5.19** Both manifolds show changes in the line shape from Lorentz to Fano resonances and vice-versa. This behavior has been linked to a control of the q-parameter with the NIR pulse, discussed in detail in [116]. For the highest intensities the doubly excited states are completely washed out, while the singly excited resonance lines are still clearly visible.

Therefore, different thresholds of ionization intensity are observed for the strongly correlated (doubly excited) and less correlated (singly excited) states respectively, indicating a significant role of electron interaction in the intensity-dependent ionization dynamics of

multiply excited-state configurations. The origin of these differences is explored using an *ab-initio* numerical time-dependent Schrödinger-equation simulation, where differences in the evolution of the two-electron wave function can be observed.

5.4.2. Numerical 1D-TDSE Simulations

In order to understand the underlying mechanisms of the different intensity thresholds for ionization of the resonance lines presented above, extensive numerical calculations have been performed in the course of a Master's thesis supervised in this work [203]. The principles of the 1D-TDSE simulation are discussed in section 3.2. The propagation uses a singly excited state (SES) and a doubly excited state (DES) of the same symmetry, which have roughly the same ionization potential of 0.1 a.u. to their respective continua. The states were prepared by wave function condensation using imaginary time propagation in the unperturbed potential starting from a random initial wave function. These prepared wave functions are then propagated in time with the time dependent electric field modifying the potential. The electric field used in the simulation follows equation 3.9 with a Gaussian envelope, a field strength of $\mathcal{E}_0 = 0.02$ a.u. corresponding to an intensity of ~ 15 TW/cm^2, and CEP $\Phi = 0$. For a first interpretation of the dynamics, it is most instructive to look at the wave function itself at several points in time during the pulse.

The results of this simulation are shown in figure 5.21 for the SES and figure 5.22 for the DES, respectively. The graphs show the probability density or absolute square $P_\psi = \langle\psi|\psi\rangle = |\psi|^2$ of the wave function which gives the probability to find the electrons at the coordinates (x_1,x_2) for all x_1 and x_2. The plotted times are chosen such that the cycles of the NIR pulse are sampled at four points. This way, the changes in the wave function over each maximum of the field can be tracked. Recalling the interpretation of the wave function in different sections of the grid (see section 3.2.2), figure 5.21 shows, that for the SES the population in the sections of single ionization increases while no population is in the sections indicating double ionization. So only the one active electron is ionized in this picture. However, in the DES case shown in figure 5.22 significant occupation probability is found in the regions of double ionization after the maximum of the pulse envelope is passed. This indicates that the DES possess an additional double ionization channel which may contribute to the lower intensity threshold for ionization.

While these results definitely point towards correlation effects between both excited electrons as the cause for the different intensity thresholds in the state manifolds, the exact mechanism could not yet be pinned down by these simulations. However, the results of the previous chapter indicating a significant increase in participating states and complexity of the strong-field driven dynamics in doubly excited helium allow for a second interpretation. It is possible that high number of involved excited states leads to a dephasing of the dipole response. Future experiments, measuring the photoelectrons leaving the system after the interaction with the NIR pulse utilizing for example a reaction microscopes, and further calculations are necessary to fully determine the underlying mechanism for the difference in intensity-dependent ionization.

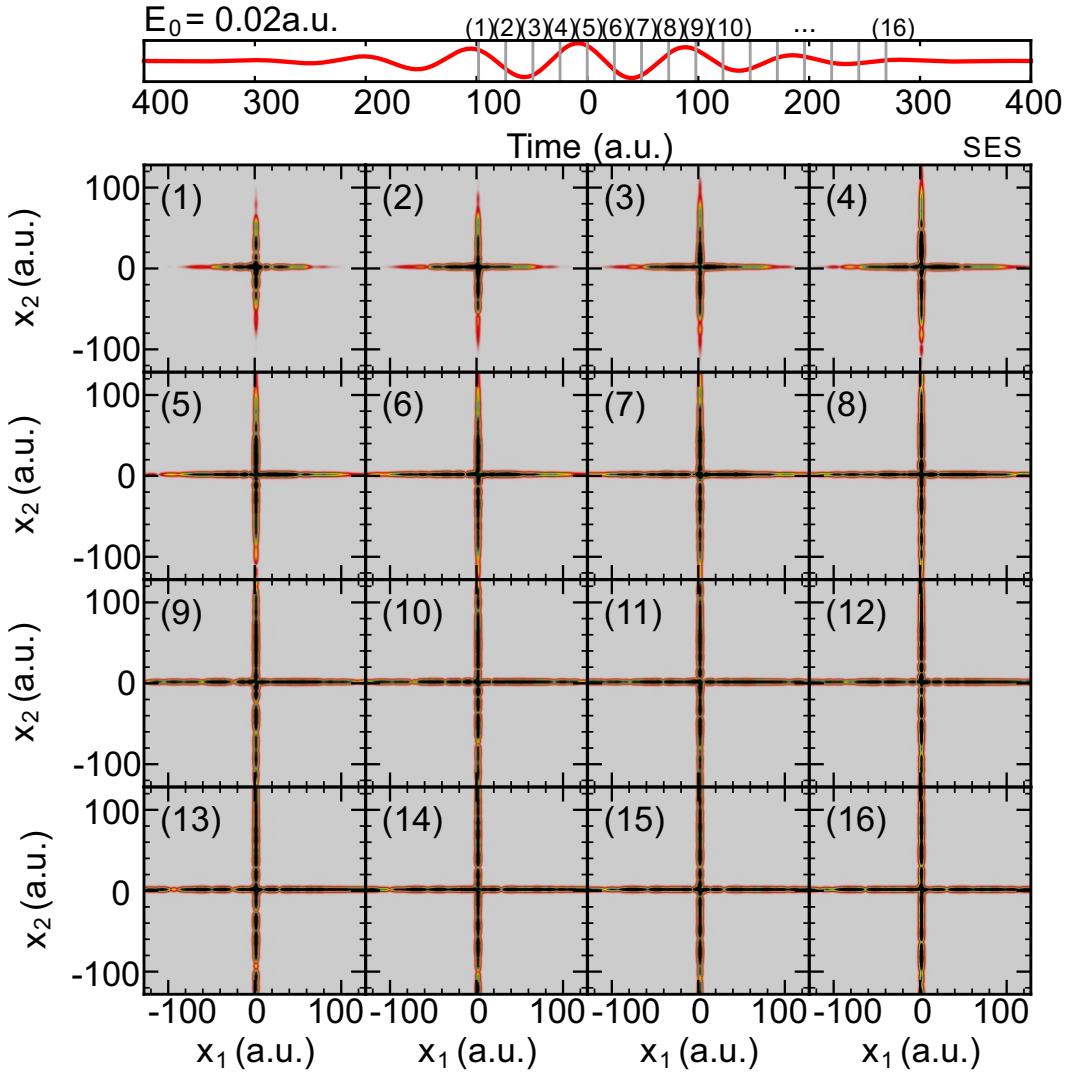

Figure 5.21.: **Snapshots of the wave function time propagation of a singly excited state** (1)-(16) show the evolution of the probability density $|\psi|^2$ given by the wave function of the singly excited state at the times indicated on the inset illustrating the electric field. For the singly excited state, no spread of the wave function outside of the single-ionization regions (see section 3.2.2) is observed. Figure adapted from [203].

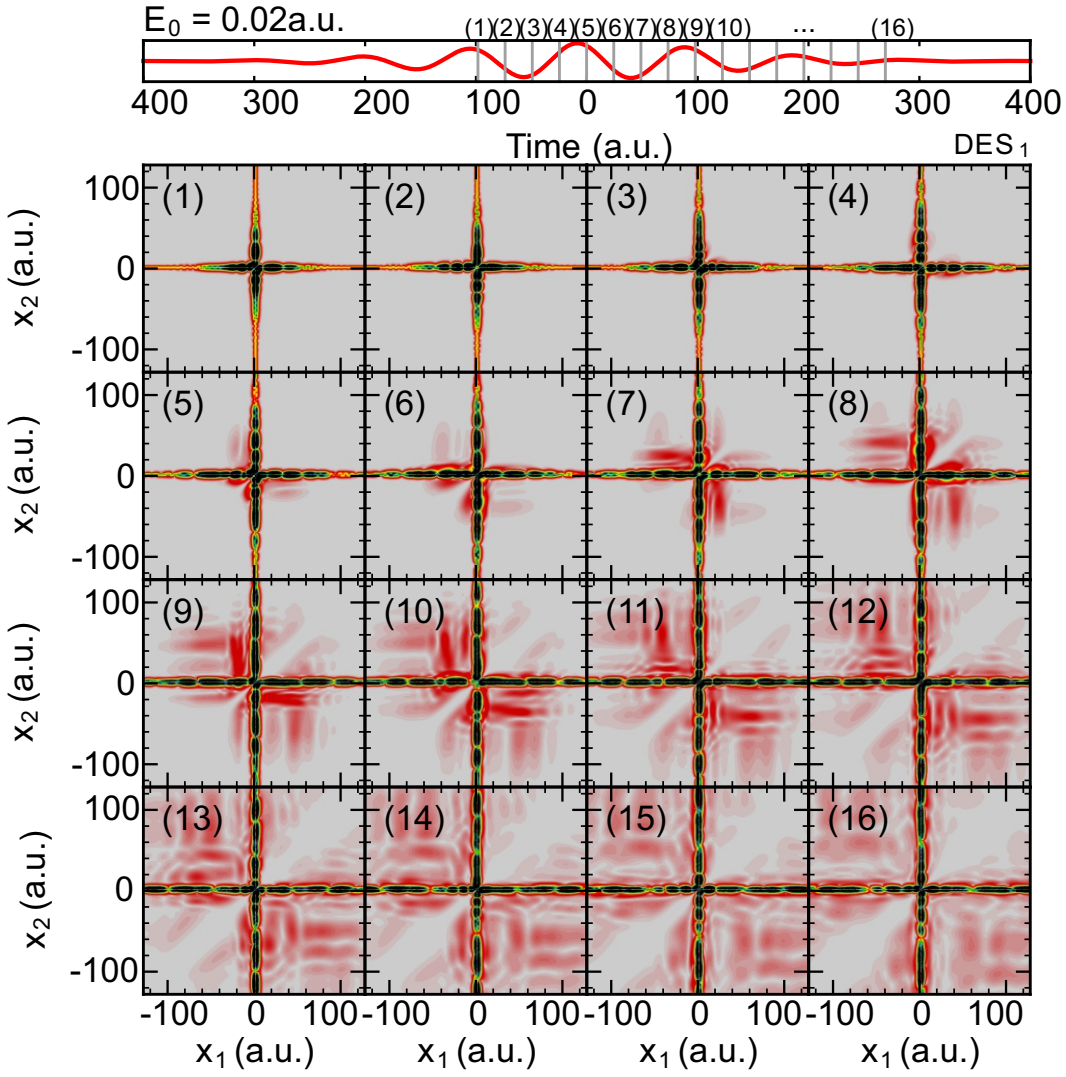

Figure 5.22.: **Snapshots of the wave function propagation of a doubly excited state** (1)-(16) show the evolution of the probability density $|\psi|^2$ given by the wave function of the doubly excited state. The considered times are the same as in figure 5.21. The wave function of the doubly excited state exhibits significant contributions outside the single ionization regions after the maximum of the electric field has passed. Figure adapted from [203].

6. Observation of Resonance Buildup

The method of strong-field spectroscopy (SFS), where an impulsive broadband response is excited by an ultrashort laser pulse and subsequently manipulated by an interaction with a strong field, represents a useful technique to study bound-state dynamics and even ionization mechanisms in quantum systems like atoms and molecules. This method aims at accessing time-resolved dynamics of systems interacting with short laser pulses ranging from perturbative coupling up to nonlinear strong-field effects and ionization. However, the effect of very high intensity laser pulses can also be used for a different type of time-resolved measurement: The strong-field ionization induced by these pulses can impose a variable time gate on processes initialized by the XUV pulse. This experimental technique uses the same setup as introduced in chapter 4 and is explained in detail in the following.

6.1. Observing Ultrafast Processes with Time-Gating based on Strong-Field Ionization

If the intensity of an ultrashort laser pulse is high enough, its interaction with an already excited target medium will completely ionize (or dephase) the atoms in the sample. This terminates any response of the system within a very short time, i.e., below the NIR pulse duration due to the nonlinear interaction. By varying the time delay between excitation and ionization, a variable time gate can be imposed on the response. Its influence can then be measured in the change of the observed spectral line shapes originating in the response of the atoms. In this way, the time-dependent formation of quantum states and interference on ultrashort time scales can be studied. Figure 6.1 a) illustrates the principle behind the time gate imposed on the response of the excited state. After the initial excitation by the XUV pulse, the response of a system can be terminated at a chosen time using the saturated ionization within a strong NIR pulse. If the detailed line shape based on this response is observed in the absorption spectrum, the formation process can be tracked by varying the time of termination (the time delay τ between the pulses).

6.2. Time-Resolved Buildup of a Fano Resonance

The gating technique has been successfully applied to the observation of the ultrafast formation of a Fano resonance in doubly excited helium. The results presented in the fol-

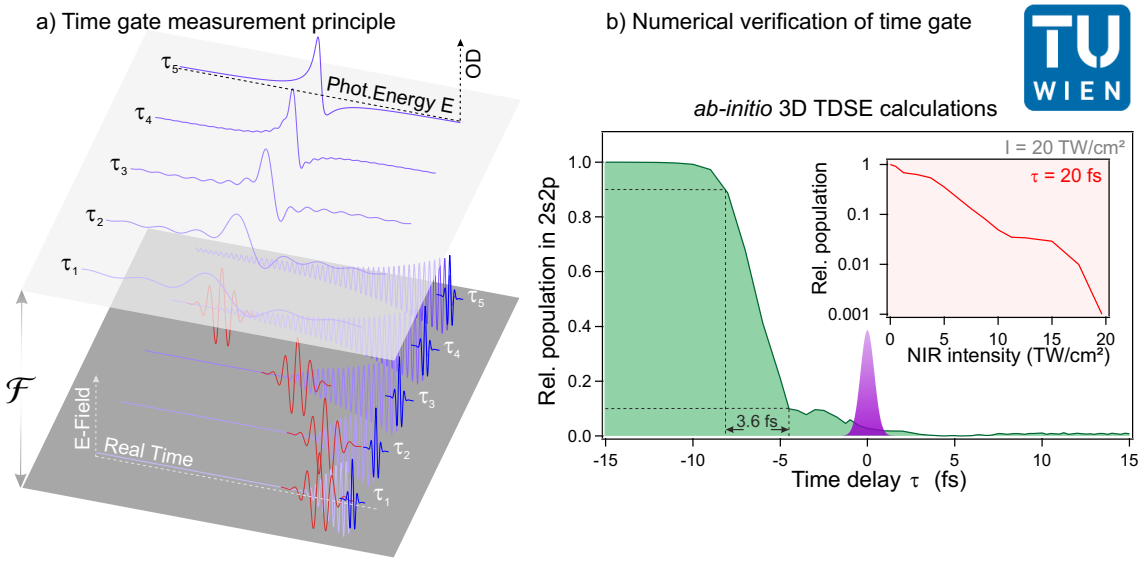

Figure 6.1.: **Illustration of the principles behind the time gate technique:** a) The lower plane (time domain) and the upper plane (frequency domain) show the relation between evolution of the temporal dipole response (lower curves) and the measured spectral line shape (upper curves). The response is excited by an ultrashort XUV pulse (blue), decays exponentially and is subsequently terminated by the interaction with the high-intensity NIR pulse (red) after a variable time delay τ_1,...,τ_5. b) Verification of the time gate by *ab-initio* calculations following section 3.3. The plot shows the occupation of the 2s2p state at a fixed time $t = 40.5$ fs after the excitation if the delay τ between the XUV and NIR pulse at 20 TW/cm^2 is varied. The decrease in population happens over the duration of 4 fs which indicates a very fast closing time compared to the states life time of $\sim$17 fs. The inset shows the population in the 2s2p state at a fixed time delay of $\tau = 20$ fs for increasing NIR intensity. For 20 TW/cm^2 less than one percent remains which demonstrates the efficiency of the gate for these intensities. Figure adapted from [229].

lowing have been published in [229] and the following discussion closely relates to this work. The characteristic asymmetric Fano resonance is found for discrete states energetically degenerate and coupled to a continuum as discussed in section 2.4.1. Since this type of configuration can occur in many classes of systems, such resonances are of interest in many fields of physics. The line shape itself results from the interference of different quantum paths with different phases depending on the energy. While several theoretical calculations predicted a time dependence of the formation of the Fano resonance caused by the interference [230–235], strong-field spectroscopy was one of the first techniques capable of measuring this time-dependent build-up for the doubly excited 2s2p state in helium. The measurement was possible using the high spectral resolution of the all-optical SFS approach together with the time-gating technique described above. The viability of this gating technique for helium as the target system is verified using full *ab-initio* calculations of the system in three dimensions (see section 3.3). The wave function evolution is calculated for the interaction with the pulse configuration in SFS. The remaining occu-

pation in the 2s2p-state at a fixed time $t = 40.5$ fs after the excitation by the XUV pulse is studied by projecting the evolved wave function onto the field free (zero NIR intensity) 2s2p-state. The results are shown in figure 6.1 b) for an NIR pulse of 20 TW/cm^2 intensity and 7 fs duration. The pulse duration was reconstructed from the data using the *in-situ* calibration method described in [223] (see appendix C). For large negative time delays the population is unaffected. However, already for $\tau \approx -5$ fs, 90% of the population is depleted by strong field ionization in the rising flank of the pulse. Complete depletion (less than 1% of the population remains) is achieved at $\tau \approx 4$ fs. The results confirm a gate closure time of about 4 fs by looking at the time-delay difference between a depletion of 10% up to 90% as indicated in the figure. This time is short compared to the $1/e$ life time of the 2s2p state of $\sim$17 fs and thus the dynamical formation of the 2s2p resonance can be sampled. Furthermore, the inset of figure 6.1 b) shows an exponential dependence of the depletion on the field strength of the applied laser pulse.

6.2.1. Experimental Results

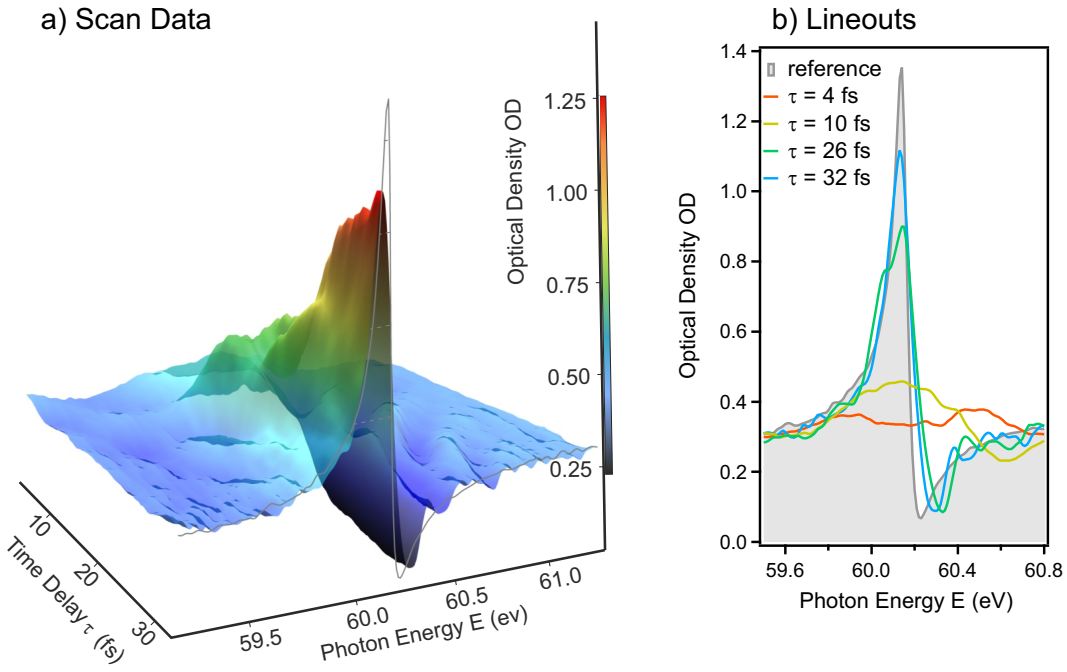

Figure 6.2.: **Data of the buildup of a Fano resonance measured using strong-field spectroscopy:** a) The absorption spectrum is shown depending on the time delay τ between excitation and ionization/termination of the response of the 2s2p doubly excited state. In the evaluation, the measured spectra were averaged over a time-delay range corresponding to one cycle of the NIR field in order to remove the fast oscillations due to resonant coupling to the $sp_{2,3+}$ state. b) Lineouts of the spectral line for different durations of the time gate (different time delay values). For small time delays the spectrum shows a broad shape and with increasing delay values the asymmetry begins to form. Figure adapted from [229].

Using the established time gate, the experimental results shown in figure 6.2 were recorded using the setup described in chapter 4 (without the *in-situ* reference). NIR pulses of 7 fs duration and peak intensity of 10^{13} W/cm^2 were used for the experiment. For small time delays τ the duration of the dipole oscillation triggered by the XUV pulse is short compared to the life time of the state. In this region the response is too short to fully form the asymmetric Fano line profile, which can be seen in figure 6.2 for $\tau < 10$ fs. The NIR pulse has the strongest impact at the time delay $\tau = 6$ fs where it almost completely washes out the spectral line. In such a case, where the state is completely depopulated right after the excitation process, the response is only determined by the interaction with the attosecond XUV pulse. As the response is cut short in time by the almost immediate ionization in the NIR pulse, the resulting spectral features extend across several eV in agreement with theory [230, 231]. If the delay τ between excitation and ionization is increased incrementally, the effective life time of the doubly excited state also increases. Now the interference with the quantum path of direct ionization can build up, which gives rise to a narrower, more asymmetric spectral line now carrying information about the autoionization process. For time delays close to the lifetime of the state ($\tau = 17$ fs), the spectral signature increasingly resembles the Fano line shape and for even larger time delays the well-known Fano resonance profile emerges. For the largest time-delay value shown in figure 6.2 the measured absorption line matches the expected Fano line shape very well. It has to be noted, that also in this comparison of the data with theoretical line shape, the finite spectrometer resolution of 50 meV FWHM, which has a significant effect on the line width, has to be taken into account. Considering the limit of $\tau \to \infty$ and following the analytic theory [231, 233, 235], it takes approximately 100 fs (140 fs) for the forming 2s2p resonance to reach 95% (99%) agreement with the theoretical line shape. Due to the optics and beam geometry in the target, larger time-delay settings than those given in figure 6.2 could not be reached. However, it was still possible to measure the main features of the build up of the Fano resonance.

6.2.2. Comparison to Theoretical Models

In order to further examine the results of the measurement of the build up presented in figure 6.2, the experimental data is compared both to absorption spectra obtained from a full *ab-initio* calculation and an analytic model following [233] and the calculations in [229]. The analytic description of the cross section is

$$\sigma(\varepsilon,\tau) \propto \mathrm{Re}\left(1 + \frac{(q-i)^2}{1-i\varepsilon}\left(1 - e^{-\frac{\Gamma}{2}(1-i\varepsilon)\tau}\right)\right), \tag{6.1}$$

where q and Γ denote the Fano q-parameter and the width of the line and ε defines the scaled photon energy according to $\varepsilon = 2(E - E_R)/\Gamma$. The results of these models are shown together with the measurement in figure 6.3, where panel a) gives the spectra calculated using the analytic theory resulting in equation 6.1, panel b) shows the results of the numeric *ab-initio* simulation and panel c) represents the experimental data already shown in figure 6.2. For this comparison the spectra obtained from theory are scaled in

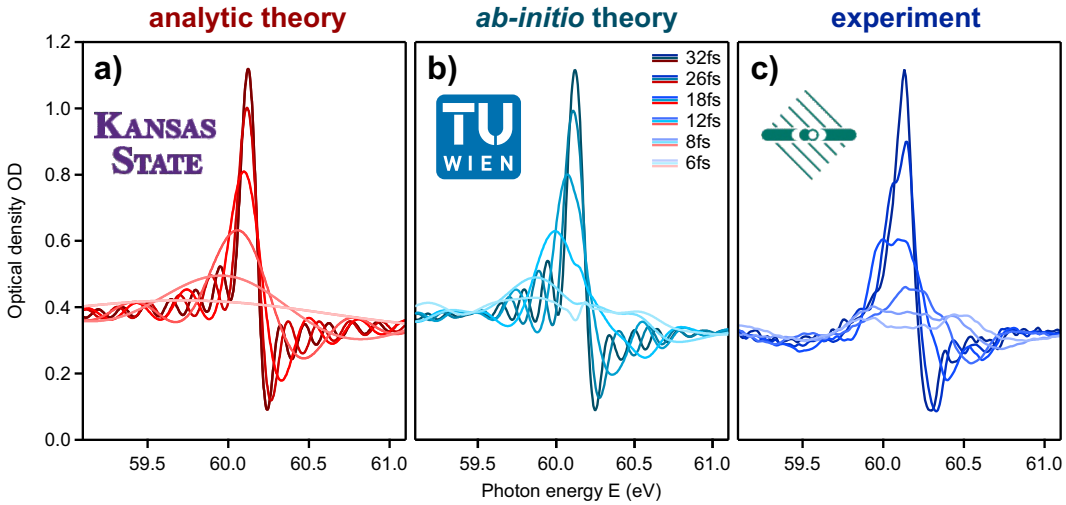

Figure 6.3.: **Comparison of the experimental data to *ab-initio* calculations and an analytic model for the Fano resonance:** a) Absorption spectra calculated using equation 6.1. b) Numerical *ab-initio* calculations for NIR pulses of 7 fs duration and peak intensity of $2 \cdot 10^{13}$ W/cm^2. c) Lineouts of the experimental data shown in figure 6.2. All spectra are plotted for a set of time-delay values indicated in the central panel. Figure adapted from [229].

amplitude with a delay-independent factor to match the experimental data. Furthermore, the closing of the gate in the *ab-initio* calculations and the experiment has a finite duration following the NIR pulse length, whereas the analytic model treats the depletion instantaneously. The effective beginning of the formation is not exactly at $\tau = 0$ in the experiment and therefore the data set obtained from analytic theory needs to be shifted by +4.5 fs in order to accurately compare it to both *ab-initio* and experimental results.
Comparing the three sets of spectral line shapes at different time delays shows very good agreement between experiment and the theoretical descriptions of the formation of the Fano resonance. The spectra match especially well for larger time-delay values where the exact shape of the NIR pulse and its finite duration does not affect the response as much as in the region of pulse overlap and shortly after. While the spectra also agree qualitatively for smaller time delays, with a broadened line shapes originating in the time-energy uncertainty relation, there remain differences especially between analytic theory and the experiment. On the one hand, the differences between *ab-initio* simulation and experimental data can be explained by the deviation of the exact experimental NIR pulse shape compared with the ideal Gaussian pulse used for the numeric calculation. On the other hand, the analytic theory deviates from the other two data sets most notably for small time delays, because in this region the strong NIR field significantly influences the excitation process by modifying the 2s2p state. Therefore, the simplified two-step picture of excitation and subsequent instantaneous depletion, as it is used in the analytic model, is no longer sufficiently accurate. This issue can be reduced by using even shorter NIR pulses which decreases the gate closing time and the region affected by pulse overlap effects. However, the overall agreement between experiment and *ab-initio* simulation proves that the time-dependent formation of the Fano resonance could be resolved using SFS and that the presented technique is viable for the observation of ultrafast correlated quantum

dynamics.
It has to be noted, that there is a complementary experiment using spectrally resolved electron interferometry [236]. Here, the buildup of a Fano resonance is resolved by measuring the amplitude and phase of a photoelectron wave packet created through a Fano resonance in helium.

6.3. Time-Resolved Buildup of a Rydberg Series

The previous section dealt with the time-dependent formation of a single Fano resonance. The presented technique, combined with the high-resolution spectrometer and *in-situ* reference measurement, can furthermore be used to study the buildup of a series of resonances belonging to highly excited and partly overlapping states. This can be used to study the formation of a continuum edge and how the coherent excitation of very closely spaced resonances belonging to highly correlated states influences their time-dependent formation.

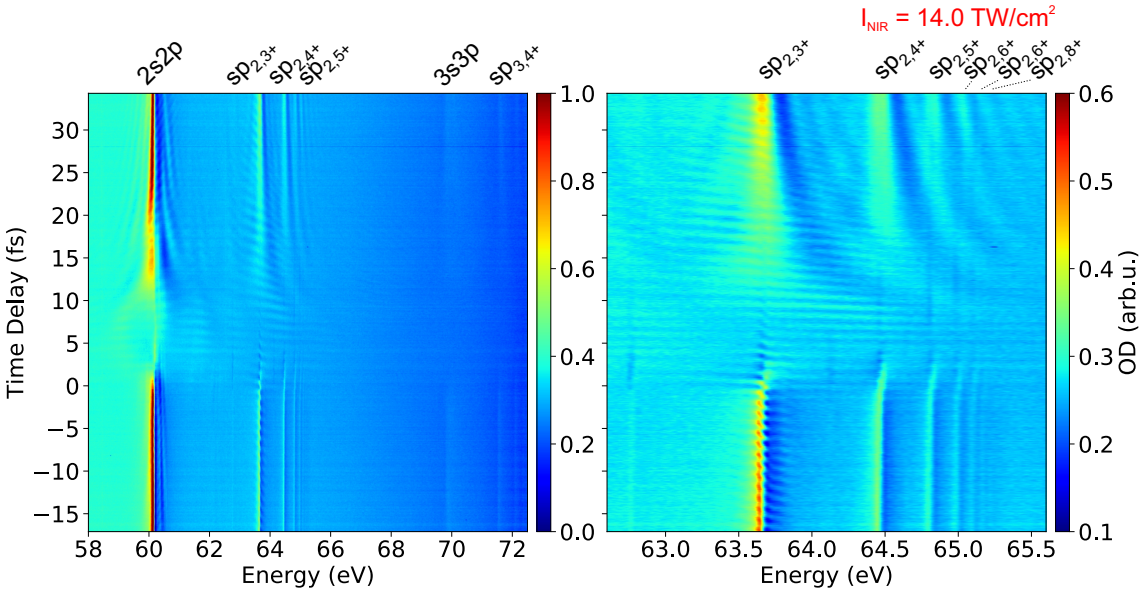

Figure 6.4.: **High-intensity time-delay scan of highly excited states in helium:** a) Full time-delay scan of the measured high-resolution absorption spectra for an intensity of 14.0 TW/cm^2. b) Zoom in along the energy axis on the $sp_{2,n+}$ Rydberg series. The spectral lines completely vanish for the chosen intensity around the time delay of 5 fs. This indicates the validity of the timing-gate approach.

6.3.1. High Resolution Time-Delay Scan

In order to study the formation of these highly excited resonances close to the continuum a measurement with high spectral and time-delay resolution, which additionally uses the *in-*

situ reference technique was carried out. The goal of this measurement is to examine how long it takes for a pair of highly excited states to be resolved into two separate resonances. In order for the time gate to be viable, NIR intensities of more than 10.0 TW/cm^2 need to be used as indicated by the calculations shown in figure 6.1 b). The measured time-delay scan for the intensity of 14.0 TW/cm^2 is shown in figure 6.4 a). In the time-delay region around $\tau = 5$ fs, shortly after the pulse overlap, the resonance lines of the highly excited states are already completely suppressed by the strong-field ionization during the NIR pulse. Again only a limited time-delay range up to $\tau = +31$ fs could be reached due to the delay mirror and focusing geometry. Neon at a backing pressure of 110 mbar is used as the conversion medium for HHG, while the helium pressure in the target is set at 75 mbar. The NIR pulse duration is again characterized using the dipole-control model [223] (see appendix C), which results in a pulse duration of $T_{NIR} = 5.7 \pm 0.1$ fs. Figure 6.4 b) shows a zoom-in of the data set along the energy axis. The Rydberg series of the $sp_{2,n+}$ states is visible up to $sp_{2,8+}$. For increasing time delay beyond 5 fs, the broad features become sharper and the spectral lines experience a slight shift towards lower energies, as the Stark shift introduced by the strong field of the NIR pulse affects the response of the bound state less (at a later time).

6.3.2. Comparison to Dipole Control Model

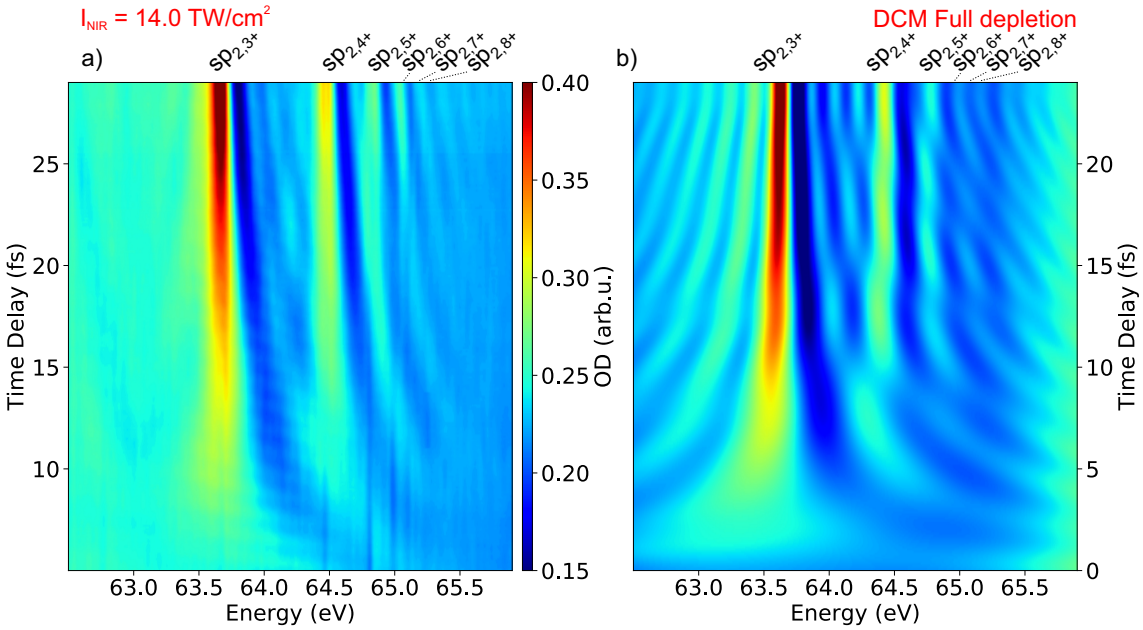

Figure 6.5.: **Comparison of the experimental data to a simulation using the dipole control model:** a) Zoom in on the observed buildup of the Rydberg series. b) Numerical calculations using the dipole control model which simulates the evolution of the dipole response that is cut off after a variable time delay τ.

As the goal is to examine the formation of partly overlapping resonances and pinpoint effects and changes in the buildup caused by interactions of different states or electron correlation, the measured data is compared to simulated spectra which use the dipole con-

trol model (DCM) [237]. In the framework of this model an initially excited response can be instantaneously cut off after a certain time delay which simulates the complete depletion of the states due to strong-field ionization via the experimental time-gating technique. The model treats all involved states completely independently, meaning that they influence each other only by optical interference in the spectrum and that no quantum or correlation effects are considered. This also implies, that the DCM does not include Stark shifts or coupling between bound and continuum states.
As it can be seen in section 5.3, the spectral lines exhibit rapid modifications of the line shape depending on the time delay. In order to compare experimental data and simulation results, these effects, originating in resonant coupling between the excited states have to be excluded, since they are not captured by the model. To this end, a cycle-averaged time-delay scan is considered, where a sliding average over one cycle of the NIR laser (time-delay range of 2.45 fs) is applied. Furthermore, because of the finite duration of the gating NIR pulse in the experiment compared to the delta like interaction in the DCM model, the experimental data has to be shifted by ~ 5 fs to allow for the correct comparison of the data. The correct delay value for the shift is determined by comparing the experimental spectrum at the latest time-delay of +31 fs to the DCM simulation and determining the best fit.
Comparing now the two data sets several differences appear. First the spectral lines in the experimental set appear shifted towards higher energies at small time delays. This is due to the Stark shift induced by the strong NIR pulse and does not show in the DCM as it is not included. Second, the spectral lines in the experiment seem to emerge faster and separate sooner than in the DCM, where this can be observed only for the lower states and at later time delays. This may be due to destrictive interference between the spectral amplitudes of the completely independently treated resonances in the DCM or interaction between the electrons which change the ionization behavior in the NIR pulse. As these effects are not included in the DCM the lines emerge at different time delays.

In order to quantify the evolution of amplitude, width and separability of the closely spaced resonances in the Rydberg series, the partly overlapping Fano resonances have to be characterized. This is done by tracking the maxima and minima of the Fano-like lineshape along the time-delay axis, as it is illustrated in figure 6.6. The function

$$F(E,E_r,\gamma,A,B,C) = A \cdot e^{-\frac{1}{2}\frac{(E-E_r)^2}{\gamma^2}} + E \cdot B + C, \tag{6.2}$$

is fitted to the extrema of the spectrum. Here, E is the energy, E_r is the energy position, γ is the width parameter, A is the amplitude while B and C parametrize a linear offset function. In the following, the Fano resonance is fitted with two Gaussians (maximum and minimum) as given in equation 6.2. The position, amplitude and width is tracked by using the n^{th} set of best fit parameters for the $(n+1)^{th}$ spectrum as initial guess parameters for the fit. With this method, the evolution of the pairs of maxima and minima belonging to each Fano resonance is tracked along the time-delay axis. In order to examine this evolution, an artificial measure to characterize the Fano resonance is introduced based on these fit parameters. Using the results of the minimum and maximum fit the Fano resonance is described by a Gaussian with the parameters A for the amplitude, Γ_{Fit} for the

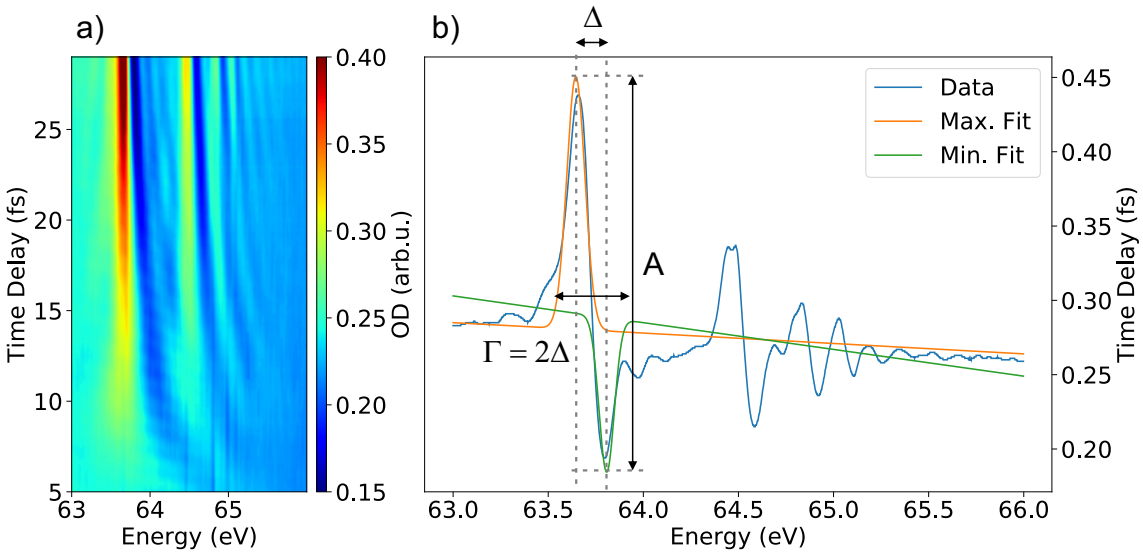

Figure 6.6.: **Tracking method of the resonances and the characterization of its widths:** a) Experimental data set of the Rydberg-series buildup. b) Illustration of the minimum and maximum peak fit used to trace the position, width and amplitude of the line shape.

width and E_R for the resonance position. The parameters for the state $\mathrm{sp}_{2,n+}$ are calculated from the fit results according to

$$A[sp_{2,n+}] = A_{Max}[sp_{2,n+}] - A_{Min}[sp_{2,n+}], \tag{6.3}$$
$$E_R[sp_{2,n+}] = (E_{r,Max}[sp_{2,n+}] + E_{r,Min}[sp_{2,n+}])/2, \tag{6.4}$$
$$\Delta_{Fit}[sp_{2,n+}] = (E_{r,Max}[sp_{2,n+}] - E_{r,Min}[sp_{2,n+}]), \tag{6.5}$$
$$\Gamma_{Fit} = 2\Delta_{Fit}. \tag{6.6}$$

The amplitude of the new measure is the difference between the amplitude of minimum and maximum, the energy position is the mean value and Γ_{Fit} was chosen as twice the energy separation of minimum and maximum. The reason for this is that for two Fano resonances to appear as separated, they need to be shifted by at least twice the separation of minimum and maximum. Otherwise the maximum of the second resonance would coincide with the minimum of the first, which would lead to the spectral amplitudes canceling each other and distorting the line shape. If equations 6.6 are applied to the fit results the data points in figure 6.7 a) are obtained for all states. Figure 6.7 b) shows a reference spectrum for negative time delay $\tau = -20$ fs, where the NIR pulse does not affect the spectral lines. Here, the error bars indicate the width characterized by Γ_{Fit}. Only the results for amplitudes $A[\mathrm{sp}_{2,n+}]$ greater than the spectral noise are plotted.

The spectral lines of all states become narrower and shift towards lower energies (their unperturbed energy positions) with increasing time delay. With the new measure the spectral lines can be defined as being separate if they are further apart than the mean value of their widths, or in other words, if the error bars in the plot do not overlap anymore. The

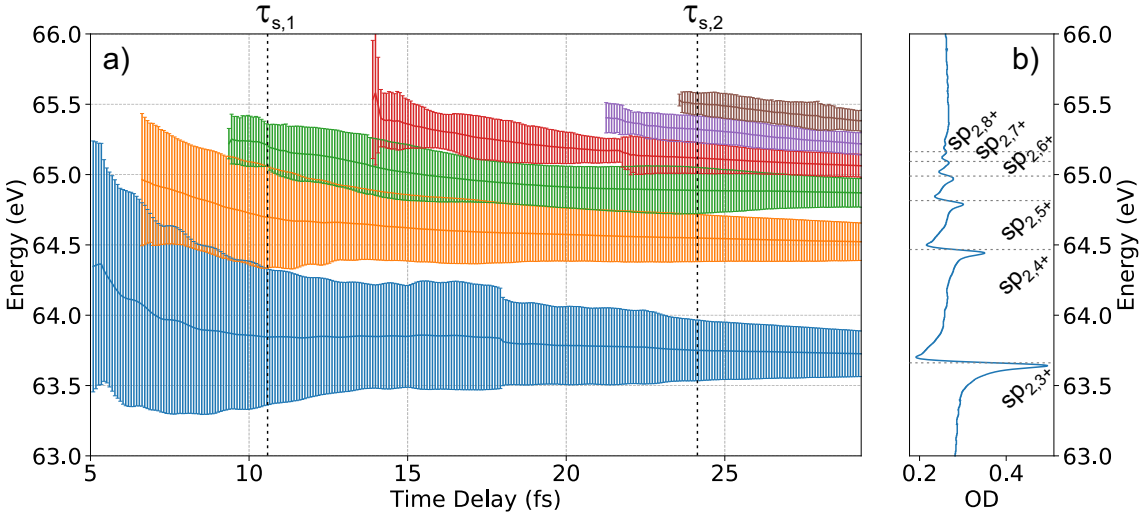

Figure 6.7.: **Analysis of the Rydberg series buildup:** a) Results of the fit algorithm in the form given by equations 6.6. The times $\tau_{s,i}$ indicate the points where spectral lines are separable for the first time during the buildup scan. b) Reference spectrum for $\tau = -20$ fs. For large positive time delays the spectral lines move towards their original position. However, for the higher-lying states the measurement of the buildup is difficult, as they partly overlap even for negative time-delays due to the insufficient spectrometer resolution.

time-delay values $\tau_{s,i}$ in figure 6.7 a) indicate the time delay where the lines become separated. This can be determined for the first two pairs of resonances ($sp_{2,3+}$, $sp_{2,4+}$) and ($sp_{2,4+}$, $sp_{2,5+}$). Unfortunately, due to the limited spectrometer resolution and time-delay range, these points could not be determined for the higher-lying resonances. For these states the resonances partly overlap even for negative time delays (or zero NIR intensity). Furthermore, figure 6.7 a) shows at which time delay the spectral lines are first discernible from the background noise. The lines appear later the closer the resonances are to the continuum. An explanation for this could be their respective proximity to the continuum or that they are more sensitive to the influence of the NIR pulse an thus the time $t = 0$ for the gating becomes different. Again, limited resolution for the higher states makes further statements about a relation between energy separation and emergence of the spectral lines very difficult. The results show that the measurement of the buildup of complex resonance structures can be achieved with the time gating technique. However, a higher spectral resolution and scanning to later delays is necessary in order to obtain for example a (possibly nonlinear) relation between relative resonance energy and time of spectral line separation, where this measurement was only able to contribute two data points. Additionally, also the preliminary measure for characterizing the evolution and separation of the Fano profiles needs to be further improved to better characterize the evolution of the resonance lines.

7. Conclusion and Outlook

The subject of this thesis is the study of nonlinear dynamics of two-electron quantum systems interacting with strong and short laser fields. To this end, the well established method of attosecond transient absorption spectroscopy with strong laser fields is applied and both experimentally and conceptually extended. This method, referred to as strong-field spectroscopy, uses the interaction with photons of an attosecond laser pulse as a probe to study ultrafast electron dynamics in bound excited states. Thus, the focus of this work lies on improving the quality of recording absorption spectra and developing methods to access time-resolved information from the obtained spectra, which is in turn applied to enhance our understanding of two-electron dynamics in external fields.

On the experimental side, the setup used to observe strong-field-induced dynamics is improved by a new technique to measure both absorption and reference spectra simultaneously. This is achieved using two-dimensional transmission gratings which effectively act as a beamsplitter for the XUV signal together with a specially designed target cell. In this way, the given experimental beam path can be maintained while measuring the spectra with the same high-resolution spectrometer. With this approach, the sensitivity to changes in the optical density due to the underlying electron dynamics can be increased by an order of magnitude. Furthermore, the *in-situ* reference allows for the accurate study of absorption effects in the continuum and the associated broad spectral features which were previously not accessible using sequentially recorded signal and reference or evaluation methods based on spectral filtering. However, due to the absorption of the grid and the losses into the unused diffraction orders the XUV flux is significantly decreased which increases measurement times. This could be even further improved by optimizing the grid layout of the transmission grating in the future. However, systematic changes in the XUV spectra that are connected to the longer measurement times are still effectively eliminated with the here developed technique of simultaneously measuring both the absorption and reference spectra.

With the experimental method for the reconstruction of the time-domain response developed in the framework of strong-field spectroscopy it is possible to extract the complex time-dependent dynamics of a quantum system induced by a general interaction from just a single absorption spectrum. The method is based on the causality properties of a response that is triggered by a laser pulse that is shorter than the time scales of all dynamics that have to be resolved. Using the inverse Fourier transform, the response can be reconstructed from the absorption spectrum using the equation

$$d(t) \propto \mathcal{F}^{-1}[iA(\omega)](t) = \frac{1}{\sqrt{2\pi}} \int iA(\omega)\, \mathrm{e}^{i\omega t}\, \mathrm{d}\omega \quad \text{for } t > 0. \tag{7.1}$$

Since no assumption about the characteristics of the interaction have been made aside from it being non-relativistic, the reconstruction method is very general and can thus be applied to complex systems with possibly overlapping resonances or absorption bands in large molecules interacting with strong laser fields. This was successfully demonstrated for a complex multi-level system. Furthermore, it is not limited to the interaction with electric fields and can be more generally applied for the reconstruction of non-equilibrium response functions of any kind of interaction, for example the magnetic dipole response, and across all spectral energy regions.
The reconstruction is successfully applied to the observation of Rabi cycling in doubly excited helium directly in the time domain. The reconstructed responses show very good agreement with full *ab-initio* calculations which solve the three-dimensional Schrödinger equation. It is also possible to observe the emergence of complexity in the driven dynamics of this system if the results are compared to more simple few-level simulations. Considering the technological aspect of light-matter interaction, it can be applied to the study of dynamic processes in laser machining, chemical dynamics, plasma dynamics and imaging of molecules which all involve (multiply) excited-state configurations as intermediate steps on the ultrafast femtosecond timescale. Regarding the aspect of the fundamental physics of few-electron dynamics, possible applications include the test and development of the theoretical description of many-electron quantum dynamics or the extraction of diagonal (populations) and off-diagonal (coherences) elements of the non-linearly driven density matrix. From the experimental point of view, the *in-situ* reference will further improve the reconstruction method, as the spectral profiles can be recorded with much more accuracy. In addition, the real-time-reconstruction approach is viable for single-shot detection of absorption spectra. This is especially interesting for absorption experiments at X-ray free electron lasers (FELs), because their high brilliance provides pulses with enough photons to get a complete absorption spectrum with a single shot, as compared to HHG sources where absorption spectra are typically accumulated over many pulses. At FELs, the reconstruction could thus be used to determine the timing and ensuing dynamics of X-ray and optical pulses, which is otherwise often lost due to temporal jitter. Also for the FEL application it would be very interesting to combine this approach with an *in-situ* reference measurement, as it is otherwise very difficult to extract the accurate absorption signals due to the stochastic nature of the pulse spectra originating in the self-amplified spontaneous emission in the pulse generation process. With all this combined, the here presented methods could thus open up a completely new approach to apply time-resolved x-ray absorption spectroscopy for the study of few-electron dynamics in small quantum systems.
Moreover, the method of strong-field spectroscopy is used to study the time-dependent evolution of the response of excited-state manifolds with different correlation properties. Again, helium serves as the most simple model target with two excited electrons, where the $\mathrm{sp}_{2,n\pm}$ series are studied. In this measurement, the *in-situ* reference greatly improved the sensitivity to spectral signatures and enabled the observation of the dynamical changes in the $\mathrm{sp}_{2,n-}$ series which only appears weakly in the absorption spectrum. This series shows significantly different behavior compared to the $\mathrm{sp}_{2,n+}$ series with abrupt phase and amplitude changes at time delay $\tau = 0$ which seem to originate in the different correlation properties. As a first attempt of an explanation the different polarizability of the involved multi-electron configurations is proposed. It is however necessary to conduct

detailed theoretical calculations and further measurements with higher spectral resolution in order to study this interesting behavior in more detail.

The presented technique of imposing a time gate on the coherent dipole response using saturated ionization in a strong and short laser field can be used to study the buildup of various dynamic processes of short-lived bound states which are observable using photon absorption spectroscopy. The method is applied to measure the time-dependent buildup of a Fano resonance which agrees very well with the analytical and numerical theoretical predictions. Furthermore the buildup of a Rydberg series of Fano resonances, a more complex resonance structure, was experimentally observed using the *in-situ* reference. While this measurement demonstrates that the time-gating technique is also viable for this complex resonance structure and provides first insights into the time-dependent emergence of such closely spaced states near the continuum threshold, further studies with improved resolution are necessary, in order to fully understand the physics involved in its formation. In the future, possible targets for buildup studies are resonances originating in electron-electron or electron-internuclear correlations in complex systems such as molecules, liquids or solids, or the signatures belonging to quasi particles in crystal structures.

A. Atomic Units

The system of atomic units is frequently used in the field of atomic and molecular physics. It is relates the physical quantities to the scales defined by the physical properties of the hydrogen atom. The following conventions $m_\mathrm{e} = e = \hbar = a_0 = \frac{1}{4\pi\varepsilon_0} = 1$ are used in this system. Table A.1 gives the basic physical quantities, their atomic units and the respective values in SI units. More information about the system of atomic units can be found in [85].

Quantity	Unit	Value
Mass	Electron mass m_e	$9.109 \times 10^{-31}\,\mathrm{kg}$
Charge	Elementary charge e	$1.602 \times 10^{-19}\,\mathrm{C}$
Angular momentum	Reduced Planck constant $\hbar$	$1.055 \times 10^{-34}\,\mathrm{J\,s}$
Length	First Bohr radius a_0	$5.292 \times 10^{-11}\,\mathrm{m}$
Velocity	$v_0 = \alpha c_0$	$2.188 \times 10^{6}\,\mathrm{m\,s^{-1}}$
Momentum	$p_0 = m_\mathrm{e} v_0$	$1.993 \times 10^{-24}\,\mathrm{kg\,m\,s^{-1}}$
Time	$\frac{a_0}{v_0}$	$2.419 \times 10^{-17}\,\mathrm{s}$
Energy	$E_\mathrm{h} = \frac{e^2}{4\pi\varepsilon_0 a_0} = \alpha^2 m_\mathrm{e} {c_0}^2$	$4.360 \times 10^{-18}\,\mathrm{J}$=27.2114 eV
Electric potential	$E_\mathrm{h}/e = \frac{e}{4\pi\varepsilon_0 a_0}$	27.2114 V
Electric field	$E_0 = \frac{e}{4\pi\varepsilon_0 {a_0}^2}$	$5.142 \times 10^{11}\,\mathrm{V\,m^{-1}}$
(Laser) Intensity	$I_0 = \frac{1}{2}\varepsilon_0 c_0 E_0^2$	$3.509 \times 10^{16}\,\mathrm{W\,cm^{-2}}$

Table A.1.: Relationship between physical quantities in the system of atomic units and the SI.

B. Numerical Simulations of Helium: Equations of Motion

B.1. Few-Level Model

The few-level model of an atomic system does not treat the time evolution of the full wave function and thus requires several input parameters like state energies, natural state life times, configuration interaction strengths and dipole transition moments for the dipole coupling terms which are proportional to the electric fields. These parameters are listed below for the model of doubly excited helium described in section 3.1. Table B.1 shows the dipole matrix elements between the bound states taken from theoretical *ab-initio* calculations which are used in the calculations.

DTM [a.u.]	$2s^2$	2s2p	$2p^2$	$sp_{2,3+}$
$2s^2$	0	-1.56	0	approx. 0
2s2p	-1.56	0	2.17	0
$2p^2$	0	2.17	0	-0.81
$sp_{2,3+}$	approx. 0	0	-0.81	0

Table B.1.: Dipole transition moments (DTM) in atomic units for the discrete states included in the few-level model calculation

The equations of motion that are solved for the discrete level model of helium are the coupled differential equations below. The result from the Schrödinger equation with the state vector expanded in the discrete basis modeled after the energy levels of doubly excited helium:

$$i\partial_t \begin{pmatrix} c_g \\ c_a \\ c_b \\ c_c \\ c_d \\ c_{\varepsilon p} \\ c_{\varepsilon s} \end{pmatrix} = \begin{pmatrix} E_g & 0 & 0 & 0 & 0 & 0 & 0 \\ 0 & E_a & -\mu_{ab}\mathcal{E}_{NIR}(t) & 0 & 0 & 0 & V_{c,\varepsilon s} \\ -\mu^*_{gb}\mathcal{E}^+_{XUV}(t) & -\mu^*_{ab}\mathcal{E}_{NIR}(t) & E_b & -\mu_{bc}\mathcal{E}_{NIR}(t) & 0 & V_{b,\varepsilon p} & 0 \\ 0 & 0 & -\mu^*_{bc}\mathcal{E}_{NIR}(t) & E_c - i\alpha_3 I^3_{NIR}(t) & -\mu_{cd}\mathcal{E}_{NIR}(t) & 0 & V_{c,\varepsilon s} \\ -\mu^*_{gd}\mathcal{E}^+_{XUV}(t) & 0 & 0 & -\mu^*_{cd}\mathcal{E}_{NIR}(t) & E_d - i\alpha_2 I^2_{NIR}(t) & V_{d,\varepsilon p} & 0 \\ -\mu^*_{g,\varepsilon p}\mathcal{E}^+_{XUV}(t) & 0 & V^*_{b,\varepsilon p} & 0 & V^*_{d,\varepsilon p} & p^2/2 - i\Gamma_{\varepsilon p} & 0 \\ 0 & V_{c,\varepsilon s} & 0 & V^*_{c,\varepsilon s} & 0 & 0 & p^2/2 - i\Gamma_{\varepsilon s} \end{pmatrix} \begin{pmatrix} c_g \\ c_a \\ c_b \\ c_c \\ c_d \\ c_{\varepsilon p} \\ c_{\varepsilon s} \end{pmatrix} \tag{B.1}$$

B.2. Few-Level Model for Complex Systems

Figure 5.3 in the main text the response reconstruction for complex systems like biologically relevant molecules or solids is discussed. In order to emulate such a system, a few-level system consisting of a ground state and $n = 50$ excited states with randomized energies in the range between 60 eV to 65 eV and linewidths randomized between 0.5 meV to 30 meV is constructed. The dipole matrix elements between the states are also randomized between -1 a.u. and 1 a.u. including matrix elements to the ground state. No symmetries and thus no dipole selection rules are considered. The randomized Hamiltonian of such a system in atomic units reads:

$$H_{rand} = \begin{pmatrix} 0 & 0.502\,\mathcal{E}_{XUV}(t) & -0.394\,\mathcal{E}_{XUV}(t) & \cdots & 0.884\,\mathcal{E}_{XUV}(t) \\ 0.502\,\mathcal{E}_{XUV}(t) & 2.229-0.012i & -0.940\,\mathcal{E}_{NIR}(t) & \cdots & 0.750\,\mathcal{E}_{NIR}(t) \\ -0.394\,\mathcal{E}_{XUV}(t) & -0.940\,\mathcal{E}_{NIR}(t) & 2.311-0.025i & \cdots & 0.535\,\mathcal{E}_{NIR}(t) \\ \vdots & \vdots & \vdots & \ddots & \vdots \\ 0.884\,\mathcal{E}_{XUV}(t) & 0.750\,\mathcal{E}_{NIR}(t) & 0.535\,\mathcal{E}_{NIR}(t) & \cdots & 2.303-0.091i \end{pmatrix}. \tag{B.2}$$

The system is propagated in time according to the description given in section 3.1.

C. NIR Pulse Characterization

C.1. Response Reconstruction and Fano Resonance Buildup Measurements

C.1.1. Temporal Characterization

The older measurements used for the application of the response reconstruction discussed in section 5.2 and the study of the time-resolved buildup of a Fano resonance were recorded using the same pulse parameters. The duration of the near-infrared pulse interacting with the target in these experiments were extracted from the data sets using the method described in [223]. Here, the dipole-control model developed in [237], Eq. (5), is fitted to the absorption line profile of a doubly excited state close to the $N = 2$ continuum. The assumption is that these highly excited states experience phase changes due to ponderomotive shifts in the NIR field.

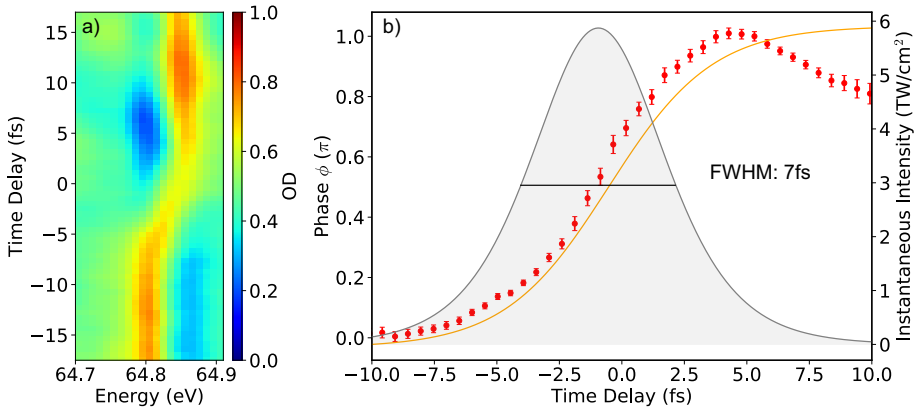

Figure C.1.: **NIR pulse temporal characterization for Response Reconstruction** a) Measured, cycle-averaged absorption spectra depending on the time delay for the $sp_{2,5+}$ Fano resonance. The dressing with the NIR pulse causes a transient ponderomotive shift. b) phase change induced by the NIR pulse extracted form the data (red). A fit with an integrated sech^2 profile (orange) yields the characterization of the pulse shape. The pulse envelope is given by the derivative of this fit (gray). For this measurement a pulse duration of $T_{NIR} = 7.0 \pm 0.2$ fs is recovered. The time delay axis is given for a first estimation of the pulse overlap using data from experimental alignment. Using the pulse position in this fit it can be calibrated more accurately.

This change is dependent on the intensity and can be recovered from the changes in line

shape which are quantified in the fit. The pulse shape is given by the derivative of this phase change. The results of the evaluation for this measurement are given in figure C.1. The position of the phase change (significant contributions for $\tau < 0$) was afterwards used to better calibrate the pulse overlap $\tau = 0$ along the time-delay axis.

C.1.2. Intensity Calibration

The intensity calibration for these measurements was performed by comparing the reconstructed responses presented in section 5.2 with full ab-initio numerical simulations with known NIR intensity.

C.2. $sp_{2,n\pm}$ and Rydberg Buildup Measurements

C.2.1. Temporal Characterization

For the high-resolution scan which also uses the in situ reference method the following NIR pulse duration was extracted using the technique described above [223]. The results of the evaluation for this measurement are given in figure C.1.

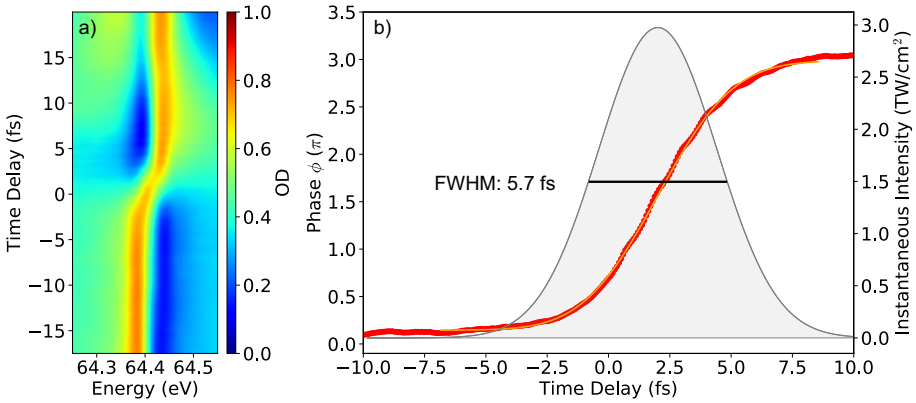

Figure C.2.: **NIR pulse temporal characterization for $sp_{2,n\pm}$ measurement** a) Measured, cycle-averaged absorption spectra depending on the time delay for the $sp_{2,4+}$ Fano resonance. The dressing with the NIR pulse causes a transient ponderomotive shift. b) phase change induced by the NIR pulse extracted form the data (red). A fit with an integrated sech^2 profile (orange) yields the characterization of the pulse shape. The pulse envelope is given by the derivative of this fit (gray). For this measurement a pulse duration of $T_{NIR} = 5.7 \pm 0.1$ fs is recovered.

C.2.2. Intensity Calibration

In general the determination of the exact pulse intensity in the focus of the target cell is very challenging without using a streaking measurement. An estimated intensity cali-

bration for the NIR pulses in this measurement was performed by determining the energy difference in the Autler–Townes (AT) splitting and calculating the NIR field strength from the equation

$$\mathcal{E} = \frac{\sqrt{\Delta E_{AT}^2 - \Delta^2}}{d_{2s2p,2p^2}}. \tag{C.1}$$

Here, ΔE_{AT} is the energy difference between the two energy positions of the spectral maxima of the AT splitting, Δ is the detuning of the laser with respect to the transition between the $2s2p$ and $2p^2$ states. The photon energy is extracted from the fast modulation across the spectral lines in the time-delay scans for moderate intensities. These modulations occur at twice the laser frequency [127, 216]. The transition dipole matrix element $d_{2s2p,2p^2} = 2.17$ a.u. is taken from numerical calculations (section 3.1). The position of the maxima are fitted from the data presented in figure C.3 a). The results of the calculation following equation C.1 including a unit conversion into intensity are shown in figure C.3 b). This plot gives the calibration curve of the intensity depending on the position of the NIR iris aperture. Because of the uncertainty in photon energy, pulse duration and position of the spectral maxima, the error is estimated to be 20%.

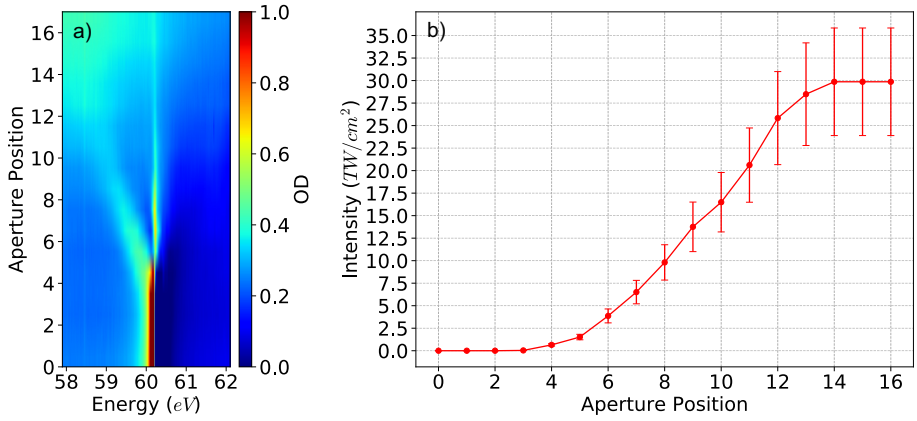

Figure C.3.: **NIR pulse intensity calibration for $sp_{2,n\pm}$ measurement** a) Measured, cycle-averaged absorption spectra depending on the NIR iris aperture position for the $2s2p$ Fano resonance. The dressing with the NIR pulse causes the Autler–Townes splitting observed on the left of the resonance. b) Calibration curve for the NIR intensity depending on aperture position.

The AT calibration method is applicable even for higher intensities because the new reference measurement method is sensitive to very weak spectral signatures.

Bibliography

[1] E. Muybridge.
Sallie Gardner at a Gallop (The Horse in Motion).
Photography, San Francisco Museum (1878).

[2] L. Dahlström.
Passive mode-locking and Q-switching of high power lasers by means of the optical Kerr effect.
Optics Communications **5**, 157 – 162 (1972).
URL http://www.sciencedirect.com/science/article/pii/0030401872900557.

[3] A. Baltuška, T. Udem, M. Uiberacker, M. Hentschel, E. Goulielmakis, C. Gohle, R. Holzwarth, V. S. Yakovlev, A. Scrinzi, T. W. Hänsch, and F. Krausz.
Attosecond control of electronic processes by intense light fields.
Nature **421**, 611–615 (2003).

[4] A. L. Cavalieri, E. Goulielmakis, B. Horvath, W. Helml, M. Schultze, M. Fiess, V. Pervak, L. Veisz, V. S. Yakovlev, M. Uiberacker, A. Apolonski, F. Krausz, and R. Kienberger.
Intense 1.5-cycle near infrared laser waveforms and their use for the generation of ultra-broadband soft-x-ray harmonic continua.
New J. Phys. **9** (2007).

[5] E. Goulielmakis, M. Schultze, M. Hofstetter, V. S. Yakovlev, J. Gagnon, M. Uiberacker, A. L. Aquila, E. M. Gullikson, D. T. Attwood, R. Kienberger, F. Krausz, and U. Kleineberg.
Single-Cycle Nonlinear Optics.
Science **320**, 1614–1617 (2008).
URL http://science.sciencemag.org/content/320/5883/1614.

[6] A. H. Zewail.
Laser Femtochemistry.
Science **242**, 1645–1653 (1988).
URL http://science.sciencemag.org/content/242/4886/1645.

[7] A. Mcpherson, G. Gibson, H. Jara, U. Johann, T. S. Luk, I. A. Mcintyre, K. Boyer, and C. K. Rhodes.
Studies of Multiphoton Production of Vacuum Ultraviolet-Radiation in the Rare-Gases.
J. Opt. Soc. Am. B **4**, 595–601 (1987).

[8] M. Ferray, A. L'Huillier, X. F. Li, L. A. Lompre, G. Mainfray, and C. Manus.
Multiple-harmonic conversion of 1064 nm radiation in rare gases.

Journal of Physics B: Atomic, Molecular and Optical Physics **21**, L31 (1988).
URL http://stacks.iop.org/0953-4075/21/i=3/a=001.

[9] P. B. Corkum.
Plasma perspective on strong field multiphoton ionization.
Phys. Rev. Lett. **71**, 1994–1997 (Sep 1993).
URL
http://link.aps.org/doi/10.1103/PhysRevLett.71.1994.

[10] K. C. Kulander, K. J. Schafer, and J. L. Krause.
In B. Piraux (Ed.), *Proceedings of the Work-shop on Super-Intense Laser Atom Physics (SILAP) III*, pp. 95–110. Plenum Press, New York (1993).

[11] B. P. e. a. Abbott.
Observation of Gravitational Waves from a Binary Black Hole Merger.
Phys. Rev. Lett. **116**, 061102 (Feb 2016).
URL https:
//link.aps.org/doi/10.1103/PhysRevLett.116.061102.

[12] J. B. J. Fourier.
Théorie analytique de la chaleur.
Firmin Didot, Paris (1822).

[13] W. Heisenberg.
Über den anschaulichen Inhalt der quantentheoretischen Kinematik und Mechanik.
Zeitschrift für Physik **43**, 172–198 (Mar 1927).
URL https://doi.org/10.1007/BF01397280.

[14] T. Brabec and F. Krausz.
Intense few-cycle laser fields: Frontiers of nonlinear optics.
Rev. Mod. Phys. **72**, 545–591 (Apr 2000).
URL https://link.aps.org/doi/10.1103/RevModPhys.72.545.

[15] P. Agostini and L. F. DiMauro.
The physics of attosecond light pulses.
Reports on Progress in Physics **67**, 813 (2004).
URL http://stacks.iop.org/0034-4885/67/i=6/a=R01.

[16] F. Krausz and M. Ivanov.
Attosecond physics.
Rev. Mod. Phys. **81**, 163–234 (Feb 2009).
URL https://link.aps.org/doi/10.1103/RevModPhys.81.163.

[17] J.-C. Diels and W. Rudolph.
Ultrashort Laser Pulse Phenomena.
Second Edition. Academic Press (2006).

[18] B. E. A. Saleh and M. C. Teich.
Fundamentals of Photonics.
Second Edition. Wiley (2007).

[19] Z. Chang.
Fundamentals of Attosecond Optics.
CRC Press (2011).

[20] R. Szipocs, K. Ferencz, C. Spielmann, and F. Krausz.
Chirped Multilayer Coatings for Broad-Band Dispersion Control in Femtosecond

Lasers.
Opt. Lett. **19**, 201–203 (1994).

[21] A. Assion, T. Baumert, M. Bergt, T. Brixner, B. Kiefer, V. Seyfried, M. Strehle, and G. Gerber.
Control of chemical reactions by feedback-optimized phase-shaped femtosecond laser pulses.
Science **282**, 919–922 (1998).

[22] A. M. Weiner.
Ultrafast optical pulse shaping: A tutorial review.
Optics Communications **284**, 3669 – 3692 (2011).
URL http://www.sciencedirect.com/science/article/pii/S0030401811003750.
Special Issue on Optical Pulse Shaping, Arbitrary Waveform Generation, and Pulse Characterization.

[23] C. Spielmann, P. F. Curley, T. Brabec, and F. Krausz.
Ultrabroadband Femtosecond Lasers.
IEEE J. Quantum Electron. **30**, 1100–1114 (1994).

[24] A. Stingl, R. Szipöcs, M. Lenzner, C. Spielmann, and F. Krausz.
Sub-10-fs mirror-dispersion-controlled Ti:sapphire laser.
Opt. Lett. **20**, 602–604 (Mar 1995).
URL http://ol.osa.org/abstract.cfm?URI=ol-20-6-602.

[25] H. W. Mocker and R. J. Collins.
Mode competition and self-locking effects in a q-switched ruby laser.
Applied Physics Letters **7**, 270–273 (1965).
URL http://dx.doi.org/10.1063/1.1754253.

[26] J.-C. Diels and W. Rudolph.
5 - Ultrashort Sources I: Fundamentals.
In J.-C. Diels and W. Rudolph (Eds.), *Ultrashort Laser Pulse Phenomena (Second Edition)*, second edition edition, pp. 277 – 339. Academic Press, Burlington (2006).
URL http://www.sciencedirect.com/science/article/pii/B9780122154935500069.

[27] M. Wollenhaupt, A. Assion, and T. Baumert.
Short and Ultrashort Laser Pulses.
In F. Träger (Ed.), *Springer Handbook of Lasers and Optics*, chapter 12, pp. 1047–1094. Springer Berlin Heidelberg, Berlin, Heidelberg (2012).
URL http://dx.doi.org/10.1007/978-3-642-19409-2_12.

[28] R. W. Boyd.
Chapter 4 - The Intensity-Dependent Refractive Index.
In R. W. Boyd (Ed.), *Nonlinear Optics (Third Edition)*, third edition edition, pp. 207 – 252. Academic Press, Burlington (2008).
URL http://www.sciencedirect.com/science/article/pii/B9780123694706000046.

[29] P. Georges, F. Estable, F. Salin, J. P. Poizat, P. Grangier, and A. Brun.
High-efficiency multipass Ti:sapphire amplifiers for a continuous-wave single-mode laser.

Opt. Lett. **16**, 144–146 (Feb 1991).
URL http://ol.osa.org/abstract.cfm?URI=ol-16-3-144.

[30] R. H. Stolen and C. Lin.
Self-phase-modulation in silica optical fibers.
Phys. Rev. A **17**, 1448–1453 (Apr 1978).
URL https://link.aps.org/doi/10.1103/PhysRevA.17.1448.

[31] D. H. Sutter, G. Steinmeyer, L. Gallmann, N. Matuschek, F. Morier-Genoud, U. Keller, V. Scheuer, G. Angelow, and T. Tschudi.
Semiconductor saturable-absorber mirror–assisted Kerr-lens mode-locked Ti:sapphire laser producing pulses in the two-cycle regime.
Opt. Lett. **24**, 631–633 (May 1999).
URL http://ol.osa.org/abstract.cfm?URI=ol-24-9-631.

[32] U. Morgner, F. X. Kärtner, S. H. Cho, Y. Chen, H. A. Haus, J. G. Fujimoto, E. P. Ippen, V. Scheuer, G. Angelow, and T. Tschudi.
Sub-two-cycle pulses from a Kerr-lens mode-locked Ti:sapphire laser.
Opt. Lett. **24**, 411–413 (Mar 1999).
URL http://ol.osa.org/abstract.cfm?URI=ol-24-6-411.

[33] S. Kim, J. Jin, Y.-J. Kim, I.-Y. Park, Y. Kim, and S.-W. Kim.
High-harmonic generation by resonant plasmon field enhancement.
Nature **453**, 757–760 (June 2008).
URL http://dx.doi.org/10.1038/nature07012.

[34] A. Vernaleken, J. Weitenberg, T. Sartorius, P. Russbueldt, W. Schneider, S. L. Stebbings, M. F. Kling, P. Hommelhoff, H.-D. Hoffmann, R. Poprawe, F. Krausz, T. W. Hänsch, and T. Udem.
Single-pass high-harmonic generation at 20.8 MHz repetition rate.
Opt Lett **36**, 3428–3430 (Sep 2011).

[35] D. Strickland and G. Mourou.
Compression of amplified chirped optical pulses.
Optics Communications **56**, 219 – 221 (1985).
URL http://www.sciencedirect.com/science/article/pii/0030401885901208.

[36] M. Nisoli, S. De Silvestri, and O. Svelto.
Generation of high energy 10 fs pulses by a new pulse compression technique.
Appl. Phys. Lett. **68**, 2793–2795 (1996).

[37] M. Nisoli, S. DeSilvestri, O. Svelto, R. Szipocs, K. Ferencz, C. Spielmann, S. Sartania, and F. Krausz.
Compression of high-energy laser pulses below 5 fs.
Opt. Lett. **22**, 522–524 (1997).

[38] C. P. Hauri, A. Guandalini, P. Eckle, W. Kornelis, J. Biegert, and U. Keller.
Generation of intense few-cycle laser pulses through filamentation - parameter dependence.
Opt. Express **13**, 7541–7547 (2005).

[39] A. Couairon, J. Biegert, C. Hauri, W. Kornelis, F. Helbing, U. Keller, and A. Mysyrowicz.
Self-compression of ultra-short laser pulses down to one optical cycle by filamentation.

Journal of Modern Optics **53**, 75–85 (2006).

[40] H. Timmers, Y. Kobayashi, K. F. Chang, M. Reduzzi, D. M. Neumark, and S. R. Leone.
Generating high-contrast, near single-cycle waveforms with third-order dispersion compensation.
Opt. Lett. **42**, 811–814 (Feb 2017).
URL http://ol.osa.org/abstract.cfm?URI=ol-42-4-811.

[41] J. Sung, J. Park, T. Imran, Y. Lee, and C. Nam.
Generation of 0.2-TW 5.5-fs optical pulses at 1ăkHz using a differentially pumped hollow-fiber chirped-mirror compressor.
Applied Physics B **82**, 5–8 (Jan 2006).
URL https://doi.org/10.1007/s00340-005-2005-0.

[42] Z. Wei, T. Hao, Y. Chen-Xia, Z. Xin, H. Xun, and W. Zhi-Yi.
Generation of Sub-2 Cycle Optical Pulses with a Differentially Pumped Hollow Fiber.
Chinese Physics Letters **27**, 054211 (2010).
URL http://stacks.iop.org/0256-307X/27/i=5/a=054211.

[43] R. Baumgartner and R. Byer.
Optical parametric amplification.
IEEE Journal of Quantum Electronics **15**, 432–444 (June 1979).

[44] A. Dubietis, R. Butkus, and A. P. Piskarskas.
Trends in chirped pulse optical parametric amplification.
IEEE J. Sel. Top. Quantum Electr. **12**, 163–172 (2006).

[45] C. Manzoni, O. D. Mücke, G. Cirmi, S. Fang, J. Moses, S.-W. Huang, K.-H. Hong, G. Cerullo, and F. X. Kärtner.
Coherent pulse synthesis: towards sub-cycle optical waveforms.
Laser & Photonics Reviews **9**, 129–171 (2015).
URL http://dx.doi.org/10.1002/lpor.201400181.

[46] D. N. Fittinghoff, P. R. Bolton, B. Chang, and K. C. Kulander.
Observation of Nonsequential Double Ionization of Helium with Optical Tunneling.
Phys. Rev. Lett. **69**, 2642–2645 (1992).

[47] A. Einstein.
Über einen die Erzeugung und Verwandlung des Lichtes betreffenden heuristischen Gesichtspunkt.
Annalen der Physik **322**, 132–148 (1905).
URL http://dx.doi.org/10.1002/andp.19053220607.

[48] S. Augst, D. D. Meyerhofer, D. Strickland, and S. L. Chin.
Laser Ionization of Noble-Gases by Coulomb-Barrier Suppression.
J. Opt. Soc. Am. B **8**, 858–867 (1991).

[49] L. V. Keldysh.
Ionization in the field of a strong electromagnetic wave.
Soviet Physics JETP **20**, 1307 (1965).
URL http:
//www.jetp.ac.ru/cgi-bin/e/index/e/20/5/p1307?a=list.

[50] A. M. Perelomov, V. S. Popov, and M. V. Terent'ev.

Ionization of atoms in an alternating electric field.
Soviet Physics JETP **23**, 924–934 (1966).
URL http:
//www.jetp.ac.ru/cgi-bin/e/index/e/23/5/p924?a=list.

[51] M. Protopapas, C. H. Keitel, and P. L. Knight.
Atomic physics with super-high intensity lasers.
Reports on Progress in Physics **60**, 389 (1997).
URL http://stacks.iop.org/0034-4885/60/i=4/a=001.

[52] V. S. Popov.
Tunnel and multiphoton ionization of atoms and ions in a strong laser field (Keldysh theory).
Physics-Uspekhi **47**, 855 (2004).
URL http://stacks.iop.org/1063-7869/47/i=9/a=R01.

[53] F. Fabre, G. Petite, P. Agostini, and M. Clement.
Multiphoton above-threshold ionisation of xenon at 0.53 *and* 1.06 µm.
Journal of Physics B: Atomic and Molecular Physics **15**, 1353 (1982).
URL http://stacks.iop.org/0022-3700/15/i=9/a=012.

[54] P. Agostini, F. Fabre, G. Mainfray, G. Petite, and N. K. Rahman.
Free-Free Transitions Following Six-Photon Ionization of Xenon Atoms.
Phys. Rev. Lett. **42**, 1127–1130 (Apr 1979).
URL
http://link.aps.org/doi/10.1103/PhysRevLett.42.1127.

[55] M. V. Ammosov, N. B. Delone, and V. P. Krainov.
Tunnel ionization of complex atoms and of atomic ions in an alternating electromagnetic field.
Soviet Physics JETP **64**, 1191–1194 (1986).
URL http:
//www.jetp.ac.ru/cgi-bin/e/index/e/64/6/p1191?a=list.

[56] A. M. Perelomov, V. S. Popov, and M. V. Terent'ev.
Ionization of atoms in an alternating electric field II.
Soviet Physics JETP **24**, 207–217 (1967).
URL http:
//www.jetp.ac.ru/cgi-bin/e/index/e/24/1/p207?a=list.

[57] A. M. Perelomov and V. S. Popov.
Ionization of atoms in an alternating electric field III.
Soviet Physics JETP **25**, 336–343 (1967).
URL http:
//www.jetp.ac.ru/cgi-bin/e/index/e/25/2/p336?a=list.

[58] G. L. Yudin and M. Y. Ivanov.
Nonadiabatic tunnel ionization: Looking inside a laser cycle.
Phys. Rev. A **6401**, 013409 (2001).

[59] N. Camus, E. Yakaboylu, L. Fechner, M. Klaiber, M. Laux, Y. Mi, K. Z. Hatsagortsyan, T. Pfeifer, C. H. Keitel, and R. Moshammer.
Experimental Evidence for Quantum Tunneling Time.
Phys. Rev. Lett. **119**, 023201 (Jul 2017).
URL https:

//link.aps.org/doi/10.1103/PhysRevLett.119.023201.

[60] T. Popmintchev, M.-C. Chen, D. Popmintchev, P. Arpin, S. Brown, S. Alisauskas, G. Andriukaitis, T. Balciunas, O. D. Mücke, A. Pugzlys, A. Baltuska, B. Shim, S. E. Schrauth, A. Gaeta, C. Hernández-García, L. Plaja, A. Becker, A. Jaron-Becker, M. M. Murnane, and H. C. Kapteyn.
Bright coherent ultrahigh harmonics in the keV x-ray regime from mid-infrared femtosecond lasers.
Science **336**, 1287–1291 (Jun 2012).
URL http://dx.doi.org/10.1126/science.1218497.

[61] K. Zhao, Q. Zhang, M. Chini, Y. Wu, X. Wang, and Z. Chang.
Tailoring a 67 attosecond pulse through advantageous phase-mismatch.
Opt. Lett. **37**, 3891–3893 (Sep 2012).
URL http://ol.osa.org/abstract.cfm?URI=ol-37-18-3891.

[62] T. Gaumnitz, A. Jain, Y. Pertot, M. Huppert, I. Jordan, F. Ardana-Lamas, and H. J. Wörner.
Streaking of 43-attosecond soft-X-ray pulses generated by a passively CEP-stable mid-infrared driver.
Opt. Express **25**, 27506–27518 (Oct 2017).
URL http://www.opticsexpress.org/abstract.cfm?URI=oe-25-22-27506.

[63] P. Jaegle.
Coherent Sources of XUV Radiation.
Springer, New York (2006).

[64] T. Brabec (Ed.).
Strong field laser physics.
Springer series in optical sciences. Springer (2008).

[65] K. J. Schafer, B. Yang, L. F. DiMauro, and K. C. Kulander.
Above Threshold Ionization Beyond the High Harmonic Cutoff.
Phys. Rev. Lett. **70**, 1599–1602 (1993).

[66] M. Lewenstein, P. Balcou, M. Y. Ivanov, A. L'Huillier, and P. B. Corkum.
Theory of high-harmonic generation by low-frequency laser fields.
Phys. Rev. A **49**, 2117–2132 (Mar 1994).
URL https://link.aps.org/doi/10.1103/PhysRevA.49.2117.

[67] R. H. Reiss.
Foundations of the Strong-Field Approximation, pp. 1–31.
Springer Berlin Heidelberg, Berlin, Heidelberg (2008).
URL http://dx.doi.org/10.1007/978-3-540-73794-0_1.

[68] A. D. Shiner, C. Trallero-Herrero, N. Kajumba, H.-C. Bandulet, D. Comtois, F. Légaré, M. Giguère, J.-C. Kieffer, P. B. Corkum, and D. M. Villeneuve.
Wavelength Scaling of High Harmonic Generation Efficiency.
Phys. Rev. Lett. **103**, 073902 (Aug 2009).
URL
http://link.aps.org/doi/10.1103/PhysRevLett.103.073902.

[69] P. M. Paul, E. S. Toma, P. Breger, G. Mullot, F. Augé, P. Balcou, H. G. Muller, and P. Agostini.
Observation of a Train of Attosecond Pulses from High Harmonic Generation.

Science **292**, 1689–1692 (2001).
URL http:
//www.sciencemag.org/content/292/5522/1689.abstract.

[70] M. J. Abel, T. Pfeifer, P. M. Nagel, W. Boutu, M. J. Bell, C. P. Steiner, D. M. Neumark, and S. R. Leone.
Isolated attosecond pulses from ionization gating of high-harmonic emission.
Chem. Phys. **366**, 9–14 (2009).

[71] G. Sansone, E. Benedetti, F. Calegari, C. Vozzi, L. Avaldi, R. Flammini, L. Poletto, P. Villoresi, C. Altucci, R. Velotta, S. Stagira, S. D. Silvestri, and M. Nisoli.
Isolated single-cycle attosecond pulses.
Science **314**, 443–446 (2006).

[72] I. J. Sola, E. Mevel, L. Elouga, E. Constant, V. Strelkov, L. Poletto, P. Villoresi, E. Benedetti, J. P. Caumes, S. Stagira, C. Vozzi, G. Sansone, and M. Nisoli.
Controlling attosecond electron dynamics by phase-stabilized polarization gating.
Nat. Physics **2**, 319–322 (2006).

[73] M. Chini, K. Zhao, and Z. Chang.
The generation, characterization and applications of broadband isolated attosecond pulses.
Nature Photonics **8**, 178–186 (Mar 2014).
URL http://www.nature.com/nphoton/journal/v8/n3/full/nphoton.2013.362.html.

[74] H. Mashiko, S. Gilbertson, C. Q. Li, S. D. Khan, M. M. Shakya, E. Moon, and Z. H. Chang.
Double optical gating of high-order harmonic generation with carrier-envelope phase stabilized lasers.
Phys. Rev. Lett. **100**, 103906 (2008).

[75] M. Hentschel, R. Kienberger, C. Spielmann, G. A. Reider, N. Milosevic, T. Brabec, P. Corkum, U. Heinzmann, M. Drescher, and F. Krausz.
Attosecond metrology.
Nature **414**, 509–513 (2001).

[76] H. G. Kurz, D. S. Steingrube, D. Ristau, M. Lein, U. Morgner, and M. Kovačev.
High-order-harmonic generation from dense water microdroplets.
Physical Review A **87**, 063811 (2013).

[77] T. T. Luu, M. Garg, S. Y. Kruchinin, A. Moulet, M. T. Hassan, and E. Goulielmakis.
Extreme ultraviolet high-harmonic spectroscopy of solids.
Nature **521**, 498â502 (May 2015).
URL http://dx.doi.org/10.1038/nature14456.

[78] P. Dirac.
The Principles of Quantum Mechanics.
International series of monographs on physics. Clarendon Press (1981).
URL https://books.google.de/books?id=XehUpGiM6FIC.

[79] D. J. Tannor.
Introduction to Quantum Mechanics: A Time-Dependent Perspective.
University Science Books, Sausalito (2003).

[80] T. Weigand.
Theoretical Quantum Mechanics PTP4 Lecture Script.
University of Heidelberg (2011).

[81] M. Vogel.
Quantum Computation and Quantum Information, by M.A. Nielsen and I.L. Chuang.
Contemporary Physics **52**, 604–605 (2011).
URL https://doi.org/10.1080/00107514.2011.587535.

[82] L. Essen and J. Parry.
An Atomic Standard of Frequency and Time Interval: A Caesium Resonator.
Nature 176, 280-282 (1955).

[83] I. I. Rabi.
Space Quantization in a Gyrating Magnetic Field.
Phys. Rev. **51**, 652–654 (1937).

[84] S. H. Autler and C. H. Townes.
Stark Effect in Rapidly Varying Fields.
Phys. Rev. **100**, 703–722 (1955).

[85] B. H. Bransden and C. J. Joachain.
Physics of atoms and molecules.
Second edition. Prentice Hall, Harlow; Munich (2007).

[86] W. Demtröder.
Laserspektroskopie.
5. Auflage. Springer, Berlin Heidelberg (2007).

[87] U. Fano.
Correlations of two excited electrons.
Rep. Prog. Phys. **46**, 97 (1983).

[88] L. Meitner.
Über die Entstehung der β-Strahl-Spektren radioaktiver Substanzen.
Zeitschrift für Physik **9**, 131–144 (Dec 1922).
URL https://doi.org/10.1007/BF01326962.

[89] U. Fano.
Sullo spettro di assorbimento dei gas nobili presso il limite dello spettro d'arco.
Il Nuovo Cimento (1924-1942) **12**, 154–161 (1935).
URL http://dx.doi.org/10.1007/BF02958288.

[90] U. Fano.
Effects of Configuration Interaction on Intensities and Phase Shifts.
Phys. Rev. **124**, 1866–1878 (Dec 1961).
URL https://link.aps.org/doi/10.1103/PhysRev.124.1866.

[91] H. Beutler.
Über absorptionsserien von argon, krypton und xenon zu termen zwischen den beiden ionisierungsgrenzen 2P3 2/0 und 2P1 2/0.
Z. Phys. A **93**, 177–196 (1935).

[92] P. Lambropoulos and P. Zoller.
Autoionizing states in strong laser fields.
Phys. Rev. A **24**, 379–397 (1981).

[93] K. Rzążewski and J. H. Eberly.

Confluence of Bound-Free Coherences in Laser-Induced Autoionization.
Phys. Rev. Lett. **47**, 408–412 (Aug 1981).
URL
https://link.aps.org/doi/10.1103/PhysRevLett.47.408.

[94] Z. Altun, S. L. Carter, and H. P. Kelly.
Photoionization cross section of neutral calcium including double electron resonances.
Phys. Rev. A **27**, 1943–1957 (Apr 1983).
URL https://link.aps.org/doi/10.1103/PhysRevA.27.1943.

[95] H. Bachau, P. Lambropoulos, and R. Shakeshaft.
Theory of laser-induced transitions between autoionizing states of He.
Phys. Rev. A **34**, 4785–4792 (1986).

[96] L. B. Madsen, P. Schlagheck, and P. Lambropoulos.
Laser-Induced Transitions between Triply Excited Hollow States.
Phys. Rev. Lett. **85**, 42–45 (2000).

[97] L. B. Madsen, P. Schlagheck, and P. Lambropoulos.
Laser-induced transitions between triply excited hollow states.
Phys. Rev. A **62**, 062719 (2000).

[98] L. B. Madsen and P. Lambropoulos.
Line shapes in photoexcitation of triply excited hollow states.
J. Phys. B **34**, 1855 (2001).

[99] S. I. Themelis, P. Lambropoulos, and M. Meyer.
Ionization dynamics in double resonance involving autoionizing states in helium: the effect of pulse shapes.
J. Phys. B **37**, 4281 (2004).

[100] *NIST Atomic Spectra Database Levels Form*.
URL http:
//physics.nist.gov/PhysRefData/ASD/levels_form.html.

[101] H. Klar.
Correlation in single- and multiphoton processes.
In F. Ehlotzky (Ed.), *Fundamentals of Laser Interactions*, volume 229 of *Lecture Notes in Physics*, pp. 149–160. Springer Berlin / Heidelberg (1985).
10.1007/3-540-15640-2_43.

[102] R. P. Madden and K. Codling.
New autoionizing atomic energy levels in He, Ne and Ar.
Phys. Rev. Lett. **10**, 516–518 (1963).

[103] J. W. Cooper, U. Fano, and F. Prats.
Classification of Two-Electron Excitation Levels of Helium.
Phys. Rev. Lett. **10**, 518–521 (1963).

[104] K. Schulz, G. Kaindl, M. Domke, J. D. Bozek, P. A. Heimann, A. S. Schlachter, and J. M. Rost.
Observation of New Rydberg Series and Resonances in Doubly Excited Helium at Ultrahigh Resolution.
Phys. Rev. Lett. **77**, 3086–3089 (1996).

[105] M. Domke, K. Schulz, G. Remmers, G. Kaindl, and D. Wintgen.
High-resolution study of P-1(0) double-excitation states in helium.

Phys. Rev. A **53**, 1424–1438 (1996).

[106] A. Bürgers, D. Wintgen, and J.-M. Rost.
Highly doubly excited S states of the helium atom.
J. Phys. B **28**, 3163 (1995).

[107] D. R. Herrick and O. Sinanoğlu.
Comparison of doubly-excited helium energy levels, isoelectronic series, autoionization lifetimes, and group-theoretical configuration-mixing predictions with large-configuration-interaction calculations and experimental spectra.
Phys. Rev. A **11**, 97–110 (1975).

[108] D. R. Herrick.
New Symmetry Properties of Atoms and Molecules, volume 52, pp. 1–115.
John Wiley & Sons, Inc. (1983).

[109] C. D. Lin.
Classification of Doubly Excited States of Two-Electron Atoms.
Phys. Rev. Lett. **51**, 1348–1351 (1983).

[110] C. D. Lin.
Hyperspherical coordinate approach to atomic and other Coulombic three-body systems.
Phys. Rep. **257**, 1 – 83 (1995).

[111] G. Tanner, K. Richter, and J.-M. Rost.
The theory of two-electron atoms: between ground state and complete fragmentation.
Rev. Mod. Phys. **72**, 497–544 (2000).

[112] V. Volterra.
Theory of Functionals and of Integrals and Integro-Differential Equations.
Dover Dover Publications, Inc., New York (1959).

[113] R. de L. Kronig.
On the Theory of Dispersion of X-Rays.
J. Opt. Soc. Am. **12**, 547–557 (Jun 1926).
URL `http://www.osapublishing.org/abstract.cfm?URI=josa-12-6-547`.

[114] H. Kramers.
La diffusion de la lumiere par les atomes.
Atti Cong. Intern. Fisici, (Transactions of Volta Centenary Congress) Como. Bd. 2 (1927).

[115] R. Kubo.
Statistical-Mechanical Theory of Irreversible Processes. I. General Theory and Simple Applications to Magnetic and Conduction Problems.
Journal of the Physical Society of Japan **12**, 570–586 (1957).
URL `https://doi.org/10.1143/JPSJ.12.570`.

[116] C. Ott, A. Kaldun, P. Raith, K. Meyer, M. Laux, J. Evers, C. H. Keitel, C. H. Greene, and T. Pfeifer.
Lorentz Meets Fano in Spectral Line Shapes: A Universal Phase and Its Laser Control.
Science **340**, 716–720 (2013).
URL `http://science.sciencemag.org/content/340/6133/716`.

[117] R. Feynman, R. Leighton, and M. Sands.
The Feynman Lectures on Physics.
Addison-Wesley (1963).

[118] M. Sargent, M. Scully, and W. Lamb.
Laser Physics.
Addison-Wesley (1974).

[119] F. Hopf and G. Stegeman.
Applied Classical Electrodynamics: Linear Optics.
Wiley (1985).

[120] C.-Y. Chung, J. Hsu, S. Mukamel, and E. O. Potma.
Controlling stimulated coherent spectroscopy and microscopy by a position-dependent phase.
Phys. Rev. A **87**, 033833 (Mar 2013).
URL
https://link.aps.org/doi/10.1103/PhysRevA.87.033833.

[121] R. W. Boyd.
Nonlinear Optics.
Second Edition. Academic Press (2003).

[122] C. Rullière (Ed.).
Femtosecond Laser Pulses.
Second Edition. Springer (2005).

[123] H. Haken and H. Wolf.
Atom- und Quantenphysik.
Springer (2004).

[124] W. Demtröder.
Experimentalphysik 3: Atome, Moleküle und Festkörper.
Springer (2010).

[125] D. J. Haxton, K. V. Lawler, and C. W. McCurdy.
Multiconfiguration time-dependent Hartree-Fock treatment of electronic and nuclear dynamics in diatomic molecules.
Phys. Rev. A **83**, 063416 (Jun 2011).
URL
https://link.aps.org/doi/10.1103/PhysRevA.83.063416.

[126] M. Marques and E. Gross.
TIME-DEPENDENT DENSITY FUNCTIONAL THEORY.
Annual Review of Physical Chemistry **55**, 427–455 (2004).
URL https:
//doi.org/10.1146/annurev.physchem.55.091602.094449.
PMID: 15117259.

[127] C. Ott, A. Kaldun, L. Argenti, P. Raith, K. Meyer, M. Laux, Y. Zhang, A. Blättermann, S. Hagstotz, T. Ding, R. Heck, J. Madroñero, F. Martin, and T. Pfeifer.
Reconstruction and control of a time-dependent two-electron wave packet.
Nature **516**, 374–378 (Dec 2014).
URL http://www.nature.com/nature/journal/v516/n7531/full/nature14026.html.

[128] Z. H. Loh, M. Khalil, R. E. Correa, and S. R. Leone.
A tabletop femtosecond time-resolved soft x-ray transient absorption spectrometer.
Rev. Sci. Instrum. **79**, 073101 (2008).

[129] W.-C. Chu, S.-F. Zhao, and C. D. Lin.
Laser-assisted-autoionization dynamics of helium resonances with single attosecond pulses.
Phys. Rev. A **84**, 033426 (2011).

[130] D. Volkov.
NA.
Z. Phys 94 250 (1934).

[131] M. D. Feit, J. A. Fleck, Jr., and A. Steiger.
Solution of the Schrödinger Equation by a Spectral Method.
J. Comput. Phys. **47**, 412–433 (1982).

[132] A. D. Bandrauk and H. Shen.
Improved exponential split operator method for solving the time-dependent Schrödinger equation.
Chemical Physics Letters **176**, 428 – 432 (1991).
URL `http://www.sciencedirect.com/science/article/pii/000926149190232X`.

[133] R. Grobe and J. H. Eberly.
Photoelectron spectra for a two-electron system in a strong laser field.
Physical Review Letters **68**, 2905–2908 (1992).

[134] R. Grobe and J. H. Eberly.
One-dimensional model of a negative ion and its interaction with laser fields.
Physical Review A **48**, 4664–4681 (1993).

[135] T. Ding.
Modellatom mit zwei Elektronen in jeweils einer Raumdimension in Wechselwirkung mit XUV- und IR-Laserfeldern.
Bachelor's thesis, Ruprecht-Karls-Universität Heidelberg (2010).

[136] G. D. Borisova.
Einfluss der Elektron-Elektron-Korrelation auf die Ionisation von Atomen in starken, ultrakurzen Laser-Impulsen.
Bachelor's thesis, Ruprecht-Karls-Universität Heidelberg, Deutschland (2015).

[137] S. L. Haan, R. Grobe, and J. H. Eberly.
Numerical study of autoionizing states in completely correlated two-electron systems.
Phys. Rev. A **50**, 378–391 (1994).

[138] L. Roso, L. Plaja, P. Moreno, E. C. Jarque, J. R. V. de Aldana, J. San Roman, and C. Ruiz.
Multielectron atomic models using the Rochester one-dimensional potential.
Laser Physics **15**, 1393–1409 (2005).

[139] D. Bauer.
Two-dimensional, two-electron model atom in a laser pulse: Exact treatment, single-active-electron analysis, time-dependent density-functional theory, classical calculations, and nonsequential ionization.

Physical Review A **56**, 3028–3039 (1997).
URL http://journals.aps.org/pra/abstract/10.1103/PhysRevA.56.3028.

[140] V. Kapoor.
Autoionization in time-dependent density-functional theory.
Physical Review A **93**, 1–8 (2016).

[141] G. Lagmago Kamta and A. F. Starace.
Multielectron system in an ultrashort, intense laser field: A nonperturbative, time-dependent two-active-electron approach.
Physical Review A **65**, 053418 (2002).
URL http://link.aps.org/doi/10.1103/PhysRevA.65.053418{%}5Cnhttp://pra.aps.org/pdf/PRA/v65/i5/e053418.

[142] G. Camiolo, G. Castiglia, P. P. Corso, E. Fiordilino, and J. P. Marangos.
Two-electron systems in strong laser fields.
Physical Review A - Atomic, Molecular, and Optical Physics **79**, 1–9 (2009).

[143] J. Feist, S. Nagele, R. Pazourek, E. Persson, B. I. Schneider, L. A. Collins, and J. Burgdörfer.
Nonsequential two-photon double ionization of helium.
Phys. Rev. A **77**, 043420 (Apr 2008).
URL
https://link.aps.org/doi/10.1103/PhysRevA.77.043420.

[144] J. Colgan and M. S. Pindzola.
Core-Excited Resonance Enhancement in the Two-Photon Complete Fragmentation of Helium.
Phys. Rev. Lett. **88**, 173002 (Apr 2002).
URL
https://link.aps.org/doi/10.1103/PhysRevLett.88.173002.

[145] S. Laulan and H. Bachau.
Correlation effects in two-photon single and double ionization of helium.
Phys. Rev. A **68**, 013409 (Jul 2003).
URL
https://link.aps.org/doi/10.1103/PhysRevA.68.013409.

[146] M. S. Pindzola, F. Robicheaux, S. D. Loch, J. C. Berengut, T. Topcu, J. Colgan, M. Foster, D. C. Griffin, C. P. Ballance, D. R. Schultz, T. Minami, N. R. Badnell, M. C. Witthoeft, D. R. Plante, D. M. Mitnik, J. A. Ludlow, and U. Kleiman.
The time-dependent close-coupling method for atomic and molecular collision processes.
Journal of Physics B: Atomic, Molecular and Optical Physics **40**, R39 (2007).
URL http://stacks.iop.org/0953-4075/40/i=7/a=R01.

[147] T. N. Rescigno and C. W. McCurdy.
Numerical grid methods for quantum-mechanical scattering problems.
Phys. Rev. A **62**, 032706 (Aug 2000).
URL
https://link.aps.org/doi/10.1103/PhysRevA.62.032706.

[148] C. W. McCurdy, D. A. Horner, and T. N. Rescigno.
Practical calculation of amplitudes for electron-impact ionization.

Phys. Rev. A **63**, 022711 (Jan 2001).
URL
https://link.aps.org/doi/10.1103/PhysRevA.63.022711.

[149] B. I. Schneider and L. A. Collins.
The discrete variable method for the solution of the time-dependent Schrödinger equation.
Journal of Non-Crystalline Solids **351**, 1551 – 1558 (2005).
URL http://www.sciencedirect.com/science/article/pii/S0022309305002164.
Papers from the Michael Weinberg Symposium.

[150] T. J. Park and J. C. Light.
Unitary quantum time evolution by iterative Lanczos reduction.
The Journal of Chemical Physics **85**, 5870–5876 (1986).
URL https://doi.org/10.1063/1.451548.

[151] E. S. Smyth, J. S. Parker, and K. Taylor.
Numerical integration of the time-dependent Schrödinger equation for laser-driven helium.
Computer Physics Communications **114**, 1 – 14 (1998).
URL http://www.sciencedirect.com/science/article/pii/S0010465598000836.

[152] J. M. Hollas.
Modern Spectroscopy.
John Wiley & Sons (2004).

[153] W. S. Boyle and G. E. Smith.
Charge coupled semiconductor devices.
The Bell System Technical Journal **49**, 587–593 (April 1970).

[154] F. Stöckmann.
Photodetectors, their performance and their limitations.
Applied physics **7**, 1–5 (May 1975).
URL https://doi.org/10.1007/BF00900511.

[155] J. Fraunhofer.
Bestimmung des Brechungs- und des Farbenzerstreungs-Vermögens verschiedener Glasarten, in Bezug auf die Vervollkommnung achromatischer Fernröhre.
Ann. Phys. **56**, 264–313 (1817).

[156] W. E. Lamb and R. C. Retherford.
Fine Structure of the Hydrogen Atom by a Microwave Method.
Phys. Rev. **72**, 241–243 (Aug 1947).
URL https://link.aps.org/doi/10.1103/PhysRev.72.241.

[157] J. Ullrich and H. Schmidt-Böcking.
Time-of-flight spectrometer for the determination of microradian projectile scattering angles in atomic collisions.
Physics Letters A **125**, 193–196 (1987).

[158] R. Dörner, V. Mergel, O. Jagutzki, L. Spielberger, J. Ullrich, R. Moshammer, and H. Schmidt-Böcking.
Cold Target Recoil Ion Momentum Spectroscopy: a 'momentum microscope' to view atomic collision dynamics.

Physics Reports **330**, 95 – 192 (2000).
URL http://www.sciencedirect.com/science/article/pii/S037015739900109X.

[159] J. Ullrich, R. Moshammer, A. Dorn, R. Dörner, L. P. H. Schmidt, and H. Schmidt-Böcking.
Recoil-ion and electron momentum spectroscopy: reaction-microscopes.
Reports on Progress in Physics **66**, 1463 (2003).
URL http://stacks.iop.org/0034-4885/66/i=9/a=203.

[160] N. Camus, B. Fischer, M. Kremer, V. Sharma, A. Rudenko, B. Bergues, M. Kübel, N. G. Johnson, M. F. Kling, T. Pfeifer, J. Ullrich, and R. Moshammer.
Attosecond Correlated Dynamics of Two Electrons Passing through a Transition State.
Phys. Rev. Lett. **108**, 073003 (Feb 2012).
URL http://link.aps.org/doi/10.1103/PhysRevLett.108.073003.

[161] K. Schnorr, A. Senftleben, M. Kurka, A. Rudenko, L. Foucar, G. Schmid, A. Broska, T. Pfeifer, K. Meyer, D. Anielski, R. Boll, D. Rolles, M. Kübel, M. F. Kling, Y. H. Jiang, S. Mondal, T. Tachibana, K. Ueda, T. Marchenko, M. Simon, G. Brenner, R. Treusch, S. Scheit, V. Averbukh, J. Ullrich, C. D. Schröter, and R. Moshammer.
Time-Resolved Measurement of Interatomic Coulombic Decay in Ne_2.
Phys. Rev. Lett. **111**, 093402 (2013).

[162] L. Fechner, N. Camus, J. Ullrich, T. Pfeifer, and R. Moshammer.
Strong-Field Tunneling from a Coherent Superposition of Electronic States.
Phys. Rev. Lett. **112**, 213001 (May 2014).
URL http://link.aps.org/doi/10.1103/PhysRevLett.112.213001.

[163] M. Eigen and L. D. Maeyer.
Self-dissociation and protonic charge transport in water and.
Proceedings of the Royal Society of London A: Mathematical, Physical and Engineering Sciences **247**, 505–533 (1958).
URL http://rspa.royalsocietypublishing.org/content/247/1251/505.

[164] W. T. Pollard and R. A. Mathies.
Analysis of Femtosecond Dynamic Absorption Spectra of Nonstationary States.
Annual Review of Physical Chemistry **43**, 497–523 (1992).
URL https://doi.org/10.1146/annurev.pc.43.100192.002433.
PMID: 1463575.

[165] P. Kukura, D. W. McCamant, and R. A. Mathies.
Femtosecond stimulated Raman spectroscopy.
Annu. Rev. Phys. Chem. **58**, 461–488 (2007).

[166] Z. H. Loh, M. Khalil, R. E. Correa, R. Santra, C. Buth, and S. R. Leone.
Quantum state-resolved probing of strong-field-ionized xenon atoms using femtosecond high-order harmonic transient absorption spectroscopy.
Phys. Rev. Lett. **98**, 143601 (2007).

[167] E. L. Saldin, E. A. Schneidmiller, and M. V. Yurkov.
The Physics of Free Electron Lasers.
Springer, Berlin Heidelberg (2000).

[168] A. L'Huillier and P. Balcou.
High-order harmonic generation in rare gases with a 1-ps 1053-nm laser.
Phys. Rev. Lett. **70**, 774–777 (Feb 1993).
URL
https://link.aps.org/doi/10.1103/PhysRevLett.70.774.

[169] J. Itatani, J. Levesque, D. Zeidler, H. Niikura, H. Pepin, J. C. Kieffer, P. B. Corkum, and D. M. Villeneuve.
Tomographic imaging of molecular orbitals.
Nature **432**, 867–871 (2004).

[170] N. Dudovich, O. Smirnova, J. Levesque, Y. Mairesse, M. Y. Ivanov, D. Villeneuve, and P. B. Corkum.
Measuring and controlling the birth of attosecond XUV pulses.
Nature physics **2**, 781–786 (2006).

[171] H. Worner, J. Bertrand, D. Kartashov, P. Corkum, and D. Villeneuve.
Following a chemical reaction using high-harmonic spectroscop.
Nature **466**, 604–607 (2010).

[172] R. Kienberger, E. Goulielmakis, M. Uiberacker, A. Baltuška, V. Yakovlev, F. Bammer, A. Scrinzi, T. Westerwalbesloh, U. Kleineberg, U. Heinzmann, M. Drescher, and F. Krausz.
Atomic transient recorder.
Nature **427**, 817–821 (2004).

[173] E. Goulielmakis, M. Uiberacker, R. Kienberger, A. Baltuška, V. Yakovlev, A. Scrinzi, T. Westerwalbesloh, U. Kleineberg, U. Heinzmann, M. Drescher, and F. Krausz.
Direct measurement of light waves.
Science **305**, 1267–1269 (2004).

[174] E. Goulielmakis, V. S. Yakovlev, A. L. Cavalieri, M. Uiberacker, V. Pervak, A. Apolonski, R. Kienberger, U. Kleineberg, and F. Krausz.
Attosecond control and measurement: Lightwave electronics.
Science **317**, 769–775 (2007).

[175] P. Eckle, M. Smolarski, P. Schlup, J. Biegert, A. Staudte, M. Schöffler, H. G. Muller, R. Dörner, and U. Keller.
Attosecond angular streaking.
Nature Physics **4**, 565–570 (Jul 2008).
URL http://www.nature.com/nphys/journal/v4/n7/full/nphys982.html.

[176] L. Torlina, F. Morales, J. Kaushal, I. Ivanov, A. Kheifets, A. Zielinski, A. Scrinzi, H. G. Muller, S. Sukiasyan, M. Ivanov, et al.
Interpreting attoclock measurements of tunnelling times.
Nature Physics (2015).

[177] Z. H. Loh, C. H. Greene, and S. R. Leone.
Femtosecond induced transparency and absorption in the extreme ultraviolet by coherent coupling of the He 2s2p (P-1(o)) and 2p(2) (S-1(e)) double excitation

states with 800 nm light.
Chem. Phys. **350**, 7–13 (2008).

[178] E. Goulielmakis, Z. H. Loh, A. Wirth, R. Santra, N. Rohringer, V. S. Yakovlev, S. Zherebtsov, T. Pfeifer, A. M. Azzeer, M. F. Kling, S. R. Leone, and F. Krausz.
Real-time observation of valence electron motion.
Nature **466**, 739–743 (2010).
URL `http://www.nature.com/nature/journal/v466/n7307/full/nature09212.html`.

[179] M. Holler, F. Schapper, L. Gallmann, and U. Keller.
Attosecond Electron Wave-Packet Interference Observed by Transient Absorption.
Phys. Rev. Lett. **106**, 123601 (Mar 2011).
URL `https://link.aps.org/doi/10.1103/PhysRevLett.106.123601`.

[180] T. Remetter, P. Johnsson, J. Mauritsson, K. Varju, Y. Ni, F. Lepine, E. Gustafsson, M. Kling, J. Khan, R. Lopez-Martens, K. J. Schafer, M. J. J. Vrakking, and A. L'Huillier.
Attosecond electron wave packet interferometry.
Nat. Physics **2**, 323–326 (2006).

[181] H. Wang, M. Chini, S. Y. Chen, C. H. Zhang, F. He, Y. Cheng, Y. Wu, U. Thumm, and Z. H. Chang.
Attosecond Time-Resolved Autoionization of Argon.
Phys. Rev. Lett. **105**, 143002 (2010).

[182] C. Ott.
Attosecond multidimensional interferometry of single and two correlated electrons in atoms.
Ph.D. thesis, Universität Heidelberg (2012).

[183] A. Kaldun.
Fano Resonances in the Time Domain - understanding and controlling the absorption and emission of light.
PhD Thesis, Universität Heidelberg (2014).

[184] A. Blättermann.
Impulsive control of the atomic dipole response in the time and frequency domain.
Ph.D. thesis, Ruperto-Carola-University of Heidelberg (2016).

[185] F. P. GmbH.
CEP4^{TM} Module for FEMTOSOURCE^{TM} rainbow^{TM}, Operators Manual, Technical report (2013).

[186] S. Koke, C. Grebing, H. Frei, A. Anderson, A. Assion, and G. Steinmeyer.
Direct frequency comb synthesis with arbitrary offset and shot-noise-limited phase noise.
Nat. Photonics **4**, 462–465 (2010).

[187] M. Hartmann.
Characterization of Few-Cycle Laser Pulses.
Master's thesis, Ruperto-Carola-University of Heidelberg (2016).

[188] R. Trebino.
Frequency-Resolved Optical Gating: The Measurement of Ultrashort Laser Pulses.

Kluwer Academic Publishers, Boston (2002).

[189] C. Iaconis and I. A. Walmsley.
Spectral phase interferometry for direct electric-field reconstruction of ultrashort optical pulses.
Opt. Lett. **23**, 792–794 (1998).

[190] J. Itatani, F. Quéré, G. L. Yudin, M. Y. Ivanov, F. Krausz, and P. B. Corkum.
Attosecond streak camera.
Phys. Rev. Lett. **88**, 173903 (2002).

[191] F. Calegari, G. Sansone, S. Stagira, C. Vozzi, and M. Nisoli.
Advances in attosecond science.
Journal of Physics B: Atomic, Molecular and Optical Physics **49**, 062001 (2016).
URL `http://stacks.iop.org/0953-4075/49/i=6/a=062001`.

[192] M. Miranda, C. L. Arnold, T. Fordell, F. Silva, B. Alonso, R. Weigand, A. L'Huillier, and H. Crespo.
Characterization of broadband few-cycle laser pulses with the d-scan technique.
Opt. Express **20**, 18732–18743 (Aug 2012).
URL `http://www.opticsexpress.org/abstract.cfm?URI=oe-20-17-18732`.

[193] M. Miranda, T. Fordell, C. Arnold, A. L'Huillier, and H. Crespo.
Simultaneous compression and characterization of ultrashort laser pulses using chirped mirrors and glass wedges.
Opt. Express **20**, 688–697 (Jan 2012).
URL `http://www.opticsexpress.org/abstract.cfm?URI=oe-20-1-688`.

[194] http://www.nist.gov/pml/data/periodic.cfm.

[195] *http://henke.lbl.gov/opticalconstants*.

[196] http://www.corning.com/emea/de/products/advanced-optics/product-materials/specialty-glass-and-glass-ceramics/glass ceramics/macor.html.
MACOR Machinable Glass.

[197] M. Schultze, A. Wirth, I. Grguras, M. Uiberacker, T. Uphues, A. Verhoef, J. Gagnon, M. Hofstetter, U. Kleineberg, E. Goulielmakis, and F. Krausz.
State-of-the-art attosecond metrology.
J. Electron. Spectrosc. Relat. Phenom. **184**, 68 – 77 (2011).

[198] L. Poletto, S. Bonora, M. Pascolini, and P. Villoresi.
Instrumentation for analysis and utilization of extreme-ultraviolet and soft x-ray high-order harmonics.
Rev. Sci. Instrum. **75**, 4413–4418 (2004).

[199] F. Calegari, M. Lucchini, M. Negro, C. Vozzi, L. Poletto, O. Svelto, S. D. Silvestri, G. Sansone, S. Stagira, and M. Nisoli.
Temporal gating methods for the generation of isolated attosecond pulses.
J. Phys. B **45**, 074002 (2012).

[200] M. Rebholz.
Design and construction of an experimental setup for multidimensional spectroscopy in the XUV/ soft-X-ray spectral region.
Master's thesis, Ruperto-Carola-University of Heidelberg (2015).

[201] *http://www.lebowcompany.com/*.
[202] *http://henke.lbl.gov/opticalconstants/filter2.html*.
[203] G. D. Borisova.
Theoretical and Experimental Studies of XUV Multielectron (Auto-)Ionization Dynamics in Helium and Molecular Hydrogen.
Master's thesis, Ruperto-Carola-University of Heidelberg (2017).
[204] L. Aufleger.
Measurement of electron dynamics in atoms and molecules with intense XUV FEL radiation.
Master's thesis, Ruperto-Carola-University of Heidelberg (2016).
[205] T. Ding.
Quantum dynamics in weak and strong fields measured by XUV nonlinear spectroscopy.
Ph.D. thesis, Ruperto-Carola-University of Heidelberg (2018).
[206] F. Kaap.
TBA.
Master's thesis, Ruperto-Carola-University of Heidelberg (2018).
[207] N. Nakano, H. Kuroda, T. Kita, and T. Harada.
Development of a flat-field grazing-incidence XUV spectrometer and its application in picosecond XUV spectroscopy.
Appl. Opt. **23**, 2386–2392 (1984).
[208] T. Kita, T. Harada, N. Nakano, and H. Kuroda.
Mechanically ruled aberration-corrected concave gratings for a flat-field grazing-incidence spectrograph.
Appl. Opt. **22**, 512–513 (1983).
[209] H. A. Rowland.
XXIX. On concave gratings for optical purposes.
Philos. Mag. Ser. 5 **16**, 197–210 (1883).
[210] H. G. Beutler.
The Theory of the Concave Grating.
J. Opt. Soc. Am. **35**, 311–350 (1945).
[211] http://www.princetoninstruments.com.
[212] V. Stooß, S. Cavaletto, A. Blaettermann, P. Birk, C. Keitel, C. Ott, and T. Pfeifer.
Real-time reconstruction of complex non-equilibrium quantum dynamics of matter.
arXiv:1706.07218 (2017).
[213] P. Hamm and M. Zanni.
Concepts and Methods of 2D Infrared spectroscopy.
Cambridge University Press (2011).
[214] S. Pabst, A. Sytcheva, A. Moulet, A. Wirth, E. Goulielmakis, and R. Santra.
Theory of attosecond transient-absorption spectroscopy of krypton for overlapping pump and probe pulses.
Phys. Rev. A **86**, 063411 (Dec 2012).
URL
https://link.aps.org/doi/10.1103/PhysRevA.86.063411.
[215] M. Wu, S. Chen, M. B. Gaarde, and K. J. Schafer.

Time-domain perspective on Autler-Townes splitting in attosecond transient absorption of laser-dressed helium atoms.
Phys. Rev. A **88**, 043416 (Oct 2013).
URL
https://link.aps.org/doi/10.1103/PhysRevA.88.043416.

[216] A. Kaldun, C. Ott, A. Blättermann, M. Laux, K. Meyer, T. Ding, A. Fischer, and T. Pfeifer.
Extracting Phase and Amplitude Modifications of Laser-Coupled Fano Resonances.
Phys. Rev. Lett. **112**, 103001 (Mar 2014).
URL https:
//link.aps.org/doi/10.1103/PhysRevLett.112.103001.

[217] H. Mashiko, T. Yamaguchi, K. Oguri, A. Suda, and H. Gotoh.
Characterizing inner-shell with spectral phase interferometry for direct electric-field reconstruction.
Nature Communications 5, 5599 (2014).

[218] S. R. Leone, C. W. McCurdy, J. Burgdörfer, L. S. Cederbaum, Z. Chang, N. Dudovich, C. H. G. Johannes Feist, M. Ivanov, R. Kienberger, U. Keller, M. F. Kling, Z.-H. Loh, T. Pfeifer, A. N. Pfeiffer, R. Santra, K. Schafer, A. Stolow, U. Thumm, and M. J. J. Vrakking.
What will it take to observe processes in 'real time'?
Nature Photonics 8, 162-166 (2014).

[219] S. Haessler, T. Balčiunas, G. Fan, G. Andriukaitis, A. Pugžlys, A. Baltuška, T. Witting, R. Squibb, A. Zaïr, J. W. G. Tisch, J. P. Marangos, and L. E. Chipperfield.
Optimization of Quantum Trajectories Driven by Strong-Field Waveforms.
Phys. Rev. X **4**, 021028 (May 2014).
URL https://link.aps.org/doi/10.1103/PhysRevX.4.021028.

[220] J. Mizrahi, B. Neyenhuis, K. G. Johnson, W. C. Campbell, C. Senko, D. Hayes, and C. Monroe.
Quantum control of qubits and atomic motion using ultrafast laser pulses.
Applied Physics B **114**, 45–61 (Jan 2014).
URL https://doi.org/10.1007/s00340-013-5717-6.

[221] R. Pazourek, S. Nagele, and J. Burgdörfer.
Attosecond chronoscopy of photoemission.
Rev. Mod. Phys. **87**, 765–802 (Aug 2015).
URL https://link.aps.org/doi/10.1103/RevModPhys.87.765.

[222] M. B. Gaarde, C. Buth, J. L. Tate, and K. J. Schafer.
Transient absorption and reshaping of ultrafast XUV light by laser-dressed helium.
Phys. Rev. A **83**, 013419 (2011).

[223] A. Blättermann, C. Ott, A. Kaldun, T. Ding, V. Stooß, M. Laux, M. Rebholz, and T. Pfeifer.
In situ characterization of few-cycle laser pulses in transient absorption spectroscopy.
Opt. Lett. **40**, 3464–3467 (Aug 2015).

URL http://ol.osa.org/abstract.cfm?URI=ol-40-15-3464.

[224] M. B. C. W. McCurdy and T. N. Rescigno.
Solving the three-body Coulomb breakup problem using exterior complex scaling.
J. Phys. B 37, R127 (2004).

[225] J. R. Harries, J. P. Sullivan, J. B. Sternberg, S. Obara, T. Suzuki, P. Hammond, J. Bozek, N. Berrah, M. Halka, and Y. Azuma.
Double Photoexcitation of Helium in a Strong dc Electric Field.
Phys. Rev. Lett. **90**, 133002 (Apr 2003).
URL
https://link.aps.org/doi/10.1103/PhysRevLett.90.133002.

[226] X. M. Tong and C. D. Lin.
Propensity Rule for Novel Selective Double Photoexcitation of Helium Atoms in Strong Static Electric Fields.
Phys. Rev. Lett. **92**, 223003 (Jun 2004).
URL
https://link.aps.org/doi/10.1103/PhysRevLett.92.223003.

[227] X. M. Tong and C. D. Lin.
Double photoexcitation of He atoms by attosecond xuv pulses in the presence of intense few-cycle infrared lasers.
Phys. Rev. A **71**, 033406 (Mar 2005).
URL
https://link.aps.org/doi/10.1103/PhysRevA.71.033406.

[228] V. Stooß, A. Kaldun, C. Ott, A. Blättermann, T. Ding, and T. Pfeifer.
Inversion symmetry breaking of atomic bound states in strong and short laser fields.
arXiv:1506.01182 (2015).

[229] A. Kaldun, A. Blättermann, V. Stooß, S. Donsa, H. Wei, R. Pazourek, S. Nagele, C. Ott, C. D. Lin, J. Burgdörfer, and T. Pfeifer.
Observing the ultrafast buildup of a Fano resonance in the time domain.
Science **354**, 738–741 (2016).
URL http://science.sciencemag.org/content/354/6313/738.

[230] M. Wickenhauser, J. Burgdorfer, F. Krausz, and M. Drescher.
Time resolved Fano resonances.
Phys. Rev. Lett. **94** (2005).

[231] T. Mercouris, Y. Komninos, and C. A. Nicolaides.
Time-dependent formation of the profile of the He $2s2p\,{}^1P^o$ *state excited by a short laser pulse*.
Phys. Rev. A **75**, 013407 (Jan 2007).
URL
https://link.aps.org/doi/10.1103/PhysRevA.75.013407.

[232] C. A. Nicolaides, T. Mercouris, and Y. Komninos.
Time-dependent formation of the profile of resonance atomic states and its dependence on the duration of ultrashort pulses from free-electron lasers.
Phys. Rev. A **80**, 055402 (Nov 2009).
URL
https://link.aps.org/doi/10.1103/PhysRevA.80.055402.

[233] W.-C. Chu and C. D. Lin.
Theory of ultrafast autoionization dynamics of Fano resonances.
Phys. Rev. A **82**, 053415 (Nov 2010).
URL
https://link.aps.org/doi/10.1103/PhysRevA.82.053415.

[234] L. Argenti and E. Lindroth.
Ionization Branching Ratio Control with a Resonance Attosecond Clock.
Phys. Rev. Lett. **105**, 053002 (2010).

[235] L. Argenti, R. Pazourek, J. Feist, S. Nagele, M. Liertzer, E. Persson, J. Burgdörfer, and E. Lindroth.
Photoionization of helium by attosecond pulses: Extraction of spectra from correlated wave functions.
Phys. Rev. A **87**, 053405 (May 2013).
URL
https://link.aps.org/doi/10.1103/PhysRevA.87.053405.

[236] V. Gruson, L. Barreau, Á. Jiménez-Galan, F. Risoud, J. Caillat, A. Maquet, B. Carré, F. Lepetit, J.-F. Hergott, T. Ruchon, L. Argenti, R. Taïeb, F. Martín, and P. Salières.
Attosecond dynamics through a Fano resonance: Monitoring the birth of a photoelectron.
Science **354**, 734–738 (2016).
URL http://science.sciencemag.org/content/354/6313/734.

[237] A. Blättermann, C. Ott, A. Kaldun, T. Ding, and T. Pfeifer.
Two-dimensional spectral interpretation of time-dependent absorption near laser-coupled resonances.
Journal of Physics B: Atomic, Molecular and Optical Physics **47**, 124008 (2014).
URL http://stacks.iop.org/0953-4075/47/i=12/a=124008.

Danksagung

Zum Abschluss der Arbeit möchte ich mich bei allen bedanken, die mich in den letzten Jahren begleitet und an der Entstehung dieser Arbeit mitgewirkt haben. Der Erfolg eines komplexen und aufwändigen Projekts wie einer Doktorarbeit ist immer verbunden mit hervorragender Teamarbeit, guter Betreuung sowie angenehmer Arbeitsatmosphäre und liegt nie ausschließlich in den Händen eines Einzelnen. Ich hatte das Glück all diese Dinge in unserer Gruppe zu erfahren. Vielen Dank, liebe *Interattos* und *X-Musicians* für die wunderbare Zeit.

Zuallererst möchte ich ganz besonders Thomas Pfeifer für die Möglichkeit danken, in seiner Gruppe zu promovieren. Vielen Dank für deine Unterstützung, die vielen Diskussionen, Ideen, die Förderung und das Vertrauen sowie die Tatsache, dass du dir trotz deiner vielen Aufgaben als Direktor bei Problemen und Fragen immer Zeit nimmst und uns weiter hilfst. Danke für die hervorragende Betreuung und natürlich auch für die Übernahme des Erstgutachtens meiner Arbeit.

Als nächstes möchte ich Professor Selim Jochim für die Übernahme des Zweitgutachtens dieser Arbeit danken.

Weiterhin möchte ich mich speziell bei Christian Ott bedanken, der seit seiner Rückkehr an das Institut zu meinem direkten Betreuer geworden ist und sich immer Zeit für uns genommen hat. Vielen Dank, für deine Hilfe, die vielen anregenden Gespräche, lehrreichen Diskussionen und Ratschläge, die maßgeblich zur Entstehung dieser Arbeit beigetragen haben.

Ein besonderer Dank geht an die Master Studenten und (späteren) Doktoranden Paul Birk, Gergana Borisova, Maximilian Hartmann sowie Alexander Blättermann, mit denen ich über die Jahre zusammenarbeiten durfte. Es war sehr angenehm, spaßig und produktiv mit euch im Labor zu stehen und neue Projekte aufzubauen, vielen Dank. Überhaupt möchte ich mich bei allen Kollegen aus der Interatto Gruppe, Martin Laux, Andreas Kaldun, Kristina Meyer, Nikola Mollov, Stephan Goerttler, Yonghao Mi, Janik Prottung und Jan Kilinc, sowie den Kollegen aus dem X-Music Team, Thomas Ding, Marc Rebholz, Lennart Aufleger, Carina da Costa Castanheira, Alexander Magunia, und allen weiteren Studenten, die über die Zeit teil der Gruppe waren, ganz herzlich für die gute Zusammenarbeit, sei es im Labor oder auf den Strahlzeiten und auch die schönen Momente abseits der Arbeit bedanken.

Außerdem möchte ich mich bei Professor Matthias Bartelmann und Professor Markus Motzkus als Teil meines Prüfungskomitees bedanken.

Weiterhin möchte ich mich bei Stefano Cavaletto und Christoph Keitel, sowie bei Stefan Donsa, Iva Brezinova und Joachim Burgdörfer und auch Chii-Dong Lin und Hui Wei für die sehr gute Zusammenarbeit und die viele hilfreichen Diskussionen bedanken.

Ebenfalls bedanke ich mich bei Jose Crespo Lopez-Urrutia und Jörg Evers die sich als Berater für meine Doktorarbeit zur Verfügung gestellt haben.

Auch möchte ich mich bei der Konstruktionsabteilung, der Werkstatt und der Elektronikabteilung des MPIK für die ausgezeichnete technische Unterstützung über die letzten Jahre bedanken.

Ein großer Dank gebührt weiter meiner Familie für ihre stetige Unterstützung.

Schließlich möchte ich mich ganz besonders bei bei meiner Freundin und zukünftigen Frau Elena Kozlikin bedanken, die mich während der letzten Jahre in guten wie in schlechten Zeiten begleitet und unterstützt hat.